NORTHWESTERN UNIVERSITY

Chemical and Mechanical Properties of Drying Oils during Polymerization

A DISSERTATION

SUBMITTED TO THE GRADUATE SCHOOL

IN PARTIAL FULFILLMENT OF THE REQUIREMENTS

for the degree

DOCTOR OF SCIENCE

Field of Materials Science and Engineering

By

Gwen dePolo

Evanston, IL

September 2023

Chemical and Mechanical Properties of Drying Oils during Polymerization

Gwen dePolo

Drying oils have been used as a binding medium for oil paints since the 15th century. These oil paints transition from a liquid-like paste to a solid-like film as a result of crosslinks forming between the oil molecules. These reactions have been extensively studied chemically, but other material properties are not as well characterized for drying oils. Oil paints are typically used in complex composite structures where the mechanical properties matter just as much as the chemical properties. This thesis focuses on understanding the evolution of mechanical properties during drying oil polymerization.

An overview of mechanical testing techniques used to study artists' paints in the last few decades is provided in Chapter 2. The effects of temperature, composition, relative humidity, and solvent exposure on the mechanical properties of a paint are discussed. Newer techniques that have the ability the monitor the evolution of mechanical properties in cultural heritage objects are also presented.

One of the challenges for most mechanical testing techniques is that they are unable to follow the evolution of mechanical properties during drying oil polymerization. In Chapter 3, the quartz crystal microbalance (QCM) is able to fill this gap, allowing changes in mass and mechanical properties to be measured during polymerization. Linseed oil samples are measured to observe these changes over several years of aging. Litharge (used to speed up polymerization) is incorporated and its effects are quantified. The temperature dependent response of a linseed oil film are measured and the lack of a well-defined glass transition temperature for the film implies that there is nano-scale heterogeneity due to variations of crosslink density in the film.

Another aspect that is not well understood is the effect of fatty acid distribution on drying oil polymerization. Chapter 4 discusses the use of time-based attentuated total reflection infrared

spectroscopy to obtain higher resolution of the chemical changes occurring during initial drying oil polymerization. Five drying oils are measured and demonstrated that there are some chemical differences depending on the fatty acid distribution of the drying oil. Incorporating litharge results in a significant reduction in the levels of oxidation reached in the drying oil films.

Acknowledgments

This thesis would not have been possible without the help of everyone who has supported me over these past five years. I wish to thank my advisors, Dr. Ken Shull, *Prof dr.* Piet Iedema, and Dr. Joen Hermans. Ken, thank you for providing so much optimism and guidance as I learned the nitty-gritty details about using the QCM. Piet, thank you for your help in maintaining my sense of the big picture, both in my thesis and in the logistics of pursuing a PhD jointly recognized by Northwestern University and the University of Amsterdam. Joen, thank you so much for all of your assistance with interpreting my FTIR data as well as your helping me feel welcome and like part of the research groups at UvA and the Rijksmuseum when I was working in Amsterdam.

I would also like to thank the following professors for serving as my committee members for the two parts of the defense: Dr. Erik Luijten, Dr. Wesley Burghardt., Dr. Linda Broadbelt, Dr. Marc Walton, Dr. John Torkelson, *Prof. dr.* Katrien Keune, *Prof. dr.* Klaas Jan van den Berg, and *Prof. dr.* Noushine Shahidzadeh. Thank you all for your willingness to be on both committees. Your insights on my research and how it can extend beyond the field of cultural heritage have been very valuable over the course of my PhD.

I would like to acknowledge all of my research collaborators, Drs. Laurence de Viguerie, Łukasz Bratasz, and Marc Vermeulen. Thank you for all of the exciting work that we have been able to pursue over the last few years as well as the research and career advice over the course of my PhD. I'm looking forward to continuing our collaborations and exploring new projects together. Thank you to my fellow graduate students in Amsterdam and Kraków, Magdalena Sobon, Sanne Berbers, and Tamika van't Hoff. You all have been extremely supportive and are excellent researchers. Best of luck completing your degrees! Michelle Hammerton, thank you for being my museum adventuring buddy whenever I was in the Netherlands. To Ari van Buren and Liesbeth Wijkhuizen, thank you both for welcoming me into your community and being good friends throughout my PhD. Hans and Jolet van Damme, thank you very much for opening your home to me for a summer and helping me find a sense of stability during my hectic research life. To the scientists at the Rijksmuseum, thank you for welcoming me into your research team and sharing your thoughts and ideas with me.

For helping to organize my public defense in Amsterdam, I would like to thank my paranymphs, Jorien Duivenvoorden and Fréderique Broers. You have both been great supporters and friends when I was staying in Amsterdam and my PhD experience was enriched by interacting with you.

To all the group members, thanks for creating both a fun and engaging environment both in the lab and the group office. To Kazi Sadman, thank you for taking me under your wing with learning how to perform and interpret QCM experiments. Without your expertise and your willingness to teach me the ropes, I would not be writing this thesis. To Yaoyao Chen, thank you for all the support you provided in the lab and throughout my first year as I settled in at the university. Your willingness to take the time and work through problems and ideas I had always made my days go more smoothly. To Qifeng Wang, for all your patience and assistance with QCM, indentation, and DMA measurements as well as brainstorming experimental processes together. To Matt Eaton and David Delgado, thanks for the help when I came to you with questions. To Tom Schmitt and Becca Harmon, thanks for being great travel buddys and collaborators. To Anthony Silvaroli and Qihua Chen, thanks for all of the adventures over the last five years. From homework sessions to banter in the office and lab, you both have made the last five years a pleasure to work in the Shull group. To YuLing Chen, Broderick Lewis, and Ben Hafner, thanks for all of the fun times and best of luck as you complete your degrees!

I have been fortunate enough to have some amazing mentors during my time at Northwestern. To Lindsay Oakley, thank you so much for taking me under your wing during my first year and then helping establish new collaborations for my research. To Stephanie Zaleski, thank you so much for all of your help and support in the lab as I started new projects. I also enjoyed all of the time we spent chatting and crafting together both in Evanston.

I wish to acknowledge the students that I have mentored over the course of my PhD. Katie Dewan and Zach Vexler, thank you for being willing to work on projects tangentially related to my research, especially when there were unexpected challenges that came up. Bela Quintas, thank you for being so excited to work on a remote research project and for providing a useful result for one of my research collaborators. Alice Tung, thank you for showing interest in my research and being so dedicated to generating new data as well as pursue topics that you will find relevant in your future career. Jazmyn Lu, thank you for your tenacity, drive to problem solve, and ability to

shine as a researcher. I wish you all the best of luck in your future career paths and am glad that I had the opportunity to mentor each of you.

To my friends in my cohort, especially Lele Mathis, Emily Greenstein, and Roger Reinertsen. You all have been fantastic friends and roommates over the years. Emily, thank you so much for all the time you spent proofreading my chapters! Thanks also to my knitting and crocheting group, Ren Lopez, Maryam Kazamzadeh-Atoufi, and Lindsay Chaney. I enjoyed all of the times that we spent crafting together while enjoying tea, movies, and conversation.

For assistance with the acid value measurements and calculations, I would like to thank Frank Filippini at OilDri Co. These measurements were instrumental to bolstering the results of Chapter 4, which I greatly appreciate.

To my siblings, Paige and Donna dePolo. Paige, thank you for all of the support, commiseration, and laughs over the course of our PhDs. Best of luck completing yours! Donna, thanks for all of the fun times when I made it back home. I can't wait to see you thrive as you start your own PhD journey. To my parents, Craig and Diane dePolo, thanks for your unwavering support, optimism, and periodic supply of tea and homemade jam. To Brandon Dodge, Kevin Hannigan, Savannah Carpenter, and Gina Storti, thank you for encouraging and believing in me, especially as I moved halfway across the country to complete this doctorate.

To my wonderful partner, Sam Sorkin. You have been a stabilizing force throughout my entire PhD journey and provided so much support, especially in these last few weeks of writing. I would also like to thank our cats, Dusk and Dawn, for their comfort, warming my lap, and demanding pets as I worked on my thesis.

Last, but certainly not least, I would like to thank the funding sources for the research included in this thesis. This thesis was supported by the NSF (DMR-1710491, OISE-1743748). The shared facilities where data was collected for this thesis include the MatCI Facility which receives support from the MRSEC Program (NSF DMR-1121262) of the Materials Research Center at Northwestern University, the Keck-II facility of Northwestern University's NUANCE Center, which has received support from the SHyNE Resource (NSF ECCS-2025633), the IIN, and Northwestern's MRSEC program (NSF DMR-1720139), and the IMSERC NMR facility at Northwestern University, which has received support from the Soft and Hybrid Nanotechnology Experimental (SHyNE) Resource

(NSF ECCS-2025633) and Northwestern University.

Contents

List of Tables

List of Figures

Chapter 1

Introduction

1.1 Overview

The field of heritage science uses scientific methods and analysis to understand the conditions, materials, and stability of cultural heritage objects. A cultural heritage object can be made from any type of material, ranging from man-made materials such as metals, glass, and ceramic to natural materials including wood, minerals, rocks, and plant-derived oils or dyes [1]. Research in heritage science not only strives to understand what materials were used to create a cultural heritage object, but also to determine how reactive the materials may be to the surrounding environment, exhibition or interaction. Model systems using contemporary materials can provide insights into the potential for the materials in objects to degrade, but having these model systems be fully representative of the historic materials can be challenging [2]. One material that has been in use for centuries, but especially since the 15^{th} century are drying oils [3]. These oils can hold pigments and additives to create paints with a wide range of properties and visual qualities [4].

Drying oils are a class of oils comprised of triglyceride molecules which have high concentrations of unsaturated fatty acid chains. These oils have been extensively studied chemically in both heritage science and food science [5–10]. From these chemical reviews of experimental and computational efforts to understand the reaction pathways governing oil polymerization, it becomes clear that drying oils are extremely complex materials. Drying oils form a solid film by undergoing oxygen induced free-radical polymerization [5]. While the governing principles of free-radical polymerization are well understood, drying oils have relatively high number of reactive sites that be present on a single triglyceride, leading to the formation of numerous reaction products and reactive chemical moeities [11]. Incorporating pigments or additives into the oils as paints, then applying the paints in overlapping layers on top of a support structure creates a composite object where the chemical nature of the components is only one facet [12]. These different layers can respond to changes in surrounding environment or a conservation treatment differently, causing added stresses or potential issues for an object if not properly accounted for before the beginning

of a treatment. One key aspect to consider alongside the chemistry of the paint are the mechanical properties, or how the paint responds to external forces, which can come from fluctuations in temperature, relative humidity, solvent exposure, or even the type of pigment used in the paint and how much it can interact or alter the composition of the paint film [13].

The mechanical properties of a polymer film, such as the paints formed from drying oils and pigments, exhibit a specific type of response called viscoelasticity. Viscoelasticity means that the material exhibits both liquid-like (viscous) and solid-like (elastic) responses when the film experiences an external force. Specialized techniques focused on measuring the mechanical properties of polymers usually can only look at the response of a polymer when it is a liquid or a solid. For the polymerization of a drying oil, understanding how the mechanical properties evolve during the initial stages of cure provides information about the stability of the polymer network over longer times. This thesis aims to monitor the evolution of the mechanical properties during oil polymerization. The chemical changes that occur within the oil films during the initial polymerization step are measured to provide more insights into how the chemical and mechanical properties of the oil film influence each other.

1.2 Outline of Research

Chapter 2 is a review published in Heritage Science that provides an overview of the research focused on measuring the mechanical properties of not only oil, but more modern paints such as alkyd and acrylic paints [14]. The challenges of studying paints, especially when used in paintings and other cultural heritage objects, are discussed and provide justification for the use of model systems as well as historic samples. Techniques are categorized by the physical state of the sample (wet paint or solid film) as well as whether the technique can be applied to model systems, historic samples, or both. For tensile testing, the most commonly applied technique to measure the mechanical properties, a summary of the metadata for sample composition, aging, and testing conditions as well as the mechanical properties are provided in Appendix A. For techniques that are more sensitive to the effects of the viscoelastic properties of paint films (dynamic mechanical analysis, rheology, indentation, and the quartz crystal microbalance), how the technique can be

used to gain insights into the mechanical properties of a paint film are discussed. Finally, this chapter highlights techniques which have been more recently applied to the study of cultural heritage and outlines how they can provide beneficial information for understanding the mechanical response of composite paint structures more fully.

Chapter 3 focuses on understanding the evolution of mechanical properties in linseed oil films during the initial polymerization phase using the quartz crystal microbalance (QCM). The data presented here show how quickly and drastically the mechanical properties change as the drying oil cures to form a solid polymer film. The QCM is well suited to follow this curing reaction because of the sample geometry, which has the film on top of the quartz substrate, with a free surface exposed to air and the oil film being thin enough to remove the diffusion barrier for oxygen. This chapter begins with an outline of the mathematical equations used to calculate the mechanical properties from the films from the data collected using the QCM, as well as a discussion of error treatment and considerations to keep in mind when calculating the mechanical properties. Three drying oils are used in this study for different measurements. Heat treated linseed oil samples are used to observe the effects of heating linseed oil with litharge on the onset and extent of cure. The second set of linseed oil samples are measured in ambient lab conditions over the course of three years to observe the longer term evolution of mechanical properties after the initial onset of cure. The third set of samples were aged for five months in ambient lab conditions, then subjected to temperature sweeps from $-40 - 80\,^{\circ}\mathrm{C}$ to measure the temperature dependent response of the polymer films. From these data, a model of nano-scale heterogeneity in the crosslink density of the oil samples is presented and compared to another well characterized crosslinked polymer system. Appendix B has the supplemental information for Chapter 3, mostly presenting of the error analysis for all of the data presented in Chapter 3.

Understanding how mechanical properties change is key to having a more complete material understanding of drying oils, but the most holistic approach to understanding the early-stage cure of drying oils incorporates both chemical and mechanical information. To build on the work collected in Chapter 3, Chapter 4 discusses time-based attenuated total reflection infrared (ATR-FTIR) spectroscopy data collected on drying oils. The drying oils measured in this study (linseed, walnut, poppyseed, safflower, and stand oils) have different initial fatty acid distributions, which

affect the onset, rate, and extent of polymerization achieved for the sample. Oil samples were measured initially at 70 °C to ensure the polymerization would be completed within a few days. The effect of drier on the resulting chemical reactivity of the polymer film is explored further by incorporating litharge into oil samples. The effect of temperature is also measured to assess the assumption that the reaction pathways most active during drying oil polymerization are relatively consistent up to 80 °C [15]. However, the largest effect on the polymerization reaction of the drying oils came from the addition of litharge at higher temperatures. These films showed very few signs of oxidation, which implies that the reaction pathways for oxidation within a paint film are very unfavorable, or effectively "arrested" after the first phase of oil reactivity induced by the presence of litharge. Drying oil films aged for one year in ambient conditions were compared with the data from early-stage cure to determine what changes persisted over longer times. Appendix C contains the supplemental information for Chapter 4, which is primarily focused on the data not shown in the main manuscript as well as detailing the methods used for characterization of the drying oils.

Finally, the research, data, and concepts of this thesis are summarized. With the main focus of this work being drying oils, the extension to the use of these techniques on pigmented oil paints is the next step for furthering these projects. Other methods for understanding how the network topology of the polymer networks are formed from drying oils will also provide more insights into the reactivity and potential diffusion. By combining knowledge of the network topology, chemical reactivity, and mechanical properties of drying oils, especially when they are used in oil paints, will provide art conservators and heritage scientists the fundamental understanding of these complex material systems, supporting their efforts of conservation of cultural heritage objects for use by future generations.

Chapter 2

After the Paint has Dried: A review of testing techniques for studying the mechanical properties of artists' paint

This chapter is adapted from the following peer-reviewed article: dePolo, G.E.; Keune, K.; Walton, M.; Shull, K.R. After the Paint has Dried: a review of testing techniques for studying the mechanical properties of artists' paint. *Heritage Science,* **2021**, *9*:68, https://10.1186/s40494-021-00529-w

2.1 Introduction

2.1.1 Overview

Paint is a ubiquitous component of art objects and a research subject that has received prominent attention for many years in both industry and cultural heritage. A great amount of research has focused on understanding the chemical changes of the curing processes of paints, but they only partially capture the overall stability of a paint film. [6, 7, 9, 16] The mechanical properties play a key role in assessing its stability over the lifetime, providing information about the stiffness, toughness, and the likelihood of crack formation, among other things. The most recent review paper discussing the mechanical properties of paint was published thirty years ago, emphasizing the role that temperature (T) and relative humidity (RH) play on brittleness of these films. [17] In the present review our aim is to compile the innovative mechanical testing techniques that have been developed in the last two decades, together with the data derived from these experiments. It is shown how this area of research has grown and begun to provide possibilities for contributing to improved conservation practices.

Paints are typically comprised of a pigment for coloration, a binding medium, and other additives that can adjust the optical properties and workability of the paint film. All paint materials have several properties that change over time, initially being a liquid-like film that evolves into a solid-like paint film. This transition from liquid- to solid-like behavior can occur two ways: through a drying process, where solvents added to the system evaporate out of the paint film, or through

curing, where crosslinking and other chemical reactions occur within the pain film to increase the stiffness. The timescale over which these drying and/or curing processes occur can vary greatly, from a few hours (acrylics) to months (alkyds) to decades (oil-based paints). [18, 19] As the paint transitions from liquid-like to solid-like, the stiffness of the paint film can typically increase several orders of magnitude. For oil-based paints, the mechanical properties can continue to change over the long periods of time that the curing process is ongoing, motivating active research into the mechanical properties of these paints. Alkyd and acrylic paints, since they are modern paints that have been in use for less than 100 years, have also been a strong focus of research efforts in the last few decades. Other historic paints, such as distemper or egg tempera, are known to have a short drying phase and to form stiff, brittle films. [18, 20] Once tempera paints solidify, the mechanical properties remain fairly stable, so they have not been the focus of more recent research efforts. Distemper paintings are rare to find in a pristine condition, as many have been subjected to a varnish treatment, which alters the original mechanical properties of the film. [21]

The mechanical properties of a paint film are affected by the paint composition, interactions between paint layers for a composite painting structure, and the environmental conditions (temperature, relative humidity, transportation, etc.) to which a paint is subjected. Each of these contributions will be discussed in further detail in the following sections, followed by an overview of the techniques discussed in the review and at what point during the lifetime of a painting they are relevant for use.

2.1.2 Pigment to Binder Ratio

A simplified definition of a paint film is a composite material comprised of rigid pigment particles suspended in a more flexible binding medium. The concentration of pigment or additive present tends to have a strong contribution to the mechanical properties of the paint. The concentration can also vary widely depending on the desired properties and particular combination of pigments used in the paint. These relative concentrations can provide insights about the expected stiffness of paints since the additives function as rigid fillers within the binding medium matrix. The added filler is typically much stiffer than the corresponding binding medium matrix, and thus contributes to an increased stiffness of the overall paint. [22, 23] A challenge for

researchers is accurately determining the pigment to binder ratio of fully cured historic paints, which provides relevant information for understanding the mechanical properties of the paint and for understanding an artist's technique by making paint reconstructions. Two approaches to determine pigment to binder ratio that have been previously used various imaging and spectroscopic techniques to analyze these cross sections. The first approach used a sequence of μX-ray diffraction (μXRD), particle induced X-ray emission (PIXE) and backscattering spectrometry (BS) to determine the light and heavy elements present in a historic paint cross section, using the techniques together to identify the pigment(s) and estimate of the ratio of pigment to binder in the sample. [24] Alternatively, researchers have looked into the quantification of the ratio between pigment and binder on stable, liquid-like paint systems using Fourier Transform Infrared Spectroscopy (FTIR) and Raman Spectroscopy. [25] The use of these spectroscopic techniques becomes difficult on dried historic paints where the pigment, binder, or both are not stable over long periods of time, since the particular chemical peaks tracked in this study can change quite a bit over longer periods of time. Some more recent work has used X-ray micro- or nano-tomography to determine the pigment to binder ratio for the full volume of a paint sample. [26]

Some studies focused on the mechanical properties of paint have used a measurement of pigment content based on volume, pigment volume concentration (PVC), instead of pigment-to-binder ratio, which is a weight-based measurement. [27–29] Mathematical models have also been developed to describe the effects of pigment particle concentration and shape on the stiffness of the sample and have been explored in some of the studies that will be highlighted in Section 2.2. [30, 31]

2.1.3 Paintings as Multi-Layer Structures

The complexity of paint mechanical properties goes beyond the effect of a rigid filler on the stiffness of the paint. Multiple layers of paint ranging from tens of microns to 1 mm in thickness are generally utilized in the creation of a painting. These layers are placed on a support, forming a multi-layer structure where the mechanical properties of a given paint layer can be affected not only by the environmental fluctuations or conservation treatments, but also by changes in the surrounding layers (Figure 2.1). [12]

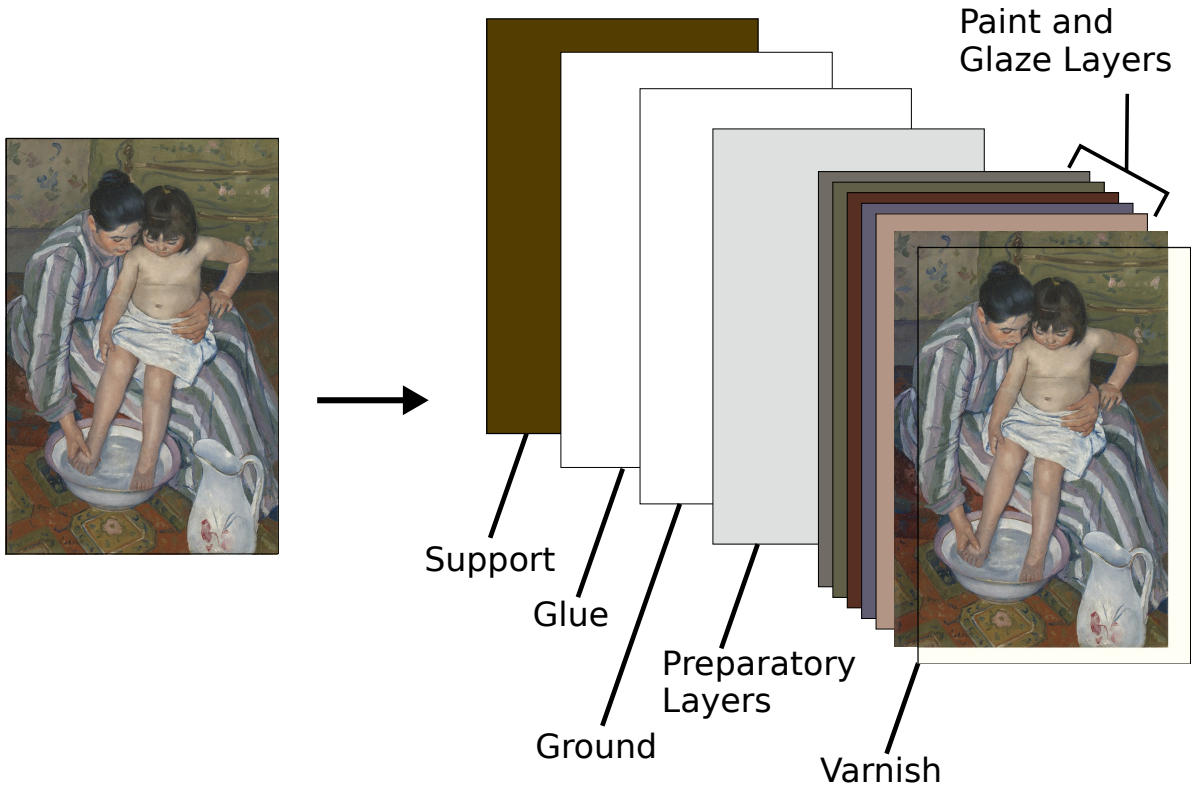

Figure 2.1: The multi-layered structure of a traditional oil painting showing the support, glue, ground, preparatory, paint/glaze, and varnish layers. The complexity of the layered structure of the painting provides an added level of difficulty for researchers when studying the mechanical properties of paints and how they affect the overall stability of the painting. Painting information: Mary Cassatt, The Child's Bath, 1893, Oil on canvas. The Art Institute of Chicago, Robert A. Waller Fund. Adapted from a figure in [12].

Obtaining information about this complex multi-layer structure presents challenges to researchers, especially understanding how each layer contributes to an overall response of the object and how the material/chemical composition influences that response. The range in size of single paint layers to entire paintings also provides a challenge for determining which length scale (*e.g.*, micron, millimeter, or meter) and therefore which technique is most relevant for understanding the mechanical response of an object. Any expansion or swelling of a given layer (such as the swelling of a canvas in response to increased RH) or significance differences in stiffness between layers (i.e. a much stiffer ground layer below a paint layer) can lead to small applied strains on the surrounding layers, causing stresses that increase the potential for cracks to form and propagate through the painting. Paint layers can also be subject to issues of adhesion, which can lead to delamination or paint loss, which is also problematic. Understanding the mechanical properties of these layers

the mechanical response to neighboring layers or environmental fluctuations are relevant when determining the overall structural stability of a painting and will be discussed within this review.

2.1.4 Craquelure

One of the main concerns for conservators is the formation or propagation of new cracks within the painting due to fluctuations in environmental conditions or as a function of transporting a painting. The craquelure present in a painting is acknowledged as an inherent part of the drying process of the paint, but the formation of new cracks from an impact, transportation, or a drastic change in environmental conditions can increase the chances for paint delamination and paint loss. The development of craquelure in paint has been an area that has been discussed fairly extensively in a qualitative nature, but has experienced difficulties in developing a standardized metric for characterizing the craquelure. [32–35] Some models have been discussed with regards to how ground layers may develop cracks as a result of environmental fluctuations. [36] Research on the craquelure formed using model colloidal systems, which can be tuned to have similar particle size and distribution as historic paint layers, has provided some information about the distinctions between drying and aging cracks, as well as the insight that as paintings age, the degree of cracking increases. [37] The research was also extended to discuss how craquelure on paintings can relate to the mechanical properties of the visible and underlying paint layers, as well as the implications of these craquelure in the routine conservation work performed on paintings. [38] These colloidal system studies provide some experimental data to correlate with the qualitative descriptions of craquelure patterns, but it can still be difficult to understand the underlying mechanisms influencing crack formation and propagation within the paint.

Two distinct length scales need to be considered when discussing crack formation in a paint layer. The first of these is the macroscopic scale of the entire painting, which determines the stresses that the paint layer is exposed to. In fracture mechanics terms these stresses define the driving force for continued growth of a crack, typically expressed in terms of an energetic driving force, $\mathcal{G}$. This quantity has units of energy per unit area, and quantifies the energy that is recovered by the overall system as the crack grows. Crack growth occurs when $\mathcal{G}$ exceeds a critical value, $\mathcal{G}_c$, that is characteristic of the paint. Growth of the crack alters the stress field around the crack itself, affect-

ing it's own trajectory and the ability of neighboring cracks to grow. These interactions determine the craquelure patterns that are observed in actual paintings, and motivate the need to understand the system behavior at the length scale of the cracks themselves. Because of the complexities of the experimental geometries in real paintings, numerical finite element methods have an important role to play at both of these length scales, although considerable insight can also be obtained from appropriate analytic expressions.[38] The main point we want to make here is that it is generally not sufficient to understand the properties of the paint in absence of an understanding of the relevant driving forces for crack propagation. These driving forces originate from a combination of external forces (*e.g.* movement, vibrations) imposed on the object and internal forces generated by the varying response of the different layers to environmental conditions.

2.1.5 Relevant Techniques

The techniques covered within this paper, along with applicability to either model systems or historic samples and when they can be used during the lifetime of a paint, are shown Table 2.1. Deciding when to use a given technique depends on the desired mechanical property and the goal of the research program, whether it's to address questions from art history (*i.e.*, how an artist achieved a specific painting effect), to monitor or assess the condition of historic objects, or to understand the fundamental responses of mockup paint samples that can be deformed and subjected to damage more readily than a historic painting. Since there can be some challenges in comparing the results obtained from model systems with historic samples (typically due to age and composition differences), these techniques have often been paired with other analytical techniques to study the chemical response of a paint and provide a more direct comparison.

Table 2.1: Summary of the techniques and defining characteristics (age of the paint, type of samples, the amount of strain applied to the sample, how invasive the technique is, and the relevant mechanical properties) for each technique discussed within this review. Definitions for mechanical properties in Relevant Data: E: elastic modulus, e_f: failure strain, σ_T: ultimate tensile strength, E^*: complex elastic modulus, tanŒ: loss tangent, η: viscosity, $d\rho$: areal density, $|G^*|\rho$: magnitude of the complex shear modulus multiplied by the density, E_r: reduced elastic modulus, H: hardness. $^+$Indicates that the technique is a numerical method.

Technique	Paint age	Sample type	Applied Strain	Sample Size	Invasiveness	Relevant Data
Tensile Testing	Dried/Aged Paint	Model Systems	Large Strain	Bulk	Invasive	Elastic Stiffness, Ultimate Mechanical Properties (E, e_f, σ_T)
Dynamic Mechanical Analysis	Dried/Aged Paint	Model Systems	Small Strain	Bulk	Invasive	Solid/Liquid -like Behavior (E^*, $\tan\phi$)
Shear Rheometry	Fresh Paint	Model Systems	Small Strain	Bulk	Invasive	Viscosity (η)
Quartz Crystal Microbalance	Fresh & Dried/Aged Paint	Model Systems	Small Strain	Thin-film	Invasive	Elastic Stiffness, Swelling ($d\rho$, $\lvert G^*\rvert\rho$, ϕ)
Nano-indentation	Dried/Aged Paint	Model Systems & Historic Samples	Small Strain	Single point/Small Sample Size	Minimally Invasive	Elastic Stiffness, Hardness (E_r, H)
Laser Shearography	Dried/Aged Paint	Model Systems & Historic Samples	Small Strain	Area of Painting	Non-Invasive	Strain Maps
Finite Element Analysis$^+$	Fresh & Dried/Aged Paint	Model Systems & Historic Samples	Simulated Large and/or Small Strain	Any Sample Size	-	Predictive Mechanical Responses
Vibration Studies	Dried/Aged Paint	Model Systems	Small Strain	Area of Painting	Minimally Invasive	Damage Risk
Single-Sided Nuclear Magnetic Resonance	Dried/Aged Paint	Model Systems & Historic Samples	_	Single Point/Small Sample Size	Non-Invasive	Comparative Stiffness

For each of the techniques in Table 2.1, we will discuss the advancements and significant results as well as future directions for their optimization and use to study paints. To help explain the types of data and the significance of results, there will first be a brief overview of the mechanical

properties investigated with each technique.

2.2 Tensile Testing

2.2.1 Static Mechanics Overview

In typical statics measurements of paint systems, a force (stress, σ) is applied to a system to cause a displacement (strain, e). The stresses can be applied in either a normal or a shear direction to the sample. For paint materials, the stresses are commonly applied through the geometries shown in Figure 2.2. These sample geometries take into consideration some of the structural aspects of the material, such as whether it is a membrane system (e.g., an individual paint layer or painting on a canvas), is attached to a rigid support (*e.g.*, painting on a wood panel), or is still in a liquid form (*e.g.*, reproductions of historic recipes). Uniaxial tensile testing (Figure 2.2a) applies force on opposing ends of a paint film, providing material properties that will be described shortly. Biaxial tensile testing (Figure 2.2b) applies tensile forces in two directions, which can be useful when looking at the composite structure of a paint layer on a support (i.e. a linen canvas). However, the composite nature of these systems can make it difficult to accurately define the individual material contributions to the overall behavior. Four point bending (Figure 2.2c) applies forces on either side of a sample in such a way as to cause both compressive and tensile forces at the center of the sample. If there is an adhesive or filler material being used on a wooden object, these tests are useful for determining the potential failure conditions of the conservation materials.

The stress-strain behavior for a material can exhibit a range of phenomena, depending on the temperature and timescale of the measurement. In polymeric materials there is a general equivalence between time and temperature, with similar behavior obtained either by decreasing the temperature or increasing the time scale of the measurement. For artist paints, the properties also evolve with time, adding another dimension of complexity. Generic results obtained from a uniaxial tensile test are shown in Figure 2.3. While not all of these behaviors are necessarily observed in the same material, the following general regimes can often be identified, based on 4 different temperature regimes (T_1, T_2, T_3 and T_4).

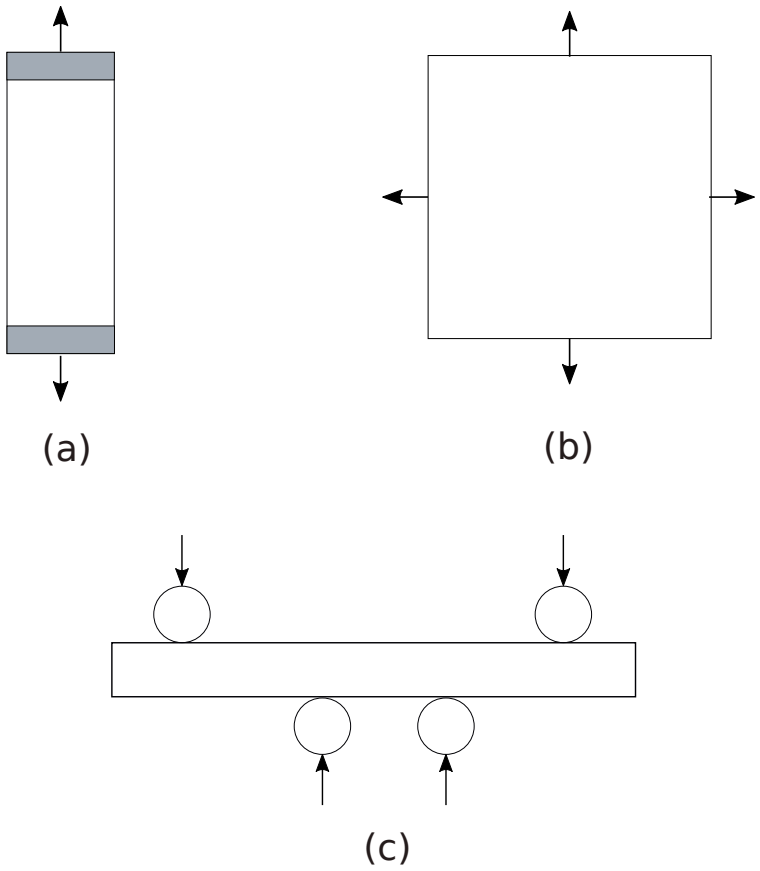

Figure 2.2: Schematics of a) uniaxial tensile, b) biaxial tensile, c) and 4-point bending experimental geometries. The grey regions in a) indicate where clamps are attached to the sample.The arrows indicate the direction of applied force in each experimental geometry.

- T_1: Brittle behavior of a glassy material. This is generally observed at sufficiently low temperatures.
- T_2: Ductile behavior followed by localized thinning of the sample and failure.
- T_3: Ductile behavior with substantial localized deformation after yield.
- T_4: uniform deformation of a very soft, rubber material.

Note that Figure 2.3 is highly qualitative and does not accurately capture the detailed changes that are observed. As one follows the blue arrow from T_4 to T_1, the polymer sample would pass through the glass transition temperature, T_g, which is the point when a polymer transitions from

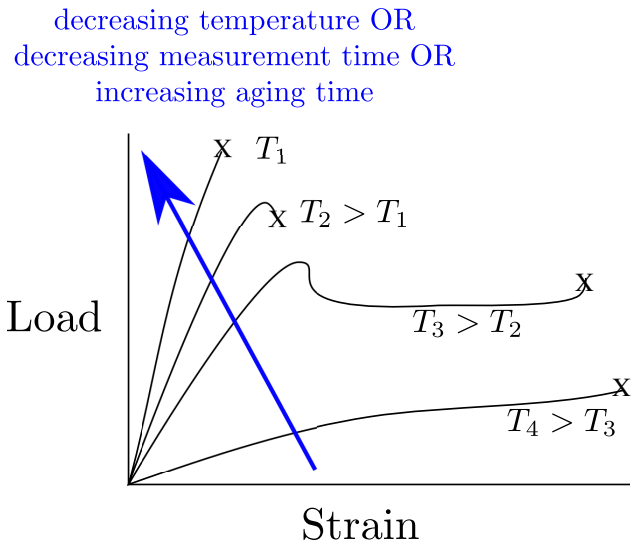

Figure 2.3: Typical generic temperature behavior at different temperatures shown with a qualitative load (stress) vs. strain plot. As the temperature decreases from T_4 to T_1, the sample exhibits more brittle behavior. This trend is also equivalent to increasing the strain rate (or decreasing the measurement time) used for the tensile test.

a rubbery, more flexible response to a glassy, more brittle response. A more quantitative example of a tensile test is the stress-strain curve for the 8-year-old lead white sample shown in Figure 2.4. These curves provide several results that help the researcher understand the overall mechanical behavior of the paints. The elastic modulus (E) (a.k.a. Young's modulus) can be determined from the from the slope of the curve at low strains and is shown by the line extended from the stress strain curve. When the paint film begins to yield, the slope of the stress strain curve decreases. The stress at which this yield point occurs is known as the yield stress ($œ_Y$). Not all paint samples exhibit a yield stress either due to the softness of the material or to the viscoelastic behavior of the film. For cases where a yield stress is not present in the data, a secant modulus (E_s) can be calculated using the following equation:

$$E_s = \frac{\sigma}{e} \tag{2.1}$$

where common values of e are less than or equal to 0.05. The end of a tensile test usually occurs when there is a failure such as a fracture in the paint sample. The stress and strain values at this point, the ultimate tensile strength ($œ_T$) and strain to fracture (e_f) respectively, are useful material properties for characterizing the limits of a sample.

These static tensile measurements require larger samples, making them impractical for measure-

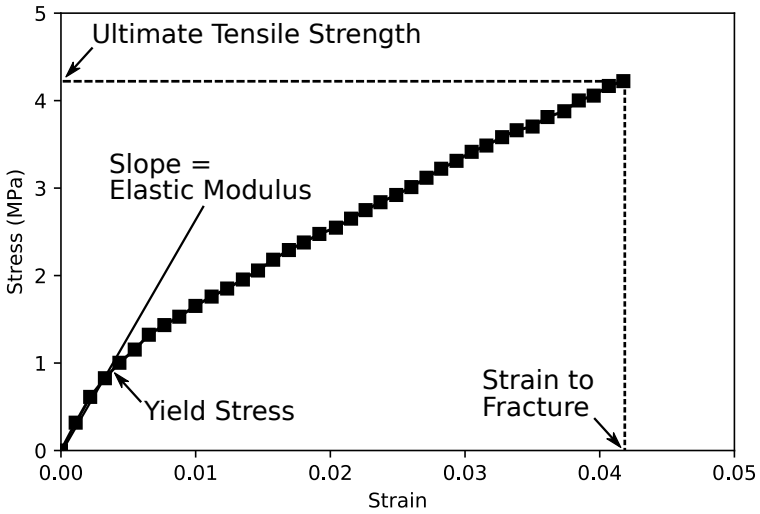

Figure 2.4: Sample stress (MPa) vs. strain plot for an 8-year-old lead white paint film in acid refined linseed oil. The relevant mechanical properties that can be determined using these curves are also displayed on the graph. Data replotted from [39].

ment of historic paints and requiring the use of either model systems or sacrificial collection samples. The sample geometry for tensile tests also requires solid samples, which means the paints have to dry for at least 1 week (acrylic) to 1 month (oil) before measurements can be taken. The instruments used for these measurements can be modified to include environmental chambers that control T and RH, some of the more important practical parameters for understanding the material properties of paints.

2.2.2 Uniaxial Extension

Uniaxial tensile testing of paint samples has been one of the most commonly used techniques for investigating the mechanical properties of paints in cultural heritage over the last few decades. A summary of the references that have used tensile testing to measure the mechanical properties of paint materials is shown in Table 2.2.[1]

[1]To help understand and look at overarching trends in the mechanical properties of paints studied using uniaxial testing, we compiled a summary of the reported mechanical property data from studies focusing on oil, alkyd, and acrylic paints as well as some paint consolidants and grounds. See Appendix A for these summary tables.

Table 2.2: Summary table of the types of paints and testing parameters varied in the studies that used uniaxial tensile testing to investigate mechanical properties. Abbreviations in the table: Temp. = tem- perature, RH = relative humidity, Solv. Exp. = Solvent exposure, Sample comp. = Sample composition. Sample composition includes changes in binding medium, pigment type and composition, and sample thickness. Aging refers to both natural and accelerated aging of samples.

Reference	Oil	Alkyd	Acrylic	Filler, Ground, Support	Temp.	RH	Solv. Exp.	Strain Rate	Sample Comp.	Aging
Mecklenburg, 1991 [40]	✓				✓	✓			✓	✓
Erlebacher, 1992 [41]		✓	✓		✓	✓			✓	
Mecklenburg, 1994 [42]			✓						✓	
Whitmore, 1995 [43]			✓							✓
Tumosa, 1999 [39]	✓						✓		✓	
Mecklenburg, 2001 [44]	✓									✓
Carr, 2003 [45]	✓					✓			✓	✓
Mirone, 2004 [46]		✓							✓	✓
Meckelburg, 2004 [13]	✓				✓	✓	✓		✓	✓
Hagan, 2004 [47]			✓		✓	✓	✓		✓	✓
Erhardt, 2005[48]	✓									✓
Tumosa, 2005 [49]	✓								✓	
Young, 2007 [50]	✓	✓	✓						✓	✓
Hagan, 2007 [27]		✓	✓			✓		✓	✓	
Young, 2008 [51]	✓	✓	✓		✓	✓			✓	✓
Fuesers, 2008 [52]	✓	✓					✓		✓	
Ormsby, 2008 [53]			✓		✓	✓			✓	
Fuster-Lopez, 2008 [54]				✓		✓			✓	

Reference	Oil	Alkyd	Acrylic	Filler, Ground, Support	Temp.	RH	Solv. Exp.	Strain Rate	Sample Comp.	Aging
Carlyle, 2008 [55]				✓		✓			✓	
Hagan, 2009 [56]			✓		✓	✓		✓	✓	
Hagan, 2010 [30]			✓		✓		✓	✓	✓	
Hagan, 2011 [31]			✓					✓	✓	
Tumosa, 2013 [57]	✓								✓	✓
Mecklenburg, 2013 [58]	✓	✓					✓		✓	✓
Domenech-Carbo, 2013 [59]			✓				✓		✓	
Hagan, 2015 [60]			✓		✓			✓	✓	
Fuster-López, 2016 [61]	✓								✓	✓
Krzemien, 2016 [62]				✓		✓				
Penava, 2016 [63]				✓					✓	
Hagan, 2017 [64]	✓	✓	✓		✓			✓	✓	
Fuster-López, 2017 [65]	✓					✓			✓	✓
Doutre, 2017 [66]				✓		✓			✓	
Roche, 2018 [67]	✓		✓		✓	✓			✓	✓
Fuster-López, 2019 [68]	✓	✓							✓	✓
Bridarolli, 2020 [69]				✓		✓			✓	

From the references in Table 2.2, Figure 2.5 provides an overview of the range of E from the samples tested as a function of age (associated with the curing time) of the samples, which spans four orders of magnitude. While this graph does not show a strong trend in the data, it does highlight one main takeaway about analyzing these data: it is difficult to analyze trends in the data using only a single variable from these uniaxial tensile tests. As discussed above, the type of pigment

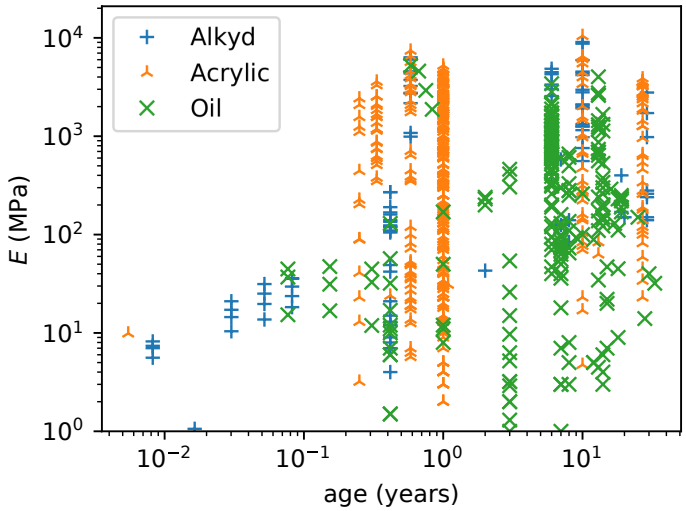

Figure 2.5: Plot showing elastic modulus (MPa) vs aging time (years) from uniaxial tensile tests of oil, alkyd, and acrylic paints. The graph does not account for testing variables such as T, RH, solvent exposure, or pigment/particle type used in the paint medium, contributing for the wide spread of the modulus data. Data compiled in this graph are from [13, 27, 30, 31, 39, 41, 44–47, 49, 51–53, 56–61, 64, 65, 68, 70, 71].

used will impact the pigment to binder ratio of a given sample. Inorganic pigments also tend to be much stiffer than the binding media, also leading to a significant increase in the stiffness of the sample. Many of the studies focused on the effects of temperature [13, 30, 40, 41, 47, 51, 53, 56, 60, 64, 67] and relative humidity [13, 27, 40, 41, 45, 47, 51, 53, 54, 56, 62, 67, 69] on the stiffness of the sample. There is a general trend across all three binding media classes of increasing stiffness as the temperature of a paint decreases, shown in Figure 2.6, which would indicate that the increase in stiffness is controlled more by the properties of the binding medium than the particular pigment used. For all these general classes of binding media, $-10°$C is below their T_g , which leads to a glassier, more brittle response from the samples. When the RH is increased for a paint system, researchers observed a general softening phenomenon occur since water can act as a plasticizer in most paint films, leading to a decrease in the stiffness that can range from 30-90%. [2] [13, 27, 40, 41, 45, 47, 51, 53, 54, 56, 62, 67, 69] When the RH is decreased, the paints become stiffer as less ambient water is present, showing anywhere from 40-300% increase in the stiffness.

Another common variable for the material response of paint materials is solvent exposure to as-

[2]For all of the ranges presented for changes in stiffness as a result of a change in a testing parameter, the range has been estimated across all binding media and sample compositions in an attempt to show the maximum impact a particular parameter can have on the stiffness.

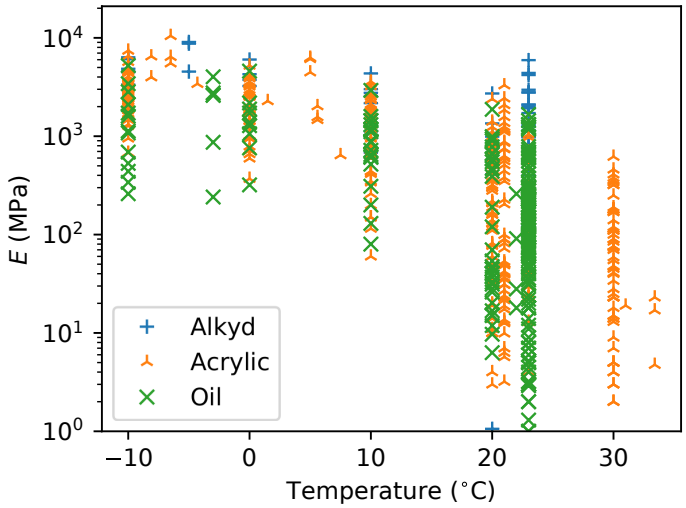

Figure 2.6: Plot showing the elastic modulus (MPa) vs temperature (°C) from uniaxial tensile tests of oil, alkyd, and acrylic paints. The graph does not account for other testing variables such as age, RH, solvent exposure, or pigment/particle type used in the paint medium. Data compiled in this graph are from [13, 27, 30, 31, 39, 41, 44–47, 49, 51–53, 56–61, 64, 65, 68, 70, 71].

sess the effects of solvents commonly used for cleaning paintings. [13, 30, 39, 47, 52, 58, 59, 72] The most common trend after exposure to volatile solvents was that the paint films would become embrittled, exhibiting stiffer, more brittle responses (anywhere from 100-900% increase in the stiffness) due to the leaching and volatilization of low molecular weight components. Yet, exposure to non-volatile solvents resulted in increased plasticity of the paint films (up to a 74% decrease in the stiffness). [39] Results from uniaxial tensile tests are also dependent on the strain rate of the test, or how quickly the sample is deformed. As the strain rate is increased, the paint film has less time to respond to the deformation taking place, leading to a stiffer, glassier response. Hagan *et al.* varied the strain rate during their research on acrylic and oil-based paint systems to apply time temperature superposition (explained more fully in Section 2.3) to their results and observe the material response over a wider range of testing strain rates. [30, 31, 56, 60, 64] The studies also considered the effects of PVC as well as the shape of the pigment particles on the overall response of the pigment/binding medium composite sample using mathematical models focused on filler effects in a composite, highlighting the importance of understanding the PVC of a paint sample. [31] There is a challenge of the composition of the binding medium and PVC not being readily available for commercial artists' paints, but with enough time and access to analytical tools they can be determined. Not all the responses are explained through pigment type or

filler concentration, though, because the alkyd paints continue to increase in stiffness as a function of time regardless of pigment, shown in Figure 2.7, whereas the oil and acrylic paint classes do not show any trends as a function of age due to convolution from other testing parameters.

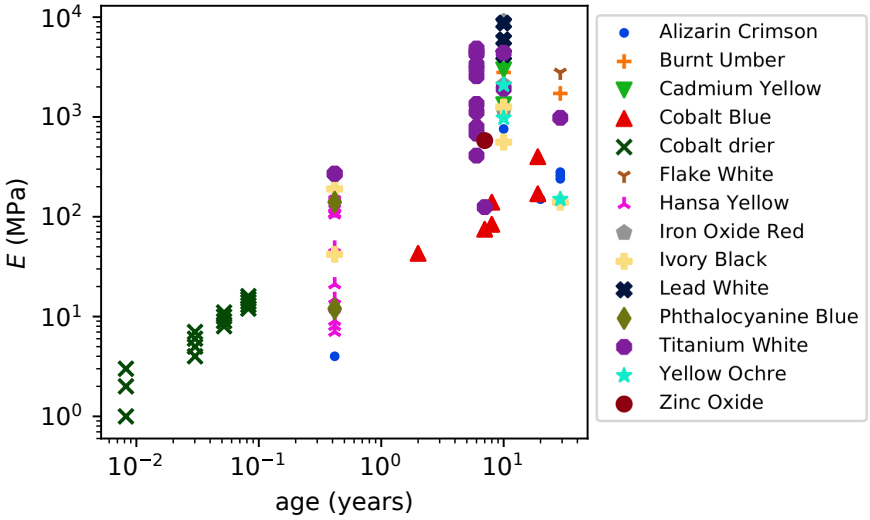

Figure 2.7: Plot showing the elastic modulus (MPa) vs age (years) for the alkyd paints. The wide spread in the value of the elastic modulus for Hansa Yellow is due to solvent exposure. The spread in the data for Titanium White is due to temperature variations. Data compiled in this graph are from [41, 46, 52, 58, 64, 68].

One of the main drawbacks to using model systems for paints is their relatively young age; they are typically 30 years old at their oldest. While this age range is more relevant for the newer alkyd or acrylic paint classes, it becomes difficult to draw conclusions about the expected material responses of oil paints that are 50 years or older. While accelerated aging may be a way to address this issue, previous research has shown that without careful tailoring of the study, accelerated aging of the paint film enables different chemical reaction pathways than natural aging for oil paints, which can make comparisons difficult. [15] Some theoretical extrapolations can be made about the response by observing the changes in stress at constant strains. Over longer times, the stress begins to follow a linear trend when plotted against the natural log of time, which allows researchers to create theoretical stress-strain curves that can be more predictive. [13, 48] This analysis method provides a good first approximation for some brittle paints, but it has not been applied to softer paint systems or to paint systems where the stiffness remains constant, but the flexibility of the paint film decreases.

Some of the studies shown in Table 2.2 focus on other materials found in the multi-layered struc-

ture of a painting than paint. Researchers have studied the response of grounds to RH to determine ideal storage conditions and the effects of drying shrinkage on the formation of cracks within the ground. [62, 66] The stiffness of canvas as a function of the orientation of the weave of the sample has also been explored using uniaxial extension, demonstrating that the stiffness is strongly dependent on the orientation that the load is applied to the canvas. [63] Samples comprised of multiple layers (*i.e.*, paint-paint or canvas-paint) can provide some insights into the response of the composite to changes in temperature or relative humidity, but it becomes difficult to determine which aspects of the composite structure are contributing to those changes. [50, 67, 69, 73]

Uniaxial tensile testing provides researchers with the ability to investigate the effects of T, RH, solvent exposure, and PVC on the mechanical properties of paint, but these investigations can only be performed on model systems due to the relatively large amounts of sample required for measurements.

2.2.3 Biaxial Extension

When we consider the composite nature of paintings, those mounted on stretchers experience stresses to the paint layers from two directions, which can be difficult to capture using only the uniaxial extension test. The way that paintings are mounted to stretchers is very similar to how they would be studied using biaxial extension (Figure 2.2b), making this technique a relevant method for studying these model systems. To address the complexity of observing stresses in two directions, Young developed a biaxial tensile testing system that would be compatible with painting mockups. [74] An electronic speckle pattern interferometer was incorporated into the instrumentation to help determine the amount of strain occurring in each direction during the tensile tests. [75] The biaxial setup has been used to assess the behavior and interaction of glue, oil, and flour paste grounds when they are applied to canvases. [55] The glue and oil grounds demonstrated stronger changes as a function of RH than the flour paste grounds, but the flour paste grounds were not as stiff as the other two grounds. [55] Using the biaxial geometry to investigate canvases and paint layers allows researchers to investigate how the mechanical response of a canvas-paint composite sample will be affected by environmental changes since the response of the composite system will be different dependent on the canvas weave direction. Due to the

isotropic nature of paint samples, when using this geometry both E and Poisson's ratio (ν),the lateral strain that occurs perpendicular to the applied stress, can be determined. One important aspect to keep in mind is that the corners of the sample will act as stress concentrators when placed under tension (see Section 2.7.2), which can cause issues during data analysis. A workaround can be to remove the corners of the model samples or to use computational simulations to study the impact of the corners of a sample more fully. From a materials characterization standpoint biaxial testing provides information that is comparable to what is obtained from uniaxial testing. It's primary use as described above is in studying the mechanical response of the overall composite painting structure under realistic loading conditions.

2.2.4 Bending Geometries

As was mentioned earlier, a bending geometry allows one to investigate both compressive and tensile forces applied to a material, especially if those are potential forces that need to be accounted for in a rigid art object. Young *et al.* performed a study of adhesives and fillers that are typically used in the conservation of panel paintings, which can have a large range of stresses applied as a function of environmental shifts (typically T or RH). [76] With the bending geometry, it was easier to determine whether the failure of the joints studied was due to the adhesive or to the wooden support. [76] The load curves from this research were compressive rather than tensile, generating stiffness measurements that are not as directly comparable to the tensile data shown earlier. These more rigid paint composite systems can also be more thoroughly studied through computational simulation, which will be discussed more in Section 2.7.2. This geometry had targeted benefits of exploring the response of paints, adhesives, and fillers on rigid substrates, but is not as useful beyond this targeted application.

2.3 Dynamic Mechanical Analysis

Dynamic mechanical analysis (DMA) is a technique ideally suited for studying viscoelastic samples such as paints. Most DMA studies of artists' paints have used a similar sample geometry and force application as uniaxial tensile testing (see Figure 2.2). Unlike tensile testing, which ap-

plies a fixed stress or strain rate, DMA samples undergo oscillatory loading conditions to look at the frequency dependent response common to polymer-based systems, including artists' paints. Quantifying this behavior is important when planning storage, travel, or exhibition conditions and conservation treatments for a work of art. In DMA experiments, the stress is applied as a function of time ($\sigma(t)$), which leads to a time dependent expression for the elastic modulus, $E(t)$, which for an oscillatory stress and strain can also be notated as a complex function, E^*:

$$E^* = E' + iE'' = |E^*|\, e^{i\phi}, \tag{2.2}$$

where E' is the storage modulus that describes the solid-like behavior of the sample, E'' is the loss modulus that describes the liquid-like behavior, $|E^*|$is the magnitude of the complex elastic modulus, and ϕ is the viscoelastic phase angle, which describes the phase difference between the oscillatory stress and strain. The two right sides of Equation 2.2 can be related through these two equations:

$$E' = |E^*| \cos\phi \tag{2.3}$$

$$E'' = |E^*| \sin\phi. \tag{2.4}$$

We can combine Eqs. 2.3 and 2.4 to get the following expression for $\tan\phi$ (also known as $\tan\delta$ in literature), commonly referred to simply as the loss tangent:

$$\tan\phi = \frac{E''}{E'}. \tag{2.5}$$

For samples that are thermorheologically simple, or have the relaxation times present in the sample that are all affected the same way by temperature, frequency sweep experiments can be performed at various temperatures and used to generate a master curve of both E^* and $\tan\phi$ using time-temperature superposition. [77] From these master curves of the complex elastic modulus versus shifted frequency, the glassy and rubbery regimes of a sample are visible. The peak of a $\tan\phi$ versus temperature plot is a measure of the glass transition temperature, T_g, where the sample transitions from rubbery behavior above the T_g to a more brittle, glassy response below T_g.

Due to the nature of polymer relaxation times, the T_g is also partially dependent on the frequency of the measurement. In a typical amorphous polymer, increasing the frequency of measurement by an order of magnitude increases T_g by about 3 °C, which is important to remember when comparing data between different techniques that use a different base frequency, such as will be discussed in Section 2.5. Shift factors (a_T) are used to align the E^* and tanϕ to the values for a given reference temperature by shifting the data horizontally along the frequency axis, using the underlying assumption for time-temperature-superposition to apply these shift factors. Figure 2.8 provides example master curves of $|E^*|$ as a function of frequency and of tanϕ and a_T as a function of temperature for an alkyd binding medium commercially made by Galkyd and aged for 159 days before testing. In Figure 2.8a, $|E^*|$ spans over 15 decades of frequency, showing the rubbery-like behavior on the lower left of the graph and the glassy behavior on the upper right. The tanϕ curve shows a peak around 26 °C, which would be a rough estimate of the T_g for this alkyd binding medium. Mathematical models are often used to describe the shift factors and predict the response of the polymers [77], but are not discussed in this review.

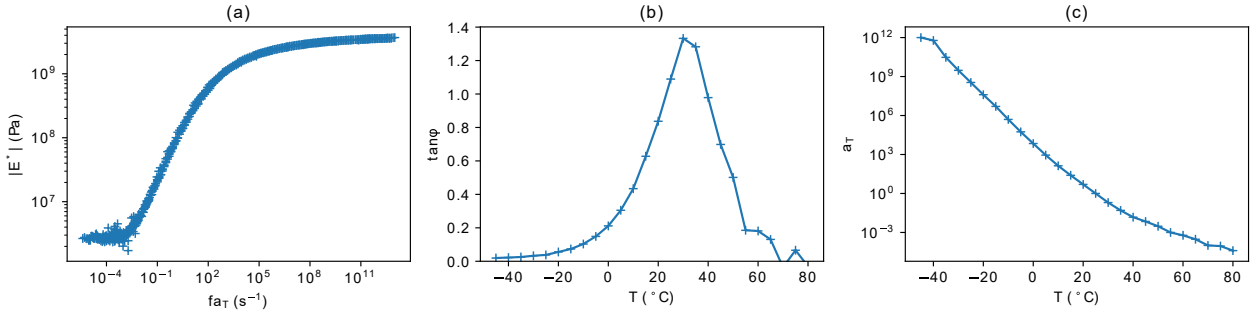

Figure 2.8: Plots showing master curves for the a) complex elastic modulus ($|E^*|$) versus frequency, b) tan ϕ versus temperature, and c) the shift factors (a_T) versus temperature obtained from a DMA experiment on a commercial Galkyd alkyd binding medium that has been aged for 159 days. The complex elastic modulus shows the frequency dependent behavior of the Galkyd binding medium, tanŒ provides an estimate of the glass transition temperature for this system, and the shift factors can provide insights into the overall polymer behavior of the Galkyd system. Data reproduced from [78].

Hedley *et al.* presented some of the earliest foundational work using DMA on artists' paints to assess changes in mechanical responses of lead white ("medium lean") and burnt sienna ("medium rich") samples after exposure to solvents typically used for cleaning. [79] Using a shear stress geometry and temperature range from $5 - 100$°C, an increase of G' (loss shear modulus, defined in a similar way to the E') and significant reduction in tan(δ) for the burnt sienna samples indi-

cated leaching and embrittlement after solvent exposure; the lead white samples showed minimal change in response after solvent exposure. [79] Samples of the same pigments aged 15 years were explored over a range of relative humidities (54-94%) and compared to composite samples of canvas, primer, and a white oil paint layer from a rear primed painting, which demonstrated a softening behavior with an increase in relative humidity.[80] Foster *et al.* modified a DMA system to work with a controlled RH chamber in order to study how the RH and curing process of polyester/melamine paint systems affect the glass transition temperature. [81] The analysis performed on E' and $\tan\phi$ master curves is a good example and illustrates just how much information is obtained through these experiments.

Ormsby *et al.* focused on acrylic paints, specifically investigating the effects of solvent exposure on the chemical, optical, and physical properties of the samples.[82] Comparisons between acrylic brands and exposure methods of swabbing or immersion were considered, showing a strong effect on the dimensional extension of samples after being immersed in the solvents, especially more polar solvents. The T_g of the samples would increase with extended immersed solvent exposure, showing an opposite trend than previous data on oil paints, most likely due to embrittlement of the acrylic paints as a result of the solvent exposure. The samples that were swabbed experienced significantly smaller changes in the DMA data, leading to the conclusion that using swabs for solvent exposure will reduce the overall changes to the bulk properties of the paint compared to full immersion of the paint film, even if some surfactants are lost at the surface of the film. [82] Titanium white acrylic paints exposed to temperature and RH sweeps showed typical responses corresponding to an embrittlement/decrease in T_g with a decrease in RH, indicating a strong relationship between the water content of the paint and the mechanical properties. [83] Some samples that were thermally aged exhibited smaller $\tan(\delta)$, peaks, indicating stiffer films than the naturally aged films and potentially better coalescence of the paint films. The onset of a brittle response from alkyd and acrylic based grounds was investigated using the T_g from DMA to help confirm the ductile to brittle transition as temperatures were dropped from 20°C to −10°C. [51] Phenix performed an extensive survey of T_g values of oil paints and how they were affected by the type of pigment and the age of the paint sample (1-16 years), finding that the range of T_gs varied widely with sample composition. [84] Most samples in the study demonstrated an increase

in T_g with age, indicating an embrittlement effect that could pose potential long term issues for paintings stored in a museum environment.

The application of time-temperature superposition to DMA data collected over a range of temperatures allows researchers to access a much wider range of measurement frequencies than typically accessed with other methods. Sturdy *et al.* used DMA to understand the material response of a commercially produced alkyd based binding medium (Galkyd) as a function of curing time and filler content of zinc oxide, providing a survey of the effects of filler content and the compatibility between DMA, the quartz crystal microbalance (QCM), and nanoindentation for studying paint materials. [29, 78] These studies also compared the material responses measured using DMA and the QCM, demonstrating that both techniques are able to capture the glassy material response well. Verifying the general response regime of a viscoelastic system using the T_g is also fairly common; a linseed oil with zinc/lead white ionomer system determined the T_g of samples with DMA to inform diffusion models for solvent exposure of the ionomer systems, which are used to study the mechanisms controlling the formation of metal carboxylates, or metal soaps, within a paint film. [85] More recently, the mechanical properties of oil paints aged 6 years with several additives including fatty acids (both with and without a metal base), linseed oil, and alumina hydrate were observed and quantified using the DMA to studying commercial Winsor & Newton oil paints, commonly used by contemporary artists. [86] With more linseed oil, the T_g of paints decreased, while alumina hydrate increased the T_g; the added fatty acids did not have a consistent effect on the T_g. [86] Quantification of the effects of solvent exposure (immersion and sponge) for a water-sensitive yellow ochre paint using DMA and nanoindentation indicated that full immersion had the higher chance of embrittling the paint films than the sponge cleaning, highlighting the importance of choosing the appropriate method and solvent when preparing to clean a specific paint. [87] A study that focused on the material response of composite sample was Bridarolli *et al.*, which assessed the change in E' of consolidants that are commonly used as treatments on degraded canvases as a function of relative humidity to determine their effectiveness and viability for use in conservation treatments. [69]

Most research on paint samples using DMA have emphasized the importance of T_g in assessing the overall response of the paint as well as providing a metric for understanding the type of re-

sponse (i.e. more glassy/brittle or rubbery/ductile) to expect from paint samples. T_g of a paint is also an important parameter to know when adding an infill to a painting to ensure there are not added stresses created within the paint layers through a mismatch of mechanical properties. Due to the amount and geometry of the sample necessary to perform these measurements, model systems are typically used, introducing challenges when drawing conclusions about the behavior of "young" paint samples (1-15 years) and using them to predict the behavior of older paint samples (100+ years). When time-temperature superposition is used for a DMA experiment, one can obtain more information about a single paint film than from a typical tensile testing experiment. There are some nuances to be aware of when determining the T_g of the paint sample, but the papers in this section provide guidance towards understanding those nuances.

2.4 Shear Rheometry

Shear rheometry can be viewed as a version of DMA that is used in a shear geometry and well suited for samples with a liquid character. It has been used to study historic paint formulations, varnish, and glaze recipes, with an emphasis on understanding on how the recipe influenced the overall texture and visual presentation of paintings today. These experiments are typically performed using either the parallel plate geometry, shown in Figure 2.9a, or the cone and plate geometry, shown in Figure 2.9b. Samples studied using these geometries experience shear forces, resulting in the measurement of a complex shear modulus, G^*, analogous to the complex elastic modulus, E^* defined in Section 2.3. For isotropic materials, which have the same bulk properties in all directions, the shear modulus can be related to elastic modulus through the following expression that also involves Poisson's ratio, ν.

$$E = 2G(1+\nu). \tag{2.6}$$

For liquids and relatively soft polymers at temperatures above their glass transition temperature, $\nu \approx 0.5$ and $E \approx 3G$. In an oscillatory experiment where the complex shear modulus, G^*, is obtained, $E^* \approx 3G^*$, $E' \approx 3G'$ and $E'' \approx 3G'' =$, where G' and G'' are the storage and loss shear moduli, defined as described in Section 2.3, but with G', G'' and G^* replacing E', E'' and E^*.

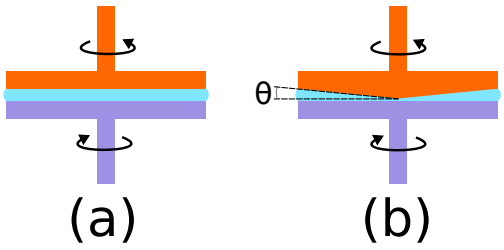

Figure 2.9: Schematic of the cone and plate geometry for shear rheometry. The blue portion is the sample, the purple arm is the base plate, and the orange portion is the top plate, which is either a flat plate or a cone. The angle θ indicates the angle of the cone, which is typically between 0.25 and 4°. The arrows indicate the direction of force applied to the sample. The figure is modified from an image licensed under the Creative Commons Attribution-Share Alike 3.0 Unported license.

Originally developed for use in industry, shear rheometry has been used for about 70 years to understand the mechanical properties of paints. Due to the longstanding use of the technique, best practices for measuring the mechanical properties of historic recipes have been described in some detail. [88, 89] One of the earliest reported discussions about the composition of the paint affecting the rheological behavior of the paint examined the state of white impastos used by Rembrandt, concluding that the proportions of pigment and driers resulted in a thixotropic behavior of the paint, with the viscosity decreasing with increasing strain rate. Not only did such insights provide a greater understanding of Rembrandt's paint structures, it was shown that these data could be used to relate the artist's technique to the measured yield stress of the paint. [90] Further surveys of the effects of adding resins, solvents, and pigments on the viscosity and resulting yield stress of paints, glazes, and varnishes has broadened the knowledge base for thinking about how these historic recipes influenced the response and characteristic appearance that we associate with these materials. [4, 91, 92] More recent research has focused on studying the rheological properties of gumtion, an experimental paint material that added resin to the oils to decrease the drying time of the paint, and the effects of fillers such as calcite on the workability of lead white paints. [93, 94] For instance, the amount of pigment Van Gogh needed to create the impasto effects in his paintings was connected to the relationship between the yield stress and pigment concentration. [28] Rheology has also been used to characterize plant-oil based inks (similar recipes to oil-based paints) to optimize their properties as well as adhesive combinations to maximize their effectiveness as consolidant materials. [95–97] Thixotropic behavior and the effects of pigment concentrations on the flow of the paint through rheology provides both important conservation data explaining causes

of sagging, drippings, or flaking of paintings as well as art historical insights into how historical recipes can be correlated to artist technique.

2.5 Quartz Crystal Microbalance

Originally used as a technique for studying small mass changes, the QCM has been developed to study the viscoelastic properties of biological and polymer-based systems. [98] Many of the advancements in determining the viscoelastic properties over the past decade have been developed by the Johannsmann group. [99, 100] The QCM measures the impedance spectra of a quartz crystal when an oscillating voltage is applied to electrodes on either surface of the crystal as shown in Figure 2.10. When a sample film is deposited on one surface of the crystal, the resonant frequencies are shifted, allowing one to determine both the mass and mechanical properties of the sample.

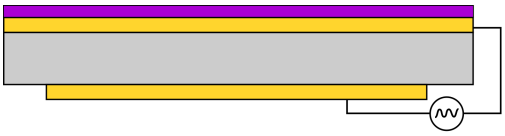

Figure 2.10: Schematic of a quartz crystal used on the QCM. The grey is the AT-cut quartz crystal, which has a resonant frequency of 5 MHz. The gold layers are the electrodes which conduct the oscillating voltage, shown in the circle at the lower right of the diagram. The purple layer is a sample that has been deposited onto the crystal and typically has a thickness less than 10 ¯m.

Resonant frequencies of quartz crystals are typically in the megahertz (MHz) regime, which means the QCM probes material responses in the "glassy regime" for most polymer and paint systems. Sample preparation is important because the thickness of the sample plays a critical role in the ability to obtain meaningful data. A broader discussion about the range of material properties probed by the QCM and the required thicknesses to detect those properties has been previously published by the Shull group. [101, 102] In brief, polymer samples prepared to target viscoelastic properties can range from hundreds of nanometers to 10 ¯m in thickness. Such small sample sizes can effectively be treated as a skin layer since there is minimal diffusion required before a sample is equilibrated with its environment. Having an exposed surface of the sample also facilitates measurements of temperature, humidity, and solvated atmospheres, and the use of non-invasive molecular characterization techniques (*e.g.*, FTIR, Raman). For paint model systems, data

collection can begin within a few minutes of casting, rather than having to wait for months before the sample becomes touch dry, allowing the study of paint model systems through the entire curing process.

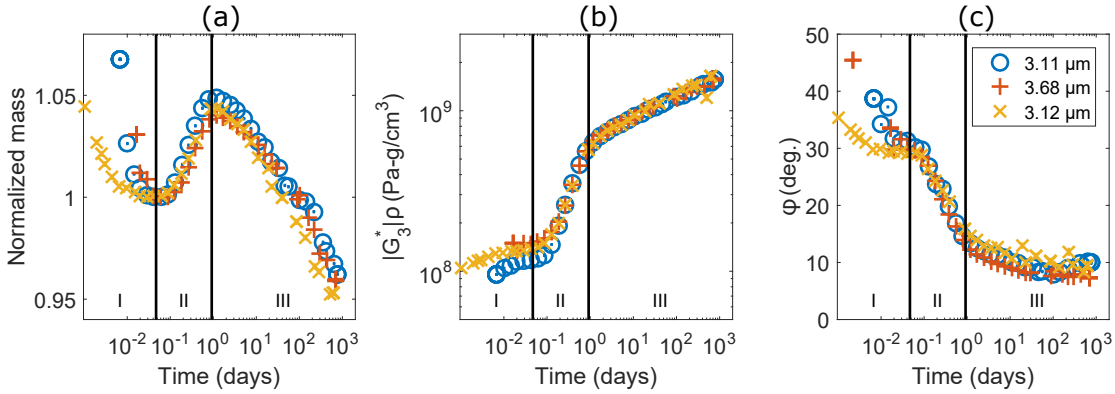

Figure 2.11: Representative QCM data during the drying and curing of a commercial Galkyd alkyd binding medium sample showing a) normalized mass, b) the complex shear modulus of the third harmonic multiplied by density ($|G_3^*|\rho$), and c) the viscoelastic phase angle (ϕ) as a function of time. The three regions shown on the plot are representative of the I) solvent evaporation, II) oxygen uptake, and III) long term curing behavior of the alkyd samples. Data reproduced from [78].

The curing behavior of a commercial alkyd binding medium was measured over the course of three years, as well as the effects of temperature and the filler effects when zinc oxide was added. [29, 78, 103] Analyzing both the mass and the mechanical properties of a sample can provide a clearer picture about how the material responses of paint films change as a function of their environment as demonstrated in Figure 2.11. From these data, Sturdy *et al.* determined three distinct regions during the curing process of the alkyd paint system: solvent evaporation (region I) taking place in the first few hours of data collection, short term curing where oxygen uptake happens (region II) during the first day, and long term curing over the following three years (region III). It is possible to see the impact of these mass fluctuations on the mechanical properties, with the short term curing region showing the steepest rise in stiffness (shown by the sharp increase in $|G_3^*|\rho$ (product of the magnitude of the complex shear modulus at 15 MHz and the film density) and decrease in ϕ (viscoelastic phase angle at 15 MHz) of Figure 2.11b and c). Even after three years, the complex shear modulus of the alkyd samples continued to increase, supporting the understanding that paint systems continue to experience chemical changes years after they are cast onto the quartz crystal. The QCM is versatile enough to incorporate solvent exposure for understand-

ing the swelling behavior of paints, providing the capability to study the effects of plasticization on the overall stability of a paint sample. Samples can also be exposed to UV light to understand the effects on the mechanical properties of paints with photosensitive pigments, and the temperature-dependent response of the the sample can also be probed [101]. These temperature-dependent measurements are a particular focus of ongoing research because they probe molecular relaxations in the material that are likely coupled to the ductile/brittle transition in the material, complementing information obtained from more traditional measurements of the glass transition temperature. While these samples can be exposed to a wide range of environmental conditions, it is dependent on good contact between the sample surface and the quartz crystal, making it difficult to use the QCM to study historic paint samples directly. These studies provide initial steps for being able to understand more fully the initial curing stages of binding media, how they affect the overall paint material response, and begin to investigate more targeted questions related to curing and degradation processes in paints.

2.6 Nanoindentation

2.6.1 Technique background

All the techniques described up to this point in the review require the use of model systems in order to obtain the mechanical properties of paints. These techniques provide useful information and can allow a wider range of experiments to be performed (especially those that are more destructive in nature), but there can be difficulties relating these results back to actual historic paints. One technique well suited to bridge the gap between model systems and historic paint samples is nanoindentation. The small sample size required to obtain data about the modulus, stiffness, and hardness of a paint sample is well suited for use on cross sections from paintings. Typically, the indentations are $\sim 2^{-}$mdeep and $\sim 2-5^{-}$m wide, making them nearly invisible to the naked eye. Oliver and Pharr have outlined the methodology for contact mechanics of elastic-plastic materials, which has been widely incorporated into nanoindentation analysis. [104] Oyen and Cook summarized how contact mechanics analysis can be expanded to include a wider range of tip shapes, two of which are shown in Figure 2.12, and accommodate material responses that are viscous,

expanding contact mechanics to use on biological and polymeric based materials. [105]

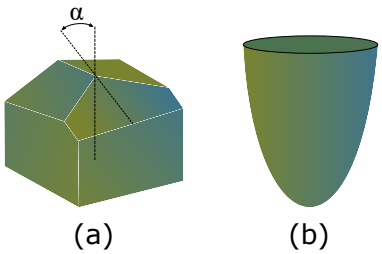

Figure 2.12: Geometry of a) a Berkovich tip and b) a spherical tip commonly used in indentation experiments on paint materials. The angle, α, is 65.35° for a standard Berkovich tip. The figure is based on images available in the public domain through Wikimedia Commons.

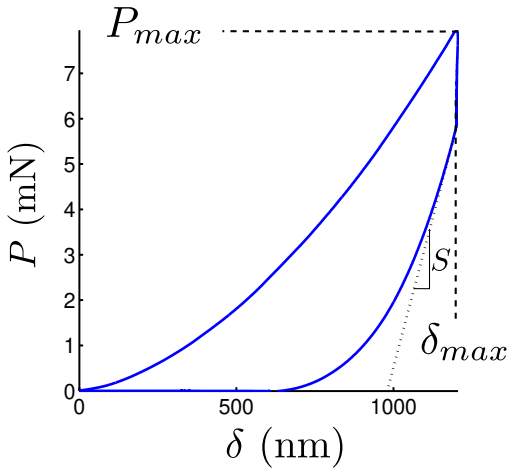

Figure 2.13: Typical load-displacement curve for indentation of the polyester resin used to embed the paint samples, labeled to illustrate the values of P_{max}, h_{max} and δ_{max} and S.

Material properties are obtained from load-displacement curves, such as the one shown in Figure 2.13. Note that a displacement of zero is defined as the point where initial contact is made between the indenter and the material. Because most paint materials have a time-dependent response, the detailed protocol control for controlling the displacement will affect the measurement. The load-displacement curve shown in Figure 2.13 shows an experimental protocol where the displacement increased at a constant rate from zero to a maximum value of δ_{max} during a loading time of ≈1s. The displacement is then fixed at this maximum value for ≈ 1 minute, and is then decreased at the same rate as that used for the loading portion of the experiment. It is also common to have the holding condition be based on a fixed load. The elastic modulus is obtained from the unloading

stiffness, S, defined as the slope of the initial portion of the unloading curve (see Figure 2.13). For a parabolic indenter where the contact between the indenter and the material has a radius of a, the following expression for S is used to extract the elastic properties:

$$S = 2a_{max}E_r. \tag{2.7}$$

Here E_r is the reduced modulus obtained from plane strain geometries like the indentation experiments of interest here. It involves the following combination of the elastic modulus and Poisson's ratio:

$$E_r = \frac{E}{(1-\nu^2)}. \tag{2.8}$$

The quantity a_{max} is the contact radius radius established for $\delta = \delta_{max}$, which for a parabolic indenter is given by the following expression:

$$a_{max} = \sqrt{\delta_{max}R}. \tag{2.9}$$

where R is the radius of curvature of the indenter at its tip.

For non-parabolic indenters and those for situations where material yielding needs to be accounted for (as with the Berkovich indenters shown in Figure 2.12a, a generalization of Eqs. 2.7 and 2.9 needs to be utilized. The most commonly used procedure was developed by Oliver and Pharr[104], and involves the following:

1. Replacement of a_{max} with an effective radius, a_{eff}. The area of a circle with this radius is the same as the actual maximum contact area between the indenter and the material:

$$\pi a_{eff}^2 = A_{max}. \tag{2.10}$$

2. Definition of a contact depth, δ_c, which accounts for deformation of the material outside the

contact zone. The Oliver and Pharr expression for δ_c is:

$$\delta_c = \delta_{max} - 0.75\frac{P_{max}}{S}. \tag{2.11}$$

3. Use of a relationship between A_{max} and δ_{max} which depends only on the indenter geometry. For a Berkovich indenter this relationship is:

$$A_{max} = 24.5\delta_c^2. \tag{2.12}$$

For a parabolic indenter of with tip radius of curvature R, this relationship is:

$$A_{max} = 2\pi\delta_c R. \tag{2.13}$$

These equations enable the maximum contact radius (or the effective maximum contact radius, a_{eff}) to be obtained from load-displacement relations directly without direct visualization of the contact radius, a determination of the reduced modulus, $E/\left(1-\nu^2\right)$.

The other property that is often obtained from a nanoindentation experiment is the hardness, H, given by the ratio of the load to the projected contact area:

$$H = \frac{P_{max}}{A_{max}}. \tag{2.14}$$

While a value of H can be obtained from Eq. 2.14 for any tip shape, it is usually used with tips with sharp edges, like the Berkovich tip. In these cases the material deforms plastically in the regions near the indenter edges, and the hardness is taken as a measure of the yield stress of the material. In these cases indentation necessarily involves irreversible deformation of the material, and limits measurements of historic samples to regions of the paint that are not visible (small portions taken from underneath the frame, for example). Indentation probes a volume of the sample with dimensions controlled by a_{max}, and this length scale controls both the depth that is sampled in the measurement and the lateral resolution that is obtained. This length scale is in turn controlled by the size of the indenter tip and the depth of the indent in the sample, and is much

smaller for atomic force microscopy than for nanoindentation.

2.6.2 Advancements for Artists' Paints

In cultural heritage research, nanoindentation has been used to correlate changes of mechanical properties with optical and chemical changes as a function of aging or light exposure for natural and synthetic binding media. [106] Comparisons between reconstructed and historic paint samples of white pigments used by Van Gogh demonstrated that the age of the sample had a direct effect on the resulting reduced modulus (with the modulus of historic samples being up to an order of magnitude higher than the reconstructed samples), highlighting one of the main issues for studying model systems. [107] However, the authors of this study also concluded that it can be difficult to determine an accurate modulus for a paint due to the filler behavior of pigment particles in the paint samples. The presence of these stiffer pigment particles causes significant increases in the reduced modulus near the particles. More recent studies using nanoindentation have incorporated comparisons of the data from nanoindentation with data from DMA and dynamic vapor sorption to understand how each technique showed the changes in mechanical properties when subjected to variations in RH. [108] Measurements on the same zinc oxide filled alkyd samples with DMA, QCM and nanoindentation have confirmed the compatibility of the three techniques when the frequency of the measurement is appropriately taken into account. [29] Fujisawa *et al.* add a compliance term to their determination of mechanical properties to account for edge effects of the stiffer embedding resin on a paint sample. [109] A more systematic study with nanoindentation focused on understanding edge effects for cross sections mounted in resin, showing how these effects impact the data obtained from the experiments. [110] Since paint samples are typically mounted in resin materials that can exhibit a higher modulus, Freeman *et al.* explored the minimum size required of cross sections to be able to minimize an artificial stiffening affect from the resin substrate. Initial steps have been taken towards mapping the mechanical properties of an entire painting cross section, which will be an important method for being able to probe the mechanical properties of historic paints more readily. [111] More work remains to be done in order to refine this mapping technique and adapt it to paintings. Resolving effects of solvent cleaning for a water sensitive oil paint were studied with nanoindentation as well as DMA to determine

how much surface and bulk mechanical properties would be effected, where most of the data for sponge cleaned samples exhibited statistically insignificant changes. [87]

In tandem with expanding the use of nanoindentation through mapping and optimizing the analysis of cross sections, atomic force microscopy has the potential to be applied to painting cross sections to obtain mechanical properties. Since the AFM tip is smaller than the tip of a nanoindenter, it can provide a higher resolution of the surface mechanical property data across the paint sample. One issue that needs to be considered with the AFM is that for very small contact dimensions the effect of adhesive interactions become more important. When these effects are appropriately accounted for, the AFM can be used to quantify the viscoelastic properties of a material. The approach has been validated for an acrylic system [112, 113], and similar approaches can in principle be used to investigate the properties of aged paint systems. A variety of complications exist when applying the technique to heterogeneous systems like actual artist's paints [114], but the availability of commercial AFM instrumentation with the ability to obtain load/displacement curves over a small region of the sample may prove to be useful in the field of cultural heritage.

2.7 Developing Research Directions

2.7.1 Laser Shearography

One technique developed in the last couple of decades to observe changes in the mechanical properties of paintings is laser shearography. As shown in the schematic in Figure 2.14, interference patterns of a painting are collected before and after a slight thermal, acoustic, or vibrational excitation caused by the diffuse light sources in the image. The interference patterns are used to create a phase map of the painting surface, which can be unwrapped to generate a displacement gradient map, also known as a strain map.

Kalms *et al.* focused on developing a setup that would be mobile enough to easily set up in a museum environment and be stable enough to provide interferograms that were sensitive to changes in the painting after thermal loading, but not sensitive to slight environmental changes in the surrounding conditions. [116, 117] The sensitivity of the phase maps obtained through laser shearography helps researchers observe defects such as cracks, paint losses, and delaminations

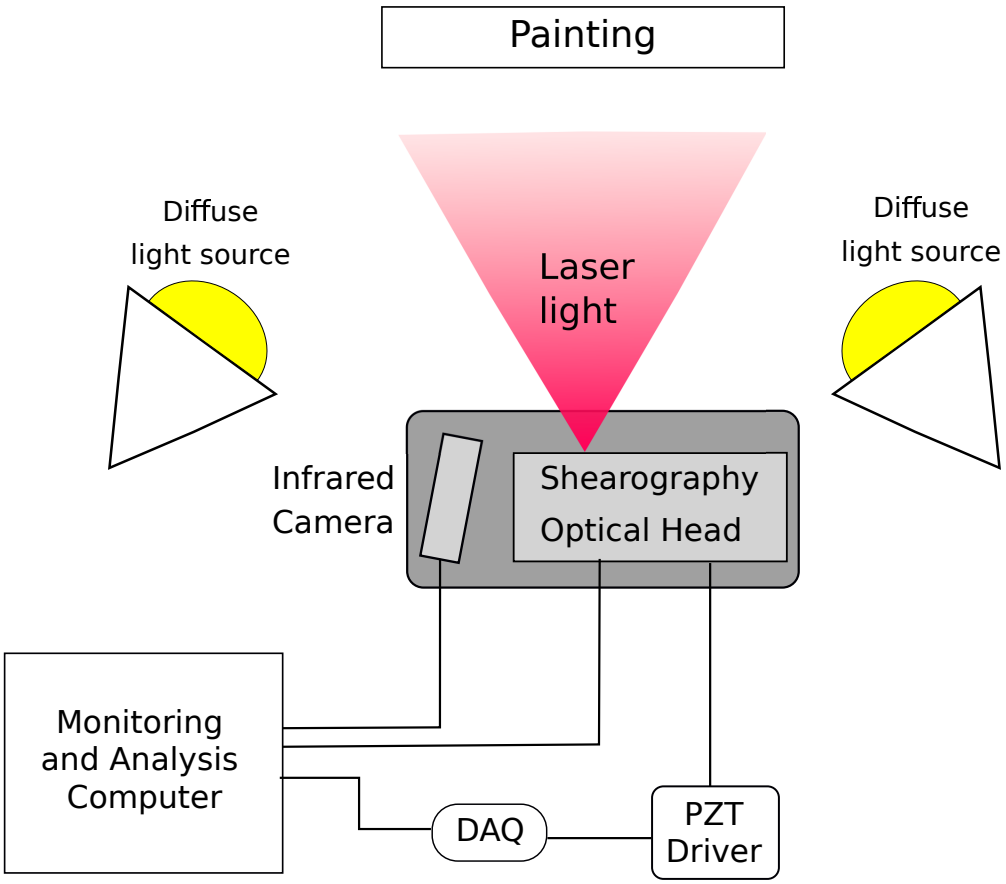

Figure 2.14: Schematic of a shearography setup for measuring slight thermal changes in paintings as a result of a diffuse light source. The laser light from the optical head is used to obtain the phase maps of the surface before and after the thermal loading of the painting. The phase shifting is achieved using a piezoelectric transducer driver (PZT driver) and an analog output card (DAQ). Modeled after and adapted from Klausmeyer *et al.*[115]

more easily, especially if the defects are subsurface. The maps are also capable of serving as a diagnostic tool for cultural heritage, guiding attention to areas that need more immediate attention during a conservation survey. The sensitivity of laser shearography to detect delaminations, impacts on a painting surface, and the propagation of cracks through paint layers was successfully demonstrated with mockup samples. [118] The use of strain maps to show the potential areas of concern and highlight areas of potential degradation in the paintings have been optimized for ease of interpretation by conservators. [119] Shearography has also been paired with other imaging techniques such as terahertz imaging, fringe projections to observe 3D topographic maps, and reflectance transformation imaging to provide more complete datasets for diagnosing defects and changes in a painting after environmental fluctuations or transport. [115, 120, 121]

Some optimization of strain maps from the displacement gradients was also performed on a test painting to quantify the strain experienced by a painting as a result of cycling lights in a museum setting. [115, 122] Comparing the phase maps of defects in paintings to simulated phase maps generated using finite element analysis (see Section 2.7.2), allow researchers to understand the nature of defects within a painting and to vary the parameters of the defect until the simulated map matches the experimentally observed map, which can be useful for understanding how different defects/areas of degradation within a painting can affect the resulting phase map. [123]

Laser shearography shows great promise as a diagnosis and monitoring tool for performing preliminary conservation surveys and tracking the state of a painting, especially after transport for an exhibition. The mobility of the setup allows it to be fairly cost effective for a museum setup. While it takes some time to gain the experience to interpret the data from the phase maps, the strain maps are a useful tool for understanding the mechanical response of the painting to slight fluctuations in its environment.

2.7.2 Finite Element Analysis

2.7.2.1 Technique Background

When a paint layer is considered in the context of a painting, there can be range of complex stresses applied to the layer by the neighboring layers and quantifying the stresses can be difficult using free standing films. One way to look at understanding these stresses is to use finite element analysis (FEA), which is capable of modeling the field responses (such as stresses or strains) for complicated objects. A brief description of the process for using FEA is that the geometry is discretized into smaller elements, a simplified material model is chosen that resembles the expected response from the object, boundary and load conditions are applied, then the solutions are calculated to determine the field responses to the given load. When the geometry is defined, material properties need to be inputted, which typically include the elastic modulus, Poisson's ratio, and hygric or thermal expansion coefficients, depending on the type of loading the object will experience. These material properties are usually informed from experimental data using one of the techniques previously discussed in this review. How the material will respond to a load also needs to be de-

fined; the most common responses are isotropic (the same response in all directions) for paints or grounds and orthotropic (some directional dependence) for wood and some canvas substrates. The ability to break down the object geometry into smaller elements allows easier comparison of the stress/strain response on the micro and macroscopic scale, which is one of the strengths of this technique. Selection of a material model is determined by the expected response from a material. The two models that have been applied to cultural heritage objects are a linear elastic model, assuming a fairly elastic response of the material, or a visco-hyperelastic model, which allows for more time dependent deformation of the object. [124] The boundary and load conditions are used to constrain the geometry and explicitly define the scenario being modeled, for example, a strain being applied as a displacement along one axis of the model. The results from a simulation are typically displayed as field maps, such as the stress field depicting the horizontal stresses in a gesso ground layer shown in Figure 2.15. For this particular example, the highest areas of stress are immediately next to the crack tip, which is functioning as a stress concentrator within this layer. From these stress fields, the energy release rate can be determined by integrating the area around the crack tip. Comparing the value of the energy release rate to values of $\mathcal{G}_c$ obtained from measurements on model materials will indicate if the crack would continue to propagate under these conditions.

FEA is a very powerful method and allows the comparison of a range of material properties and scenarios in a relatively short time compared to preparing that range of experiments, there are also some things to keep in mind when reviewing the results of a simulation. The outputs from a simulation are heavily dependent on the material properties inputted, which can make it challenging to extend the use of a simulation beyond its initial goal. The results from a FEA model need to be validated against either experimental values (e.g. the expected results from the experiment that provided the material property inputs) or against analytical models. A balance also needs to be struck between the computational expense of running the model with its overall accuracy, which can make it difficult to model some non-linear behavior that would be expected from paints and paintings.

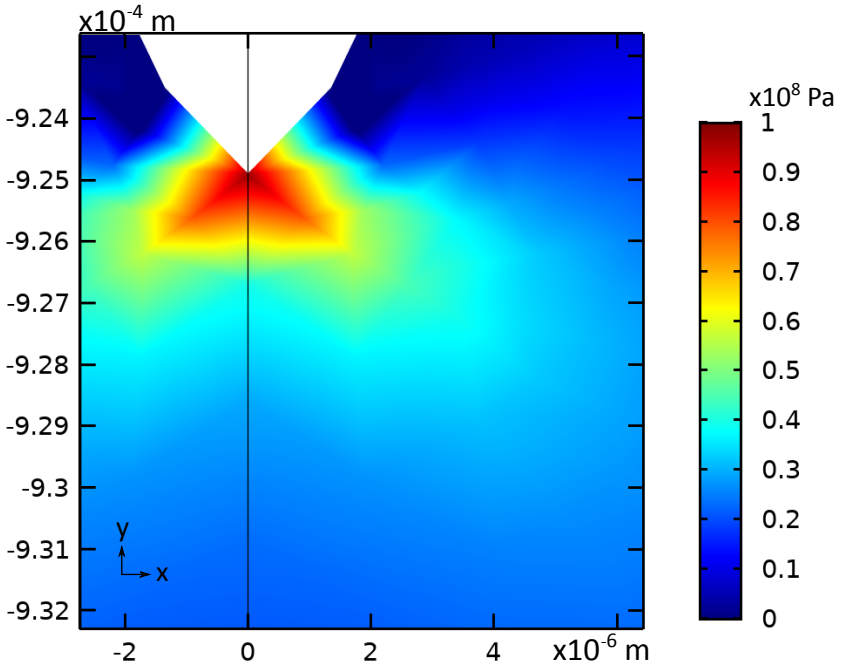

Figure 2.15: A stress field surrounding a crack tip depicting the horizontal stresses in a gesso ground layer, indicating that the highest stresses in the ground layer are occurring at the crack tip, which is functioning as a stress concentrator. The FEA simulation used to create this stress field is based on the simulations used in Bratasz *et al.* [125]

2.7.2.2 Application to Cultural Heritage

An area of cultural heritage research that has begun using FEA more often focuses on understanding craquelure development and the mechanisms governing crack opening or delamination. For the papers discussed in this section, all use a linear elastic model as their material model unless otherwise specified. Mecklenburg's work using FEA focused on the understanding of the response of paintings to T or RH fluctuations, out of plane bending of the canvas due to vibrations from transport, and an impact force on the side and corner of a painting to simulate a painting being dropped, comparing the resulting simulated craquelure patterns to ones observed in painting mock ups. [40, 71, 126] Further studies of vibrations affecting canvas paintings have been carried out to assess the vibrational modes that are most relevant to consider. [127] Bratasz *et al.* used a more targeted FEA approach to study the behavior of gesso ground layers on a wood substrate, focusing on how the response of the ground layer translates to the development of a craquelure pattern that is less susceptible to environmental fluctuations. [125, 128] Eumelen *et al.* have investigated the growth behavior of metal soaps combined the chemical information related

to the diffusion of metal soaps into aggregates with estimated mechanical properties for a paint layer to both understand the directionality of metal soap formation and the most likely regions for cracks to form within the model from the stresses caused by the aggregates. [129] More recent investigations from Bosco *et al.* have been focused on understanding the underlying deformation mechanisms that can lead to crack opening or delamination when a paint layer is exposed to flexural stresses as a result of increased moisture. [130, 131]

An additional area where FEA can be applied for cultural heritage research is to simulate long term fatigue behavior. The simulations can study the potential for cyclic fatigue that would cause failure or delamination of a paint layer, which was performed using a visco-hyperelastic material model since the timescales of fatigue responses tend to be more viscoelastic in nature. [124] Computational simulations studying fatigue behavior in paintings provide the flexibility to test multiple parameters and draw preliminary conclusions on a faster timescale than can be done with experiments, which is useful for informing conservator practice on a wide range of paintings varying in composition and structural support in a relatively short time. FEA can also be used to generate displacement fields as a result of thermal excitation, as was shown by Buchta *et al.* when observing defects using laser shearography. [123]

While being able to test a wide range of parameters using FEA simulations is a strong benefit of the technique, there is a major caveat: one needs to insure the results are physically relevant. Accurate determination of the critical energy release rate, $\mathcal{G}_c$, mentioned above, is one example. Informing the models using material properties for the paints or paintings of interest is a key step towards validating and extending the model.

2.7.3 Vibration Studies

Another potential source of damage to paintings is from vibrations causing flaking or crack formation, whether from transport conditions, acute scenarios such as a construction project, or more diffuse ambient noise in or around a museum. When these vibrations occur, they tend to apply an oscillating stress over a longer period of time, which can lead to longer term fatigue responses of the painting. Conservative limits for vibrations during a construction along with a proposed plan for assessment of a construction project was outlined thoroughly by Johnson *et al.* to determine

a vibration range of 1.5-4.0 mm/s depending on the frequency of the vibration. [132] Assessing these sources of vibration and understanding the effects on the longevity of objects in the museum has been assessed through the detection of background vibrations in museum as well as exposure of model systems to sustained periods of vibration to determine thresholds for damage to objects. Wei *et al.* assessed the affects of these background vibrations within a museum setting to understand some thresholds of safety for paintings and objects, determining it to be somewhat lower than expected. [133] A particular case study where vibrations are more problematic are pastel paintings, or paintings where powdery pigment layers are applied to the support. Due to the low level of adhesion between the paint layers and support, pastel paintings are a useful case study for assessing the potential limit of material loss due to vibrations before the painting is noticeably damaged. [134]

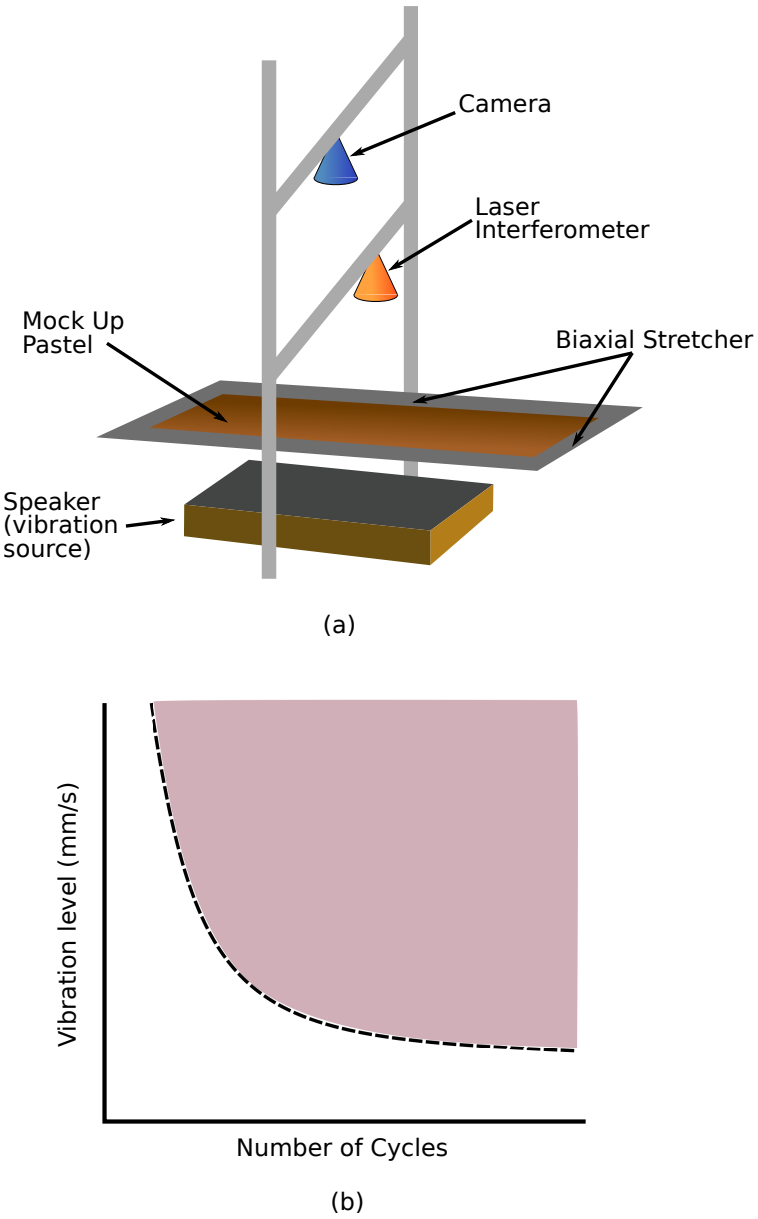

Figure 2.16: The a) schematic of a vibration fatigue stage setup for mock up pastel paintings and b) a modified Wöhler curve showing the vibration level versus the number of cycles of vibrations. The dashed curve is the fatigue limit for the mock up, above which (and emphasized by the shaded region of the plot) the pastel mock up would be damaged by the vibrations. The schematic of the setup is based off the setup used in [135].

Shown in Figure 2.16, a biaxial tension setup with mockup canvases is used to generate modified Wöhler curves (displacement of material versus number of cycles) to correlate the amount of vibration sustained by an object with the overall loss of material and minimum amount of acceptable loss from pastel paintings as determined by imaging and conservator observation. [134] Within

this setup, a laser interferometer is used to track the amplitude of the vibrations and the camera is used to monitor the overall surface damage of the canvas. These fatigue tests can provide useful information about the amount of vibration that can be sustained before damage, which when paired with information about display and travel of an object, can help curators and conservators determine the best lifetime decisions to maintain the best conditions for a pastel painting as long as possible. While pastel paintings are more sensitive to damage by vibration than other paintings, these types of fatigue tests can be used to assess the chances of new craquelure formation in an object, especially after travel or acute exposure to sustained vibrations. Efforts in this area have focused on understanding the effects of pigment size on the stability of the pastel painting, incorporating high speed imaging to understand the resonant vibration modes of a canvas more fully, and working on more directly relating the data from mockup samples to actual museum objects. The latter point would allow the use of Wöhler curves as a predictive tool for determining if moving a pastel is within a safe limit.

2.7.4 Single Sided Nuclear Magnetic Resonance

Paintings that undergo solvent exposure for cleaning treatments tend to experience embrittlement of the surface paint layers. A more thorough review discussing the chemical changes and implications has been recently published. [136] A fairly novel way of studying paintings has been explored by researchers to correlate the mechanical properties with chemical changes in paint is single sided nuclear magnetic resonance (NMR), or NMR relaxometry. [137] This technique uses a NMR-MOUSE (Mobile Universal Surface Explorer) to look at the relaxation times within a layer using a locally generated magnetic field and detector. Transverse relaxation times (T_2), related to spin-spin interactions of the material being studied, can be recorded in depth profiles and can be related to the stiffness of a material. If a material has reduced intermolecular motion (such as a cross-linked paint material), T_2 will decrease as the stiffness increases. [137] Single-sided NMR has been employed to look at both PVC and the effects of solvent on painting materials. Model systems of traditional oil paints, water-miscible oil paints, and acrylic paints with varying PVC values were studied to determine if the comparative results could be quantified as a function of increasing PVC. [26, 137–140] One of these studies looked to extend their findings with young

model systems to see if they could develop a protocol for determining the age of paint materials based on the response of the relaxations times, which was unfortunately inconclusive. [139] Single-sided NMR has also been used to study the effects of solvent exposure on the stiffness of paints. The first study assesses previous solvent treatments of a 17th century painting through comparison with another similar painting from the *Pipenpoyse Wedding Set*, demonstrating that a cleaning treatment performed on one of the paintings had a statistically significant effect on the stiffness, most likely due to a redistribution of low molecular weight molecules through the paint layer.[141] A more recent study used both single-sided NMR and solid phase microextraction to investigate the effectiveness of swab or gel cleaning of more green solvents for painting cleaning and is able to demonstrate that the gel method produces a reduced paint response and showed less penetration into the paint layer than the swab method. [142] While this technique does not provide absolute information about the stiffness of the paint layer, single-sided NMR can provide relevant information about stiffness changes over the depth profile of a paint layer, which can be especially useful when investigating the solvent response of a paint material.

2.8 Conclusions

When considering the mechanical properties of paints, there are quite a few factors that need to be considered. It is important to understand the material properties of both the binding medium and the pigment, which can be partially informed from chemical analysis, as well as the pigment concentration and how it affects the overall properties of the paint. Since paintings are multi-layered structures, there also have to be considerations for the interactions (both chemical and mechanical) between layers. Beyond the paint composition and structure, the environmental factors (*e.g.*, T, RH, vibrations, and solvent exposure) can affect the response of the paint and need to be accounted for when considering a conservation treatment.

Several techniques have been developed over recent decades to help provide this information. Tensile testing, DMA, rheology, and the QCM can provide information about the mechanical properties of paints from the liquid to the solid state, creating a data set that is more comprehensive and complete than any dataset provided by a single technique. These techniques are limited to

model systems, but with the correct assumptions and comparisons to historic samples, the data can be used to inform conservation treatments. Techniques that are directly applicable to historic objects have been developed and adapted from industrial applications for cultural heritage, which expands the breadth of knowledge accessible to conservators. Nanoindentation can provide an estimate of the stiffness of a paint cross section and allow a conservator to explore the temperature and solvent response of the cross section before beginning a treatment. Laser shearography, since it is both portable and non-invasive, is a technique that will be most useful for both initial surveys of a new painting in the collection (pinpointing areas most in need of deeper investigation) and for a painting traveling on exhibition (to track the amount of damage accumulated as a result of travel). Computational studies using FEA can allow researchers to consider both the macroscopic and microscopic length scales affecting the mechanical properties of a paint simultaneously as well as explore a wide parameter space more rapidly than experiments, given that the models are well informed and verified via theories or experimental comparison. Studies analyzing the vibration response of model systems and generating predictive curves that can be used to assess objects in a museum, especially more sensitive objects such as pastel paintings, give some insights into how much travel and exhibition an object can endure before it needs restoration or to be retired. Single-sided NMR is emerging as a non-invasive technique that can provide useful depth profiles of comparative stiffness measurements, which can provide information about PVC or previous solvent exposure of a painting sample.

To continue progressing the field and to provide relevant information for conservators, research efforts expanding the breadth of pigments investigated with these techniques will provide data to compare to when determining a conservation treatment for an object. Information about paint samples can also be expanded by combining any of the techniques discussed in the paper, requiring an understanding of how the techniques can complement each other. Extrapolating expected material responses of historic paints from relatively young model systems continues to be a challenge for researchers and requires systematic efforts to look at aging trends and see if they can be extrapolated to longer times for a wider range of paint materials. Expanding the efforts of performing optical or in situ measurements of paintings to obtain mechanical properties is very appealing, especially when surveying objects for conservation treatment. [2] One potential way

to push this direction forward is to collaborate with industry, adapting their existing technology to work for paintings. [143] The choice of which techniques are most relevant to use is also two potential research aims: to answer technical art history questions (*e.g.*, such as determining an artist's historic formulation) and to expand the knowledge base of relevant materials in ways that benefit the conservation community. The purpose of this review has been to describe past work while highlighting newer capabilities that we expect to be useful in addressing these aims, in hope that the interdisciplinary collaborations enabling success would continue to flourish.

Chapter 3

Using the quartz crystal microbalance to monitor the curing of drying oils

3.1 Introduction

Since the 15th century, linseed oil has been commonly used by painters as a binding medium for paints [3]. One of the material properties that drew painters to using linseed oil was its ability to mix with pigments and additives, coat surfaces well, and then undergo a curing process to form a solid film. In drying oils such as linseed oil, a polymer film forms as a result of an auto-oxidation process where peroxide, ether, and $C-C$ crosslinks are formed as a result of oxygen reacting with unsaturated fatty acid chains in triglyceride molecules of the oil [5, 7, 10]. While there are many chemical reactions that contribute to the curing process of drying oils, on a more macroscopic level the oil will transition from being liquid-like to solid-like as the polymer film forms. The stiffness of a polymer system increases as crosslinks form between polymer chains. Crosslink formation in drying oils is typically considered a slow curing process, while most synthetic polymer systems use ultraviolet light, temperature, or chemical initiators to induce and accelerate this process [144–147]. Drying oils play a prominent role as binding medium in artworks. As such, it is important to learn how drying oils form networks in order to ultimately understand long-term degradation and the factors that influence network stability [48, 148–150]. The network formation process of linseed oil has been investigated extensively through chemical investigations including infrared spectroscopy and chromatographic analysis [148, 151–154], but the mechanical properties during the initial curing step have never been properly characterized. The sol-gel transition associated with polymer network formation makes the most common approaches to measuring the mechanical properties of this film impractical to use. Rheology is most ideally used on liquid-like samples and has been used to understand the flow and application properties of paints and drying oils with an emphasis on the effects of historic preparation recipes for these oils [4, 93, 94, 155, 156]. Tensile

testing, dynamic mechanical analysis and micro-/nanoindentation can be used to investigate the mechanical properties of dried films, but the samples must be solid in order to be measured, making these techniques not feasible to use on oil films that have not reached an initial state of cure [13, 14, 44, 48, 82, 83, 107, 108, 110, 111, 157].

The quartz crystal microbalance (QCM) is an uniquely suitable technique to measure the mechanical properties of a polymer film experiencing a sol-gel transition. This technique uses the piezoelectric properties of quartz to propagate a mechanical shear wave at high frequencies (MHz) through a film of interest [98, 99]. The resulting shifts in the resonant frequencies of the quartz crystal can be used to determine the mass and mechanical properties of the film [158]. A QCM sample typically has a surface of the film open to the surrounding environment, which can make it an ideal technique for looking at changes in the mechanical properties as a result of temperature, relative humidity, or exposure to solvent [78, 103, 146, 159, 160]. The films of interest are also fairly thin (on the order of $0.7 - 6$ ¯m), effectively removing any diffusion barrier that would be present for a bulk film. The QCM has been previously used to characterize the evolution of mechanical properties in many polymer systems, including that of an alkyd binding medium which undergoes a similar curing mechanism to that of linseed oil [78, 102, 103, 146, 158, 160–166]. However, sample preparation and the choice of harmonics can impact the mass and mechanical properties of polymer films determined with the QCM. In this work, these considerations are thoroughly discussed for linseed oil. The temperature dependent response of linseed oil is investigated and provides insights into network topology for a cured oil film.

3.2 QCM theory and sample regimes

3.2.1 Background

The QCM applies an oscillating voltage between two gold electrodes on either side of the quartz disk and induces the high frequency mechanical shear wave which can propagate into any film or liquid on the quartz surface . Before a sample is applied to the quartz crystal, the resonant frequencies of the odd numbered harmonics for the bare crystal are recorded. When a sample is applied, the resonant frequencies broaden and are shifted lower in frequency as the added sample

slightly dampens the response of the quartz crystal. Impedance spectra are measured for the resonant frequencies, consisting of conductance (G_p, mSiemens) and susceptance (B_p, mSiemens). The conductance peak is characterized by two parameters, the frequency value, f_n, and the dissipation, or the half width half maximum value of the peak, Γ_n [99]. Figure 3.1 shows the conductance and susceptance peaks of the 3rd and 5th harmonics for a linseed oil film. For these peaks, there are anharmonic sidebands starting to overlap with the harmonic peak. A multi-peak fitting routine is applied to accurately determine the value of Γ_n.

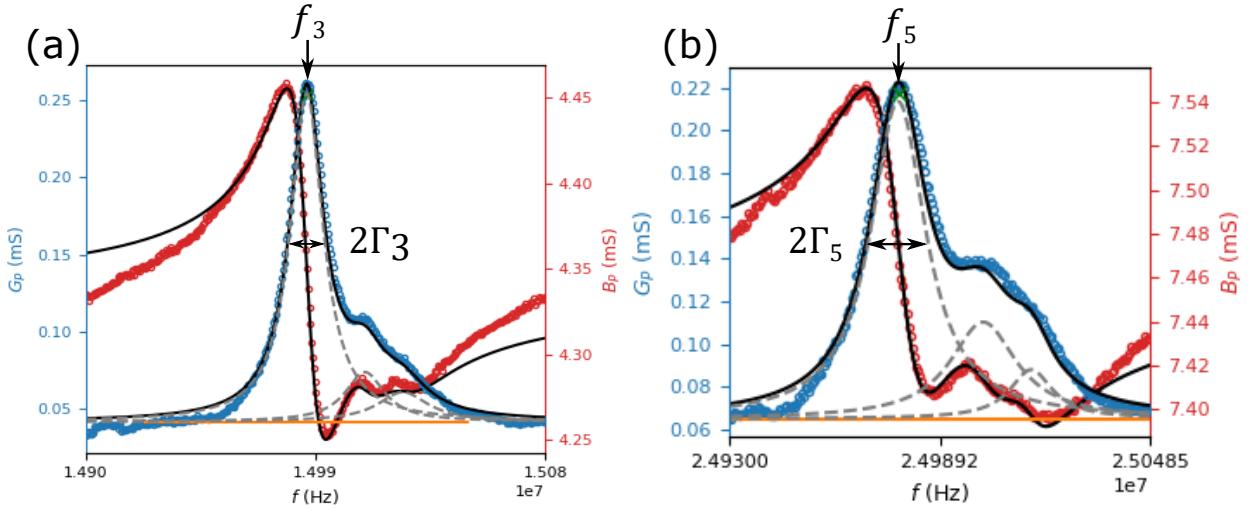

Figure 3.1: Conductance (G_p, blue) and susceptance (B_p, red) peaks from the (a) 3rd, 15 MHz and (b) 5th, 25 MHz harmonics from impedance data of a bulk linseed oil measurement using the QCM. The resonant frequency and two times the bandwidth are denoted by f_n and $2\Gamma_n$, respectively. These peaks are fit using a Lorentzian distribution and multiple peaks are used to account for the asymmetric nature of the frequency data. The grey dashed curves indicate the individual peaks that are summed together to generate the black solid line of the fit to the blue conductance data. The orange line at the bottom of both graphs indicates the data used to calculate the fit. Δf_n and $\Delta\Gamma_n$ are determined from the leftmost peak when multiple peaks are used to fit the conductance spectrum.

The shift in f_n and Γ_n can be determined between the measurements of the crystal with and without a polymer film applied and expressed as a complex frequency shift, Δf_n^*,

$$\Delta f_n^* = \Delta f_n + i\Delta\Gamma_n. \tag{3.1}$$

The complex frequency shift can also be expressed as a function of the complex load impedance of the polymer film, ΔZ_n^*,

$$\Delta f_n^* = \frac{i f_1 \Delta Z_n^*}{\pi Z_q}, \tag{3.2}$$

where $f_1 = 5\,\text{MHz}$ is the fundamental resonant frequency of the quartz crystal and $Z_q = 8.84x10^6\ \text{kg/m}^2\text{s}$ is the acoustic impedance of the quartz crystal [100]. How ΔZ_n^* is expressed for a QCM sample is very dependent on the sample geometry. An important assumption of these governing equations for determining the mass and mechanical properties of QCM samples is that the films are homogeneous both in composition and mechanical properties [158].

In this study, the two sample geometries shown in Figure 3.2 are used to understand how the mechanical properties of linseed oil evolve as the film cures and transitions from liquid-like to solid-like. Figure 3.2a shows a bulk sample geometry while Figure 3.2b shows a thin film sample. Previous work from the Shull group has discussed the relationships between the mechanical properties, thickness, and resulting data that can be obtained from polymer films; four regions can be defined: the Sauerbrey regime (where only mass is obtained), the bulk regime (only mechanical property information is obtained), the viscoelastic regime (where mass and mechanical property information are obtained), and the overdamped regime (where neither mass nor mechanical properties can be obtained) [101, 102].

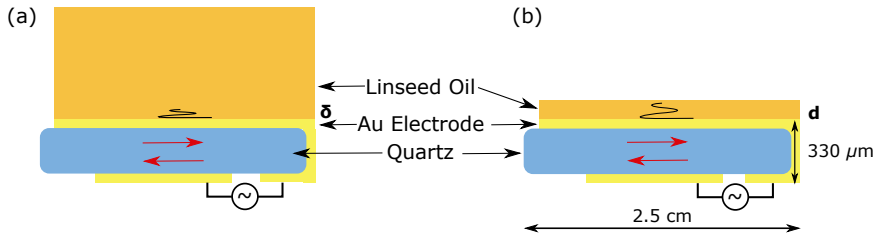

Figure 3.2: The (a) bulk and (b) viscoelastic thin film sample geometries used for experiments with the quartz crystal microbalance (QCM) in this study. The quartz crystal sample substrate consists of a quartz disk (thickness of 330 μm and a diameter of 2.5 cm) with two gold (Au) electrodes on either surface. When an oscillating voltage (represented by the squiggle inside of the circle) is passed between the two electrodes, a mechanical shear wave is induced in the quartz disk, indicated by the red arrows in the schematic. The mechanical shear wave propagates into the linseed oil sample at the resonant frequency for the quartz, which is 5 MHz for AT-cut quartz. δ refers to the decay length of the mechanical shear wave and d is the thickness of the polymer film.

3.2.2 Sauerbrey regime

In the Sauerbrey regime, the polymer film loaded onto the quartz disk is very thin, resulting in small dissipation values of the resonant frequency harmonics. This makes the complex load impedance of the polymer film purely inertial in nature [158]. The resonant frequency shift caused by the polymer film can be defined as the Sauerbrey frequency shift, Δf_{sn}, and is expressed as:

$$\Delta f_{sn} = \frac{2nf_1^2}{Z_q}\rho \mathrm{d}, \tag{3.3}$$

where n is the harmonic of interest, ρ is the density of the polymer, and d is the thickness of the film. The value of ρd is known as the areal density and is the mass per unit area of the film.

3.2.3 Bulk regime

For the bulk regime, the mechanical shear wave does not reach the end of the sample, but is only sensitive to the region closest to the surface of the crystal. The mass cannot be determined and the mechanical properties are obtained from the sample within several microns of the surface of the quartz disk. This region is defined as the decay length (δ) of the shear wave and is determined by the viscosity of the sample as described by the equation

$$\delta_n = \frac{(|\mathrm{G_n^*}|/\rho)^{1/2}}{2\pi f_n \sin(\phi_n/2)} = \frac{(2\pi f_n|\eta_n^*|/\rho)^{1/2}}{\sin(\phi_n/2)}, \tag{3.4}$$

where $|\mathrm{G_n^*}|$ is the magnitude of the complex shear modulus for a given harmonic of the resonant frequency n, ρ is the density of the polymer film, f_n is the resonant frequency at a given harmonic, ϕ_n is the viscoelastic phase angle, and $|\eta_n^*|$ is the magnitude of the complex viscosity. The magnitude of the complex viscosity is related to the complex shear modulus by the following relationship:

$$|\eta_n^*|\rho = \frac{-i|\mathrm{G_n^*}|\rho}{2\pi f_n}. \tag{3.5}$$

For samples in the bulk regime with a lower stiffness (i.e. more liquid-like), $|\eta_n^*|$ may be a more relevant property to report than $|G_n^*|$. In the bulk regime, the complex frequency shift from one

harmonic is needed to determine the mechanical properties. Δf_n^* for a sample in this regime, the frequency and dissipation shifts can be expressed as:

$$\Delta f_n = \frac{f_1}{\pi Z_q}(|G_n^*|\rho)^{1/2}\sin(\phi_n/2) \tag{3.6}$$

and

$$\Delta\Gamma_n = \frac{f_1}{\pi Z_q}(|G_n^*|\rho)^{1/2}\cos(\phi_n/2). \tag{3.7}$$

3.2.4 Viscoelastic regime

In the viscoelastic regime, the mechanical shear wave propagates through the entire linseed oil film and the thickness (d) can also be determined. From a single harmonic, there are only two data values collected, Δf_n and $\Delta\Gamma_n$. If three unknowns are to be calculated for a QCM sample in the viscoelastic regime ($|G_n^*|\rho$, ϕ_n, and dæ), a second harmonic must be used to provide a third data value [167]. When two harmonics are used, the notation for the QCM calculation to determine the mass and mechanical properties is $'x, y : x'$, where x and y are the values of the harmonic. The values before the colon are Δf_n of the harmonics while the value after the colon is $\Delta\Gamma_n$. In order to use the two harmonics, an assumption is made that ϕ is unchanged for the harmonics of interest, which comes from treating the magnitude of the complex shear modulus as having a power-law frequency dependence over a large frequency range [158]. For this constant phase angle approximation, the dependence of $|G_n^*|$ on the harmonic value, n, can be defined as

$$|G_n^*| \propto n^{\phi/90}. \tag{3.8}$$

When selecting which harmonics to use, it is important to consider the potential limitations that can be present. The fundamental harmonic, f_1, is very rarely used for determining the mechanical properties of a film due to the issues with poor energy trapping, or concentrating the mechanical shear wave over the electrode, that results from the geometry of the quartz crystal [100, 168]. There are two main factors that contribute to being able to calculate the mechanical properties from a

given pair of harmonics: a large enough separation of the frequency shifts for the two harmonics when they are normalized by the value of the harmonic, $\Delta f_n/n$, and $\Delta\Gamma_n$ being sufficiently large ($>\sim 100-300$ Hz). There is also an upper bound for the value of $\Delta\Gamma_n$. As $\Delta\Gamma_n$ approaches 15 kHz, it becomes difficult to accurately resolve the harmonic peak with a Lorentzian fit. The larger $\Delta\Gamma_n$ becomes, the harmonic peak amplitude decreases, to the point where the peak can no longer be distinguished from the background noise.

The acoustic impedance in the viscoelastic regime needs to be expressed using a generalized form of the complex load impedance [158]

$$\Delta Z_n^* = iZ_n^* \tan(\mathrm{k_n^* d}) \tag{3.9}$$

where $\mathrm{k_n^*}$is the complex wavenumber. $\mathrm{k_n^*}$ is related to the acoustic shear impedance (Z_n^*) by the following expression

$$\mathrm{k_n^*} = \frac{2\pi n f_1 \rho}{Z_n^*} = \frac{2\pi}{\lambda_n}\left[1 - i\tan(\phi_n/2)\right]. \tag{3.10}$$

The wavelength of the mechanical shear wave (λ_n) is expressed with respect to $|\mathrm{G_n^*}|\rho$ and ϕ by

$$\lambda_n = \frac{1}{f_n}\left(\frac{|\mathrm{G_n^*}|}{\rho}\right)^{1/2}\frac{1}{\cos(\phi_n/2)}. \tag{3.11}$$

For ease of notation, the term d/λ_n is defined as

$$\frac{\mathrm{d}}{\breve{}_{\mathrm{n}}} = \frac{\mathrm{d}\rho f_n \cos(\phi_n/2)}{(|G_n^*|\rho)^{1/2}}. \tag{3.12}$$

Using eq. 3.2 and 3.9-3.11, a generalized expression of Δf_n^* can be written as

$$\frac{\Delta f_n^*}{\Delta f_{sn}} = \frac{-\tan\{(2\pi\mathrm{d}/\lambda_n)(1-\mathrm{i}\tan(\phi_n/2))\}}{(2\pi d/\lambda_n)(1-\mathrm{i}\tan(\phi_n/2))}. \tag{3.13}$$

The real component of eq. 3.13 is Δf_n and the imaginary component is $\Delta\Gamma_n$ using the relationship defined in eq. 3.1. The data from a QCM experiment is numerically solved using the relationships

in eq. 3.12 and 3.13.

3.2.5 Error analysis and contour plots

Uncertainty in measurements using the QCM comes from two main sources: 1) the experimental errors that come from the polymer film not having uniform lateral composition and thickness as well as 2) from the uncertainty in the measured values of f_n and Γ_n [101, 158]. As the first one is very difficult to mathematically represent, we only consider the second source of error. Two approaches are used to define the uncertainty in the measurements of f_n and Γ_n in this work. The first is an assumption that the error is a certain percentage of f_n or Γ_n for a given harmonic, which works well for estimating the error in low viscosity systems or when only one harmonic is used for determining the mechanical properties. In this study, the assumed error is set to be 5% of f_n or Γ_n . The second is estimating the variation induced by inserting and removing a bare quartz crystal into the sample holder for measurement. For most harmonics, the estimated error from this variation is defined as $\Delta f_n^{err} = n * 15\,\text{Hz}$ and $\Delta\Gamma_n^{err} = 2\,\text{Hz}$. These error values are used when the mechanical properties are calculated from two harmonics. After determining the error values to be used for a calculation, the sensitivity of the calculated mass and mechanical properties to the measured quantities is assessed. The sensitivities can be expressed as a partial derivative of the calculated value to the measured value. As an example, the sensitivity of the calculated viscoelastic phase angle of the third harmonic, ϕ_3, to the measured value of $\Delta\Gamma_5$ for a '3.5:5' calculation would be written as $\partial(\phi_3)/\partial\Delta\Gamma_5$. The total error for a calculated property would be determined by the summing in quadrature of the contributions from each of the measured values. Therefore, the total error for ϕ_3 in a '3.5:5' calculation would be

$$(\phi_3)^{err} = \left(\left(\frac{\partial(\phi_3)}{\partial\Delta f_3} \Delta f_3^{err} \right)^2 + \left(\frac{\partial(\phi_3)}{\partial\Delta f_5} \Delta f_5^{err} \right)^2 + \left(\frac{\partial(\phi_3)}{\partial\Delta\Gamma_5} \Delta\Gamma_5^{err} \right)^2 \right)^{1/2}. \tag{3.14}$$

After the calculation of the mass and mechanical properties for a QCM sample, it is important to verify that the numerical solving of the QCM equations is providing reasonable and physically relevant values for the calculated properties. Since we are using only three of the four values from the two chosen harmonics to determine the calculated properties, we can uses this fourth

value to check the accuracy. From the calculated properties, the frequency and dissipation shifts that would be expected to determine those mechanical properties can be determined. Comparing these 'back-calculated' shifts to the experimental values of the frequency and dissipation shifts provides a sense of how accurately the calculated mechanical properties have been determined.

Another way to assess the accuracy and physicality of properties for a QCM sample is by using contour plots. These plots provide information about how sensitive the frequency and dissipation shifts for a given sample are to the calculated values of $|G_n^*|\rho$ and ϕ_n. Figure 3.3 shows the generalized contour plots for Δf_n and $\Delta\Gamma_n$ normalized by the Sauerbrey shift, Δf_{sn} (eq. 3.3) and is a visual representation of how eq. 3.13 is related to the mechanical properties for a polymer film. The y axis is ϕ_n and the x axis shows d/λ_n, which is proportional to $\sqrt{|G_n^*|}$. The color maps of the contour plot show how the variation in $\Delta f_n/\Delta f_{sn}$ and $\Delta\Gamma_n/\Delta f_{sn}$ can affect the uniqueness of the calculated solution for the mechanical properties.

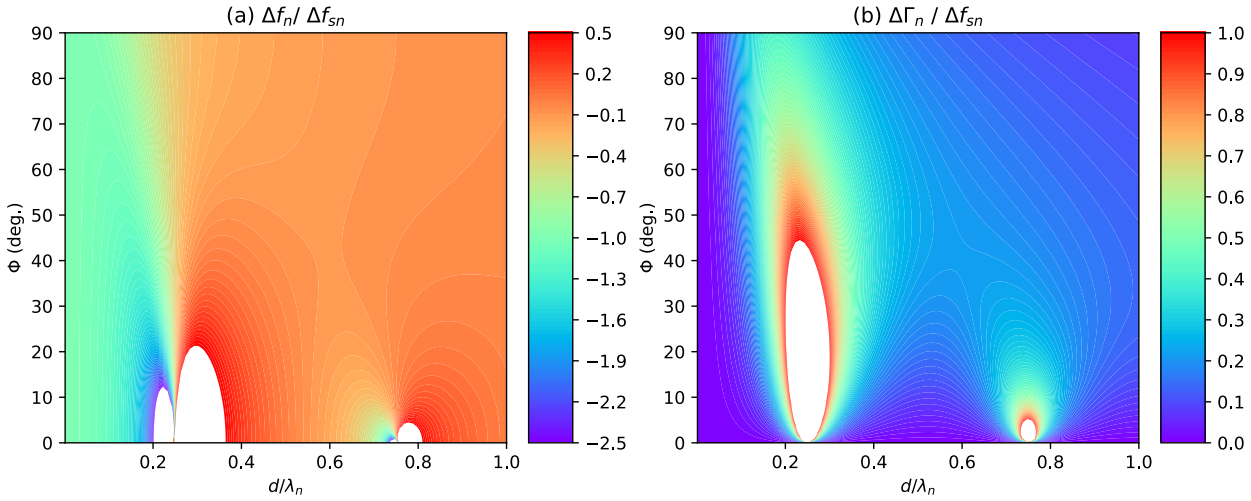

Figure 3.3: Contour plots showing a visualization of the relationships represented by eq. 3.13 of the generalized response of QCM samples and how the mechanical properties are related to the complex frequency shift, Δf_n^*. Plot (a) shows the changes in $\Delta f_n/\Delta f_{sn}$ (the real component of eq. 3.13) and plot (b) shows the changes in $\Delta\Gamma_n/f_{sn}$ (the imaginary component of eq. 3.13). The generalized response is determined by normalizing the components of Δf_n^* by the Sauerbrey shift, Δf_{sn}. The areas in white on the contour plots are regions of film resonance, where the QCM is insensitive to the mechanical property information for a polymer film.

There are some relationships that can be explained using Figure 3.3. Samples that have a more elastic response (i.e. high $|G_n^*|\rho$ and low ϕ) tend to have a lower value of $d/\lambda_n$and lower ϕ_n and will have data plotted in the lower left corners of Figure 3.3. Samples that are in the bulk

regime tend to have a very high ϕ_n as well as a larger value of d/λ_n, which would push the data values towards the upper right corner of the plots. The QCM is most sensitive to films with mechanical properties that have values in the ranges $0.05 < d/\lambda_n < 0.2$ and $0 < \phi_n < 60$, which corresponds to the leftmost lower two thirds of the plots. This region is typically where most samples in the viscoelastic regime tend to have their data propagate on the contour plots. The regions shown in white in Figure 3.3 are areas of film resonance. Film resonance for a QCM crystal is where reflection of the mechanical shear wave off the top surface of a viscoelastic thin film sample destructively interferes with the shear wave propagating from the quartz crystal, resulting in a region where it becomes very difficult to calculate the mechanical properties from the frequency and dissipation shifts. This phenomenon typically occurs around $d/\lambda_n \sim 0.25$ and $d\lambda_n \sim 0.75$ and is more fully discussed by Denolf *et al.* [158].

3.3 Materials and Methods

3.3.1 Materials

Three different types of linseed oil were used in this study: boiled linseed oil from Sigma Aldrich (SA) , cold-pressed linseed oil from Kremer Pigmente (KP), and refined linseed oil from Winsor & Newton (WN). Litharge (PbO) was purchased from Sigma Aldrich and mixed with the cold-pressed linseed oil in amounts of $x = 5$ and 20% by mass of PbO. To combine with the linseed oil from Kremer, PbO was placed into a mortar and ground with a few drops of oil. The rest of the oil was added to the PbO paste in a beaker and heated at 150 °C for 2 hours under magnetic stirring. The linseed oils from Sigma Aldrich and Winsor & Newton were used as is. As preparation layers for the substrate, either polystyrene (192k MW, Sigma Aldrich) or 1-propanethiol were used. Toluene, turpentine, mineral spirits, and tetrahydrofuran were used as solvents during the spin casting for the pretreatment and oil films. The oils were cast on quartz crystal electrodes (AT-cut, 2.54 cm diameter, 330 μm thickness) purchased from Renlux (Nanshan, China) and Advanced Wave Sensors (AWS, Valencia, Spain).

3.3.2 Sample preparations and measurements

3.3.2.1 Substrate pretreatment

Linseed oil does not wet surfaces well as a thin film, especially below a 1 mm thickness on quartz or gold, which are the components of the QCM crystals. To address this issue, two procedures were developed. The first procedure (used for SA, WN, and lead treated oil films) involved spin-coating a 15-20 nm layer of polystyrene onto the crystal. A 0.5% by mass solution of polystyrene in toluene was used to cast the film with the following spin coating conditions: 4500 rpm with a 1 s acceleration time for 60 s. The second procedure (found to be better for the KP oil films) involved immersing the crystal in a 1% by mass solution of 1-propanethiol in toluene for six hours to allow adhesion of the alkane-thiol to the crystal. After immersion, the crystal was rinsed with ethanol.

3.3.2.2 Crystal referencing and spin-coating of oil films

Once the prelayer (either alkane-thiol or polystyrene) was added to the crystal, the complex frequency shift of the crystals was measured. For the alkane-thiol, there was minimal change to the complex frequency while for the polystyrene film, there was a frequency shift without a bandwidth increase, meaning that a very thin layer of the polystyrene was deposited on the crystal. The mass of the film from the Sauerbrey equation was consistent with the film thickness as measured by ellipsometry. After the prelayer was added to the crystal, a reference measurement for the crystal was measured. If temperature sweeps were performed, the reference was measured from -40 to 100°C.

Two procedures were used for spin coating to achieve the desired thicknesses of oil films. For SA and WN oil films, the following spin conditions were used: 10000 rpm with a 1.25 s acceleration time for 5 s. A resting period of 60 s before starting the spin coating routine helped the oil coat the crystals more evenly. For the KP linseed oil films, all solutions were filtered (450 nm, PTFE) just before coating. The spin conditions ranged between $5000 - 8000$ rpm with a 2 s acceleration time for 90 s. As the treatment of oil with litharge induces an increase of the viscosity of the system, it was thinned using 25 wt% turpentine, which minimized precipitation of the oil solution

and was least likely to attack the pre-layer. The SA and WN oils were diluted to 20 wt% with tetrahydrofuran before spin coating.

3.3.2.3 Quartz crystal microbalance measurements

The quartz crystal microbalance consists of a N2PK Vector Network Analyzer and sample holders are from AWS. For the bulk measurements, a sample holder with a tube cap was used. Once the crystal was inserted, 0.5 mL of SA oil was added on top of the crystal and data was collected for three days. Oil thin films were cast and exposed to ambient lab conditions ($20-22$ °C, $20-25\%$ RH) with periodic measurements as the samples aged. Temperature sweeps were carried out on WN oil thin films from -40 to 80°C were performed at 5 months, 11 months, and 14 months. The temperature sweeps used a stage designed and built by AWS. The data collection and refitting of the impedance and conductance spectra was performed using in-house built Python programs [169]. Reflection Fourier Transform Infrared Spectroscopy (Refl-FTIR) was used to assess if the temperature sweeps had induced any chemical changes beyond those expected as a result of aging (see Appendix B for description of the methods and further discussion).

3.4 Results

3.4.1 Bulk data

A bulk sample of the SA linseed oil was measured to determine the initial viscosity, the change in mechanical properties over time, and the extent to which those changes could be observed using this experimental geometry. The magnitude of the complex shear modulus, the magnitude of the complex viscosity, and the viscoelastic phase angle over time are shown in Figure 3.4. The 3rd harmonic was used to determine the mechanical properties with the error bars estimated to be 5% of the frequency and dissipation values.

At the initial times for the sample in Figure 3.4, the complex shear modulus is 3.2 MPa $\cdot$ g/cm^3 and the complex viscosity is 34.5 mPa $\cdot$ s $\cdot$ g/cm^3. These values are similar to the viscosity determined from steady state flow rheological measurements ($\eta = 43.9$ mpa $\cdot$ s; $|G_n^*| = 4.1$ MPa at 25 °C).

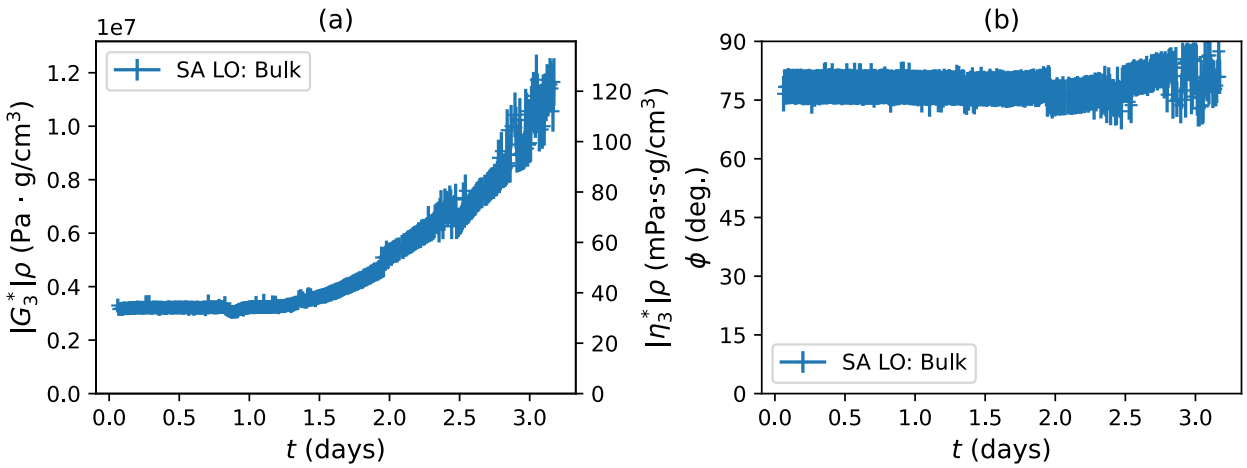

Figure 3.4: Measurements on bulk SA linseed oil sample: (a) magnitude of the complex shear modulus and complex viscosity over time and (b) the viscoelastic phase angle over time. Error bars assume approximately 5% error of the measurement of Δf_3 and $\Delta\Gamma_3$.

For measurements at other temperatures, see Appendix B. The $|G_3^*|\rho$, $|\eta_n^*|\rho$, and ϕ data remain constant for the first 1.5 days before showing an increase in the complex modulus and wider variation in the viscoelastic phase angle along with a slight increase. This initial period of constant data is mostly affected by the presence of antioxidants in the linseed oil, which will react with oxygen before the auto-oxidation process begins. Auto-oxidation induces crosslink formation in the oil and increases the complex shear modulus/viscosity as well as the decay length, defined in eq. 3.4. Once the complex shear modulus and viscosity have increased by a factor of 4, the dissipation of the third harmonic becomes too large and the sample response has moved into the overdamped regime from than the bulk regime [102]. Table 3.1 provides the decay length for water (a Newtonian liquid) and the SA LO bulk sample at early and later times of cure.

Table 3.1: The magnitude of the complex shear modulus, magnitude of the complex viscosity, and decay length values for water and SA LO bulk sample at early and late stages of drying. All values are reported for the 3rd harmonic ($f_3 = 15$ MHz.).

	$\|G_3^*\|\rho$ (Pa · g/cm^3)	$\|\eta_n^*\|\rho$ (mPa · s)	δ_3 (nm)
Water	$1x10^5$	1	150
Linseed oil, t = 1 hr	$4x10^6$	40	986
Linseed oil, t = 72 hr	$2.1x10^7$	210	2522

Since the bulk samples are only able to measure viscoelastic property changes over the first few days of cure in linseed oil samples, thin films in the viscoelastic regime will provide more infor-

mation about the curing process at longer times.

3.4.2 Thin film samples

3.4.2.1 Untreated linseed oil

Two linseed oils with different processing conditions, SA and WN, were measured in ambient lab conditions and the evolution of mechanical properties was followed. For the SA oil, two different analysis approaches were used to understand the data and are shown in Figure 3.5. For earlier times ($t < 55$ days), only one harmonic was used with a fixed value for $d\rho$. The value of $d\rho$ was then varied by a determined percentage (in this case, 3%) to assess the amount of variation in the mechanical properties and the sensitivity of the properties to the thickness of the film. Figure 3.6 shows the corresponding contour plots for the SA LO sample. The 5$^{\text{th}}$ harmonic could not be used to determine the mechanical properties at earlier times because the 5$^{\text{th}}$ harmonic $\Delta\Gamma/n$ values start out well above 10 kHz and then both the $\Delta\Gamma/n$ and the $\Delta f/n$ values end up in a region of film resonance (the areas of white in the contour plots shown in Figure 3.6) for most of the first 55 days. As mentioned in the Section 3.2, film resonance is a region of the mechanical property space that the QCM is insensitive and unable to accurately calculate the properties, so data which ends up in this region cannot be used.

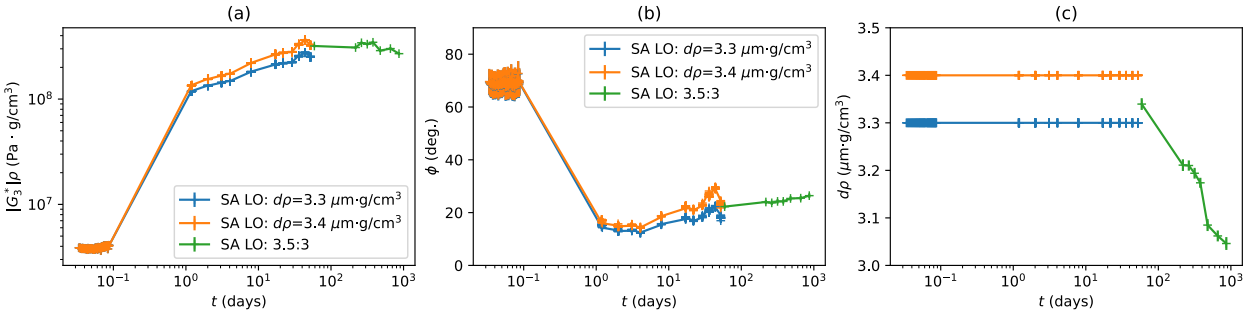

Figure 3.5: The evolution of mechanical properties over time of the SA LO sample. The (a) magnitude of the complex shear modulus, $|G_3^*|\rho$, (b) viscoelastic phase angle, ϕ, and (c) the areal density, $d\rho$. The first two calculations use only the 3$^{\text{rd}}$ harmonic and a fixed thickness listed in the legend. The calculation at later times is a '3.5:3' with the error bars determined from the uncertainties in the QCM reference measurements of a bare crystal.

By contrast, the complex frequency shift of the 3$^{\text{rd}}$ harmonic is stable and in regions of the contour plot where it can be used to determine the mechanical properties. The fixed film thickness was

varied by 3% to provide some understanding of the variation in mechanical properties while using the one viable harmonic for analysis. There is no difference in $|G_3^*|$æ or ϕ seen during the first day of measurement, indicating that the solution for these mechanical properties is unaffected by the thickness variation and therefore fairly stable. This analysis also indicates that this film at initial times is exhibiting mechanical properties that are liquid-like enough to be closer to the bulk regime than the viscoelastic regime. After the first day of aging, some differences in the calculated mechanical properties begin to be visible. There is a difference of $\sim$ 12% in the mechanical properties in when the thickness of the film is changed by 3%. After 55 days of aging, the 5th harmonic could be used because it had moved out of the film resonance region into a region with lower d/λ values as shown in Figure 3.6. The general trends in the mechanical properties are similar to those shown in Figure 3.8 where there is a rapid increase in $|G_3^*|\rho$ and decrease in ϕ at early times followed by a smaller changes and a decrease in $d\rho$ at longer times. The plots showing the back-calculated and experimental $\Delta f/n$ and $\Delta\Gamma/n$ data are provided in Figure B.6.

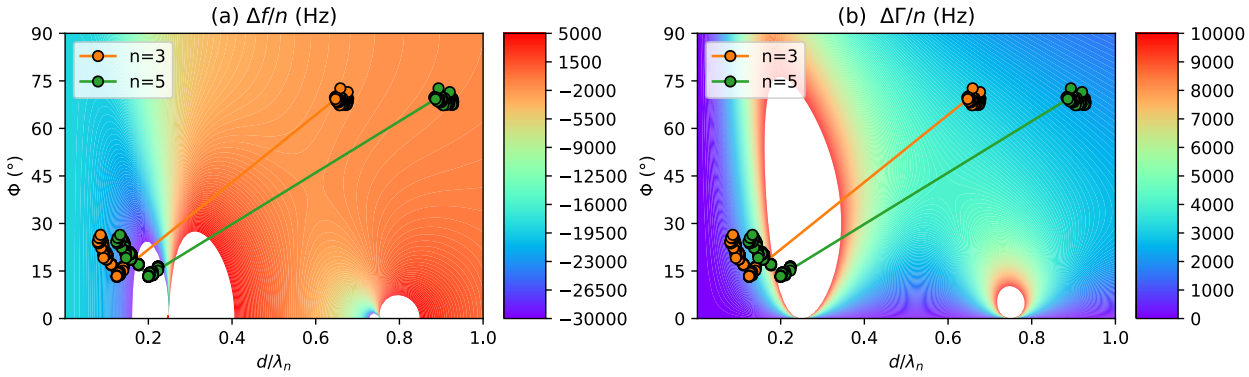

Figure 3.6: (a) Contour plot for the experimental $\Delta f/n$ values, and (b) contour plot for the experimental $\Delta\Gamma/n$ values of a data for the SA LO sample. The colors on the contour plots provide information about what frequency and dissipation shifts relate to the mechanical properties of the sample. For this LO sample, the early times are in the upper right corner with high d/λ (equivalent to a lower complex shear modulus) and high phase angle. As the sample polymerizes and ages as a solid film, the data shift to the lower left corner of the plot. The areas of white on the contour plots are where the film resonance phenomenon occurs, meaning that any data in this region cannot be used to calculate the mechanical properties.

As a comparison of the effect of processing conditions, two WN LO films were cast and measured over a similar period of time as the SA LO sample (Figure 3.7). While the value of the modulus is larger than that for the SA LO (also most likely due to the different processing conditions), there is still the steady growth in $|G_3^*|\rho$ while ϕ remains relatively constant and $d\rho$ gradually decreases

over time. The similar trends of the mechanical properties and thickness data for the KP, SA, and WN LO films indicate that the QCM samples are able to accurately capture the polymerization behavior of these films. Not all of the changes in these trends are monotonic, but it is unclear what is causing these jumps in the data. The check and contour plots for these samples are provided in Figures B.7 and B.8.

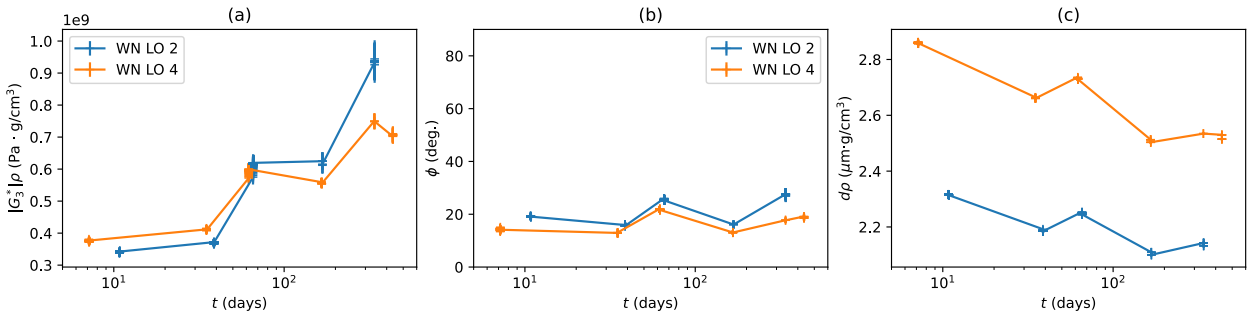

Figure 3.7: The evolution of mechanical properties over time for WN LO thin films. The (a) magnitude of the complex shear modulus, $|G_3^*|\rho$, (b) viscoelastic phase angle, ϕ, and (c) the areal density, $d\rho$. Error bars are calculated from the uncertainties in the QCM reference measurements of a bare crystal. .

3.4.2.2 Litharge treated linseed oil

The next comparison we investigated was the use of heating litharge with linseed oil, which has been a common technique used by painters throughout history to reduce the drying time of the oil paints and improve the properties for paint application to a surface [154, 170–172]. For these measurements, a cold-pressed linseed oil (KP LO) was chosen as one of the more common historical treatments. The mechanical properties of the KP films are summarized in Figure 3.8.

One important thing to note for these samples is the similarity of $|G_3^*|\rho \sim 300 - 900\,\text{MPa} \cdot \text{g/cm}^3$ at times greater than 100 hours for all the samples. This range of values for the KP LO and KP LO PbO samples are comparable to values of the modulus of oil paints measured using tensile testing as well as comparable to the modulus of a commercial alkyd binding medium [13, 44, 78]. The differences between the values of $|G_3^*|\rho$ of the KP LO and SA LO samples are most likely due to the litharge treatment of the KP LO samples, which induces the formation of lead soaps within the oil film. Another important note to make is that most of the time, we assume the density of polymer films t o be $\rho \sim 1\,\text{g/cm}^3$, allowing use to treat $|G_3^*|\rho \approx |G_3^*|$. Since there are samples

with a fairly large amount of litharge added to the KP 20% LO sample, Table 3.2 provides the density values using the same method to calculate the density as Sturdy *et al.* [29]. Using the calculated density, the range in the modulus data is actually $|G_3^*| \sim 250 - 800$ MPa, which is still comparable to previous work. There are not large differences between the KP LO samples with differing concentrations of PbO added, but it is possible that for the temperature and high frequencies of measurement, there QCM is not sensitive to the variations in mechanical properties. If there were temperature data for these samples, it is possible that the different concentrations of PbO would cause differences in mechanical properties, especially at lower temperatures.

Fairly large error bars are present for some of the later time points of $|G_3^*|\rho$ and for most of the data shown in Figure 3.8b. For the thickness regime of these LO samples, we are getting closer to the Sauerbrey regime limit, where the mechanical property information is more difficult to measure, especially at longer times. If the values of $\Delta\Gamma_n$ and the separation between the frequency shifts (seen as separation of the harmonic data when they are normalized to their harmonic, $\Delta f_n/n$) get too small, the error in the mechanical properties can become quite large. Another factor that can impact the error estimate is the stability of the film quality over longer experimental times. Even with the alkane-thiol or polystyrene pre-layer, these oil films can still dewet from the quartz months or even years after the film was cast. The resulting heterogeneity of film composition was not accounted for in the assumptions used to determine the viscoelastic properties, but it is also difficult to capture accurately through the error analysis. The thickness data reported in Figure 3.8c was also compared to the thickness measured using ellipsometry (see method in Appendix B) and reported in Table 3.2. For the KP LO samples with 0% or 5% PbO added, the QCM reports a thickness that is $\sim 5 - 15\%$ larger than the ellipsometry thickness. For the 20% KP LO sample, the QCM thickness is $\sim$ 15% smaller than the ellipsometry thickness. One factor that may be contributing to the discrepancies in the QCM and ellipsometry thicknesses is that the density value is calculated for the oil in the liquid state and does not account for any changes in density as the film polymerizes. The density would be expected to increase as the oil films polymerize, but we do not know how to approximate this increase accurately.

Two of the KP LO samples capture the evolution of the mechanical properties during the initial polymerization of the film, KP LO and KP 5% PbOa. During this initial polymerization step, a

Table 3.2: Comparison of the thickness as measured using ellipsometry compared to the areal density measured using the QCM. All thicknesses are reported in nanometers. The following densities are used for linseed oil and litharge: $\rho_{LO} = 0.93\,g/cm^3$, $\rho_{PbO} = 9.24\,g/cm^3$ and the values were calculated using the method described by Sturdy *et al. [29]*. The densities of the heat treated oils are determined using the reported density values and the wt% of litharge in the linseed oil films.

Sample name	Density ρ (g/cm^3)	QCM $d\rho$ ($nm \cdot g/cm^3$)	QCM d (nm)	Ellipsometry d (nm)
KP LO	0.93	740	795	746
KP 5% PbOa	0.97	766	789	-*
KP 5% PbOb	0.97	615	634	536
KP 5% PbOc	0.97	980	1010	880
KP 20% PbO	1.13	1850	1637	1800

rapid increase of $|G_3^*|\rho$, decrease in ϕ, and the initial increase followed by a decrease in $d\rho$ at longer times are visible. These rapid changes in the mechanical properties are due to oxygen uptake by the LO film, which fuels the auto-oxidative polymerization of the films. The main difference between these two films is the time at which this rapid polymerization occurred, being at about 25 hours and $3-5$ hours for the KP LO and KP 5% PbOa films, respectively. This difference in the rate of initial polymerization is a result of using litharge as a dryer and heat treatment for linseed oil. Since the KP 5% PbOa sample has the most data recorded for the earliest time window, there is the most information about the initial polymerization step where the film is transitioning from exhibiting more liquid-like to more solid-like mechanical properties. To fully capture this region of transition, two different calculations were used, '3,5:5' and '5,9:9'. The next two figures help illustrate the logic for choosing these two different calculations to understand sample KP 5% PbOa. The comparison of back-calculated to experimental values and contour plots are shown for the '3,5:5' calculation in Figure 3.9 and the same plots for the '5,9:9' solution are shown in Figure 3.10.

For the '3,5:5' calculation used at early times, there is good separation of the frequency shifts for the 3rd and 5th harmonics and the dissipation shifts are also fairly large (> 1000 Hz). As a point of comparison, the dissipation shifts for the 7th and 9th harmonics are getting close to the upper limit where the harmonic frequencies can be accurately fit, which is typically between 15 and 20 kHz. However, after the first four hours of data collection for this sample, the differences in $\Delta f_n/n$ and the values of $\Delta\Gamma$ between the 3rd and 5th harmonics become too small to accurately determine

the viscoelastic properties of the film. These changes can be seen in Figure 3.9a with the 3rd and 5th harmonic values for $\Delta f_n/n$ being < 100 Hz apart and Figure 3.9b, where the values for $\Delta\Gamma_3$ decrease to be < 100 Hz. When these values get too small, the resulting error of the solution grows significantly and other harmonics should be used to calculate the mechanical properties of this film later in the polymerization. For the data plotted in Figure 3.9c and 3.9d, the data for later times are closer to the lower left portion of the contour plots. This trend is due to the rapid increase in $|G_3^*|\rho$ (proportional to a decrease in the value of d/λ_n on the x-axis) and rapid decrease in ϕ. The color changes on the contour plot correspond to the regions where the variation of $\Delta f/n$ and $\Delta\Gamma/n$ are greatest, indicating where the equations for determining the mechanical properties of a sample would be most sensitive to those shifts in the frequency and dissipation data. The color variation under the data points in these contour plots provides information about the uniqueness of the mechanical property solutions for each QCM film.

The $\Delta\Gamma/n$ values and the differences in $\Delta f/n$ are also decreasing for the 7th and 9th harmonics, which means that they can potentially be used to determine the mechanical properties. After 4 hours, a '5.9:9' calculation becomes the most reliable calculation to use. There is enough separation of the $\Delta f/n$ values between the 5th and 9th harmonics and the $\Delta\Gamma_9$ values are around 9000 Hz, which makes it easier to determine the mechanical properties of this oil film. Figure 3.10b shows good agreement between the back-calculated and experimental values of $\Delta\Gamma_5$, an indicator that the QCM solution for the mechanical properties agrees well with our experimental values. In the contour plots shown in Figure 3.10c and 3.10d, the points at later times also trend towards the lower left of the plot, corresponding to the increasing $|G_3^*|\rho$ and decreasing ϕ shown in Figure 3.8a and 3.8b. These comparison and contour plots are very important to use in order to fully understand the accuracy and errors that we see in the mechanical properties of our films. The comparison and contour plots for the rest of the data shown in Figure 3.8 are provided in Figures B.2-B.5.

3.4.3 Temperature dependent response of oil films

To measure the temperature dependent response, linseed oil films that had remained compositionally stable (i.e. had not experienced any dewetting of the film during aging) were chosen. WN

LO 4 was stable enough to perform temperature sweeps from $-40-80$ °C. Data up to 60 °C are shown in Figure 3.11 because above 60 °C, the data became too difficult to fit and determine Δf_n^* because the films are too liquid-like. As the temperature decreases, $|G_3^*|\rho$ increases and ϕ remains relatively constant for the high frequency measurements. The error bars also increase at lower temperatures because the differences between the $\Delta f/n$ values of the 3rd and 5th harmonics almost overlap (see the check solutions in Appendix B). The near overlap of the $\Delta f/n$ values makes both of the harmonics more sensitive to the error estimate used and this effect is amplified in the temperature sweeps at later times. There is some variation and hysteresis in $d\rho$, which is most likely due to absorption and evaporation of water in and out of the film. As the temperature is decreased, the relative humidity above the sample will increase to be well above 90 %RH [173]. Since there are no diffusion limitations for these thin films, it can be assumed that the film would reach full saturation with water during the temperature decrease, which has been previously reported to be a $\sim$ 5% increase in the mass for linseed oil and ionomerized linseed oil films [85]. Since these films were exposed to 80°C for a short period of time, Refl-FTIR was performed to determine if there was any degradation due to the high temperature exposure. The spectra are shown in Figure B.12 and show the expected spectra for linseed oil films after 1-2 years of aging.

From the temperature sweeps, the glass transition temperature (T_g) region can be assessed. For comparison, the temperature data from Figure 3.11 are compared to a well-characterized epoxy system using the diglycidyl ether of bisphenol A (DGEBA) as the epoxide, polypropylene oxide based-Jeffamine D-2000 as a flexible amine crosslinker, and 4,4'-methylenebis(cyclohexylamine) (PACM) as a rigid amine crosslinker [174]. In the study, Masser *et al.* showed that the mixture of flexible and rigid amine crosslinkers leads to nano-scale heterogeneity within the polymer network. The heterogeneity broadens the number of relaxation times that contribute to the T_g of the epoxy system, which results in a less steep decrease of the $|G_3^*|\rho$ and a broadened peak region at higher temperatures in ϕ, shown in Figure 3.12. When these differences are compared to the PACM 0 sample, it is easier to see how the broadening of the temperature range affects the temperature dependent response of the epoxy system. The response of the WN LO system as a function of temperature is similar to that of the PACM 0.8 epoxy. The ϕ of the WN LO samples is higher than that of the epoxy, but this difference is due to the QCM measuring at high frequencies

(15 MHz) compared to DMA measurements ($0.1 - 100$ Hz).

Given the complexity of the reaction mechanisms during polymer formation in linseed oil, it is difficult to provide an exact description of the lengthscale or causes of heterogeneity in the polymerized oil. While previous research has used differential scanning calorimetry and dynamic mechanical analysis to report the T_g of oils and paint films, the presence of pigments or processing conditions of the polymer network formation may contribute to a smaller range of relaxation times contributing to the T_g [85, 157, 175]. One potential explanation for nano-scale heterogeneity present in the WN LO 4 sample is described by Kryven *et al.*, where they used random graph modeling to understand the reactivity factors that can affect bond formation within and between oil monomer molecules [176]. When it was assumed that increased monomer connectivity led to an increased probability of intramolecular bond formation rather than intermolecular crosslinks, polymer clusters of high connectivity were initially formed that would eventually connect to other clusters, forming a heterogeneous connectivity network. Figure 3.13 provides a 2D spatial representation of what a polymer network with nanoscale heterogeneity may look like based on this hypothesis of polymer cluster formation at long cure times.

The crosslink density will have a noticeable effect on the relaxation times of the polymer network and the degree of variation in crosslink density is believed to contribute to the broadening of the decrease in $|G_3^*|\rho$ and flattening of the peak typically seen in ϕ values shown in Figure 3.12.

3.5 Conclusions

The QCM is effective for tracking polymer network formation, especially for polymer systems that undergo a sol-gel transition such as linseed oil. Following the evolution of mechanical properties during polymerization shows confirms that these properties can continue to change over years as the oil films undergo longer term chemical reactions. A more thorough discussion of how resonant frequency harmonics are determined for calculating the mass and mechanical properties of QCM samples is provided. The comparison and contour plots for samples are used to explain the process for error analysis and understanding the accuracy of the QCM calculations. The importance of sample quality and its effect on the calculated error for polymer films is also discussed.

The effect of using litharge to treat linseed oil samples reduced the onset of polymerization by $\sim 5x$, but at longer times the mechanical properties seem to reach similar values regardless of the heat treatment. The longer term trends of the curing of linseed oil samples with different processing conditions are compared and shown to have similar trends. When a temperature sweep was performed on one of the viscoelastic LO samples, it was found that there was not a clearly defined value for T_g. However, upon comparison to another well characterized crosslinked polymer network, it was proposed that there could be nano-scale heterogeneity in the polymer network due to variations in crosslink density, which contribute to a broadening of the relaxation times for the polymer network. As shown by the hysteresis in the mass during temperature sweeps, the QCM is very sensitive to these mass changes and can be used to further investigate moisture sorption and solvent interactions of linseed oil films.

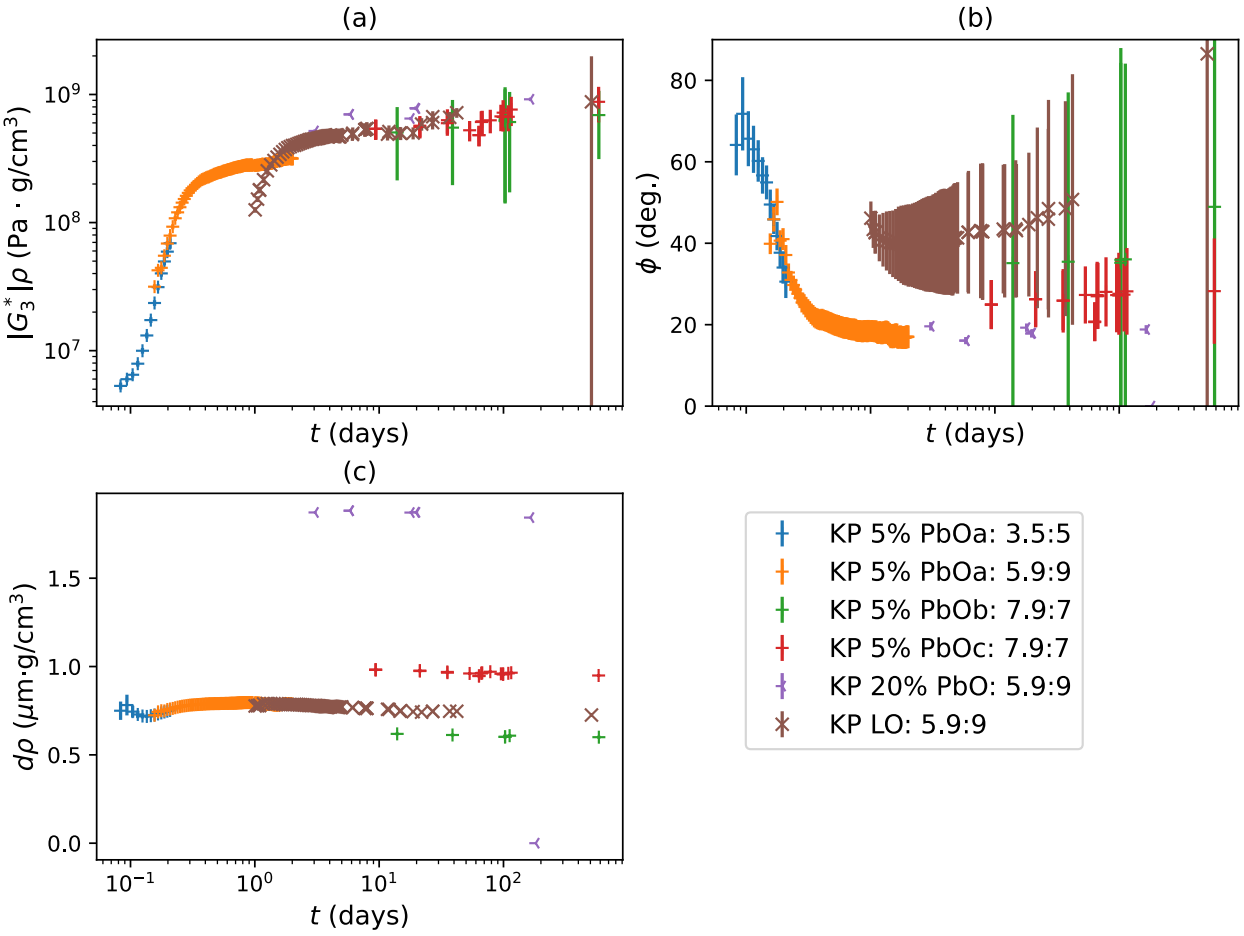

Figure 3.8: The evolution of mechanical properties for the KP LO films with various wt% of PbO used to treat the oils before casting films. The (a) magnitude of the complex shear modulus, $|G_n^*|\rho$, (b) viscoelastic phase angle, ϕ_n, and (c) areal density, dρ. The harmonics used to determine the mechanical properties are provided in 'x,y:z' format, where x and y are the harmonics used for frequency shifts while z is the harmonic used for dissipation shift. The error bars are based on uncertainties resulting from the variation seen in reference data for bare QCM crystals and is more fully described in Section 3.2.5.

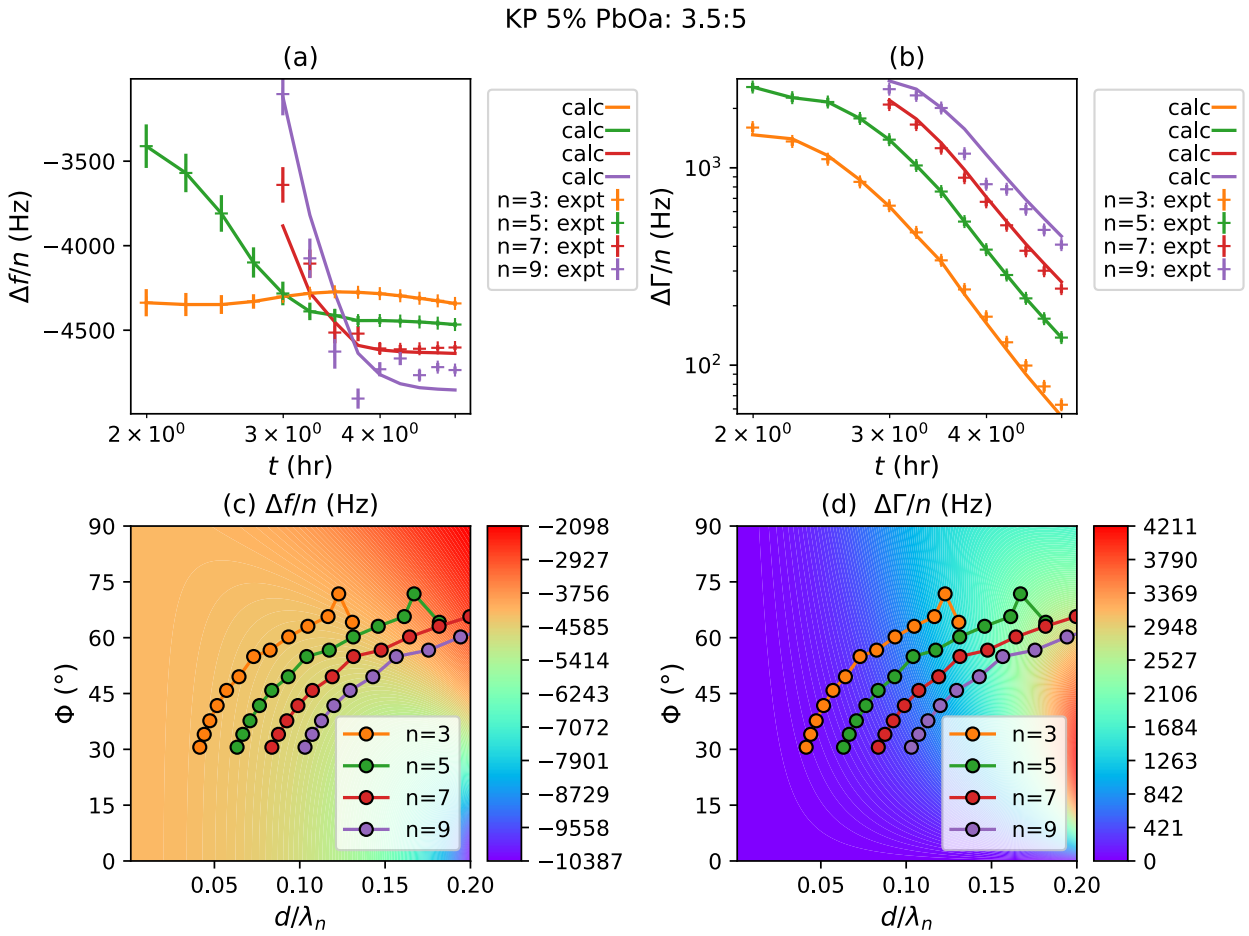

Figure 3.9: '3.5:5' calculation for the KP 5% PbOa sample: a comparison of the (a) experimental values of $\Delta f/n$ to the back-calculated solutions, (b) experimental values of $\Delta\Gamma/n$ to the back-calculated solutions, (c) contour plot for the experimental $\Delta f/n$ values, and (d) contour plot for the experimental $\Delta\Gamma/n$ values. Good agreement of the solution for the mechanical properties is determined by comparing the back-calculated value from the solution not used in the calculation (in this case, the $\Delta\Gamma_3$) with the experimental data.

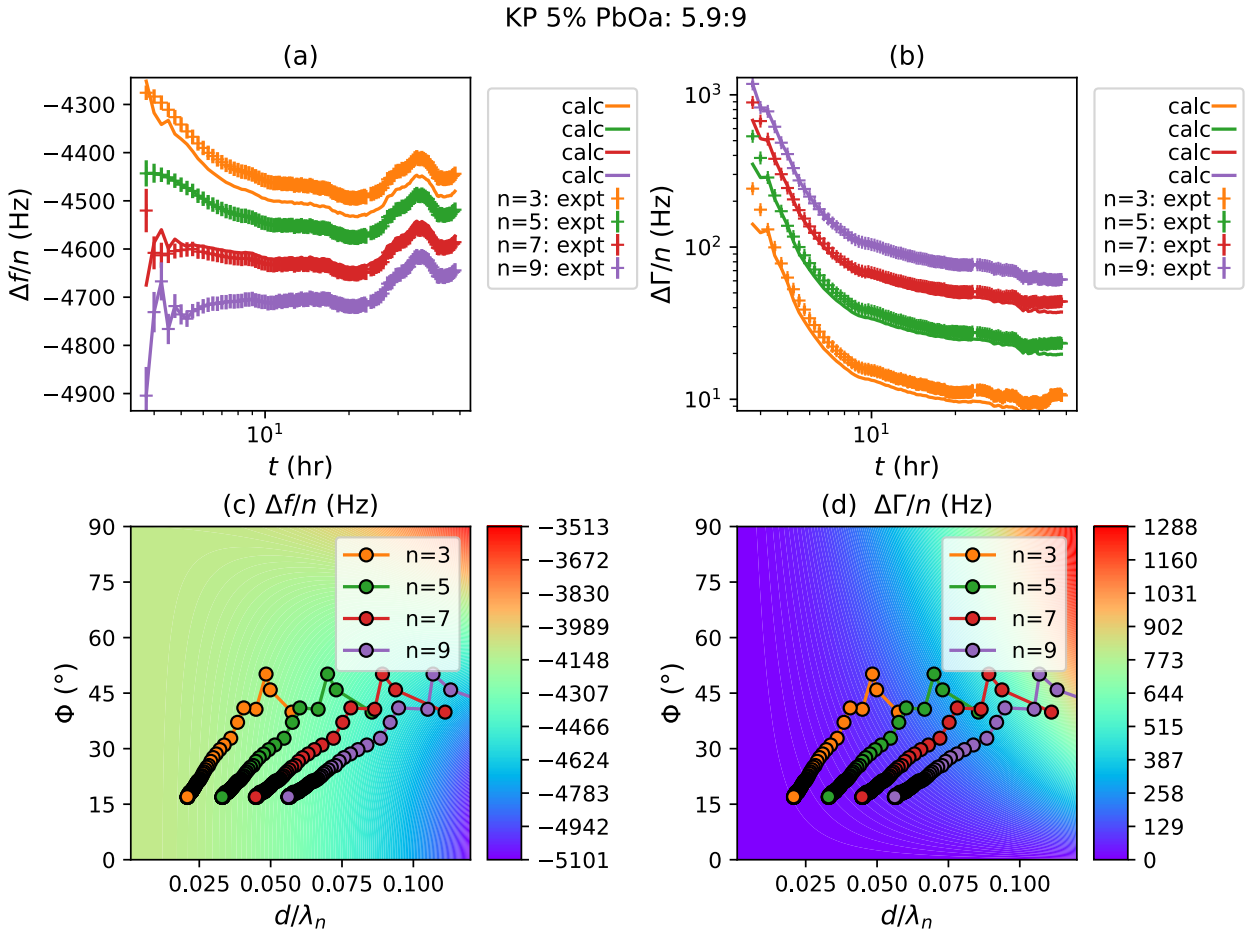

Figure 3.10: '5.9:9' calculation for the KP 5% PbOa sample: a comparison of the (a) experimental values of $\Delta f/n$ to the back-calculated solutions, (b) experimental values of $\Delta\Gamma/n$ to the back-calculated solutions, (c) contour plot for the experimental $\Delta f/n$ values, and (d) contour plot for the experimental $\Delta\Gamma/n$ values. Good agreement of the solution for the mechanical properties is determined by comparing the back-calculated value from the solution not used in the calculation (in this case, the $\Delta\Gamma_5$) with the experimental data.

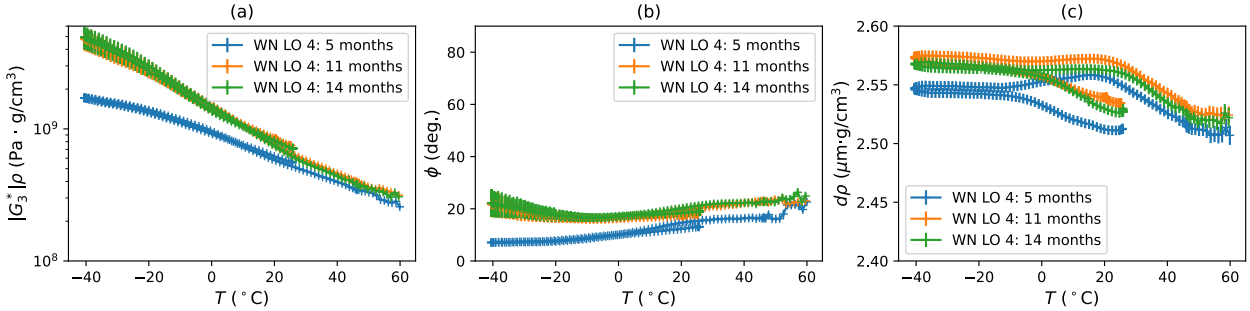

Figure 3.11: The temperature dependent mechanical properties for WN LO 4. The (a) magnitude of the complex shear modulus, $|G_3^*|\rho$, (b) viscoelastic phase angle, ϕ, and (c) the areal density, $d\rho$, are measured from $-40-60$°C. The error bars are determined from the differences between the back-calculated and experimental values of the check-solutions.

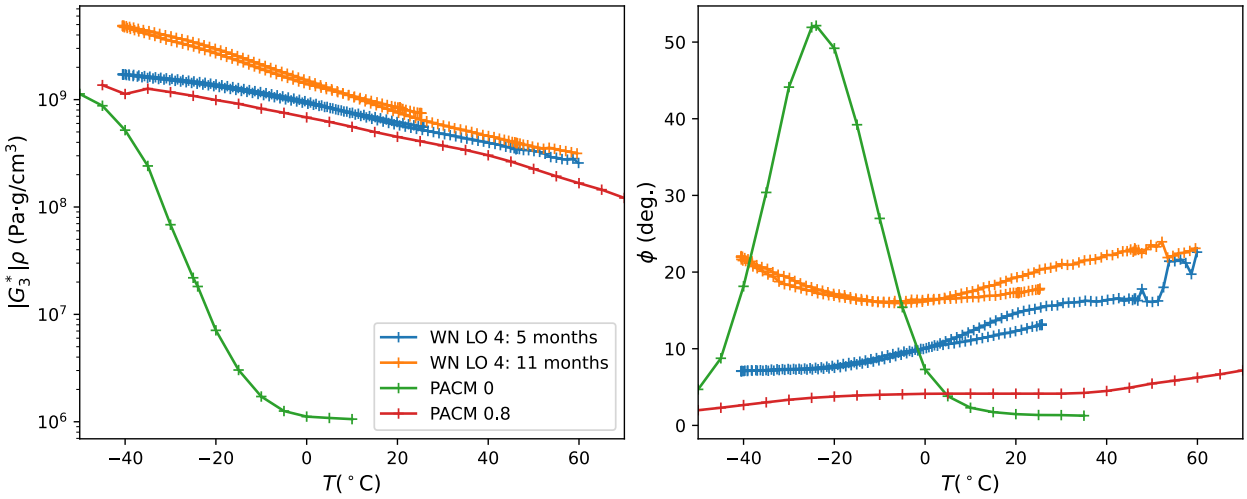

Figure 3.12: The (a) magnitude of the complex shear modulus ($|G_3^*|\rho$) and (b) viscoelastic phase angle (ϕ) as a function of temperature for the WN LO temperature sweeps and for the DGEBA/Jeffamine/PACM systems. The ratio between the DGEBA and Jeffamine/PACM systems are stoichiometric for an epoxy system. 'PACM 0' refers to the amine fraction being completely Jeffamine while the 'PACM 0.8' has 80% PACM and 20% Jeffamine for the amine fraction. The reported ff T_g value for PACM 0 = −24°C and for PACM 0.8 = −28°C. Data reproduced with permission from [174]

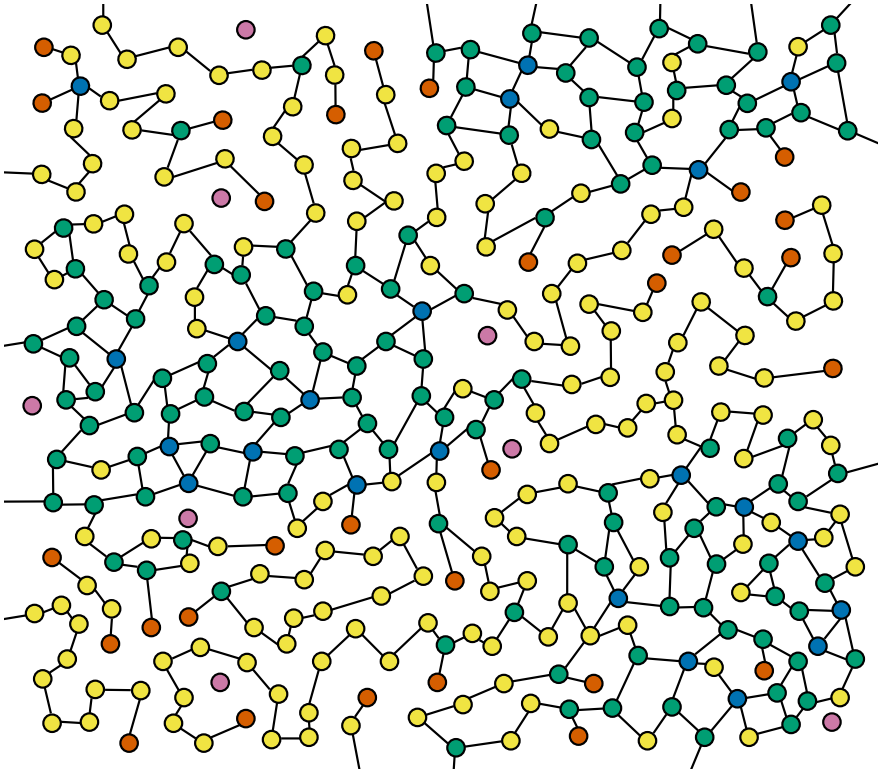

Figure 3.13: Schematic describing an example of a crosslinked polymer network with nanoscale heterogeneity. The colors are used to show molecules with different numbers of crosslinks between them. Pink molecules have zero, orange have one, yellow have two, green have three, and blue have four crosslinks. Regions where green molecules are dominant have high crosslink density while regions where yellow and orange molecules are dominant have low crosslink density. The crosslink density in the polymer network will affect the breadth of relaxation times of the polymer chains, which is the main contribution to the T_g. This figure is based on the concluding figures in [176].

Chapter 4

Chemical characterization of drying oils during early-stage curing using time-based attenuated total reflection infrared spectroscopy

4.1 Introduction

The curing process of oil paints is known to comprise of a large number of reaction pathways as well as being greatly affected by the environmental conditions and the components of the paint mixtures [5, 7, 10, 177]. On top of the many potential reaction pathways, the drying oil undergoes a physical transition, changing from a liquid comprised of triglyceride oil molecules to a solid, cross-linked polymer system. In this study, we are focused on understanding what effect variations in the initial fatty acid distribution of the drying oil and the presence of drier mixed with the oil have on the chemical composition of the polymer network.

One of the most common drying oils used for oil paints, linseed oil, has been the focus of previous research on the effect of drying conditions, type of pigment used, and the presence of driers on polymer formation [151, 178–182]. Many analytical techniques have been used to follow the chemical changes that occur in linseed oil during its curing phase, including Fourier transform infrared (FTIR) spectroscopy, nuclear magnetic resonance (NMR), dynamic scanning calorimetry (DSC), size exclusion chromatography (SEC), and gas chromatography paired with mass spectrometry (GC/MS) [149, 151, 153, 154, 156, 178–190]. Linseed oil has also been a focus of food science as researchers have worked to understand the oxidative instability of linseed oil, which impacts its usefulness as a health supplement [187, 191, 192]. Other recent work has investigated utilizing linseed oil as a component of self-healing coatings for steels [193]. Many of the FTIR studies have focused on how functional group IR vibrational bands shift and peak areas change as a result of the curing process; most peak assignments made in this work were confirmed via these papers [151, 154, 178–180, 183, 185, 186, 188, 189]. Similarly, NMR has been utilized to understand how the initial chemical compositions of conjugated and non-conjugated fatty acids on the

oil monomers and explain differences in how a polymer network was formed [189]. More recently, solid state NMR has been used to look at the relaxation times within the formed polymer network and assess the extent of crosslinking [194]. DSC has been used to look at the effect of antioxidants on the onset of the initial polymerization reaction in drying oils as well as to determine the time during polymerization when there are high concentrations of radicals and peroxides within the oil network [187, 190]. However, DSC is not chemically specific and a second technique is needed to verify the nature of the thermal transition observed. SEC and GC/MS are typically used on the solvent extractable components of the oil network, typically the low molecular weight byproducts from the curing reactions [148, 151, 153, 184]. Fragments of the polymer network can be investigated using pyrolysis GC/MS (py-GC/MS) [150, 156, 190, 194]. The challenges of using GC/MS or py-GC/MS to understand a polymer network are that the solvent extractable components provide incomplete information about the polymer network. The volatized fragments are difficult to relate back to the original polymer network, which makes understanding the polymer network very difficult and non-quantitative [150].

Due to its popularity and prominence in oil paints, most of previous studies have focused only on linseed oil, with some cursory mentions of results about the properties of other drying oils [178]. Drying oils are comprised of triglyceride molecules with a distribution of fatty acid chains attached to the glycerol backbone, which can be saturated or unsaturated. Since other drying oils with lower percentages of linolenic fatty acids are known to experience less yellowing than linseed oil samples, modern paint formulations may mix these drying oils with or completely replace linseed oil to reduce the amount of yellowing that may occur as a paint film ages. While there has been some claims in literature that the different fatty acid distributions of drying oils do not impact the polymer network formed by these oils at longer times [178], we have reason to believe that there can be an impact on the extent and distributions of crosslinks formed within the oil network. We use time-based attenuated total reflection FTIR (ATR-FTIR) spectroscopy to measure the initial chemical changes within drying oils at a higher time resolution and employ more rigorous analysis to the observed vibrational band changes during the cure of various drying oils. The effects of temperature and incorporation of a lead drier are also measured to understand how these external factors affect the kinetics of network formation in the drying oils.

Recently, there have been comparisons made for pigmented samples using both linseed and safflower oils to understand the effects of both the type of drying oil and pigment on the resulting polymer network [150, 190, 195]. One of the major conclusions from these studies was that there is an inverse relationship between the level of crosslinking in a pigment/oil network and the level of oxidative degradation present in the film. Through the work presented here, we believe that the relationship between extent of crosslink formation and level of oxidative degradation within an oil film is more nuanced. Another recent study investigated the the likelihood of lead formate formation during early stages of cure by adding minium to various drying oils [196]. Along with detecting lead formate signals for all of the drying oils over time, the levels of amorphous lead soap formation observed via x-ray diffraction by Švarcová *et al.* varied greatly depending on the type of drying oil. This variation in the amount of lead soaps formed in the drying oil network implies that the kinetics of these reactions can be directly affected by the distribution of fatty acids participating in oil polymerization. This variation in one aspect of the resulting polymer network is one of the main motivations for further investigating the effects of fatty acid distribution on drying oil network formation.

4.1.1 Oil Polymerization Background

The chemical reactions that govern the curing of drying oils can become very complicated and difficult to fully understand even through the use of computational methods [10]. The curing of drying oils undergoes a type of free-radical polymerization (FRP) known as autoxidation, where oxygen catalyzes the creation of radicals to propagate polymer network formation [5]. A partial reaction scheme describing some of the relevant chemical reactions for this chapter is shown in Figure 4.1. At the beginning of the polymerization reaction, a radical will abstract a bis-allylic hydrogen between non-conjugated cis C = C bonds in the fatty acid chains (Figure 4.1 shows this abstraction occurring on a linoleic fatty acid). The resulting carbon radical reacts with oxygen to form a peroxide radical ($OO^{\cdot}$). The peroxide radicals can then undergo several reactions, including forming hydroperoxide via hydrogen abstraction, radical recombination reactions, or beta scission reactions to form another carbon radical and an aldehyde. The hydroperoxide formed can be decomposed to form an alkoxy radical ($O^{\cdot}$). The rate of hydroperoxide decomposition can be

accelerated by either elevated temperature or the incorporation of a metal-based drier to form carbon radicals, which typically decrease the time until the onset of the first phase of oil reactivity commonly found in drying oil cure (referred to as onset delay in this chapter) [154, 177]. The carbon radicals react through either radical recombination or radical addition to form oligomers that with enough time combine to form a polymer network. Since many of these carbon radicals a situated near the unsaturations found in the fatty acid chains, these C = C bonds undergo conjugation and isomerization reactions, which are followed more in depth during the course of this chapter. Two types of conjugated C = C bonds are highlighted in this schematic, a conjugated trans-trans C = C bond (observed in FTIR at 986 cm^{-1}) and a conjugated trans-cis C = C bond (observed at 950 cm^{-1}). All recombination and addition reactions are possible with both conjugated C = C bonds; for clarity of the reaction scheme they are not all shown. Three types of crosslinks can be formed in the drying oil network: peroxy (C – O – O – C), ether (C – O – C), or alkyl (C – C, which are not shown in Figure 4.1) crosslinks [177].

For this chapter, we will refer to the period of time when the chemical reactions shown in Figure 4.1 occur most rapidly as the first phase of oil reactivity. Since FRP forms random polymer networks, the kinetics of the polymerization reactions can affect the resulting network topology [197]. Previous research has discussed a hypothesis of clusters of crosslinked oligomers of oil molecules forming, which then react together over longer times to percolate and form the polymer network [176, 198–200]. This cluster model is likely to result in nano-scale heterogeneity due to the variations in crosslink density within the polymer network; this hypothesis is also discussed in Chapter 3. If the initial polymerization step occurs rapidly for a FRP, it is likely that the polymer network will form according to this cluster-based model; if the initial polymerization step occurs slowly, then the resulting crosslink density should be more homogeneous throughout the polymer network.

During this first phase of oil reactivity, the polymer network is very active and can undergo many chemical reactions and conversions alongside the C = C bond reactions. For example, primary and secondary alcohols formed during the C = C reactions can be oxidized to form aldehydes, ketones, acids, and eventually secondary oxidation products [154]. We show the formation of a gamma lactone as a secondary oxidation product in Figure 4.1 as a ring closing reaction of an

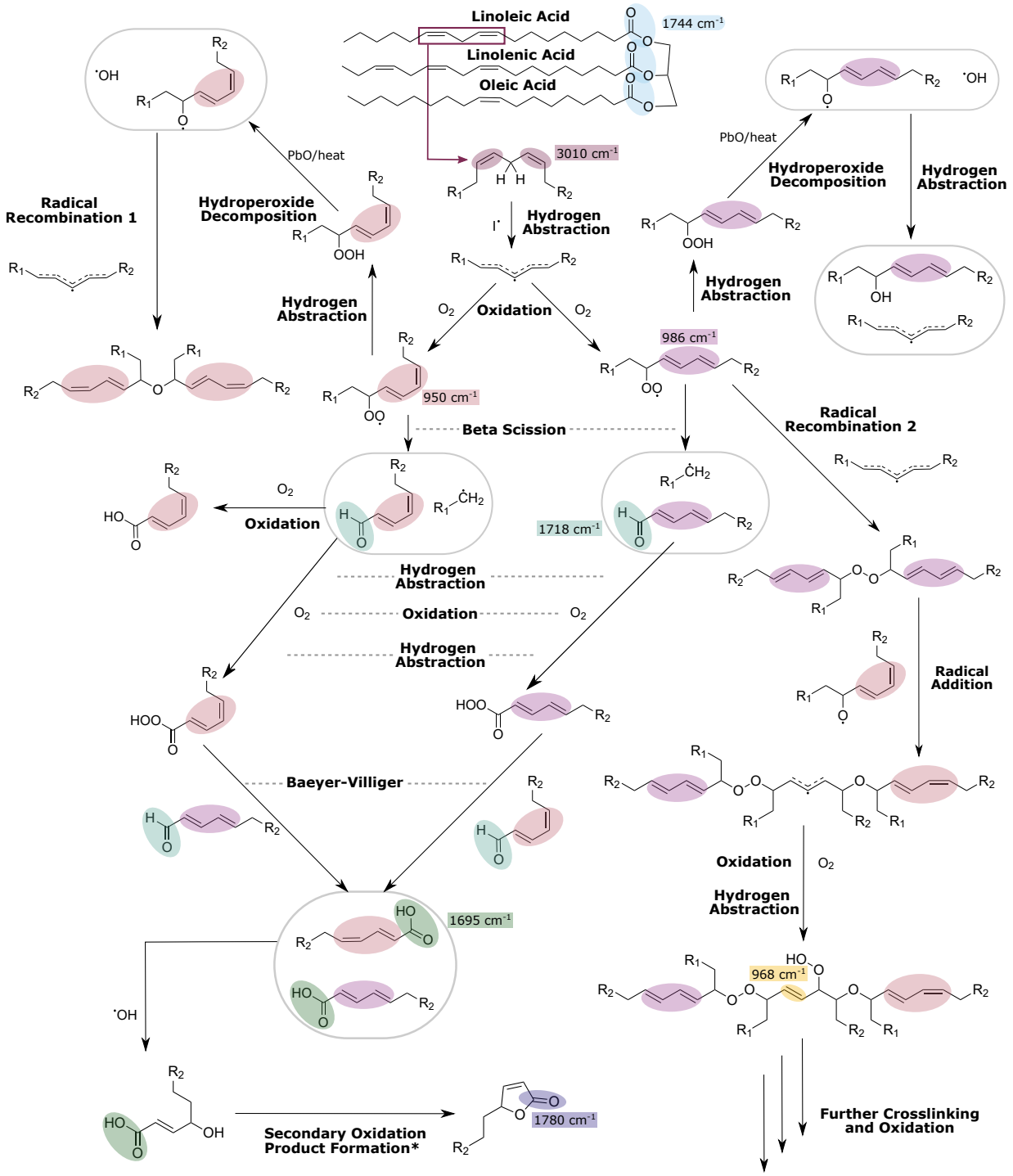

Figure 4.1: A partial scheme describing the auto-oxidation process that occurs within drying oils. The reaction begins with a radical species abstracting a bis-allylic hydrogen from a linoleic acid of the representative triglyceride oil molecule. The chemical reactions following this initial hydrogen abstraction were selected to highlight the FTIR vibrational bands analyzed within this chapter. The colored circles and the highlighted wavenumber values provide information about the important reactions for crosslink formation as well as further oxidation within the film. Chemical structures within light gray boxes are both products of the chemical reaction. The gray dashed lines are guides for the eye when the same reaction label applies to two reactions in the scheme. *While the formation of a secondary oxidation product is shown here as a gamma lactone formed by the ring closing of an alcohol-substituted carboxylic acid, there are other potential reaction pathways or oxidation products that can occur in this region.

alcohol-substituted carboxylic acid, but gamma lactones can also be formed via a second order reaction of a primary alcohol with an unsaturated carboxylic acid. The unsaturation present in the gamma lactone can shift the carbonyl band vibration to be between 1773 and 1780 cm^{-1} [201]. Several other potential secondary oxidation products can be formed that have a carbonyl vibrational band occur around 1780 cm^{-1} [151, 180, 202]; the gamma lactone is the easiest to include in Figure 4.1 because it can be formed from an unsaturated carboxylic acid and the ring closing to form the gamma lactone would be thermodynamically favorable. As more oxidation reactions occur in the polymer network, the network is believed to become more susceptible to solvent exposure or fluctuations in the surrounding environment [194, 203]. The increased susceptibility of a drying oil film to the surrounding environment can be referred to as oxidative degradation because the network can be broken down through reactions such as hydrolysis or chain scission [182].

Understanding these aspects of the drying oil polymerization, it becomes easier to see how variations in the fatty acid distribution, and therefore initial concentrations of bis-allylic hydrogens present in the drying oil, could affect the resulting amount of heterogeneity found in a polymer network topology. The inclusion of driers would also increase the likelihood of network heterogeneity by accelerating hydroperoxide decomposition and decreasing the overall time the oil is in the first phase of oil reactivity. Time-based attenuated total reflection FTIR (ATR-FTIR) spectroscopy is used to follow the FRP reactions for five drying oils (linseed, safflower, walnut, poppyseed, and stand). Stand oil is a version of linseed oil that is prepolymerized by subjecting the oil to high temperatures ($\sim$ 300 °C) in an anoxic environment. Some researchers claim that the prepolymerization reactions at high temperatures forms crosslinks through either a Diels-Alder reaction between the double bonds found in the fatty acid chains or through C = C bonds reacting with a methylene radical [204]. By using a higher time resolution than most previous research, the relationship between polymerization kinetics and the effects on polymer network formation is observed and discussed. The addition of a drier is measured to investigate whether driers affect the balance of reaction pathways or the extent of polymerization. Temperature effects are also measured to observe the relationship between the rate of polymerization and temperature as well as confirm that the elevated temperatures are not significantly changing the primary polymerization reaction pathways. Several approaches are used to analyze the ATR-FTIR data, including

difference spectra, tracking peak changes as a function of time, and using a linear combination of Gaussian functions to determine the contributions of individual peaks in regions with significant overlap between the peaks. The resulting differences between the drying oils provide insights into how the initial fatty acid composition can affect which reaction pathways are favored during the initial polymerization. Comparisons to longer times are made through oil films that have been cured for 1 year to determine if the differences observed during the initial polymerization persist to longer times.

4.2 Materials and Methods

4.2.1 Materials

Five drying oils were used for this time-based ATR-FTIR study: linseed oil (cold-press, Kremer Pigmente), walnut oil (cold-pressed extra pale, Chelsea Classical studio), stand oil (bottle read van der linde kunstschilders-teken-en grafisch materiaal, from the reference collection of the Rijksdienst voor het Cultureel Erfgoed), safflower oil (verfmolen "De Kat"), and poppyseed oil (purified, Talens). Lead (II) oxide (PbO, litharge) was purchased from Alfa Aesar.

4.2.2 Methods

The fatty acid composition of the drying oils was calculated using ^{1}H and ^{13}C NMR spectra. Acid values were determined using a titration protocol adapted from AOCS Official Method Ca 5a-40. Further details of these methods are described in section C. ATR-FTIR measurements were performed using a Perkin Elmer Frontier spectrometer equipped with a heatable diamond GladiATR module (Pike Technologies). Spectra were collected from $4000 - 400\,\mathrm{cm}^{-1}$ using a single scan and $4\,\mathrm{cm}^{-1}$ resolution for each time point. For the pure oil samples, the ATR top plate was heated to 70 °C, then a background measurement was performed. When the temperature was varied, the ATR top plate was brought to the temperature of interest, then a background was performed at that temperature before application of the sample. A drop of the oil sample was then applied on the diamond crystal to create a thin film and ensure full coverage. Spectra were measured every

1-5 minutes for $20 - 70$ hrs, or until the disappearance of the peak at $3010\,\mathrm{cm}^{-1}$, which can be viewed as the end of the initial curing phase, as well as a stabilization of other features within the spectra. For samples where litharge was added, 5% by weight of litharge was added to the oil, then ground in a mortar and pestle for 5 minutes until the litharge/oil mixture was smooth. The mixture was then applied to the diamond crystal and measured. If the peak at $3010\,\mathrm{cm}^{-1}$ had not disappeared (often the case in the samples with litharge present), but there was stabilization of the spectra for $3 - 4$ hours, the measurement was also stopped.

4.3 Results and Discussion

4.3.1 Oil characterization

The acid values and distribution of fatty acids in the drying oils are presented in Table 4.1. The five drying oils can be split into three categories: oils with linolenic acid present (linseed and walnut oil), oils with no linolenic acid and a high amount of linoleic acid (safflower and poppyseed oil), and an oil prepolymerized by heating in an anoxic environment (stand oil). The prepolymerization would lead to the formation of oligomers of the oil molecules, meaning the fatty acid distribution is incomplete representation of the composition of the stand oil and is omitted. The acid values provide information about the amount of free fatty acids present in the drying oil, which are assumed to be % of oleic acid for these calculations. For the linseed (LO) and walnut (WO) oils, the values (equivalent to $\sim$ 1% of free fatty acids among the triglyceride molecules in the oil sample) are fairly similar, which makes sense since both of these oils were cold-pressed. The acid value for poppyseed (PO) is lower than LO and WO, most likely due to the difference in processing conditions. PO was indicated to have some refinement performed, which usually has a step that removes free fatty acids present in the drying oil. The acid value for safflower oil (SaO) is in between the values of PO and LO/WO, which indicates that the safflower oil may have had some refining occur during the processing step, but that information was not provided by the oil manufacturer. For the stand oil (StO) there is a larger acid value (equivalent to $\sim$ 3% free fatty acids among the triglyceride molecules), which could be the result of this bottle of oil having been opened previously and exposed to oxygen over the course of many years. Quantifying the initial

Table 4.1: The acid values and fatty acid distributions of the five drying oils used in this study. The acid values are reported with the standard deviation of triplicate measurements.

Drying Oil	Acid Value (mg_{NaOH}/g_{oil})	% Linolenic (18:3)	% Linoleic (18:2)	% Oleic (18:1)	% Saturated (18:0/16:0)	Unconjugated cis C = C from NMR*	Unconjugated cis C = C from FTIR*
Linseed	1.67 $\pm$ 0.02	52.7	19.2	18.3	9.8	1.0	1.0
Walnut	1.54 $\pm$ 0.07	16.2	54.6	18.7	10.4	0.82	0.83
Poppyseed	0.40 $\pm$ 0.01	0	74.7	15.3	10	0.77	0.78
Safflower	1.10 $\pm$ 0.03	0	75.2	15.2	9.6	0.77	0.75
Stand**	4.19 $\pm$ 0.06	-	-	-	-	-	0.29

*Values are normalized to the value of double bonds present in linseed oil, which should have the highest amount due to the largest presence of linolenic acid.
**Calculating a fatty acid distribution for stand oil would not accurately capture the composition of the oil because it is pre-polymerized in an oxygen free environment.

compositions of each oil is important in order to discuss the differences observed in the initial rapid polymerization step. The oils with linolenic acid present in the fatty acid distribution are expected to undergo the primary polymerization step fairly rapidly due to the higher concentration of bis-allylic hydrogens present in the fatty acid chains. The oils with predominantly linoleic acid present should react more slowly in the primary polymerization step and reach a greater level of crosslinking. The stand oil being prepolymerized will probably undergo the primary polymerization step over a much longer period of time and incorporate a lower level of oxygen into the network because there are fewer bis-allylic hydrogens present than in the other oil samples.

Figure 4.2 provides an example of the data from a time-based ATR-FTIR measurement for WO at 70 °C. The colors of the spectra indicate the time at which they were collected, with darker colors being earlier times and lighter colors indicating later times in the measurement. These types of plots are the starting point to determine what regions are most interesting to investigate further and provide the most information about the polymer networks formed from the drying oils. The following sections will go into more detail about those regions of interest and what they indicate about the rate of polymerization and extent of oxidation.

4.3.2 Rates of polymerization

One of the initial observations from Figure 4.2 is that the peak associated with the $\nu(CH)$ adjacent to an unconjugated cis C = C bond (i.e. the $\nu(C = \underline{C - H})$) centered at 3010 cm^{-1} disappears

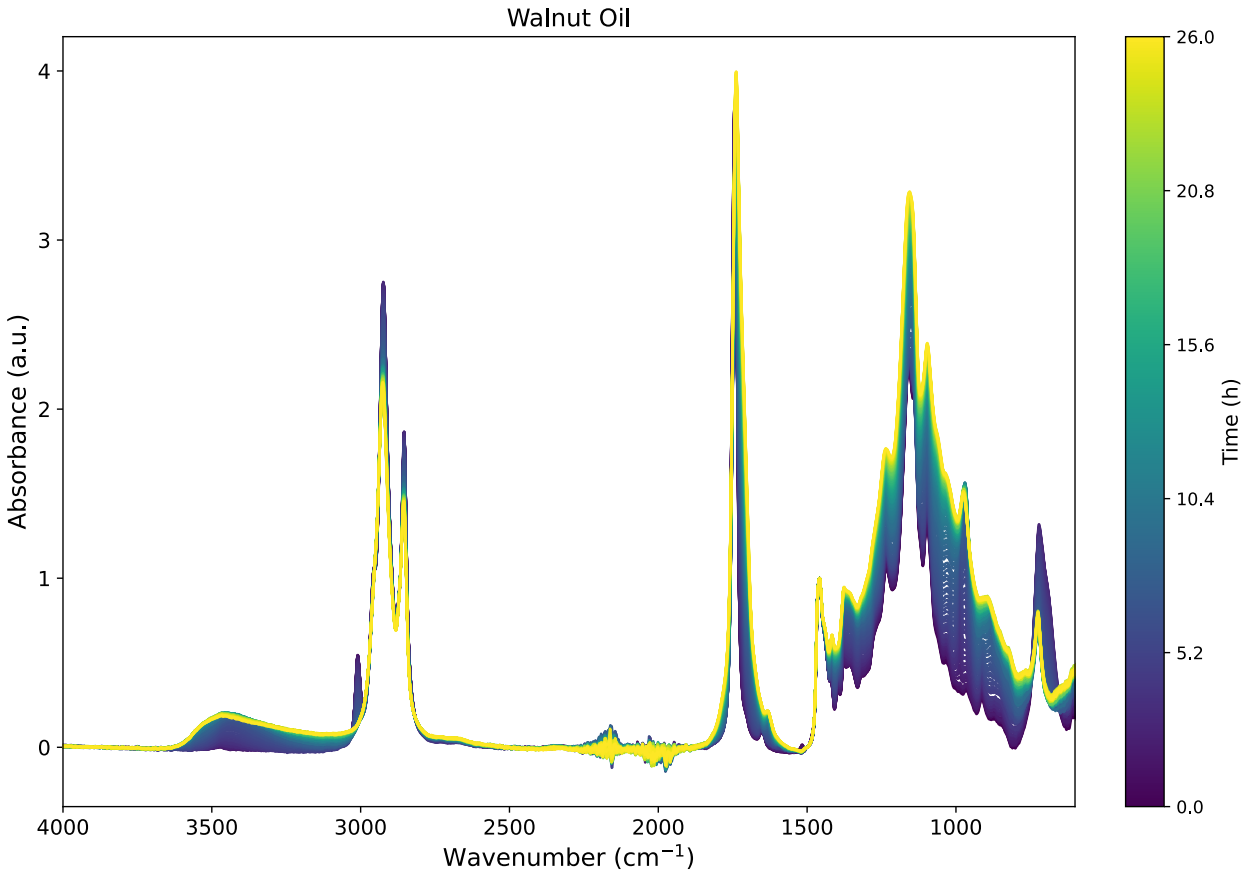

Figure 4.2: ATR_FTIR spectra during the initial rapid polymerization step for walnut oil (WO) at 70 °C. The spectra are baseline corrected using a set of linear baselines connecting the spectral values at 3900, 2500, 1900, and 1500 cm^{-1} and are normalized to the $\delta(CH_2)$ at 1465 cm^{-1} associated with the fatty acid backbone chains. The color bar on the right correlates the color of the spectra with the time of cure, with purple being the initial time point and yellow being the final time point.

quickly during the primary polymerization. This $\nu(CH)$ peak disappears as the C = C bonds are conjugated and isomerized through the abstraction of a bis-allylic hydrogen from the fatty acid chain. Figure 4.3 shows the decrease in the normalized intensity for the oil and oil + litharge samples. The absorbance is normalized to the initial absorbance of the LO sample, which should have the highest concentration of cis C = C bonds within the oil based on the fatty acid distributions in Table 4.1. The initial normalized absorbance values for WO, PO, SaO, and StO are in good agreement with the percentages of double bonds calculated from Table 4.1, validating this normalization method. The decrease in the absorbance of the 3010 cm^{-1} peak shows three different trends for the drying oils. LO and WO have an onset delay, or the time it takes for the absorbance of the 3010 cm^{-1} to begin decreasing, within 10 hours of the start of the measurement and a steep slope for this decrease, indicating a high level of hydrogen abstraction occurring within the drying oil. Even though PO and SaO samples have an onset delay that lasts longer than 1 day, they also have fairly sharp decrease in the absorbance after the onset of initial rapid polymerization, indicating a high level of hydrogen abstraction occurring. StO exhibits a gradual and slow decrease in this absorbance over the entire length of the measurement. The much slower decrease in StO can be attributed to the much lower initial concentration of bis-allylic hydrogens as a result of the pre-polymerization of StO. The oligomers formed in StO can also affect the diffusion rates of both the bis-allylic hydrogens near unconjugated cis C = C bonds and radicals necessary for hydrogen abstraction to take place. The shapes of the curves for the 3010 cm^{-1} peak absorbance follows a trend for a pseudo-first order reaction, which has previously been reported for ethyl linoleate systems [205]. By contrast, the oil + litharge samples (Figure 4.3b) show a very rapid decrease in the intensity of the 3010 cm^{-1} peak followed by a sudden drop in the rate of decrease. Also, the unconjugated cis C = C bonds in the oil + litharge samples are not completely converted as was seen in the oil samples. Based on these differences, there seems to be a two-step kinetic process present for oil + litharge systems. One explanation of this two-step process is that after the initial rapid conversion of the unconjugated cis C = C peaks, there is a sol-gel phase transition that occurs within the oil + litharge sample which decreases the diffusion rate of the reactants for hydrogen abstraction along with reducing the overall kinetics of the system. As a result, the oil + litharge samples require much longer times than the measurements performed in this study to achieve the same level of conversion of the unconjugated cis C = C bonds observed in the oil

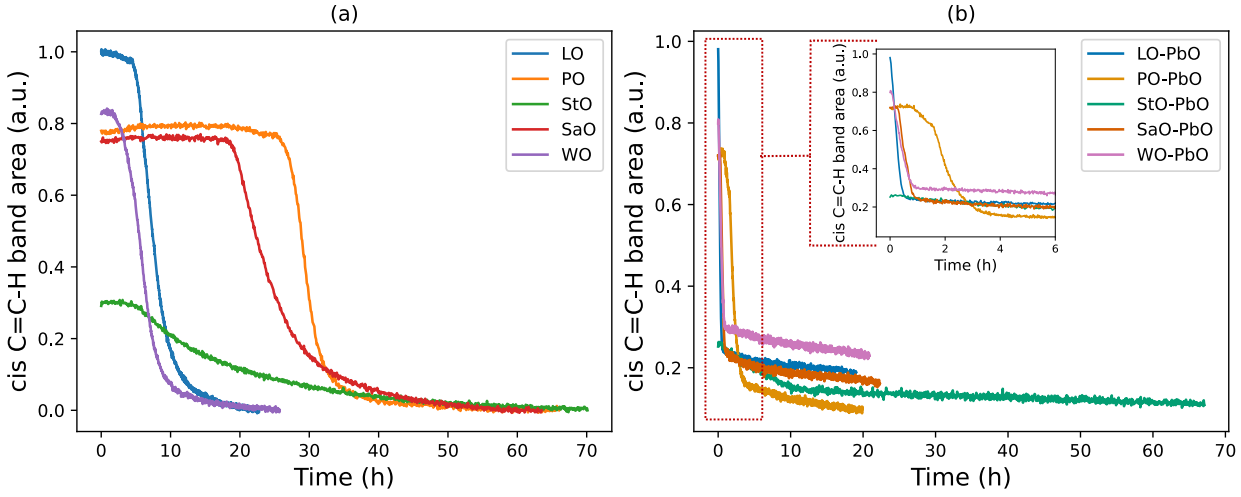

Figure 4.3: Comparison of the intensity for the 3010 cm^{-1} non-conjugated cis $\nu(C = C - H)$ peak over time for (a) oils and (b) oils with 5 % by weight litharge as a drier at 70°C. An inset is provided in (b) to show the initial decreases in the peak intensity at shorter times. A baseline correction was done using a line drawn between $3040 - 2990\,cm^{-1}$ to isolate the 3010 cm^{-1} peak before tracking the intensity changes over time. The starting points are normalized to the initial values of the LO sample, which has the highest amount of C = C bonds present of all the oils. Upon visual inspection, the 3010 cm^{-1} was no longer present at the end of cure for the data shown in (a), so the end values are fixed to be zero.

samples.

Further along in the FRP reactions of the drying oils, conjugated C = C bonds are formed on the fatty acid chains. The conjugated C = C bonds are further reacted to form a non-conjugated trans C = C bond, which is seen in the lower right of Figure 4.1 where oxidation and hydrogen abstraction occur after a radical addition step forms a carbon radical. The signatures for these chemical moieties occur between 930 and 1000 cm^{-1} in the IR region for ω(CH) next to the C = C bonds. This region was isolated for further study by subtracting a linear baseline between 1000 and 925 cm^{-1} before performing analysis. There are three peaks of interest within this region: the peak at 986 cm^{-1} attributed to $\omega(\text{conjugated trans} - \text{trans C} = \underline{\text{C} - \text{H}})$, the peak at 968 cm^{-1} attributed to $\omega(\text{non} - \text{conjugated trans C} = \underline{\text{C} - \text{H}})$, and the peak at 950 cm^{-1} attributed to $\omega(\text{conjugated trans} - \text{cis C} = \underline{\text{C} - \text{H}})$ [154, 183]. A linear combination of Gaussian functions were used to capture each peak's contribution to the absorbance between $1000 - 925\,cm^{-1}$. Figure 4.4 shows an example of the fitting of data using a linear combination of the Gaussian functions for the PO sample at $\sim$ 26 hours of cure, well into the initial polymerization step. From the Gaussian

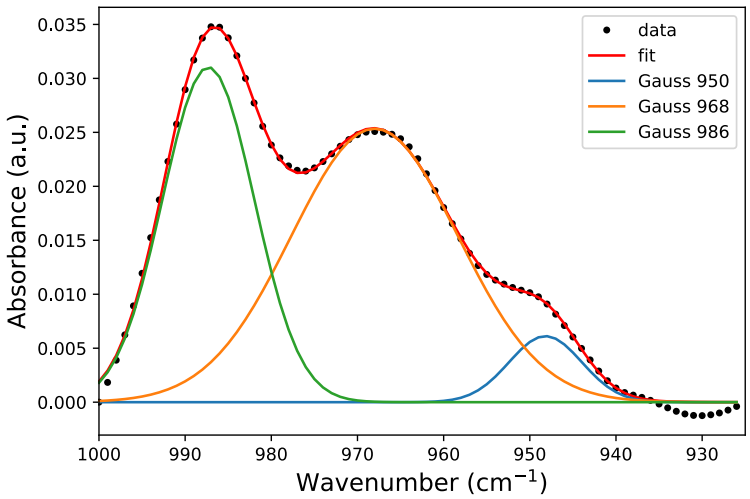

Figure 4.4: An example of using a linear combination of three Gaussian functions to fit the individual contributions of the $\omega(\mathrm{CH})$ between $900 - 1000\,\mathrm{cm}^{-1}$ for the PO measured at 70 °C at $\sim$ 26 hours. These data are baseline corrected between 925 and $1000\,\mathrm{cm}^{-1}$. The peak at $986\,\mathrm{cm}^{-1}$ is attributed to the $\omega(\text{conjugated trans} - \text{trans}\,\mathrm{C} = \underline{\mathrm{C} - \mathrm{H}})$, at $968\,\mathrm{cm}^{-1}$ is attributed to the $\omega(\text{non} - \text{conjugated trans}\,\mathrm{C} = \underline{\mathrm{C} - \mathrm{H}})$, and at $950\,\mathrm{cm}^{-1}$ is attributed to the $\omega(\text{conjugated trans} - \text{cis}\,\mathrm{C} = \underline{\mathrm{C} - \mathrm{H}})$.

curves, the individual peaks can be monitored over time using the peak area.

The three $\omega(\mathrm{CH})$ peaks in this region provide some insights into how quickly the C = C bonds are being converted and reacted during the initial rapid polymerization step. Figure 4.5 provides a comparison of the peak areas for the $\omega(\mathrm{CH})$ adjacent to C = C for LO, PO, and StO both with and without litharge. For the LO sample, there is no contribution from any of the peaks until just before 5 hours, at which point, the concentration of non-conjugated trans C = C bonds grows rapidly (the growth of this species corresponds well with the decrease of the non-conjugated cis C = C concentration measured using the peak at $3010\,\mathrm{cm}^{-1}$). The conjugated C = C bond concentration also grows to a lesser extent, but decrease at the end of the measurement while the non-conjugated trans C = C bond concentration remains dominant. The PO sample shows different responses for the $\omega(\mathrm{CH})$ concentrations. At the initial onset of polymerization, the conjugated trans − trans C = C bond concentration grows fastest, but is overtaken by the non-conjugated trans C = C bond concentration after a couple of hours. The concentrations of both conjugated C = C bonds also decay more rapidly than the non-conjugated trans C = C bond. The non-conjugated trans C = C bond also decreases to a much greater extent than in the LO sample; however, this decrease is due to the PO sample being measured for much longer after the initial

polymerization step was completed. The longer measurement of the PO sample provides more time for the non-conjugated trans C = C bond to further react within the polymer network. Comparing the concentration of the conjugated trans-cis C = C concentration (986 cm^{-1}) for both LO and PO, the concentration in PO is almost nonexistent while there is a substantial concentration in the LO sample. This trend is also present in the WO and SaO samples, even though the conjugated trans-cis C = C bond concentration is less pronounced in the WO compared to the LO (see the data in Figure C.8) and indicates that the formation of the conjugated trans-cis C = C bonds is less favorable in polymer systems that do not have linolenic acid present in the fatty acid distribution. StO, being prepolymerized, starts out with an observable non-conjugated trans C = C bond concentration and very small contributions from the two conjugated C = C bonds. All three C = C bonds slowly decrease over time, but the non-conjugated trans C = C bond is still quite large at the end of the measurement of the initial polymerization step.

The formation of conjugated C = C bonds is most present during the first phase of oil reactivity, which makes sense considering they are the direct result of peroxide radical formation in the polymer network. As the concentrations of the conjugated C = C bonds decrease, the rate of the initial hydrogen abstraction of a bis-allylic hydrogen is also decreasing, meaning that the peroxide radicals are no longer being formed and that further crosslink formation will be outside of this first phase. For LO and WO, the high levels of non-conjugated trans C = C bonds seem to indicate that level of crosslink formation is more limited to peroxy and alkoxy crosslinks rather than alkyl crosslinks. By contrast, PO and SaO have significant decreases in the non-conjugated trans C = C bond concentration, indicating a greater chance that alkyl crosslinks are also being formed. These differences in the extent of conversion and saturation of these C = C bonds would seem to indicate that the presence of linolenic acid decreases the time of the first phase of oil reactivity, which could lead to incomplete conversions of C = C bonds to form crosslinks in the polymer network. This phenomenon has been previously observed for linseed oils where linolenic and linoleic concentrations were varied and the extent of crosslink formation was compared [188].

When compared to the oil samples, we see quite a different response for the oil + litharge samples presented in Figure 4.5. At the same time as the initial decrease in the non-conjugated cis $\nu(C = \underline{C - H})$ peak at 3010 cm^{-1}, there is a corresponding rapid increase in the non-conjugated

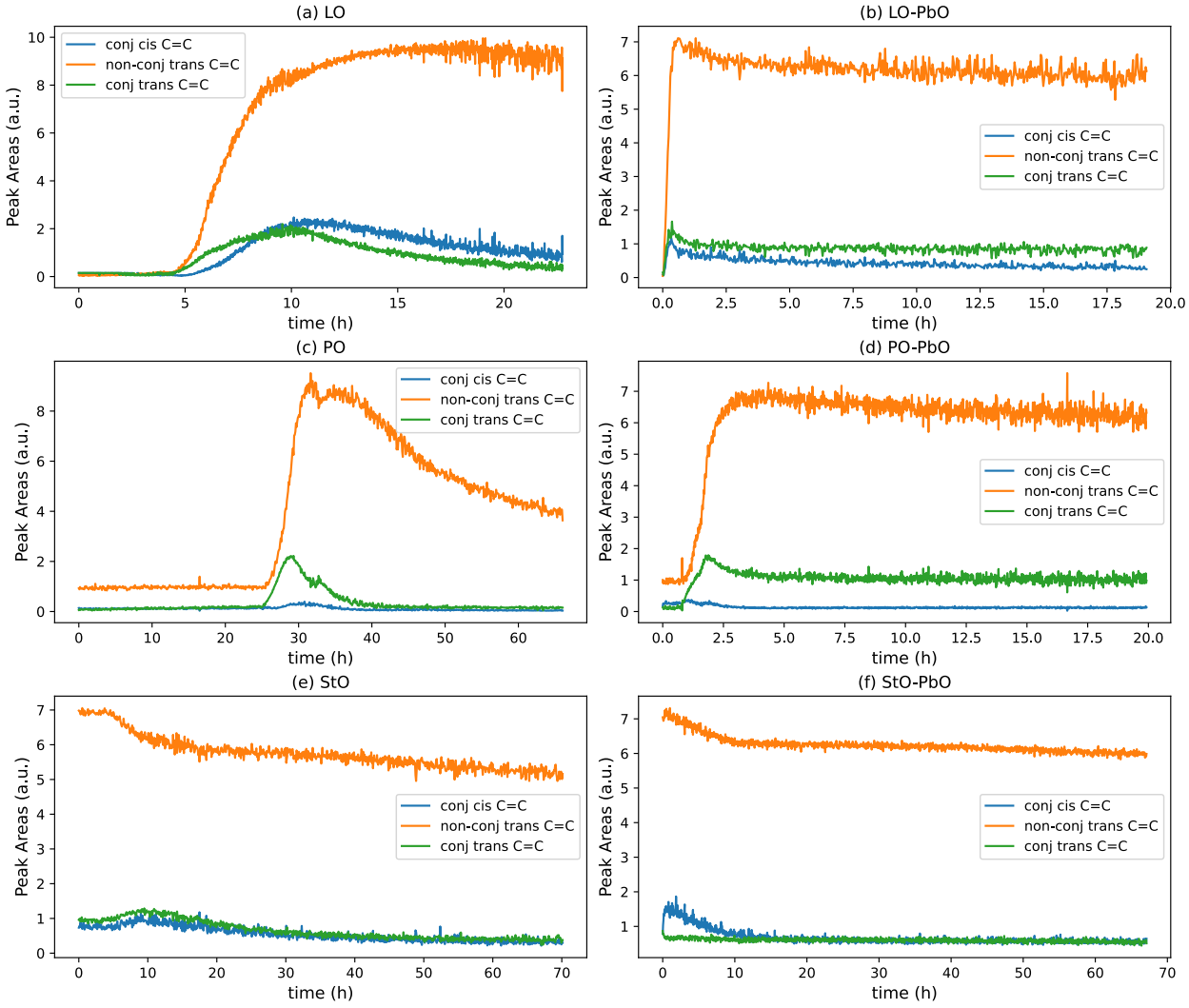

Figure 4.5: Comparison of the changes in the peak areas of the Gaussians used to fit the ω(CH) peaks at 950, 968, and 986 cm^{-1}. The peak areas are shown for (a) linseed oil, (b) linseed oil + litharge, (c) poppyseed oil, (d) poppyseed oil + litharge, (e) stand oil, and (f) stand oil + litharge. For this figure, 'conj cis C = C' refers to the conjugated trans-cis C = C peak and 'conj trans C = C' refers to the conjugated trans-trans C = C peak. The Gaussian fitting was performed after baseline correcting using a set of linear baseline between 925 and 1000 cm^{-1} for each sample. The peak areas are calculated by multiplying the amplitude and the standard deviation to compare the prominence and rate of growth for the individual peaks in each sample. Graphs for the other oils in this work are provided in Appendix C.

trans C = C bond concentration for the LO-PbO and PO-PbO samples. The conjugated C = C bond concentrations also increase, with both bonds equally increasing in the LO-PbO and the conjugated trans-trans C = C bond growing more rapidly in PO-PbO. After these initial increases, there is a very sudden decrease followed by a much more gradual decrease in the concentrations of the conjugated C = C bonds and the non-conjugated trans C = C bond, corresponding to the discontinuity observed in the absorbance decrease Figure 4.3. This rapid increase and decrease of the LO, WO, and SaO conjugated C = C bond concentrations especially highlight this conversion; PO has a more gradual decrease compared to the other three drying oils and does not exhibit as much of a discontinuity in Figure 4.3. The StO-PbO sample shows a similar response to the StO sample, but the decrease in the C = C bond concentrations is less pronounced in the StO-PbO sample. The rapid change in the oil + litharge samples during the first phase of oil reactivity followed by very slow decreases in the peak areas support the notion that the first phase of oil reactivity starts very quickly and lasts for a much shorter time than in the oil samples. The decreased formation of conjugated C = C bonds after the discontinuity supports the idea of the drying oil experiencing a sol-gel phase transition which "arrests" the first phase of oil reactivity. This "arresting" of the polymer network can be attributed to the increased rate of hydroperoxide decomposition and how that difference affects both the diffusion rate of radical species in the oil network as well as the possibility that the bis-allylic sites where hydrogen abstraction occurs become too far apart within the oil network to continue forming conjugated C = C bonds. The litharge appears to be a less effective through drier at 70 °C with how many non-conjugated cis C = C bonds remain after the first phase of oil reactivity is completed. This change in the role that litharge plays in the curing of drying oils is within the realm of possibility because lead compounds can interact with drying oils to accelerate the oxidation of oils as well as the polymerization process [206].

Exactly tracking how the non-conjugated trans C = C is consumed using ATR-FTIR is not feasible because the reaction pathways of drying oil polymerization are extremely complicated. Once the non-conjugated trans C = C is formed, it is significantly more stable than the conjugated C = C bonds and requires the presence of a radical species to be further consumed to form a C − C bond. One potential method that the non-conjugated trans C = C bond can form an ether crosslink by reacting with an alkoxy radical ($RO^{\bullet}$) [8, 184].

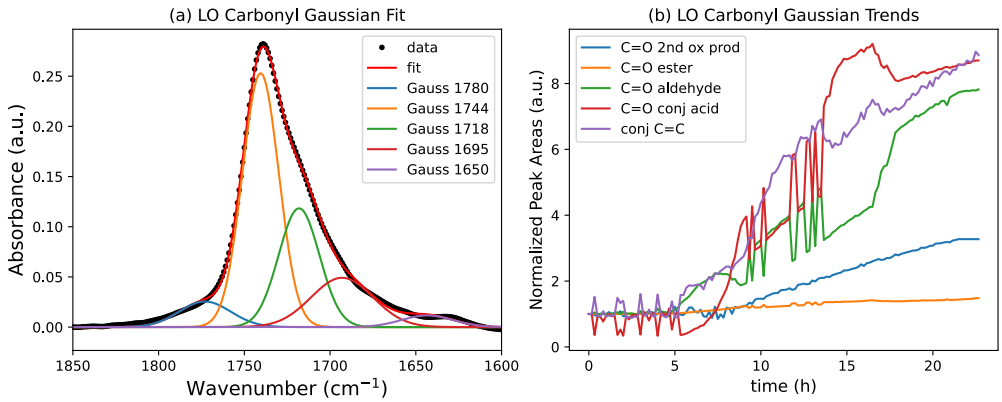

Figure 4.6: Peak fitting using five Gaussian functions of the carbonyl region in the LO sample measured at 70 °C. (a) An example of the Gaussian peak fits to the experimental ATR-FTIR data measured at $\sim$ 20 hours. (b) The changes in the peak areas of each Gaussian over the time of measurement. The peak areas are normalized to the initial area of each peak at t = 0 hrs. The FTIR data used for the Gaussian fitting was baseline corrected using a line drawn between 1850 and 1470 cm^{-1}.

4.3.2.1 Why Gaussian fitting cannot be applied to other regions

After seeing how well the Gaussian fitting routine worked for the region of the $\omega(CH)$ near C = C bonds (e.g. exhibited well defined peaks during the first phase of oil reactivity and mostly smooth changes in the peak areas over the time of the measurement), an attempt was made to perform a similar fitting of the carbonyl region using Gaussian functions. The second derivative of the FTIR spectra for the drying oils was used to determine the most prominent carbonyl peaks to fit with Gaussian functions and resulted in five total peaks for the region between 1850 and 1600 cm^{-1}. An example of a second derivative for the FTIR spectrum of LO is shown in section C. Five peaks were used to fit the distribution of $\nu(C = O)$ in the carbonyl band: 1780 cm^{-1} (secondary oxidation products), 1744 − 1740 cm^{-1} (ester), 1718 cm^{-1} (aldehyde), 1695 cm^{-1} (acid conjugated with another double bond), and 1650 − 1630 cm^{-1} (stretching mode of C = C transitioning from non-conjugated to conjugated). Figure 4.6 is an example of the result for a least-squares fit of Gaussians to the spectrum of LO measured at 70 °C. As can be seen in Figure 4.6a, there is good agreement between the Gaussian model (red line) and the experimental data (black dots). However, when peak areas are compared in Figure 4.6b, it becomes clear that there are several close lying minimum solutions for the Gaussian model, leading to discontinuous jumps in the peak areas of carbonyl bands over time.

One of the major contributions to the challenges with using Gaussian functions to determine the contributions of peaks in the carbonyl region is that there are potentially other $\nu(C=O)$ moieties (e.g. saturated/unsaturated ketones or non-conjugated acids) present in this region than are observed in the second derivative plot. The center frequency of a $\nu(C=O)$ band can also be shifted by a few wavenumbers or significantly broadened as the oil network transitions from a liquid to a solid film. These changes in the $\nu(C=O)$ bands make it very difficult to both place tight constraints on the Gaussian model used for fitting the FTIR data and achieve smooth fits of the peak area changes over time. Without clear indications of where these moieties may contribute to the overall intensity of the carbonyl band, more peaks cannot be added to the Gaussian model with any certainty that the $\nu(C=O)$ moeities are well represented in this region. In this study, pursuing an alternative route of analysis of the carbonyl band was chosen to avoid these issues.

4.3.3 Oxidation of polymer networks

As the $C=C$ bonds are reacting with oxygen radicals to form crosslinks, there are also side reactions that will further oxidize other regions of the fatty acid chains in the oil monomers. The evolution of the carbonyl region is one where we can follow some aspects of oxidation in the drying oils. Figure 4.7a shows the evolution of the carbonyl region for linseed oil over time. The carbonyl stretch is initially centered at $1744\,cm^{-1}$ as a carbonyl in an ester ($\nu(C=O)_{ester}$). As the drying oil polymerizes, peaks associated with the formation of carbonyl stretches near aldehydes ($^{\circ}(C=O)_{aldehyde}$) and acids conjugated to other double bonds ($\nu(C=O)_{acid,\,conj}$) appear at $1718\,cm^{-1}$ and $1695\,cm^{-1}$, respectively[154, 179]. At longer times, the growth of what are generally called secondary oxidation products ($\nu(C=O)_{2nd\,ox}$) occurs as a shoulder centered at $1780\,cm^{-1}$. Literature has attributed one of the secondary oxidation products represented by the $1780\,cm^{-1}$ shoulder to potentially be gamma lactones [185]. For these four carbonyl bands, the absorbance values over time are plotted in Figure 4.7b-f. Figure 4.7b shows the growth of the $\nu(C=O)$ bands by subtracting from the initial value from each band. In this figure, the shift of $\nu(C=O)_{ester}$ from 1744 to $1740\,cm^{-1}$ contributes to the initial decrease and increase in the ester stretch. The $\nu(C=O)_{aldehyde}$ peak starts growing at the same time as the shift of the $\nu(C=O)_{ester}$, after ~ 4 hours. The $\nu(C=O)_{acid\,conj}$ begins to increase after ~ 5 hours have passed and the rate

of increase is overall slower than that of the $\nu(C=O)_{aldehyde}$ peak. At ~ 8 hours, the growth of the secondary oxidation products peak begins, but to a much lesser extent than the other $\nu(C=O)$ peaks. For Figure 4.7c-f, the values are normalized by the initial absorbance of the $\nu(C=O)_{ester}$.

The changes in the $\nu(C=O)_{acid,\,conj}$ and the secondary oxidation peaks are compared for the oil and oil + litharge samples in Figure 4.7c-f. Since the overall shape of the changes for $\nu(C=O)_{aldehyde}$ and $\nu(C=O)_{acid,\,conj}$ peaks are similar in shape and grouping of the oils, only the $\nu(C=O)_{acid,\,conj}$ peaks are shown. For the oil samples, the trends between Figure 4.7c and e are very similar. The growth of the peaks occurs at an earlier time for LO and WO than PO and SaO. The StO sample slowly increases over the entire period of measurement. The extent of growth for the secondary oxidation products is much smaller than the corresponding growth of the $\nu(C=O)_{acid,\,conj}$ peaks, confirming that these products are formed later on during the first phase of oil reactivity. When comparing the oil to the oil + litharge samples, the oil + litharge samples appear to be much less reactive. The $\nu(C=O)_{acid,\,conj}$ peak for the litharge shows a rapid increase but then a gradual decrease or stabilization of the absorbance values. This decrease can be attributed to the conversion of the $\nu(C=O)_{acid,\,conj}$ peaks to $\nu(COO-Pb)$ peaks, which occur between 1450 and 1600 cm^{-1}. The lead carboxylate peaks for the oil + litharge samples are provided in section C, but will not be discussed further here due to the complexity of those peaks. The growth of the $\nu(C=O)_{2nd\,ox}$ peak is greatly reduced in the oil + litharge samples, which seems to indicate that the $\nu(C=O)_{acid,\,conj}$ moieties are reactants for the formation of the $\nu(C=O)_{2nd\,ox}$ moieties. If we use gamma lactones as one poential secondary oxidation product, we observe that one of the precursors for gamma lactone formation can be an unsaturated $\nu(C=O)_{acid,\,conj}$ [185]. Despite the accelerated curing kinetics in oil +litharge systems observed by following the $C=C$ conversions, we see slower growth of the high wavenumber shoulder in the carbonyl band. When this information is paired with the knowledge that lead carboxylates are also forming in the film, we can conclude that the inclusion of litharge is leading to less oxidized oil films after the first phase of oil reactivity.

The $C-O$ and OH regions of the oil and oil + litharge samples are compared since growth in these regions would indicate more oxidative reactions occurring within the oil film. As these regions increase in intensity over time, more ether, alcohol, aldehyde, acid, and other moieties are being

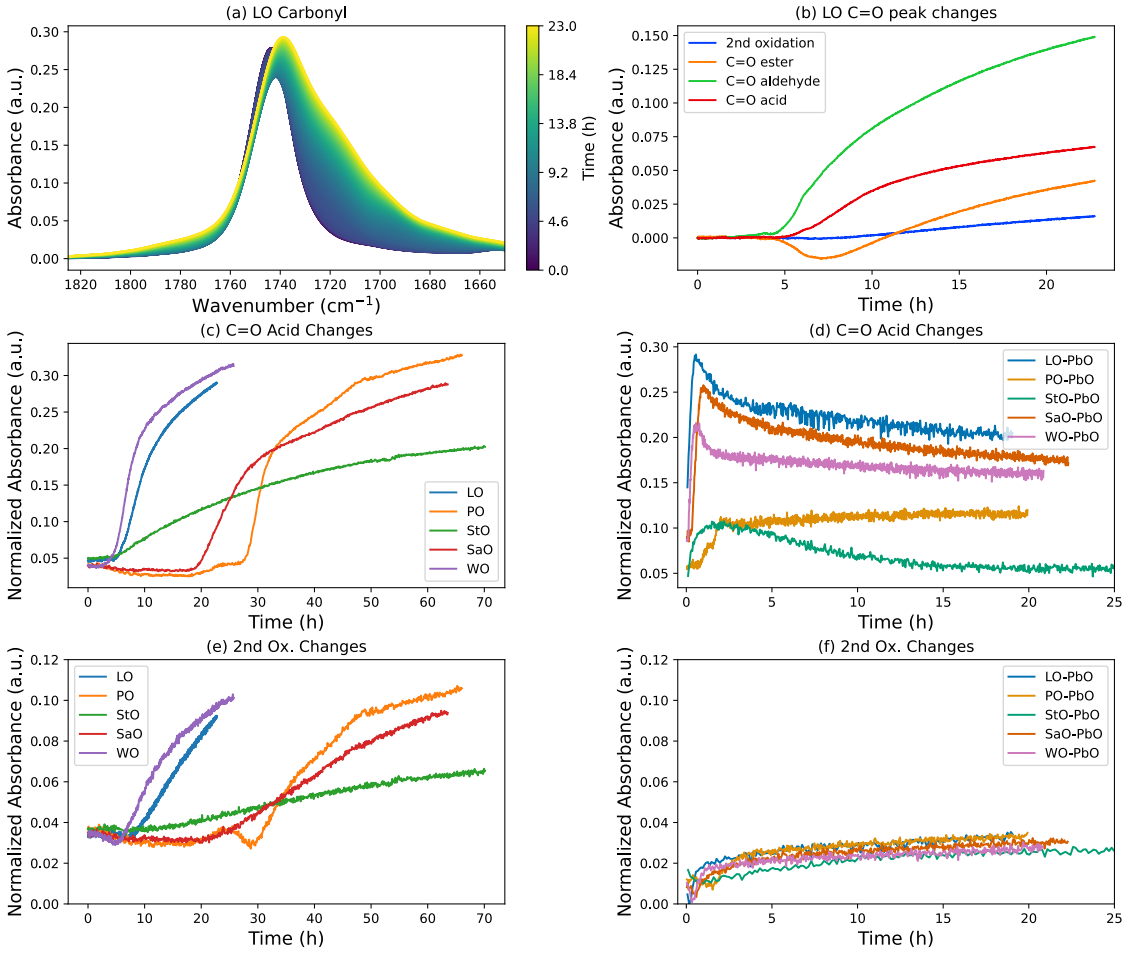

Figure 4.7: The (a) evolution of the carbonyl region over time for LO at 70 °C. (b) the growth of the absorbance values for the $\nu(\mathrm{C=O})$ bands for the LO sample shown in (a). To clearly show the times when the $\nu(\mathrm{C=O})$ peaks begin to grow, the data shown in (b) are the differences from the initial absorbances of each peak. Comparisons of the $\nu(\mathrm{C=O})_{\mathrm{acid}}$ at 1695 cm^{-1} for the (c) oils and (d) oils + litharge, and the secondary oxidation products at $\sim$ 1780 cm^{-1} for (e) oils and (f) oils + litharge systems. Data shown in (c), (d), (e), and (f) are normalized to the initial value of the $\nu(\mathrm{C=O})_{\mathrm{ester}}$ at 1744 cm^{-1}. Data shown (a), (b), (c), and (e) were baseline corrected to 1850 cm^{-1} while (d), and (f) were baseline corrected using a line drawn between 1850 and 1810 cm^{-1}.

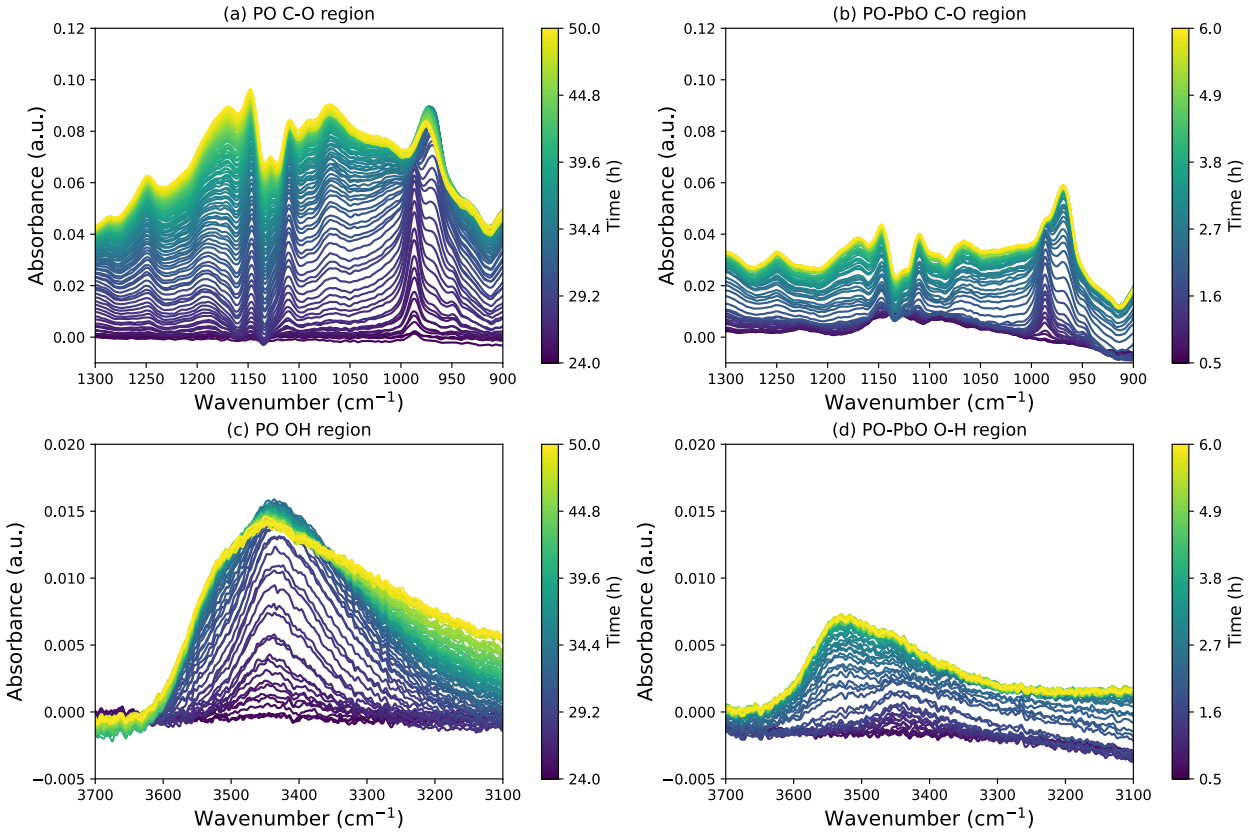

Figure 4.8: Difference spectra showing the changes in the $C-O$ region of the IR spectra over time for (a) PO and (b) PO-PbO measured at 70 °C. Difference spectra showing the changes in the OH region over time for (c) PO and (d) PO-PbO are also shown. The PO sample shown in (a) and (c) is baseline corrected using linear baselines drawn between 3900, 2500, 1900, and 1500 cm^{-1} while the PO-PbO sample is baseline corrected using linear baselines drawn between 3900, 2500, and 1900, cm^{-1}.

formed where oxygen is incorporated into the oil network. Figure 4.8 shows the difference spectra for the $C-O$ ($1300-1100\,cm^{-1}$) and OH ($3700-3100\,cm^{-1}$) regions of PO and PO-PbO measured at 70 °C. The increase in the $C-O$ and OH regions is much more pronounced for the PO sample than for the PO-PbO sample. The shapes of the OH bands also vary significantly, indicating that there are differences in the relative amounts of different OH species contributing to the overall band.

For the PO-PbO sample, most of the changes in the C-O and OH regions occur at early times of the measurement, corresponding with the first phase of oil reactivity. At longer times for PO-PbO, there is a slight increase in the overall intensity of the $C-O$ region while the $O-H$ region appears to have almost no growth. The PO samples are used as an example, but the trends seen here are

also similar for LO, WO, SaO, and StO. The data in Figures 4.3, 4.7, and 4.8 all present the oil + litharge samples as less reactive at longer times, especially after the first phase of oil reactivity. It is possible the further reactivity of the oil + litharge samples is arrested due to the formation of clusters of high crosslink density, which may affect the diffusion rates of the radicals necessary to form more crosslinks or increase the levels of oxidation within the oil film. Some researchers have discussed the possibility of clustered areas of high crosslink density forming in polymer networks governed by free-radical polymerization, which could be a relevant question to investigate with further characterization of the topological nature of the formed polymer network [176, 197–199].

4.3.4 Effect of Temperature

Initial measurements of the oil and oil + litharge samples were at 70 °C in order to perform these experiments on a timescale that was feasible for data collection. In order to assess the effects of temperature on the overall kinetics of the first phase of oil reactivity, measurements of the LO-PbO and PO-PbO samples were collected for temperatures between 30 and 70 °C with 10° intervals (drier was added to make data collection feasible within a practical amount of time). The results for these samples are summarized in Figure 4.9. The LO and PO data measured at 70 °C are also included as a comparison for the changes in the oil without litharge present. For the LO-PbO samples, the initial decrease in the cis $C=C$ stretch at 3010 cm^{-1}has a slightly longer onset delay as the temperature decreases. The rate of decrease in the peak also slows as the temperature is decreased, with the effect becoming especially pronounced in the LO-PbO40 and LO-PbO30 samples. The shape of the unconjugated cis $^{\circ}$ ($C=\underline{C-H}$) band loses the discontinuity-like behavior seen in Figure 4.3b as the temperature is decreased. What this phenomenon indicates is that the presence of litharge at elevated temperatures decreases the onset delay of the first phase of reactivity and the way that litharge interacts with the drying oil appears to change during the course of cure. As the temperature is decreased, there are fewer discontinuities present in the chemical moieties, indicating less evidence of a sol-gel phase transition occurring within the oil + litharge system and affecting the overall reactivity of the system. For the peaks associated with the carbonyl stretch, there is still a decrease seen in the LO-PbO samples of the $\nu(C=O)_{acid}$ peaks. The effect is fairly similar for the measurements at 70, 60, and 50 °C, but the changes in the peak for the

40 and 30 °C samples are different. The initial generation of the $\nu(C=O)_{acid}$ peak is much more gradual and also decreases more gradually over time. The decrease indicates that there is still conversion of the $\nu(C=O)_{acid}$ to $\nu(COO-Pb)$ happening within the oil network. The growth of the secondary oxidation peaks in the LO-PbO samples also splits into two general responses. The LO-PbO samples at and above 50 °C demonstrate the rapid increase and then little change initially while the samples below 50 °C exhibit a much more gradual growth of the secondary oxidation peaks and are even less pronounced than the higher temperature peaks.

The PO-PbO samples show a greater range of variation as a function of temperature. As can be seen in Figure 4.9d-f, there is again a clustering of the response for samples at and above 50 °C and below 50 °C. The samples at and above 50 °C show a fairly short onset delay of the first phase of oil reactivity and sharp decrease in the absorbance of the non-conjugated cis C = C peak which also corresponds with the initial rapid increase in the $\nu(C=O)_{acid}$ and the secondary oxidation peaks. The rate of decrease for the non-conjugated cis C = C bond has a discontinuous response, indicating that the phase transition and arresting of the first phase of oil reactivity is more likely at higher temperatures. The decrease in PO-PbO40 is slower for the non-conjugated cis C = C bond and no exhibits a discontinuity, which causes growth of the $\nu(C=O)_{acid}$ band to occur later as well as less conversion to the $\nu(COO-Pb)$ peak. The response for PO-PbO30 has a much longer onset delay and then a very slow decrease in the absorbance of the non-conjugated cis C = C peak as well as much less conversion of these bonds over the time of the measurement.

To further understand the effects of temperature on the curing kinetics of drying oils, a sample of LO was measured at 50 °C and the changes in the C − O and OH regions are compared to the LO-PbO50 sample through the use of difference spectra in Figure 4.10. For these two samples, there is still a greater growth of both the C − O and the OH regions in the LO-50 sample than the LO-PbO50 sample, indicating that the observed reduction is more likely caused by the presence of the litharge. When comparing the LO measurements performed at 70 °C and 50 °C (see Figures 4.3, 4.5, and C.9), the overall trends of the C = C bonds are qualitatively very similar. The main difference is that the onset delay for the LO-50 sample is larger than for the LO-70 sample. Therefore, when there is no litharge present in the drying oil, performing the polymerization at higher temperature just affects the rate of cure and not the overall chemistry of cure. When litharge is

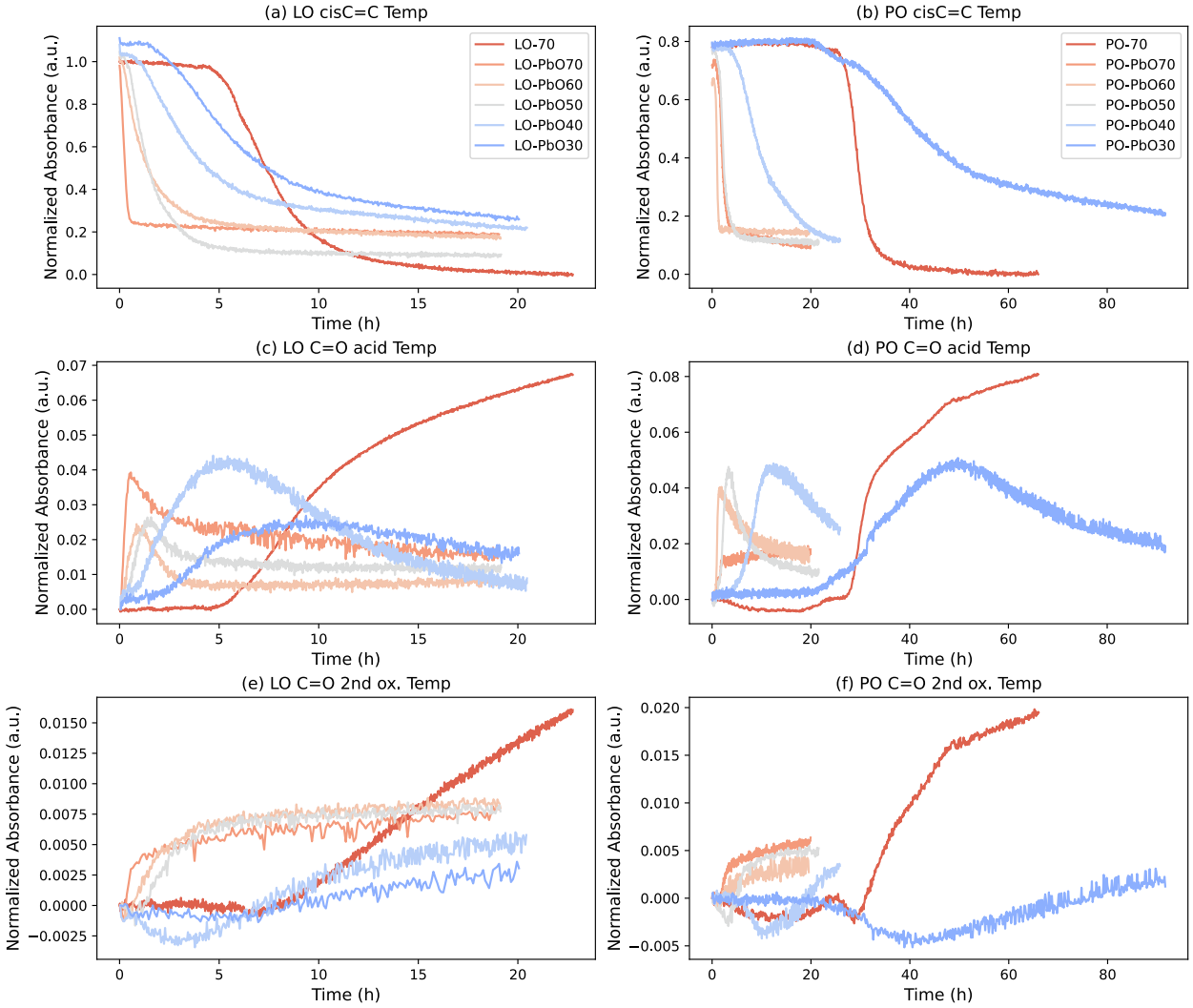

Figure 4.9: Comparisons of changes in chemical moieties in LO-PbO (a, c, e) and PO-PbO (b, d, f) samples over time for temperatures between $30 - 70\,^{\circ}\mathrm{C}$. The changes in the normalized absorbance of the $\nu(\mathrm{CH})$ next to a cis C = C at different temperatures are shown for (a) LO-PbO and (b) PO-PbO. The$\nu(\mathrm{CH})$ next to a cis C = C is baseline corrected using a linear baselines drawn between 3040 and 2990 cm^{-1}. These data are normalized to the initial value of the LO sample measured at 70 °C shown in Figure 4.3(a). The changes in the $\nu(\mathrm{C=O})_{\mathrm{acid,\,conj}}$ peaks are shown for (c) LO-PbO and (d) PbO at different temperatures. The changes in the secondary oxidation products are shown for (e) LO-PbO and (f) PO-PbO for cure at different temperatures. The data shown in (c), (d), (e), and (f) are baseline corrected using linear baselines drawn between 1850 and 1810 cm^{-1} and then subtracted from the initial absorbance value of the sample to emphasize the changes in the absorbance of the peaks.

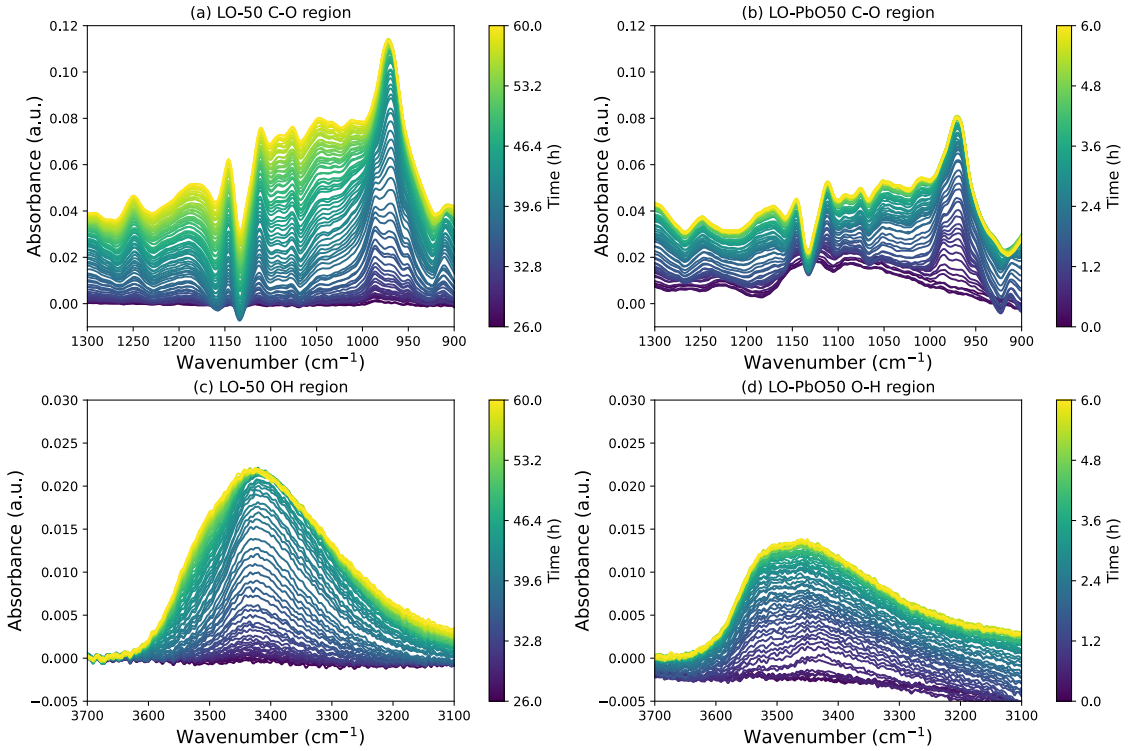

Figure 4.10: The changes in the C − O region of the IR spectra over time for (a) LO-50 and (b) LO-PbO50, both measured at 50 °C. The changes in the OH region over time for (c) LO-50 and (d) LO-PbO50 are also shown. The LO-50 sample shown in (a) and (c) is baseline corrected using linear baselines drawn between 3900, 2500, 1900, and 1500 cm^{-1} while the LO-PbO50 sample is baseline corrected using linear baselines drawn between 3900, 2500, and 1900, cm^{-1} The data shown in this figure are difference spectra, where the data are subtracted from the initial spectrum value, which makes it easier to see the changes in these regions.

incorporated into the drying oils at elevated temperatures, there appears to be the potential to activate a different reaction pathway that would promote an arresting of the first phase of oil reactivity and potentially promote a more heterogeneous cluster-based oil network. As a result, researchers should take care with future cure studies when using both temperature and litharge to accelerate the polymerization of drying oils.

4.3.5 Oils after 1 year of cure

Films of the oils were prepared and allowed to cure in ambient lab conditions (∼ 22 °C, and 50% RH) for one year to see if the differences observed during early stages of cure persisted over longer times. ATR-FTIR spectra were collected and are shown in Figure 4.11. After one year, LO, WO, PO, and SaO show very similar spectra. StO shows signs of lower levels of

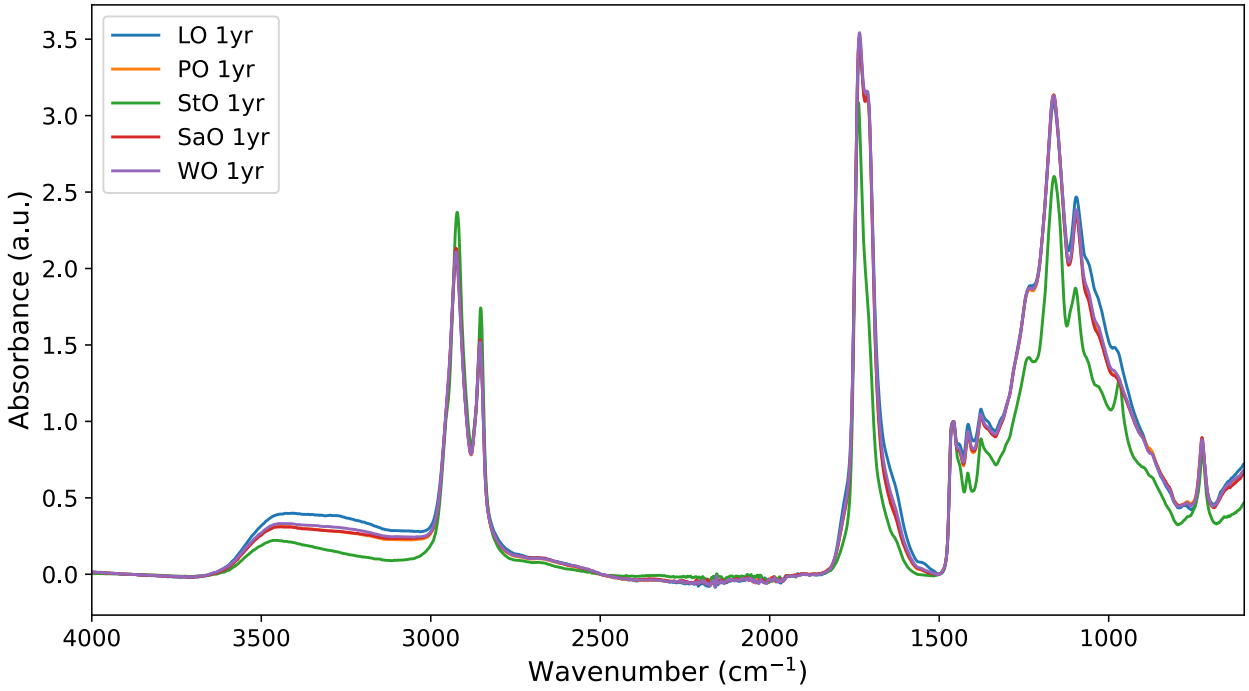

Figure 4.11: FTIR spectra ($4000 - 600\,\mathrm{cm}^{-1}$) of linseed, walnut, safflower, poppyseed, and stand oils after 1 year of curing in ambient conditions. The spectra are baseline corrected using linear interpolations between 3900, 2500, 1900, $1500\,\mathrm{cm}^{-1}$ and normalized to the $\delta(CH_2)$ at $1465\,\mathrm{cm}^{-1}$.

oxidation in the polymer film, evidenced by the slightly higher absorbance values in the $\nu(CH)$ region between $2750 - 3000\,\mathrm{cm}^{-1}$, the decreased absorbance values in the OH, carbonyl, and $C - O$ regions. These differences indicate that the initial anoxic polymerization undergone by StO lead to differences in the polymer network at longer times. With this lower level of oxidation in StO, it would take much longer to reach the same levels of oxidation and reactivity as the other drying oils observed in this study. There is the possibility that the initial conditions for StO are such that is actually unable to reach the same levels of oxidation as the other drying oils.

For the other four oils, the spectra are similar for this longer time point. The carbonyl band is dominated by the $\nu(C=O)_{\text{ester}}$ at $1740\,\mathrm{cm}^{-1}$ and the $\nu(C=O)_{\text{saturated acid}}$ at $1710\,\mathrm{cm}^{-1}$. When compared to the ATR-FTIR spectra collected at the end of the measurement (Figure C.7), the peaks at $1780\,\mathrm{cm}^{-1}$ and at $1695\,\mathrm{cm}^{-1}$ have not grown very much, indicating that the moieties contributing to these peaks have most likely been consumed by other chemical reactions by this point in the oil cure. While chemically similar as evidenced by the ATR-FTIR spectra shown in Figure 4.11, these data do not provide information about the topological nature of the network. More differ-

ences may also occur in the ATR-FTIR spectra of these drying oils if driers or pigments are also incorporated, which will be a focus of extensions of this work. It may be that for the LO and WO samples, which had an initial rapid conversion of the C = C in the fatty acid chains, there may be a greater extent of heterogeneity on the nano-scale related to the crosslink density of the oil network than in the PO and SaO samples.

4.4 Conclusion

In this chapter, the effects of the fatty acid distribution, inclusion of a lead drier, and temperature are investigated using time-based ATR-FTIR. How rapidly the C = C were conjugated, isomerized, and reacted into a saturated form during the first phase of oil reactivity seemed to have the greatest effect on the extent of crosslink formation in the polymer film as well as the extent of oxidation evident in the ATR-FTIR spectra. The fatty acid distribution affected the likelihood of the formation of conjugated trans-cis C = C bonds. For oils with mostly linoleic acid in the fatty acid distribution, conjugated trans-cis C = C bonds were not a significant part of the conversion of the C = C bonds. This means that the reaction pathways to form conjugated trans-cis C = C bonds are only favored with majority linolenic acids, where there are more bis-allylic sites for potential hydrogen abstraction. Less oxidation was present in the oil samples if the non-conjugated cis C = C bonds were converted quickly or if the consumption of those bonds had a discontinuity present at longer times. Observing less oxidation is also supported by reduced growth of the carbonyl, C − O, and OH regions in the spectra. The reduced extent of crosslinking is a potential indicator of a heterogeneous polymer network due to variations in the crosslink density. A heterogeneous network is possible if a cluster-formation polymer network model is used to understand the impacts of these variations in the chemical reactivity of the oil film on the resulting polymer network topology. The presence of litharge in the oil sample had a much greater effect on the first phase of oil reactivity than the differences in fatty acid distributions between the drying oils. The discontinuous nature of oil + litharge samples at higher temperatures seem to indicate that how litharge interacts with the drying oil is become a two-stage process, with a phase of higher reactivity followed by a phase of lower reactivity. Future researchers should keep this in mind as they prepare samples with lead driers at accelerated temperatures. Comparing the rates of growth of

shoulders in the carbonyl band between oil and oil + litharge samples has indicated a more direct link that secondary oxidation products are formed from $\nu(C=O)_{acid,\,conj}$ moieties than has been previously shown.

The temperature response shows increased onset delays with decreasing temperature, but the presence of litharge still plays a role in reducing the overall extent of oxidation present within the oil films. The arresting of the reactivity of the network in the presence of litharge is most likely due to a sol-gel phase transition affecting the ability of reactants for the initial hydrogen abstraction to diffuse through the sample, slowing down the overall kinetics of the oil + litharge samples. After one year of cure, the chemical differences between LO, WO, SaO, and PO have reduced significantly. StO still shows lower levels of oxidation after one year of cure due to the initial pre-polymerization under anoxic conditions that the oil experienced. From the data presented in this chapter, there are indicators that the initial rate of polymerization during the first phase of oil reactivity affects the resulting network topology and possibly the reactivity of the polymer network at longer times of cure.

Chapter 5

Conclusion and Future Work

5.1 Concluding Remarks

Throughout this thesis, the importance of understanding the chemical and mechanical properties of oil films is emphasized, especially as they evolve during polymerization. A review of the state of the field for measuring and monitoring mechanical properties of paint films focuses on both the well established and understood techniques as well as highlighting some more recent techniques which may provide more tools for in-situ monitoring of mechanical properties or changes within a composite paint structure. The quartz crystal microbalance (QCM) is presented as a suitable technique for monitoring mechanical property evolution during the polymerization process of drying oils, covering the physical transition of the liquid oil forming a solid polymer film. A detailed discussion of the governing equations, error analysis, and importance of sample preparation are emphasized. The mechanical response of a bulk oil sample is measured, but can only be followed for the first few days of cure before the film becomes too thick and stiff to measure using the QCM. The use of litharge as a heat-treatment increases the onset of polymerization by a factor of two. During polymerization, the elastic modulus of the oil film increases by 2-3 orders of magnitude during the first 24 hours and then experiences a much slower rate of increase at longer times. Temperature sweeps are performed on oil films during aging to observe the temperature dependent response. To explain the lack of a well defined glass transition temperature, a model of nano-scale heterogeneity is proposed for the oil film. Based on structural differences observed in another well-characterized crosslinked system and some computational modeling of polymer network formation, we hypothesize that the domains of heterogeneity in this polymer film are due to differences in crosslink density. The chemistry of the polymerization reaction is followed for drying oils with different fatty acid distributions using ATR-FTIR. A summary reaction scheme is presented to highlight both the formation of different types of C = C bonds as well as the oxidation products during the first phase of oil reactivity. For oils without a high enough concentration of linolenic acid present, it appears that one reaction pathway to form conjugated trans-cis C = C

bonds is much less favorable. The effect of incorporating a litharge as a drier is shown to have a much greater effect on both the extent of crosslinks formed and the extent of oxidation observed observed in the oil films. The reduced crosslinking and oxidation in the oil + litharge samples at high temperatures would seem to imply that litharge is not able to function as effectively as a through drier when at elevated temperatures. This effect is reduced with a reduction in the temperature at which polymerization takes place, but there is still less evidence of oxidation than in the oil + litharge films. For oil films that aged for a year, the spectra for most drying oils are very similar. However, with the initial differences in the conversions of unsaturated bonds in fatty acid chains to crosslinks, there could still be differences in the network topology to which ATR-FTIR is insensitive.

5.2 Future Directions for Research

While it is important to have an understanding of the evolution of chemical and mechanical properties of drying oils, it is an incomplete representation of an oil paint. Recent research has highlighted how the combination of drying oil and pigment impacts the resulting chemical and rheological properties of the oil paint greatly [149, 156, 182, 190]. It would be useful to incorporate pigments into QCM samples of drying oils and monitor the differences in the mechanical properties of the oil paint system during polymerization. Some previous research has performed measurements of zinc white or titanium white oil films using the QCM [29, 207]. When incorporating pigments into QCM oil samples, it is important to ensure that the particle sizes are fairly small (hundreds of nanometers) and are well distributed within the paint film to ensure the uniform composition assumption is met to calculate the mechanical properties.

For both oil and pigmented systems, the QCM is well suited for further experimental investigation. The open face of the sample allows for environmental exposure, opening up the possibility of exploring the effects of solvent exposure, humidity fluctuations, and further studies investigating the temperature dependent mechanical properties of the oil films [78, 159, 162]. Solvent exposure to perform extractions of the non-crosslinked components of the drying oil films could also be used to understand crosslink density in the oil networks. These measurements would be

especially interesting to perform on oil films with drier present, where there may be variations or diffusion barriers to forming a uniformly crosslinked network. The QCM sample geometry is also easily combined with other techniques (reflectance infrared spectroscopy, headspace gas chromatography-mass spectrometry) to monitor the chemical and mechanical properties simultaneously. With the complexity of polymerization observed in drying oils forming solid films, these combinations could be useful for providing more information about the fundamental material properties of drying oil films.

Time-based ATR-FTIR spectroscopy can also be used to explore the chemical differences that arise from combinations of pigments and driers to the various drying oils measured in this thesis. Similar measurements to those performed in this study could be extended to longer times at elevated temperatures to observe further changes in the carbonyl band or the point in time when the FTIR spectra of the drying oils become very similar. Comparing oil + litharge samples that have been aged for at least one year would also be a useful comparison for understanding if the 'arresting' of the polymer network observed at early times persist. Exploring other types of driers such as through driers (e.g. lead acetate, aluminum), surface driers (e.g. cobalt or manganese driers), or auxillary driers (e.g. zinc or calcium) would provide insights into how each category of drier affected the chemical reactivity of the oil film as well as the onset of polymerization. The strength of pigment/drying oil interactions may also be affected by the fatty acid distribution of the drying oil. A good starting place for investigating these interactions would be the well-characterized ionomer network of oils with zinc white [208–210]. Peak profiles of chemical moeities can also be useful measures of relative concentrations as experimental validation for computational reaction network modeling of drying oil polymerization, especially to longer times than have been previously been achieved [211, 212]. Measuring the changes in mechanical properties of the different drying oils, either during polymerization using the QCM or at different points during aging using oscillatory atomic force microscopy, can provide insights into the overall level of crosslinking that has occurred within the oil network as a result of polymerization.

Understanding more about how the mechanical and chemical properties of drying oil films are influenced by the network topology would be another useful research direction to pursue. This avenue would be challenging, especially with the many reaction pathways that are active dur-

ing polymerization. However, there appears to be some promise in the use of multiple quantum nuclear magnetic resonance (NMR) or network disassembly spectrometry [213]. Multiple quantum NMR can measure the fraction of local network structures present in a sample through the use of a multicomponent function. Network disassembly spectrometry analyzes the degradation products of a chemically labeled polymer network that has been broken down into smaller components. From a computational perspective, modeling of network topology can be pursued through the use of random graph modeling or the use of molecular dynamics [176, 214]. These computational approaches can provide a statistical representation for the network topology of a polymer film, but it would be extremely difficult to create an exact representation of the network formed from a free-radical polymerization.

As more researchers in the field of heritage science consider the material properties of cultural heritage objects, many research questions would benefit from the combined approach of measuring the chemical and mechanical properties of a material. As plastics and synthetic polymers are more commonly found in cultural heritage objects, understanding potential degradation mechanisms and how to slow their progress has become a major challenge. The composite nature of many cultural heritage objects also makes investigating the chemical and mechanical interactions important, especially for exhibition and storage conditions. This more holistic approach to understanding materials used in cultural heritage objects can better inform the decisions surrounding their preservation, effectively extending the lifetime of the object and the knowledge that can be gained from it.

Bibliography

[1] K. T. Faber, F. Casadio, A. Masic, L. Robbiola, M. Walton, Looking Back, Looking Forward: Materials Science in Art, Archaeology, and Art Conservation, Annual Review of Materials Research 51 (1) (2021) 435–460. doi:10.1146/annurev-matsci-080819-013103.

[2] P. Walter, L. de Viguerie, Materials science challenges in paintings, Nature Materials 17 (2) (2018) 106–109. doi:10.1038/nmat5070.

[3] J. D. J. van den Berg, Analytical chemical studies on traditional oil paints, Doctoral, University of Amsterdam (2002).

[4] L. de Viguerie, G. Ducouret, F. Lequeux, T. Moutard-Martin, P. Walter, Historical evolution of oil painting media: A rheological study, Comptes Rendus Physique 10 (7) (2009) 612–621. doi:10.1016/j.crhy.2009.08.006.

[5] H. Wexler, Polymerization of Drying Oils, Chem. Rev. 64 (6) (1964) 591–611. doi:10.1021/cr60232a001.

[6] M. Soucek, T. Khattab, J. Wu, Review of autoxidation and driers, Progress in Organic Coatings 73 (4) (2012) 435–454. doi:10.1016/j.porgcoat.2011.08.021.

[7] Juita, B. Z. Dlugogorski, E. M. Kennedy, J. C. Mackie, Low temperature oxidation of linseed oil: A review, Fire Science Reviews 1 (1) (2012) 3. doi:10.1186/2193-0414-1-3.

[8] K. Schaich, Challenges in Elucidating Lipid Oxidation Mechanisms: When, where, and how do products arise?, in: Lipid Oxidation: Challenges in Food Systems, AOCS Press, 2013, pp. 1–52.

[9] J. Honzíček, Curing of Air-Drying Paints: A Critical Review | Industrial & Engineering Chemistry Research, Ind. Eng. Chem. Res. 58 (28) (2019) 12485–12505.

[10] Y. Orlova, R. E. Harmon, L. J. Broadbelt, P. D. Iedema, Review of the kinetics and simulations of linseed oil autoxidation, Progress in Organic Coatings 151 (2021) 106041. doi:10.1016/j.porgcoat.2020.106041.

[11] N. A. Porter, S. E. Caldwell, K. A. Mills, Mechanisms of free radical oxidation of unsaturated lipids, Lipids 30 (4) (1995) 277–290. doi:10.1007/BF02536034.

[12] R. Leonardi, NUCLEAR PHYSICS and PAINTING: Sub-topic of the wide and fascinating field of SCIENCE and ART, Nuclear Physics A 752 (2005) 659–674. doi:10.1016/j.nuclphysa.2005.02.152.

[13] M. F. Mecklenburg, C. S. Tumosa, D. Erhardt, The Changing Mechanical Properties of Aging Oil Paints, in: P. Vandiver, J. Mass, A. Murray (Eds.), Materials Issues in Art and Archeology VII, Materials Research Society, Warrendale, PA, 2004, pp. 13–24.

[14] G. dePolo, M. Walton, K. Keune, K. R. Shull, After the paint has dried: A review of testing techniques for studying the mechanical properties of artists' paint, Heritage Science 9 (1) (2021) 68. doi:10.1186/s40494-021-00529-w.

[15] D. Erhardt, C. S. Tumosa, M. F. Mecklenburg, Natural and accelerated thermal aging of oil paint films, Studies in Conservation 45 (sup1) (2000) 65–69. doi:10.1179/sic.2000.45.Supplement-1.65.

[16] R. van Gorkum, E. Bouwman, The oxidative drying of alkyd paint catalysed by metal complexes, Coordination Chemistry Reviews 249 (17) (2005) 1709–1728. doi:10.1016/j.ccr.2005.02.002.

[17] S. W. Michalski, Paintings - Their Response to Temperature, Relative Humidity, Shock, and Vibration, in: M. Mecklenburg (Ed.), Art in Transit: Studies in the Transport of Paintings, National Gallery of Art, Washington, D.C., 1991.

[18] A. van Loon, P. Noble, A. Burnstock, Ageing and deterioration of traditional oil and tempera paints, in: Conservation of Easel Paintings, first edition Edition, no. Routledge Series in Conservation and Museology, Routledge, London/New York, 2012, pp. 214–41.

[19] T. Learner, Modern Paints, in: Conservation of Easel Paintings, first edition Edition, Routledge Series in Conservation and Museology, Routledge, London/New York, 2012, pp. 242–251.

[20] E. Hermens, J. H. Townsend, Binding Media in Western easel painting, in: Conservation of Easel Paintings, first edition Edition, Routledge Series in Conservation and Museology, Routledge, London/New York, 2012, pp. 207–213.

[21] A. Rothe, Andrea Mantega's "Adoration of the Magi", in: Historical Painting Techniques, Materials, and Studio Practice, Preprints from the Symposium at the University of Leiden, the Netherlands, The Getty Conservation Institute, 1995, pp. 111–116.

[22] K. Sato, The mechanical properties of filled polymers, Progress in Organic Coatings 4 (4) (1976) 271–302. doi:10.1016/0300-9440(76)80010-0.

[23] D. Y. Perera, Effect of pigmentation on organic coating characteristics, Progress in Organic Coatings 50 (4) (2004) 247–262. doi:10.1016/j.porgcoat.2004.03.002.

[24] L. de Viguerie, L. Beck, J. Salomon, L. Pichon, Ph. Walter, Composition of Renaissance Paint Layers: Simultaneous Particle Induced X-ray Emission and Backscattering Spectrometry, Anal. Chem. 81 (19) (2009) 7960–7966. doi:10.1021/ac901141v.

[25] R. Wiesinger, L. Pagnin, M. Anghelone, L. M. Moretto, E. F. Orsega, M. Schreiner, Pigment and Binder Concentrations in Modern Paint Samples Determined by IR and Raman Spectroscopy, Angewandte Chemie International Edition 57 (25) (2018) 7401–7407. doi:10.1002/anie.201713413.

[26] X. Liu, V. Di Tullio, Y.-C. Lin, V. De Andrade, C. Zhao, C.-H. Lin, M. Wagner, N. Zumbulyadis, C. Dybowski, S. A. Centeno, Y.-c. K. Chen-Wiegart, Nano- to microscale three-dimensional morphology relevant to transport properties in reactive porous composite paint films, Scientific Reports 10 (1) (2020) 18320. doi:10.1038/s41598-020-75040-6.

[27] E. Hagan, M. Charalambides, T. J. S. Learner, A. Murray, C. T. Young, Factors Affecting the Mechanical Properties of Modern Paints, in: Modern Paints Uncovered: Proceedings from the Modern Paints Uncovered Symposium, Getty Conservation Institute, Los Angeles, 2007, pp. 227–235.

[28] J. Salvant Plisson, L. de Viguerie, L. Tahroucht, M. Menu, G. Ducouret, Rheology of white paints: How Van Gogh achieved his famous impasto, Colloids and Surfaces A: Physicochemical and Engineering Aspects 458 (2014) 134–141. doi:10.1016/j.colsurfa.2014.02.055.

[29] L. F. Sturdy, M. S. Wright, A. Yee, F. Casadio, K. T. Faber, K. R. Shull, Effects of zinc oxide filler on the curing and mechanical response of alkyd coatings, Polymer 191 (2020) 122222. doi:10.1016/j.polymer.2020.122222.

[30] E. W. S. Hagan, M. N. Charalambides, C. R. T. Young, T. J. S. Learner, S. Hackney, Viscoelastic properties of latex paint films in tension: Influence of the inorganic phase and surfactants, Progress in Organic Coatings 69 (1) (2010) 73–81. doi:10.1016/j.porgcoat.2010.05.008.

[31] E. W. S. Hagan, M. N. Charalambides, C. R. T. Young, T. J. S. Learner, S. Hackney, Micromechanics models for predicting tensile properties of latex paint films, in: T. Proulx (Ed.), Time Dependent Constitutive Behavior and Fracture/Failure Processes, Volume 3, Conference Proceedings of the Society for Experimental Mechanics Series, Springer, New York, NY, 2011, pp. 297–306. doi:10.1007/978-1-4419-9794-4_41.

[32] S. Keck, Mechanical Alteration of the Paint Film, Studies in Conservation 14 (1) (1969) 9–30.

[33] S. Bucklow, The description of craquelure patterns, Studies in Conservation 42 (3) (1997) 129–140. doi:10.1179/sic.1997.42.3.129.

[34] S. L. Bucklow, A Stylometric Analysis of Craquelure, Computers and the Humanities 31 (1998) 503–521.

[35] S. Bucklow, Classification of Craquelure, in: J. Hill Stoner, R. Rushfield (Eds.), Conservation of Easel Paintings: Principles and Practice, Butterowrth-Heinemann, London/New York, 2012, pp. 285–290.

[36] S. W. Michalski, Crack mechanisms in gilding, in: Gilded Wood: Conservation and History, Sound View Press, Madison, Connecticut, 1991, pp. 171–181.

[37] F. Giorgiutti-Dauphiné, L. Pauchard, Painting cracks: A way to investigate the pictorial matter, Journal of Applied Physics 120 (6) (2016) 065107. doi:10.1063/1.4960438.

[38] L. Pauchard, F. Giorgiutti-Dauphiné, Craquelures and pictorial matter, Journal of Cultural Heritage 46 (2020) 361–373. doi:10.1016/j.culher.2020.08.007.

[39] C. S. Tumosa, J. Millard, D. Erhardt, M. F. Mecklenburg, Effects of solvents on the physical properties of paint films, Preprints, ICOM Committee for Conservation, 12th Triennial Meeting, Lyon 1 (1999) 347–352.

[40] M. F. Mecklenburg, C. S. Tumosa, An Introduction into the Mechanical Behavior of Paintings Under Rapid Loading Conditions, in: Art in Transit: Studies in the Transport of Paintings, National Gallery of Art, Washington D.C., 1991, pp. 137–171.

[41] J. D. Erlebacher, E. Brown, M. F. Mecklenburg, C. S. Tumosa, The Effects of Temperature and Relative Humidity on the Mechanical Properties of Modern Painting Materials, in: Materials Issues in Art and Archaeology III, Vol. 267, Materials Research Society, San Francisco, 1992, pp. 359–370. doi:10.1557/PROC-267-359.

[42] M. F. Mecklenburg, C. S. Tumosa, J. D. Erlebacher, Mechanical Behavior of Artist's Acrylic Paints Under Equilibrium Conditions, in: Division of Polymer Chemistry, Vol. 35, American Chemical Society, Washington, D.C., 1994, pp. 297–298.

[43] P. M. Whitmore, V. G. Colaluca, The Natural and Accelerated Aging of an Acrylic Artists' Medium, Studies in Conservation 40 (1) (1995) 51–64. arXiv:1506611, doi:10.2307/1506611.

[44] M. F. Mecklenburg, C. S. Tumosa, Traditional Oil Paints: The Effects of Long-Term Chemical and Mechanical Properties on Restoration Efforts, MRS Bulletin 26 (01) (2001) 51–54. doi:10.1557/mrs2001.19.

[45] D. J. Carr, C. R. T. Young, A. Phenix, R. D. Hibberd, Development of a Physical Model of a Typical Nineteenth-Century English Canvas Painting, Studies in Conservation 48 (3) (2003) 145–154. doi:10.1179/sic.2003.48.3.145.

[46] G. Mirone, B. Marton, G. Vancso, Elastic modulus profiles in the cross sections of drying alkyd coating films: Modelling and experiments, European Polymer Journal 40 (3) (2004) 549–560. doi:10.1016/j.eurpolymj.2003.10.017.

[47] E. Hagan, A. Murray, Effects of Water Exposure on the Mechanical Properties of Early Artists' Acrylic Paints, in: Materials Issues in Art and Archaeology VII, Vol. 852, Materials Research Society, Boston, 2004, pp. 41–47.

[48] D. Erhardt, C. S. Tumosa, M. F. Mecklenburg, Long-Term Chemical and Physical Processes in Oil Paint Films, Studies in Conservation 50 (2) (2005) 143–150. doi:10.1179/sic.2005.50.2.143.

[49] C. Tumosa, D. Erhardt, M. Mecklenburg, X. Su, Linseed Oil Paint as Ionomer: Synthesis and Characterization, in: Materials Issues in Art and Archaeology VII, Vol. 852, Materials Research Society, Boston, 2005, pp. 25–31.

[50] C. Young, Interfacial Interactions of Modern Paint Layers, in: Modern Paints Uncovered: Proceedings from the Modern Paints Uncovered Symposium, Getty Conservation Institute, Los Angeles, 2007, pp. 247–256.

[51] C. Young, E. Hagan, Cold temperature effects of modern paints used for priming flexible supports, in: Preparation for Painting: The Artists' Choice and Its Consequences, Archetype Publications, London, 2008, pp. 172–179.

[52] O. Fuesers, S. Zumbühl, The Influence of Organic Solvents on the Mechanical Properties of Alkyd and Oil Paint, in: IR, NIR, VIS UV Raman, Jerusalem, Israel, 2008, pp. 1–14.

[53] B. Ormsby, E. Hagan, P. Smithen, T. J. S. Learner, Comparing contemporary titanium white-based acrylic emulsion grounds and paints: Characterisation, properties and conservation, in: Preparation for Painting: The Artists' Choice and Its Consequences, Archetype Publications, London, 2008, pp. 163–171.

[54] L. Fuster-López, M. Mecklenburg, M. Castell-Agusti, V. Guerola-Blay, Filling materials for easel paintings: When the ground reintegration becomes a structural concern, in: Preparation for Painting: The Artists' Choice and Its Consequences, Archetype Publications, London, 2008, pp. 180–186.

[55] L. Carlyle, C. Young, S. Jardine, The mechanical response of flour-paste grounds, in: Preparation for Painting: The Artist's Choice and Its Consequences, Archetype Publications, London, 2008, pp. 123–131.

[56] E. W. S. Hagan, M. N. Charalambides, C. T. Young, T. J. S. Learner, S. Hackney, Tensile properties of latex paint films with TiO2 pigment, Mech Time-Depend Mater 13 (2) (2009) 149–161. doi:10.1007/s11043-009-9076-y.

[57] C. S. Tumosa, M. F. Mecklenburg, Oil Paints: The Chemistry of Drying Oils and the Potential for Solvent Disruption, in: New Insights into the Cleaning of Paintings: Proceedings from the Cleaning 2010 International Conference, Universidad Politecnica de Valencia and Museum Conservation Institute, no. 3 in Smithsonian Contributions to Museum Conservation, Smithsonian Scholarly Press, Washington, D.C., 2013, pp. 51–58.

[58] M. Mecklenburg, C. S. Tumosa, E. Vicenzi, The Influence of Pigments and Ion Migration on the Durability of Drying Oil and Alkyd Paints, in: New Insights into the Cleaning of Paintings: Proceedings from the Cleaning 2010 International Conference, Universidad Politecnica de Valencia and Museum Conservation Institute, no. 3 in Smithsonian Contributions to Museum Conservation, Smithsonian Scholarly Press, Washington, D.C., 2013, pp. 59–67.

[59] M. T. Doménech-Carbó, M. F. Silva, E. Aura-Castro, A. Doménech-Carbó, L. Fuster-López, J. V. Gimeno-Adelantado, S. U. Kröner, M. L. Martínez-Bazán, X. Más-Barberá, M. F. Mecklenburg, L. Osete-Cortina, D. J. Yusá-Marco, Multitechnique Approach to Evaluate Cleaning treatments for Acrylic and Polyvinyl Acetate Paints, in: New Insights into the Cleaning of Paintings: Proceedings from the Cleaning 2010 International Conference, Universidad Politecnica de Valencia and Museum Conservation Institute, no. 3 in Smithsonian Contributions to Museum Conservation, Smithsonian Scholarly Press, Washington, D.C., 2013, pp. 125–134.

[60] E. W. S. Hagan, M. N. Charalambides, C. R. T. Young, T. J. S. Learner, The effects of strain rate and temperature on commercial acrylic artist paints aged one year to decades, Appl. Phys. A 121 (3) (2015) 823–835. doi:10.1007/s00339-015-9423-6.

[61] L. Fuster-López, F. C. Izzo, M. Piovesan, D. J. Yusá-Marco, L. Sperni, E. Zendri, Study of the chemical composition and the mechanical behaviour of 20th century commercial artists' oil

paints containing manganese-based pigments, Microchemical Journal 124 (2016) 962–973. doi:10.1016/j.microc.2015.08.023.

[62] L. Krzemień, M. Łukomski, Ł. Bratasz, R. Kozłowski, M. F. Mecklenburg, Mechanism of craquelure pattern formation on panel paintings, Studies in Conservation 61 (6) (2016) 324–330. doi:10.1080/00393630.2016.1140428.

[63] Ž. Penava, D. Š. Penava, M. Tkalec, Experimental Analysis of the Tensile Properties of Painting Canvas, Autex Research Journal 16 (4) (2016) 182–195. doi:10.1515/aut-2015-0023.

[64] E. W. S. Hagan, Thermo-mechanical properties of white oil and acrylic artist paints, Progress in Organic Coatings 104 (2017) 28–33. doi:10.1016/j.porgcoat.2016.10.019.

[65] L. Fuster-López, M. Mecklenburg, A Look into Some Factors Influencing the Film Forming Properties of Oil Paint Films in Copper Paintings and the Effects of Environment in Their Structural Behavior, in: L. Fuster-López, I. Chulia Blanco, M. F. Sarrio Martin, M. L. Vasquez de Agredos Pascual, L. Carlyle, J. Wadum (Eds.), Paintings on Copper and Other Metal Plates: Production, Degradation, and Conservation Issues, Universidad Politecnica de Valencia, Valencia, 2017, pp. 95–102.

[66] M. Doutre, A. Murray, L. Fuster-López, Effects of Humidity on Gessoes for Easel Paintings, MRS Proc. 1656 (2017) 167–171. doi:10.1557/opl.2014.828.

[67] A. Roche, A. Soldano, The Effect of Changes in Environmental Conditions on the Mechanical Behaviour of Selected Paint Systems, Studies in Conservation 63 (sup1) (2018) 216–221. doi:10.1080/00393630.2018.1504434.

[68] L. Fuster-López, F. C. Izzo, V. Damato, D. J. Yusà-Marco, E. Zendri, An insight into the mechanical properties of selected commercial oil and alkyd paint films containing cobalt blue, Journal of Cultural Heritage 35 (2019) 225–234. doi:10.1016/j.culher.2018.12.007.

[69] A. Bridarolli, A. Nualart-Torroja, A. Chevalier, M. Odlyha, L. Bozec, Systematic mechanical assessment of consolidants for canvas reinforcement under controlled environment, Heritage Science 8 (1) (2020) 52. doi:10.1186/s40494-020-00396-x.

[70] M. F. Mecklenburg, C. C. Institute, S. Institution, National Gallery of Art (U.S.), T. Gallery (Eds.), Art in Transit: Studies in the Transport of Paintings, National Gallery of Art, Washington, 1991.

[71] M. F. Mecklenburg, M. McCormick-Goodhart, C. S. Tumosa, Investigation into the Deterioration of Paintings and Photographs Using Computerized Modeling of Stress Development, Journal of the American Institute for Conservation 33 (2) (1994) 153–170. arXiv:3179424, doi:10.2307/3179424.

[72] S. Zumbuhl, F. Attanasio, N. C. Scherrer, W. Muller, N. Fenners, W. Caseri, Solvent Action on Dispersion Paint Systems and the Influence on the Morphology - Changes and Destruction of the Latex Microstructure, in: Modern Paints Uncovered: Proceedings from the Modern Paints Uncovered Symposium, Getty Conservation Institute, Los Angeles, 2007, pp. 257–268.

[73] D. Rogala, P. DePriest, A. E. Charola, R. Koestler, The Mechanics of Art Materials and Its Future in Heritage Science, no. 10 in Smithsonian Contributions to Museum Conservation, Smithsonian Scholarly Press, Washington D.C., 2019.

[74] C. R. T. Young, R. D. Hibberd, Biaxial Tensile Testing of Paintings on Canvas, Studies in Conservation 44 (2) (1999) 129–141. arXiv:1506725, doi:10.2307/1506725.

[75] C. Young, Measurement of the biaxial properties of nineteenth century canvas primings using electronic speckle pattern interferometry, Optics and Lasers in Engineering 31 (2) (1999) 163–170. doi:10.1016/S0143-8166(99)00007-X.

[76] C. Young, P. Ackroyd, R. Hibberd, S. Gritt, The mechanical behaviour of adhesives and gap fillers for re-joining panel paintings., in: National Gallery Technical Bulletin, Vol. 23, National Gallery Publications, London, 2002, pp. 23–96.

[77] H. F. Brinson, L. C. Brinson, Polymer Engineering Science and Viscoelasticity: An Introduction, 2nd Edition, Springer, New York, 2015.

[78] L. F. Sturdy, A. Yee, F. Casadio, K. R. Shull, Quantitative characterization of alkyd cure kinetics with the quartz crystal microbalance, Polymer 103 (2016) 387–396. doi:10.1016/j.polymer.2016.09.063.

[79] G. Hedley, M. Odlyha, A. Burnstock, J. Tillinghast, C. Husband, A study of the mechanical and surface properties of oil paint films treated with organic solvents and water, Journal of Thermal Analysis 37 (9) (1991) 2067–2088. doi:10.1007/BF01905579.

[80] M. Odlyha, T. Y. A. Chan, O. Pages, Evaluation of relative humidity effects on fabric-supported paintings by dynamic mechanical and dielectric analysis, Thermochimica Acta 263 (1995) 7–21. doi:10.1016/0040-6031(94)02387-4.

[81] G. M. Foster, S. Ritchie, C. Lowe, Controlled temperature and relative humidity dynamic mechanical analysis of paint films, Journal of Thermal Analysis and Calorimetry 73 (1) (2003) 119–126. doi:10.1023/A:1025133508109.

[82] B. Ormsby, T. J. S. Learner, G. M. Foster, J. R. Druzik, M. Schilling, Wet Cleaning Acrylic Emulsion Paint Films: An Evaluation of Physical, Chemical, and Optical Changes, in: Modern Paints Uncovered: Proceedings from the Modern Paints Uncovered Symposium, Getty Conservation Institute, Los Angeles, 2007, pp. 189–200.

[83] B. Ormsby, G. Foster, T. Learner, S. Ritchie, M. Schilling, Improved controlled relative humidity dynamic mechanical analysis of artists' acrylic emulsion paints: Part II. General properties and accelerated ageing, J Therm Anal Calorim 90 (2) (2007) 503–508. doi:10.1007/s10973-006-7725-9.

[84] A. Phenix, Thermal Mechanical Transitions in Artists' Oil Paints and Selected Conservation Materials: A Study by Dynamic Mechanical Analysis (DMA), in: AIC Paintings Specialty Group, 2009, p. 18.

[85] L. Baij, J. J. Hermans, K. Keune, P. D. Iedema, Time-Dependent ATR-FTIR Spectroscopic Studies on Solvent Diffusion and Film Swelling in Oil Paint Model Systems, Macromolecules 51 (18) (2018) 7134–7144. doi:10.1021/acs.macromol.8b00890.

[86] C. K. Andersen, A. Freeman, M. N. Mortensen, V. Beltran, M. Łukomski, A. Phenix, Mechanical and Moisture Sorption Properties of Commercial Artists' Oil Paints by Dynamic Mechanical Thermal Analysis (DMA), Nanoindentation, and Dynamic Vapour Sorption (DVS), in: Conservation of Modern Oil Paintings, Springer, 2019, pp. 403–417.

[87] A. A. Freeman, J. Lee, C. K. Andersen, N. Fujisawa, M. Łukomski, B. Ormsby, A pilot study of solvent-based cleaning of yellow ochre oil paint: Effect on mechanical properties, Heritage Science 9 (1) (2021) 28. doi:10.1186/s40494-021-00501-8.

[88] E. K. Fischer, Rheological properties of commercial paints, Journal of Colloid Science 5 (3) (1950) 271–281. doi:10.1016/0095-8522(50)90030-4.

[89] R. R. Eley, Applied rheology and architectural coating performance, J Coat Technol Res 16 (2) (2019) 263–305. doi:10.1007/s11998-019-00187-5.

[90] K. Groen, Investigation of the Use of the Binding Medium by Rembrandt, Zeitschrift fur Kunsttechnologie und Konservierung 2 (1997) 207–227.

[91] L. de Viguerie, G. Ducouret, M. Cotte, F. Lequeux, P. Walter, New insights on the glaze technique through reconstruction of old glaze medium formulations, Colloids and Surfaces A: Physicochemical and Engineering Aspects 331 (1) (2008) 119–125. doi:10.1016/j.colsurfa.2008.07.037.

[92] S. Tirat, J.-P. Echard, A. Lattuati-Derieux, J.-Y. Le Huerou, S. Serfaty, Reconstructing historical recipes of linseed oil/colophony varnishes: Influence of preparation processes on application properties, Journal of Cultural Heritage 27, Supplement (Wooden Musical Instruments) (2017) S34–S43. doi:10.1016/j.culher.2017.08.001.

[93] L. de Viguerie, M. Jaber, H. Pasco, J. Lalevée, F. Morlet-Savary, G. Ducouret, B. Rigaud, T. Pouget, C. Sanchez, P. Walter, A 19th Century "Ideal" Oil Paint Medium: A Complex Hybrid Organic–Inorganic Gel, Angewandte Chemie International Edition 56 (6) (2017) 1619–1623. doi:10.1002/anie.201611136.

[94] L. de Viguerie, H. Glanville, G. Ducouret, P. Jacquemot, P. A. Dang, P. Walter, Re-interpretation of the Old Masters' practices through optical and rheological investigation: The presence of calcite, Comptes Rendus Physique 19 (7) (2018) 543–552. doi:10.1016/j.crhy.2018.11.003.

[95] A. Blayo, A. Gandini, J.-F. Le Nest, Chemical and rheological characterizations of some vegetable oils derivatives commonly used in printing inks, Industrial Crops and Products 14 (2) (2001) 155–167. doi:10.1016/S0926-6690(01)00079-6.

[96] M. N. Belgacem, A. Blayo, A. Gandini, Organosolv lignin as a filler in inks, varnishes and paints, Industrial Crops and Products 18 (2) (2003) 145–153. doi:10.1016/S0926-6690(03)00042-6.

[97] D. Cimino, O. Chiantore, E. R. de La Rie, C. W. McGlinchey, R. Ploeger, T. Poli, J. A. Poulis, Binary mixtures of ethylene containing copolymers and low molecular weight resins: A new approach towards specifically tuned art conservation products, International Journal of Adhesion and Adhesives 67 (2016) 54–62. doi:10.1016/j.ijadhadh.2015.12.026.

[98] K. A. Marx, Quartz Crystal Microbalance: A Useful Tool for Studying Thin Polymer Films and Complex Biomolecular Systems at the Solution-Surface Interface, Biomacromolecules 4 (5) (2003) 1099–1120. doi:10.1021/bm020116i.

[99] D. Johannsmann, Viscoelastic, mechanical, and dielectric measurements on complex samples with the quartz crystal microbalance, Physical Chemistry Chemical Physics 10 (31) (2008) 4516. doi:10.1039/b803960g.

[100] D. Johannsmann, The Quartz Crystal Microbalance in Soft Matter Research, Soft and Biological Matter, Springer International Publishing, Cham, 2015. doi:10.1007/978-3-319-07836-6.

[101] K. R. Shull, M. Taghon, Q. Wang, Investigations of the high-frequency dynamic properties of polymeric systems with quartz crystal resonators, Biointerphases QCM2020 (1) (2020) 021012. doi:10.1116/1.5142762@bip.2020.QCM2020.issue-1.

[102] G. E. dePolo, E. Schafer, K. Sadman, J. Rivnay, K. R. Shull, Sample Preparation in Quartz Crystal Microbalance Measurements of Protein Adsorption and Polymer Mechanics, JoVE (Journal of Visualized Experiments) (155) (2020) e60584. doi:10.3791/60584.

[103] L. Sturdy, F. Casadio, M. Kokkori, K. Muir, K. R. Shull, Quartz crystal rheometry: A quantitative technique for studying curing and aging in artists' paints, Polymer Degradation and Stability 107 (2014) 348–355. doi:10.1016/j.polymdegradstab.2014.02.009.

[104] W. Oliver, G. Pharr, An improved technique for determining hardness and elastic modulus using load and displacement sensing indentation experiments, Journal of Materials Research 7 (06) (1992) 1564–1583. doi:10.1557/JMR.1992.1564.

[105] M. L. Oyen, R. F. Cook, A practical guide for analysis of nanoindentation data, Journal of the Mechanical Behavior of Biomedical Materials 2 (4) (2009) 396–407. doi:10.1016/j.jmbbm.2008.10.002.

[106] O. Chiantore, D. Scalarone, The Macro- and Microassessment of Physical and Aging Properties in Modern Paints, in: Modern Paints Uncovered: Proceedings from the Modern Paints Uncovered Symposium, Getty Conservation Institute, Los Angeles, 2007, pp. 96–104.

[107] J. Salvant, E. Barthel, M. Menu, Nanoindentation and the micromechanics of Van Gogh oil paints, Appl. Phys. A 104 (2) (2011) 509–515. doi:10.1007/s00339-011-6486-x.

[108] C. K. Andersen, A. Freeman, M. N. Mortensen, V. Beltran, M. Łukomski, A. Phenix, Mechanical and Moisture Sorption Properties of Commercial Artists' Oil Paint by Dynamic Mechanical Thermal Analysis (DMA), Nanoindentation, and Dynamic Vapour Sorption (DVS), in: K. J. van den Berg, I. Bonaduce, A. Burnstock, B. Ormsby, M. Scharff, L. Carlyle,

G. Heydenreich, K. Keune (Eds.), Conservation of Modern Oil Paintings, Springer International Publishing, Cham, 2019, pp. 403–418. doi:10.1007/978-3-030-19254-9_32.

[109] N. Fujisawa, M. Łukomski, Nanoindentation near the edge of a viscoelastic solid with a rough surface, Materials & Design 184 (2019) 108174. doi:10.1016/j.matdes.2019.108174.

[110] A. Freeman, M. Łukomski, V. Beltran, Mechanical characterization of a cross-sectional TiO2 acrylic-based paint by nano-indentation, Journal of the American Institute for Conservation 59 (1) (2020) 27–39. arXiv:https://doi.org/10.1080/01971360.2019.1603062, doi:10.1080/01971360.2019.1603062.

[111] M. Tiennot, E. Paardekam, D. Iannuzzi, E. Hermens, Mapping the mechanical properties of paintings via nanoindentation: A new approach for cultural heritage studies, Scientific Reports 10 (1) (2020) 7924. doi:10.1038/s41598-020-64892-7.

[112] M. Chyasnavichyus, S. L. Young, V. V. Tsukruk, Probing of Polymer Surfaces in the Viscoelastic Regime, Langmuir 30 (35) (2014) 10566–10582. doi:10.1021/la404925h.

[113] P. V. Kolluru, M. D. Eaton, D. W. Collinson, X. Cheng, D. E. Delgado, K. R. Shull, L. C. Brinson, AFM-based Dynamic Scanning Indentation (DSI) Method for Fast, High-resolution Spatial Mapping of Local Viscoelastic Properties in Soft Materials, Macromolecules 51 (21) (2018) 8964–8978. doi:10.1021/acs.macromol.8b01426.

[114] D. W. Collinson, M. D. Eaton, K. R. Shull, L. C. Brinson, Deconvolution of Stress Interaction Effects from Atomic Force Spectroscopy Data across Polymer-Particle Interfaces, Macromoleculesdoi:10.1021/acs.macromol.9b01378.

[115] P. Klausmeyer, M. Cushman, I. Dobrev, M. Khaleghi, E. J. Harrington, X. Chen, C. Furlong, Quantifying and Mapping Induced Strain in Canvas Paintings Uising Laser Shearography, in: The Noninvasive Analysis of Painted Surfaces: Scientific Impact and Conservation Practice, no. 5 in Smithsonian Contributions to Museum Conservation, Smithsonian Scholarly Press, Washington D.C., 2016, pp. 1–13.

[116] M. K. Kalms, W. Osten, W. P. O. Jueptner, Advanced shearographic system for nondestructive testing of industrial and artwork components, in: S. Deng, T. Okada, K. Behler, X. Wang (Eds.), Photonics Asia 2002, Shanghai, China, 2002, p. 34. doi:10.1117/12.482923.

[117] M. K. Kalms, W. P. O. Jueptner, A Mobile Shearography System for Non-Destructive Testing of Industrial and Artwork Components, Key Energy Materials 295–296 (2005) 165–170. doi:10.4028/www.scientific.net/KEM.295-296.165.

[118] R. M. Groves, W. Osten, M. Doulgeridis, E. Kouloumpi, T. Green, S. Hackney, V. Tornari, Shearography as part of a multi-functional sensor for the detection of signature features in movable cultural heritaged, in: C. Fotakis, L. Pezzati, R. Salimbeni (Eds.), Optical Metrology, Munich, Germany, 2007, p. 661810. doi:10.1117/12.727497.

[119] R. M. Groves, A. Li, X. Liu, S. Hackney, X. Peng, W. Osten, 2.5D virtual reality visualisation of shearography strain data from a canvas painting, in: L. Pezzati, R. Salimbeni (Eds.), SPIE Europe Optical Metrology, Munich, Germany, 2009, p. 739109. doi:10.1117/12.827519.

[120] R. M. Groves, B. Pradarutti, E. Kouloumpi, W. Osten, G. Notni, 2D and 3D non-destructive evaluation of a wooden panel painting using shearography and terahertz imaging, NDT & E International 42 (6) (2009) 543–549. doi:10.1016/j.ndteint.2009.04.002.

[121] M. Morawitz, N. Hein, I. Alexeenko, M. Wilke, G. Pedrini, C. Krekel, W. Osten, Optical Methods for the Assessment of Transport and Age Induced Defects of Artwork, in: W. Osten (Ed.), Fringe 2013, Springer, Berlin, Heidelberg, 2014, pp. 951–955. doi:10.1007/978-3-642-36359-7_180.

[122] M. K. Meybodi, I. Dobrev, P. Klausmeyer, E. J. Harrington, C. Furlong, Investigation of thermomechanical effects of lighting conditions on canvas paintings by laser shearography, in: C. Furlong, C. Gorecki, E. L. Novak (Eds.), SPIE Optical Engineering + Applications, San Diego, California, USA, 2012, p. 84940A. doi:10.1117/12.958089.

[123] D. Buchta, C. Heinemann, G. Pedrini, C. Krekel, W. Osten, Combination of FEM simulations and shearography for defect detection on artwork, Strain 54 (3) (2018) e12269. doi:10.1111/str.12269.

[124] S. Tantideeravit, M. N. Charalambides, D. S. Balint, C. R. T. Young, Prediction of delamination in multilayer artist paints under low amplitude fatigue loading, Engineering Fracture Mechanics 112–113 (2013) 41–57. doi:10.1016/j.engfracmech.2013.09.011.

[125] Ł. Bratasz, K. G. Akoglu, P. Kékicheff, Fracture saturation in paintings makes them less vulnerable to environmental variations in museums, Heritage Science 8 (1) (2020) 11. doi:10.1186/s40494-020-0352-0.

[126] M. Mecklenburg, C. Tumosa, M. McCormick-Goodhardt, A general method for determining the mechanical properties needed for the computer analysis of polymeric structures subjected to changes in temperature and relative humidity, in: Materials Research Society Symposium, Vol. 267, Materials Research Society, San Francisco, CA, 1992, pp. 337–358.

[127] P. G. Chiriboga Arroyo, Finite Element Modeling of Vibrations in Canvas Paintings, Doctoral, Technische Universiteit Delft, Delft, Netherlands (2013).

[128] Ł. Bratasz, M. R. V. Sereshk, Crack Saturation as a Mechanism of Acclimatization of Panel Paintings to Unstable Environments, Studies in Conservation 63 (sup1) (2018) 22–27. doi:10.1080/00393630.2018.1504433.

[129] G. J. A. M. Eumelen, E. Bosco, A. S. J. Suiker, A. van Loon, P. D. Iedema, A computational model for chemo-mechanical degradation of historical oil paintings due to metal soap formation, Journal of the Mechanics and Physics of Solids 132 (2019) 103683. doi:10.1016/j.jmps.2019.103683.

[130] E. Bosco, A. S. J. Suiker, N. A. Fleck, Crack channelling mechanisms in brittle coating systems under moisture or temperature gradients, Int J Fract 225 (1) (2020) 1–30. doi:10.1007/s10704-020-00461-3.

[131] E. Bosco, A. S. J. Suiker, N. A. Fleck, Moisture-induced cracking in a flexural bilayer with application to historical paintings, Theoretical and Applied Fracture Mechanics 112 (2021) 102779. doi:10.1016/j.tafmec.2020.102779.

[132] A. P. Johnson, W. Robert Hannen, F. Zuccari, Vibration Control During Museum Construction Projects, Journal of the American Institute for Conservation 52 (1) (2013) 30–47. doi:10.1179/0197136012Z.0000000003.

[133] W. Wei, L. Sauvage, J. Wölk, Baseline limits for allowable vibrations for objects, in: Preventive Conservation, Vol. 1516, International Council of Museums, Paris, 2014, p. 7.

[134] L. Sauvage, W. B. Wei, M. Martinez, When Conservation Meets Engineering: Predicting the Damaging Effects of Vibrations on Pastel Paintings, Studies in Conservation 63 (sup1) (2018) 418–420. doi:10.1080/00393630.2018.1504444.

[135] L. Sauvage, H. Stratis, L. Harrison, Pastel Roundtable, Journal of Paper Conservation 19 (1) (2018) 33–35. doi:10.1080/18680860.2019.1580005.

[136] L. Baij, J. Hermans, B. Ormsby, P. Noble, P. Iedema, K. Keune, A review of solvent action on oil paint, Heritage Science 8 (1) (2020) 43. doi:10.1186/s40494-020-00388-x.

[137] N. A. Udell, R. E. Hodgkins, B. H. Berrie, T. Meldrum, Physical and chemical properties of traditional and water-mixable oil paints assessed using single-sided NMR, Microchemical Journal 133 (2017) 31–36. doi:10.1016/j.microc.2017.03.013.

[138] M. Rooney, Effect Of Pigment Volume Concentration On Physical And Chemical Properties Of Acrylic Emulsion Paints Assessed Using Single-Sided Nmr, Master of Science, College of William and Mary, Virginia (May 2018).

[139] F. Busse, C. Rehorn, M. Küppers, N. Ruiz, H. Stege, B. Blümich, NMR relaxometry of oil paint binders, Magnetic Resonance in Chemistry 58 (9) (2020) 830–839. doi:10.1002/mrc.5020.

[140] M. Rooney, T. Meldrum, Effect of pigment concentration on NMR relaxometry in acrylic paints, Magnetic Resonance in Chemistry 58 (9) (2020) 880–888. doi:10.1002/mrc.5053.

[141] G. R. Fife, B. Stabik, A. E. Kelley, J. N. King, B. Blümich, R. Hoppenbrouwers, T. Meldrum, Characterization of aging and solvent treatments of painted surfaces using single-sided NMR, Magnetic Resonance in Chemistry 53 (1) (2015) 58–63. doi:10.1002/mrc.4164.

[142] S. Prati, G. Sciutto, F. Volpi, C. Rehorn, R. Vurro, B. Blümich, L. Mazzocchetti, L. Giorgini, C. Samorì, P. Galletti, E. Tagliavini, R. Mazzeo, Cleaning oil paintings: NMR relaxometry and SPME to evaluate the effects of green solvents and innovative green gels, New J. Chem. 43 (21) (2019) 8229–8238. doi:10.1039/C9NJ00186G.

[143] K. Shull, Future Trends in Studies of the Mechanics of Artists' Paints, in: The Mechanics of Art Materials and Its Future in Heritage Science, no. 10 in Smithsonian Contributions to Museum Conservation, Smithsonian Scholarly Press, Washington D.C., 2019, pp. 87–92.

[144] R. Rahul, R. Kitey, Effect of cross-linking on dynamic mechanical and fracture behavior of epoxy variants, Composites Part B: Engineering 85 (2016) 336–342. doi:10.1016/j.compositesb.2015.09.017.

[145] D. Wang, J. Klein, E. Mejía, Catalytic Systems for the Cross-Linking of Organosilicon Polymers, Chemistry – An Asian Journal 12 (11) (2017) 1180–1197. doi:10.1002/asia.201700304.

[146] C. J. Yeh, M. Hu, K. R. Shull, Oxygen Inhibition of Radical Polymerizations Investigated with the Rheometric Quartz Crystal Microbalance, Macromolecules 51 (15) (2018) 5511–5518. doi:10.1021/acs.macromol.8b00720.

[147] J. Chen, E. S. Garcia, S. C. Zimmerman, Intramolecularly Cross-Linked Polymers: From Structure to Function with Applications as Artificial Antibodies and Artificial Enzymes, Acc. Chem. Res. 53 (6) (2020) 1244–1256. doi:10.1021/acs.accounts.0c00178.

[148] I. Bonaduce, L. Carlyle, M. P. Colombini, C. Duce, C. Ferrari, E. Ribechini, P. Selleri, M. R. Tiné, New Insights into the Ageing of Linseed Oil Paint Binder: A Qualitative and Quantitative Analytical Study, PLoS ONE 7 (11) (2012) e49333. doi:10.1371/journal.pone.0049333.

[149] F. Nardelli, F. Martini, J. Lee, A. Lluvears-Tenorio, J. La Nasa, C. Duce, B. Ormsby, M. Geppi, I. Bonaduce, The stability of paintings and the molecular structure of the oil paint polymeric network, Sci Rep 11 (1) (2021) 14202. doi:10.1038/s41598-021-93268-8.

[150] S. Pizzimenti, L. Bernazzani, M. R. Tinè, V. Treil, C. Duce, I. Bonaduce, Oxidation and Cross-Linking in the Curing of Air-Drying Artists' Oil Paints, ACS Appl. Polym. Mater. 3 (4) (2021) 1912–1922. doi:10.1021/acsapm.0c01441.

[151] M. Lazzari, O. Chiantore, Drying and oxidative degradation of linseed oil, Polymer Degradation and Stability 65 (2) (1999) 303–313. doi:10.1016/S0141-3910(99)00020-8.

[152] P. Vandenabeele, B. Wehling, L. Moens, H. Edwards, M. De Reu, G. Van Hooydonk, Analysis with micro-Raman spectroscopy of natural organic binding media and varnishes used in art, Analytica Chimica Acta 407 (1-2) (2000) 261–274. doi:10.1016/S0003-2670(99)00827-2.

[153] J. D. van den Berg, N. D. Vermist, L. Carlyle, M. Holčapek, J. J. Boon, Effects of traditional processing methods of linseed oil on the composition of its triacylglycerols, Journal of Separation Science 27 (3) (2004) 181–199. doi:10.1002/jssc.200301610.

[154] L. de Viguerie, P. A. Payard, E. Portero, Ph. Walter, M. Cotte, The drying of linseed oil investigated by Fourier transform infrared spectroscopy: Historical recipes and influence of lead compounds, Progress in Organic Coatings 93 (2016) 46–60. doi:10.1016/j.porgcoat.2015.12.010.

[155] L. Laporte, G. Ducouret, F. Gobeaux, A. Lesaine, C. Hotton, T. Bizien, L. Michot, L. de Viguerie, Rheo-SAXS characterization of lead-treated oils: Understanding the influence of lead driers on artistic oil paint's flow properties, Journal of Colloid and Interface Science 633 (2023) 566–574. doi:10.1016/j.jcis.2022.11.089.

[156] O. Ranquet, C. Duce, E. Bramanti, P. Dietemann, I. Bonaduce, N. Willenbacher, A holistic view on the role of egg yolk in Old Masters' oil paints, Nat Commun 14 (1) (2023) 1534. doi:10.1038/s41467-023-36859-5.

[157] A. Phenix, Thermal Mechanical Transitions in Artists' Oil Paints and Selected Conservation Materials: A Study by Dynamic Mechanical Analysis (DMA), in: The AIC Paintings Specialty Group, Vol. 22, American Institute for Conservation and Historic Works, Los Angeles, 2009, pp. 72–89.

[158] G. C. DeNolf, L. F. Sturdy, K. R. Shull, High-Frequency Rheological Characterization of Homogeneous Polymer Films with the Quartz Crystal Microbalance, Langmuir 30 (32) (2014) 9731–9740. doi:10.1021/la502090a.

[159] M. D. Eaton, D. Domene-López, Q. Wang, M. G. Montalbán, I. Martin-Gullon, K. R. Shull, Exploring the effect of humidity on thermoplastic starch films using the quartz crystal microbalance, Carbohydrate Polymers 261 (2021) 117727. doi:10.1016/j.carbpol.2021.117727.

[160] Y. Chen, K. R. Shull, Controlling the properties of thermoplastic starch films with hydrogen bonding plasticizers, Carbohydrate Polymer Technologies and Applications 5 (2023) 100291. doi:10.1016/j.carpta.2023.100291.

[161] E. J. Martin, M. T. Mathew, K. R. Shull, Viscoelastic Properties of Electrochemically Deposited Protein/Metal Complexes, Langmuir 31 (13) (2015) 4008–4017. doi:10.1021/acs.langmuir.5b00169.

[162] K. Sadman, Q. Wang, Y. Chen, B. Keshavarz, Z. Jiang, K. R. Shull, Influence of Hydrophobicity on Polyelectrolyte Complexation, Macromolecules 50 (23) (2017) 9417–9426. doi:10.1021/acs.macromol.7b02031.

[163] K. Sadman, C. G. Wiener, R. A. Weiss, C. C. White, K. R. Shull, B. D. Vogt, Quantitative Rheometry of Thin Soft Materials Using the Quartz Crystal Microbalance with Dissipation, Analytical Chemistry 90 (6) (2018) 4079–4088. doi:10.1021/acs.analchem.7b05423.

[164] D. E. Delgado, L. F. Sturdy, C. W. Burkhart, K. R. Shull, Validation of quartz crystal rheometry in the megahertz frequency regime, Journal of Polymer Science Part B: Polymer Physics 57 (18) (2019) 1246–1254. doi:10.1002/polb.24812.

[165] C. R. Bilchak, Y. Huang, B. C. Benicewicz, C. J. Durning, S. K. Kumar, High-Frequency Mechanical Behavior of Pure Polymer-Grafted Nanoparticle Constructs, ACS Macro Lett. 8 (3) (2019) 294–298. doi:10.1021/acsmacrolett.8b00981.

[166] L. F. Sturdy, M. S. Wright, A. Yee, F. Casadio, K. T. Faber, K. R. Shull, Effects of zinc oxide filler on the curing and mechanical response of alkyd coatings, Polymer 191 (2020) 122222. doi:10.1016/j.polymer.2020.122222.

[167] K. Sadman, Q. Wang, S. H. Chen, D. E. Delgado, K. R. Shull, pH-Controlled Electrochemical Deposition of Polyelectrolyte Complex Films, Langmuir 33 (8) (2017) 1834–1844. doi:10.1021/acs.langmuir.6b04491.

[168] P. J. Cumpson, M. P. Seah, The quartz crystal microbalance; radial/polar dependence of mass sensitivity both on and off the electrodes, Meas. Sci. Technol. 1 (7) (1990) 544. doi:10.1088/0957-0233/1/7/002.

[169] Q. Wang, M. Yang, Shullgroup/rheoQCM (2019).

[170] L. Carlyle, The Artist's Assistant: Oil Painting Instruction Manuals and Handbooks in Britain 1800-1900, with Reference to Selected Eighteenth-century Sources, Archetype Publication, London, 2001.

[171] M. Cotte, E. Checroun, J. Susini, P. Dumas, P. Tchoreloff, M. Besnard, Ph. Walter, Kinetics of oil saponification by lead salts in ancient preparations of pharmaceutical lead plasters and painting lead mediums, Talanta 70 (5) (2006) 1136–1142. doi:10.1016/j.talanta.2006.03.007.

[172] I. Kneepkens, Understanding historical recipes for the modification of linseed oil, Master of Arts, University of Amsterdam, Amsterdam (2012).

[173] R. Stull, Wet-Bulb Temperature from Relative Humidity and Air Temperature, Journal of Applied Meteorology and Climatology 50 (11) (2011) 2267–2269. doi:10.1175/JAMC-D-11-0143.1.

[174] K. A. Masser, D. B. Knorr, M. D. Hindenlang, J. H. Yu, A. D. Richardson, K. E. Strawhecker, F. L. Beyer, J. L. Lenhart, Relating structure and chain dynamics to ballistic performance in transparent epoxy networks exhibiting nanometer scale heterogeneity, Polymer 58 (2015) 96–106. doi:10.1016/j.polymer.2014.12.027.

[175] C. Duce, L. Bernazzani, E. Bramanti, A. Spepi, M. P. Colombini, M. R. Tiné, Alkyd artists' paints: Do pigments affect the stability of the resin? A TG and DSC study on fast-drying oil colours, Polymer Degradation and Stability 105 (2014) 48–58. doi:10.1016/j.polymdegradstab.2014.03.035.

[176] I. Kryven, J. Duivenvoorden, J. Hermans, P. D. Iedema, Random Graph Approach to Multifunctional Molecular Networks, Macromol. Theory Simul. 25 (5) (2016) 449–465. doi:10.1002/mats.201600052.

[177] M. D. Soucek, T. Khattab, J. Wu, Review of autoxidation and driers, Progress in Organic Coatings 73 (4) (2012) 435–454. doi:10.1016/j.porgcoat.2011.08.021.

[178] J. Mallégol, J.-L. Gardette, J. Lemaire, Long-term behavior of oil-based varnishes and paints I. Spectroscopic analysis of curing drying oils, J Amer Oil Chem Soc 76 (8) (1999) 967–976. doi:10.1007/s11746-999-0114-3.

[179] J. Mallégol, J.-L. Gardette, J. Lemaire, Long-term behavior of oil-based varnishes and paints. Photo- and thermooxidation of cured linseed oil, J Amer Oil Chem Soc 77 (3) (2000) 257–263. doi:10.1007/s11746-000-0042-4.

[180] J. Mallégol, J. Lemaire, J.-L. Gardette, Drier influence on the curing of linseed oil, Progress in Organic Coatings 39 (2) (2000) 107–113. doi:10.1016/S0300-9440(00)00126-0.

[181] I. Bonaduce, L. Carlyle, M. P. Colombini, C. Duce, C. Ferrari, E. Ribechini, P. Selleri, M. R. Tiné, A multi-analytical approach to studying binding media in oil paintings: Characterisation of differently pre-treated linseed oil by DE-MS, TG and GC/MS, J Therm Anal Calorim 107 (3) (2012) 1055–1066. doi:10.1007/s10973-011-1586-6.

[182] S. Pizzimenti, L. Bernazzani, M. R. Tinè, V. Treil, C. Duce, I. Bonaduce, Oxidation and Cross-Linking in the Curing of Air-Drying Artists' Oil Paints, ACS Appl. Polym. Mater. 3 (4) (2021) 1912–1922. doi:10.1021/acsapm.0c01441.

[183] R. J. Meilunas, J. G. Bentsen, A. Steinberg, Analysis of Aged Paint Binders by FTIR Spectroscopy, Studies in Conservation 35 (1) (1990) 33–51. arXiv:1506280, doi:10.2307/1506280.

[184] W. J. Muizebelt, J. C. Hubert, R. A. M. Venderbosch, Mechanistic study of drying of alkyd resins using ethyl linoleate as a model substance, Progress in Organic Coatings 24 (1) (1994) 263–279. doi:10.1016/0033-0655(94)85019-4.

[185] J. Mallégol, J.-L. Gardette, J. Lemaire, Long-term behavior of oil-based varnishes and paints. Fate of hydroperoxides in drying oils, J Amer Oil Chem Soc 77 (3) (2000) 249–255. doi:10.1007/s11746-000-0041-5.

[186] J. Mallégol, L. Gonon, J. Lemaire, J. L. Gardette, Long-term behaviour of oil-based varnishes and paints 4. Influence of film thickness on the photooxidation, Polymer Degradation and Stability 72 (2) (2001) 191–197. doi:10.1016/S0141-3910(00)00170-1.

[187] E. Rudnik, A. Szczucinska, H. Gwardiak, A. Szulc, A. Winiarska, Comparative studies of oxidative stability of linseed oil, Thermochimica Acta 370 (1) (2001) 135–140. doi:10.1016/S0040-6031(00)00781-4.

[188] C. Stenberg, M. Svensson, M. Johansson, A study of the drying of linseed oils with different fatty acid patterns using RTIR-spectroscopy and chemiluminescence (CL), Industrial Crops and Products 21 (2) (2005) 263–272. doi:10.1016/j.indcrop.2004.04.002.

[189] Z. O. Oyman, W. Ming, R. van der Linde, Oxidation of drying oils containing non-conjugated and conjugated double bonds catalyzed by a cobalt catalyst, Progress in Organic Coatings 54 (3) (2005) 198–204. doi:10.1016/j.porgcoat.2005.06.004.

[190] S. Pizzimenti, L. Bernazzani, M. R. Tinè, C. Duce, I. Bonaduce, Unravelling the effect of carbon black in the autoxidation mechanism of polyunsaturated oils, J Therm Anal Calorimdoi:10.1007/s10973-021-11165-8.

[191] C. Douny, R. Razanakolona, L. Ribonnet, J. Milet, V. Baeten, H. Rogez, M.-L. Scippo, Y. Larondelle, Linseed oil presents different patterns of oxidation in real-time and accelerated aging assays, Food Chemistry 208 (2016) 111–115. doi:10.1016/j.foodchem.2016.04.010.

[192] B. M. Berto, R. K. A. Garcia, G. D. Fernandes, D. Barrera-Arellano, G. G. Pereira, Linseed oil: Characterization and study of its oxidative degradation, Grasas y Aceites 71 (1) (2020) e337–e337. doi:10.3989/gya.1059182.

[193] A. C. M. Silva, M. C. da Silva, P. K. Rohatgi, R. A. Renzetti, Cobalt (II) used as a catalyst to drying properties of healing agents for self-healing coatings / Cobalto (II) utilizado como catalisador de propriedades de secagem de agentes de cura para revestimentos auto-regenerativos, Brazilian Journal of Development 8 (2) (2022) 9723–9740. doi:10.34117/bjdv8n2-085.

[194] F. Nardelli, F. Martini, J. Lee, A. Lluvears-Tenorio, J. La Nasa, C. Duce, B. Ormsby, M. Geppi, I. Bonaduce, The stability of paintings and the molecular structure of the oil paint polymeric network, Sci Rep 11 (1) (2021) 14202. doi:10.1038/s41598-021-93268-8.

[195] L. Vannoni, S. Pizzimenti, G. Caroti, J. La Nasa, C. Duce, I. Bonaduce, Disclosing the chemistry of oil curing by mass spectrometry using methyl linoleate as a model binder, Microchemical Journal 173 (2022) 107012. doi:10.1016/j.microc.2021.107012.

[196] S. Švarcová, E. Kočí, P. Bezdička, S. Garrappa, L. Kobera, J. Plocek, J. Brus, M. Šťastný, D. Hradil, Uncovering lead formate crystallization in oil-based paintings, Dalton Transactions 49 (16) (2020) 5044–5054. doi:10.1039/D0DT00327A.

[197] F. D. Lorenzo, S. Seiffert, Nanostructural heterogeneity in polymer networks and gels, Polym. Chem. 6 (31) (2015) 5515–5528. doi:10.1039/C4PY01677G.

[198] E. G. Bobalek, E. R. Moore, S. S. Levy, C. C. Lee, Some implications of the gel point concept to the chemistry of alkyd resins, J. Appl. Polym. Sci. 8 (2) (1964) 625–657. doi:10.1002/app.1964.070080207.

[199] G. V. Korolev, M. M. Mogilevich, Three-Dimensional Free-Radical Polymerization: Cross-Linked and Hyper-Branched Polymers, Vol. 131, Springer, 2009.

[200] I. Kryven, P. D. Iedema, Topology Evolution in Polymer Modification, Macromol. Theory Simul. 23 (1) (2014) 7–14. doi:10.1002/mats.201300121.

[201] A. A. Al-Saadi, J. Laane, Vibrational Spectra, Ab Initio Calculations, and Ring-Puckering Potential Energy Function for γ-Crotonolactone, J. Phys. Chem. A 111 (17) (2007) 3302–3305. doi:10.1021/jp0686011.

[202] E. Frankel, Lipid Oxidation, Progress in Lipid Research 19 (1-2) (1980) 1–22. doi:10.1016/0163-7827(80)90006-5.

[203] I. Bonaduce, C. Duce, A. Lluveras-Tenorio, J. Lee, B. Ormsby, A. Burnstock, K. J. van den Berg, Conservation Issues of Modern Oil Paintings: A Molecular Model on Paint Curing, Acc. Chem. Res. (2019) acs.accounts.9b00296doi:10.1021/acs.accounts.9b00296.

[204] O. Zovi, L. Lecamp, C. Loutelier-Bourhis, C. M. Lange, C. Bunel, Stand reaction of linseed oil, European Journal of Lipid Science and Technology 113 (5) (2011) 616–626. doi:10.1002/ejlt.201000414.

[205] S. T. Warzeska, M. Zonneveld, R. van Gorkum, W. J. Muizebelt, E. Bouwman, J. Reedijk, The influence of bipyridine on the drying of alkyd paints: A model study, Progress in Organic Coatings 44 (3) (2002) 243–248. doi:10.1016/S0300-9440(02)00057-7.

[206] C. S. Tumosa, M. F. Mecklenburg, The influence of lead ions on the drying of oils, Studies in Conservation 50 (sup1) (2005) 39–47. doi:10.1179/sic.2005.50.Supplement-1.39.

[207] T. Schmitt, A Multi-Modal Investigation into Titanium Dioxide Degradation of Oil Paints: Shedding Light on the Effect of Environmental Factors, Ph.D. thesis, Northwestern University, United States – Illinois (2022).

[208] J. J. Hermans, K. Keune, A. van Loon, R. W. Corkery, P. D. Iedema, Ionomer-like structure in mature oil paint binding media, RSC Adv. 6 (96) (2016) 93363–93369. doi:10.1039/C6RA18267D.

[209] J. J. Hermans, L. Baij, M. Koenis, K. Keune, P. D. Iedema, S. Woutersen, 2D-IR spectroscopy for oil paint conservation: Elucidating the water-sensitive structure of zinc carboxylate clusters in ionomers, Science Advances 5 (6) (2019) eaaw3592. doi:10.1126/sciadv.aaw3592.

[210] J. Hermans, K. Helwig, S. Woutersen, K. Keune, Traces of water catalyze zinc soap crystallization in solvent-exposed oil paint, Phys. Chem. Chem. Phys.doi:10.1039/D2CP04861B.

[211] Y. Orlova, I. Kryven, P. D. Iedema, Automated reaction generation for polymer networks, Computers & Chemical Engineering 112 (2018) 37–47. doi:10.1016/j.compchemeng.2018.01.022.

[212] Y. Orlova, A. A. Gambardella, R. E. Harmon, I. Kryven, P. D. Iedema, Finite representation of reaction kinetics in unbounded biopolymer structures, Chemical Engineering Journal 405 (2021) 126485. doi:10.1016/j.cej.2020.126485.

[213] Y. Gu, J. Zhao, J. A. Johnson, A (Macro)Molecular-Level Understanding of Polymer Network Topology, Trends in Chemistry 1 (3) (2019) 318–334. doi:10.1016/j.trechm.2019.02.017.

[214] A. A. Rudov, I. V. Portnov, A. R. Bogdanova, I. I. Potemkin, Structure of swollen hollow polyelectrolyte nanogels with inhomogeneous cross-link distribution, Journal of Colloid and Interface Science 640 (2023) 1015–1028. doi:10.1016/j.jcis.2023.02.090.

[215] A. J. Dijkstra, Vegetable Oils: Composition and Analysis, in: B. Caballero, P. M. Finglas, F. Toldrá (Eds.), Encyclopedia of Food and Health, Academic Press, Oxford, 2016, pp. 357–364. doi:10.1016/B978-0-12-384947-2.00708-X.

[216] A. Barison, C. W. Pereira da Silva, F. R. Campos, F. Simonelli, C. A. Lenz, A. G. Ferreira, A simple methodology for the determination of fatty acid composition in edible oils through 1H NMR spectroscopy, Magnetic Resonance in Chemistry 48 (8) (2010) 642–650. doi:10.1002/mrc.2629.

[217] AIST:Spectral Database for Organic Compounds,SDBS, https://sdbs.db.aist.go.jp/sdbs/cgi-bin/direct_frame_top.cgi.

[218] AIST:Spectral Database for Organic Compounds,SDBS, https://sdbs.db.aist.go.jp/sdbs/cgi-bin/direct_frame_top.cgi.

[219] M. F. Díaz, J. A. Gavín, Characterization by NMR of Ozonized methyl linoleate, J. Braz. Chem. Soc. 18 (3) (2007) 513–518. doi:10.1590/S0103-50532007000300003.

[220] V. Gonzalez, I. Fazlic, M. Cotte, F. Vanmeert, A. Gestels, S. De Meyer, F. Broers, J. Hermans, A. van Loon, K. Janssens, P. Noble, K. Keune, Lead(II) Formate in Rembrandt's Night Watch: Detection and Distribution from the Macro- to the Micro-scale., Angewandte Chemie n/a (n/a) (2023) 8. doi:10.1002/anie.202216478.

Appendices

A Supplementary Information for Chapter 2: Tensile testing tables

These tables contain tensile testing data from research papers published over the past 30 years (see bibliography at the end of this PDF). The tensile data are categorized by binding media (oils, alkyds, acrylics, and filler/gesso materials).

Table A.1: Summary of tensile test data for oil paint samples, including composition, aging time of the sample, testing conditions (temperature, RH, strain rate), mechanical property (Youngs modulus (E), equilibrium modulus (E_{eq}), secant modulus (E_s), tensile strength (σ_T), or yield stress (σ_Y), reference, *etc.* $^{\alpha}$Indicates a value estimated from a plot in the paper, rather than a tabulated value. $^{\beta}$Converted from stiffness values using an estimated sample thickness of 2 mm.

Sample Composition	Aging time	Mechanical Property (MPa)	Testing Conditions	Reference
Naples Yellow, Linseed Oil	13 years	E = 689	23°C, 50% RH, 0.0005 s^{-1}	[40]
Naples Yellow, Linseed Oil	13 years	E = 1172	23°C, 50% RH, 0.0005 s^{-1}, strain hardened	[40]
Naples Yellow, Linseed Oil	3.75 years	E = 304.7	23°C, 47% RH, 0.0005 s^{-1}	[40]
Naples Yellow, Linseed Oil	13 years	E = 1310	23°C, 5% RH, 0.0005 s^{-1}	[40]
Naples Yellow, Linseed Oil	13 years	E = 1440	23°C, 5% RH, 0.0005 s^{-1}, strain hardened	[40]
Naples Yellow, Linseed Oil	13 years	E = 110	23°C, 91% RH, 0.0005 s^{-1}	[40]
Naples Yellow, Linseed Oil	13 years	E = 4019	−3°C, 5% RH, 0.0005 s^{-1}	[40]
Naples Yellow, Linseed Oil	13 years	E = 2627	−3°C, 42% RH, 0.0005 s^{-1}	[40]
Naples Yellow, Linseed Oil	13 years	E = 2600	−3°C, 51% RH, 0.0005 s^{-1}	[40]
Burnt Sienna, Linseed Oil	13 years	E = 137.9	23°C, 50 % RH, 0.0005 s^{-1}	[40]
Burnt Sienna, Linseed Oil	13 years	E = 173.7	23°C, 50% RH, 0.0005 s^{-1}, strain hardened	[40]
Burnt Sienna, Linseed Oil	13 years	E = 641	23°C, 5% RH, 0.0005 s^{-1}	[40]
Burnt Sienna, Linseed Oil	13 years	E = 561	23°C, 5% RH, 0.0005 s^{-1}, strain hardened	[40]
Burnt Sienna, Linseed Oil	13 years	E = 4.48	23°C, 91% RH, 0.0005 s^{-1}	[40]

Sample Composition	Aging time	Mechanical Property (MPa)	Testing Conditions	Reference
Burnt Sienna, Linseed Oil	13 years	E = 2757	-3°C, 5% RH, 0.0005 s^{-1}	[40]
Burnt Sienna, Linseed Oil	13 years	E = 868	-3°C, 42% RH, 0.0005 s^{-1}	[40]
Burnt Sienna, Linseed Oil	13 years	E = 241	-3°C, 51% RH, 0.0005 s^{-1}	[40]
Flake White, Safflower Oil	13 years	E = 689	23°C, 50 % RH, 0.0005 s^{-1}	[40]
Flake White, Safflower Oil	3.75 years	E = 413.6	23°C, 45 % RH, 0.0005 s^{-1}	[40]

Sample Composition	Aging time	Mechanical Property (MPa)	Testing Conditions	Reference
Vermilion, Safflower Oil	13 years	E = 737	23°C, 50 % RH, 0.0005 s^{-1}	[40]
Vermilion, Safflower Oil	13 years	E = 1241	23°C, 50 % RH, 0.0005 s^{-1}, strained hardened	[40]
Vermilion, Safflower Oil	3 years	E = 462	23°C, 55 % RH, 0.0005 s^{-1}	[40]
Burnt Umber, Linseed Oil	13 years	E = 34.5	23°C, 50 % RH, 0.0005 s^{-1}	[40]
Lead White, Acid-refined Linseed Oil	8 years	E = 280[α]	23°C, 48 % RH, 0.0005 s^{-1}	[39]
Lead White, Acid-refined Linseed Oil	8 years	E = 280[α]	23°C, 48 % RH, 0.0005 s^{-1}, exposed to toluene 30 seconds, dried 24 hours	[39]
Lead White, Acid-refined Linseed Oil	8 years	E = 330[α]	23°C, 48 % RH, 0.0005 s^{-1}, exposed to toluene 1 minute, dried 24 hours	[39]
Lead White, Acid-refined Linseed Oil	8 years	E = 500[α]	23°C, 48 % RH, 0.0005 s^{-1}, exposed to toluene 1 hour, dried 24 hours	[39]
Lead White, Acid-refined Linseed Oil	8 years	E = 660[α]	23°C, 48 % RH, 0.0005 s^{-1}, exposed to toluene 24 hours, dried 24 hours	[39]
Lead White, Acid-refined Linseed Oil	8 years	E = 65[α]	23°C, 48 % RH, 0.0005 s^{-1}, exposed to toluene 1 minute, dried 1 hour	[39]
Lead White, Acid-refined Linseed Oil	8 years	E = 136[α]	23°C, 48 % RH, 0.0005 s^{-1}, exposed to triethalonamine (TEA) 1 minute, dried 24 hours	[39]

Sample Composition	Aging time	Mechanical Property (MPa)	Testing Conditions	Reference
Lead White, Acid-refined Linseed Oil	8 years	$E = 73^{\alpha}$	23°C, 48 % RH, 0.0005 s^{-1}, exposed to triethalonamine (TEA) 1 minute, toluene 1 minute, dried 24 hours	[39]
Lead White, Acid-refined Linseed Oil	8 years	$E = 250^{\alpha}$	23°C, 48 % RH, 0.0005 s^{-1}, exposed to triethalonamine (TEA) 1 minute, toluene 5 minutes, dried 24 hours	[39]
Lead White, Acid-refined Linseed Oil	8 years	$E = 5^{\alpha}$	23°C, 48 % RH, 0.0005 s^{-1}, exposed to triethalonamine (TEA) 46 hours, dried 24 hours	[39]
Malachite, Cold-pressed Linseed Oil	6 years	$E = 47^{\alpha}$	23°C, 48 % RH, 0.0005 s^{-1}	[39]
Malachite, Cold-pressed Linseed Oil	6 years	$E = 94^{\alpha}$	23°C, 48 % RH, 0.0005 s^{-1}, exposed to toluene 30 seconds, dried 24 hours	[39]
Malachite, Cold-pressed Linseed Oil	6 years	$E = 340^{\alpha}$	23°C, 48 % RH, 0.0005 s^{-1}, exposed to toluene 1 minute, dried 24 hours	[39]
Malachite, Cold-pressed Linseed Oil	6 years	$E = 1200^{\alpha}$	23°C, 48 % RH, 0.0005 s^{-1}, exposed to toluene 1 hour, dried 24 hours	[39]
Malachite, Cold-pressed Linseed Oil	6 years	$E = 786^{\alpha}$	23°C, 48 % RH, 0.0005 s^{-1}, exposed to toluene 24 hours, dried 24 hours	[39]

Sample Composition	Aging time	Mechanical Property (MPa)	Testing Conditions	Reference
Malachite, Cold-pressed Linseed Oil	6 years	E = 94$^{\alpha}$	23°C, 48 % RH, 0.0005 s^{-1}, exposed to toluene 1 minute, dried 1 hour	[39]
Lead Carbonate, Cold-pressed Linseed Oil	0.184 years	E = 18$^{\alpha}$	22°C, 50% RH, 0.0005 s^{-1}	[44]
Lead Carbonate, Cold-pressed Linseed Oil	0.269 years	E = 28$^{\alpha}$	22°C, 50% RH, 0.0005 s^{-1}	[44]
Lead Carbonate, Cold-pressed Linseed Oil	0.98 years	E = 91$^{\alpha}$	22°C, 50% RH, 0.0005 s^{-1}	[44]
Lead Carbonate, Cold-pressed Linseed Oil	10 years	E = 260$^{\alpha}$	22°C, 50% RH, 0.0005 s^{-1}	[44]
Linen coated with Animal Glue and Lead White in Linseed Oil	0 days (thermal aging)	E = 40.6$^{\beta}$	20°C, 15% RH, thermal aging at 60°C/55 % RH, 0.001 s^{-1}, samples cut along the warp direction	[45]
Linen coated with Animal Glue and Lead White in Linseed Oil	0 days (thermal aging)	E = 28.2$^{\beta}$	20°C, 55% RH, thermal aging at 60°C/55 % RH, 0.001 s^{-1}, samples cut along the warp direction	[45]
Linen coated with Animal Glue and Lead White in Linseed Oil	0 days (thermal aging)	E = 20.2$^{\beta}$	20°C, 95% RH, thermal aging at 60°C/55 % RH, 0.001 s^{-1}, samples cut along the warp direction	[45]
Linen coated with Animal Glue and Lead White in Linseed Oil	28 days (thermal aging)	E = 44.7$^{\beta}$	20°C, 15% RH, thermal aging at 60°C/55 % RH, 0.001 s^{-1}, samples cut along the warp direction	[45]

Sample Composition	Aging time	Mechanical Property (MPa)	Testing Conditions	Reference
Linen coated with Animal Glue and Lead White in Linseed Oil	28 days (thermal aging)	E = 37.0$^{\beta}$	20°C, 55% RH, thermal aging at 60°C/55 % RH, 0.001 s^{-1}, samples cut along the warp direction	[45]
Linen coated with Animal Glue and Lead White in Linseed Oil	28 days (thermal aging)	E = 15.3$^{\beta}$	20°C, 95% RH, thermal aging at 60°C/55 % RH, 0.001 s^{-1}, samples cut along the warp direction	[45]
Linen coated with Animal Glue and Lead White in Linseed Oil	56 days (thermal aging)	E = 47.3$^{\beta}$	20°C, 15% RH, thermal aging at 60°C/55 % RH, 0.001 s^{-1}, samples cut along the warp direction	[45]
Linen coated with Animal Glue and Lead White in Linseed Oil	56 days (thermal aging)	E = 31.3$^{\beta}$	20°C, 55% RH, thermal aging at 60°C/55 % RH, 0.001 s^{-1}, samples cut along the warp direction	[45]
Linen coated with Animal Glue and Lead White in Linseed Oil	56 days (thermal aging)	E = 16.8$^{\beta}$	20°C, 95% RH, thermal aging at 60°C/55 % RH, 0.001 s^{-1}, samples cut along the warp direction	[45]
Linen coated with Animal Glue and Lead White in Linseed Oil	112 days (thermal aging)	E = 44.7$^{\beta}$	20°C, 15% RH, thermal aging at 60°C/55 % RH, 0.001 s^{-1}, samples cut along the warp direction	[45]
Linen coated with Animal Glue and Lead White in Linseed Oil	112 days (thermal aging)	E = 32.8$^{\beta}$	20°C, 55% RH, thermal aging at 60°C/55 % RH, 0.001 s^{-1}, samples cut along the warp direction	[45]

Sample Composition	Aging time	Mechanical Property (MPa)	Testing Conditions	Reference
Linen coated with Animal Glue and Lead White in Linseed Oil	112 days (thermal aging)	E = 11.9$^{\beta}$	20°C, 95% RH, thermal aging at 60°C/55 % RH, 0.001 s^{-1}, samples cut along the warp direction	[45]
Cold-pressed Linseed Oil, Lead Carbonate	0.13 years	E_s = 18^{ff}	23°C, 48% RH, E_s at 1% strain	[13]
Cold-pressed Safflower Oil, Lead Carbonate	0.27 years	E_s = 24^{ff}	23°C, 48% RH, E_s at 1% strain	[13]
Cold-pressed Safflower Oil, Lead Carbonate	0.98 years	E_s = 51^{ff}	23°C, 48% RH, E_s at 1% strain	[13]
Cold-pressed Safflower Oil, Lead Carbonate	9.5 years	E_s = 93^{ff}	23°C, 48% RH, E_s at 1% strain	[13]
Cold-pressed Safflower Oil, Lead Carbonate	14.5 years	E_s = 122^{ff}	23°C, 48% RH, E_s at 1% strain	[13]
Cold-pressed Linseed Oil, Raw Umber	12.25 years	E = 5	23°C, 48% RH	[13]
Cold-pressed Linseed Oil, Red Iron Oxide	12.25 years	E = 5	23°C, 48% RH	[13]
Cold-pressed Linseed Oil, Malachite	12.25 years	E = 89	23°C, 48% RH	[13]
Cold-pressed Linseed Oil, Titanium Dioxide	12.25 years	E = 140	23°C, 48% RH	[13]
Cold-pressed Linseed Oil, Basic Lead Carbonate	12.25 years	E = 300	23°C, 48% RH	[13]
Cold-pressed Linseed Oil, Zinc Oxide	12.25 years	E = 1667	23°C, 48% RH	[13]
Cold-pressed Linseed Oil, Zinc Oxide	14.5 years	E_s = 340^{ff}	−10°C, 46% RH, E_s at 0.1% strain	[13]
Cold-pressed Linseed Oil, Zinc Oxide	14.5 years	E_s = 185^{ff}	23°C, 10% RH, E_s at 0.1% strain	[13]

Sample Composition	Aging time	Mechanical Property (MPa)	Testing Conditions	Reference
Cold-pressed Linseed Oil, Zinc Oxide	14.5 years	$E_s = 200^{ff}$	23°C, 48% RH, E_s at 0.1% strain	[13]
Cold-pressed Linseed Oil, Lead Carbonate	14.5 years	$E_s = 375^{ff}$	23°C, 10% RH, E_s at 1% strain	[13]
Cold-pressed Linseed Oil, Lead Carbonate	14.5 years	$E_s = 530^{ff}$	−10°C, 46% RH, E_s at 0.25% strain	[13]
Alkali-refined Linseed Oil (commercial), Titanium Dioxide	7.5 years, 0 days thermal aging	$E_s = 63^{ff}$	23°C, 48% RH, E_s at 1% strain, Thermal aging at 50°C	[13]
Alkali-refined Linseed Oil (commercial), Titanium Dioxide	7.5 years, 61 days thermal aging	$E_s = 85^{ff}$	23°C, 48% RH, E_s at 1% strain, Thermal aging at 50°C	[13]
Alkali-refined Linseed Oil (commercial), Titanium Dioxide	7.5 years, 126 days thermal aging	$E_s = 130^{ff}$	23°C, 48% RH, E_s at 1% strain, Thermal aging at 50°C	[13]
Alkali-refined Linseed Oil (commercial), Titanium Dioxide	7.5 years, 160 days thermal aging	$E_s = 120^{ff}$	23°C, 48% RH, E_s at 1% strain, Thermal aging at 50°C	[13]
Alkali-refined Linseed Oil (commercial), Titanium Dioxide	7.5 years, 300 days thermal aging	$E_s = 120^{ff}$	23°C, 48% RH, E_s at 1% strain, Thermal aging at 50°C	[13]
Alkali-refined Linseed Oil (commercial), Titanium Dioxide	7.5 years	$E_s = 94^{ff}$	23°C, 48% RH, E_s at 1% strain, Soaked in 60 sec, dried	[13]
Alkali-refined Safflower Oil (commercial), Titanium Dioxide	7.5 years, 0 days thermal aging	$E_s = 50^{ff}$	23°C, 48% RH, E_s at 1% strain, Thermal aging at 50°C	[13]
Alkali-refined Safflower Oil (commercial), Titanium Dioxide	7.5 years, 61 days thermal aging	$E_s = 69^{ff}$	23°C, 48% RH, E_s at 1% strain, Thermal aging at 50°C	[13]
Alkali-refined Safflower Oil (commercial), Titanium Dioxide	7.5 years, 126 days thermal aging	$E_s = 75^{ff}$	23°C, 48% RH, E_s at 1% strain, Thermal aging at 50°C	[13]

Sample Composition	Aging time	Mechanical Property (MPa)	Testing Conditions	Reference
Alkali-refined Safflower Oil (commercial), Titanium Dioxide	7.5 years, 160 days thermal aging	$E_s = 73^{ff}$	23°C, 48% RH, E_s at 1% strain, Thermal aging at 50°C	[13]
Alkali-refined Safflower Oil (commercial), Titanium Dioxide	7.5 years, 300 days thermal aging	$E_s = 99^{ff}$	23°C, 48% RH, E_s at 1% strain, Thermal aging at 50°C	[13]
Alkali-refined Safflower Oil (commercial), Titanium Dioxide	7.5 years	$E_s = 75^{ff}$	23°C, 48% RH, E_s at 1% strain, Soaked in 60 sec, dried	[13]
Red Iron Oxide in Cold-Pressed Linseed Oil	3.75 years	$E = 54^{\alpha}$	20°C, 45% RH, 0.0005 s^{-1}	[49]
Red Iron Oxide in Cold-Pressed Linseed Oil	3.75 years	$\sigma_T = 2.6^{\alpha}$	20°C, 45% RH, 0.0005 s^{-1}	[49]
Red Iron Oxide in Cold-Pressed Linseed Oil, 25% hydrolyzed	3.75 years	$E = 26^{\alpha}$	20°C, 45% RH, 0.0005 s^{-1}	[49]
Red Iron Oxide in Cold-Pressed Linseed Oil, 25% hydrolyzed	3.75 years	$\sigma_T = 0.8^{\alpha}$	20°C, 45% RH, 0.0005 s^{-1}	[49]
Red Iron Oxide in Cold-Pressed Linseed Oil, 50% hydrolyzed	3.75 years	$E = 15^{\alpha}$	20°C, 45% RH, 0.0005 s^{-1}	[49]
Red Iron Oxide in Cold-Pressed Linseed Oil, 50% hydrolyzed	3.75 years	$\sigma_T = 0.3^{\alpha}$	20°C, 45% RH, 0.0005 s^{-1}	[49]
Red Iron Oxide in Cold-Pressed Linseed Oil, 75% hydrolyzed	3.75 years	$E = 9.7^{\alpha}$	20°C, 45% RH, 0.0005 s^{-1}	[49]
Red Iron Oxide in Cold-Pressed Linseed Oil, 75% hydrolyzed	3.75 years	$\sigma_T = 0.1^{\alpha}$	20°C, 45% RH, 0.0005 s^{-1}	[49]

Sample Composition	Aging time	Mechanical Property (MPa)	Testing Conditions	Reference
Red Iron Oxide in Cold-Pressed Linseed Oil, 100% hydrolyzed	3.75 years	$E = 6.3^{\alpha}$	20°C, 45% RH, 0.0005 s^{-1}	[49]
Red Iron Oxide in Cold-Pressed Linseed Oil, 100% hydrolyzed	3.75 years	$\sigma_T = 0.1^{\alpha}$	20°C, 45% RH, 0.0005 s^{-1}	[49]
2 -layer: Michael Harding, Cadmium Sulfoselenide; Golden Acrylic Gesso Primer	6 days ambient, 0 days thermal aging	$E_s = 0.03$	20°C, 55% RH, 0.001 s^{-1}, Thermal aging: 60°C, 55% RH, E_s at 5.0% strain	[50]
2 -layer: Michael Harding, Cadmium Sulfoselenide; Spectrum Alkyd Primer	6 days ambient, 82 days thermal aging	$E_s = 0.4$	20°C, 55% RH, 0.001 s^{-1}, Thermal aging: 60°C, 55% RH, E_s at 5.0% strain	[50]
2 -layer: Michael Harding, Cadmium Sulfoselenide; Spectrum Alkyd Primer	6 days ambient, 0 days thermal aging	$E_s = 0.1$	20°C, 55% RH, 0.001 s^{-1}, Thermal aging: 60°C, 55% RH, E_s at 5.0% strain	[50]
Winsor & Newton Foundation White	7 months	E = 5230	−10°C, 55% RH, 0.002 s^{-1}	[51]
Winsor & Newton Foundation White	7 months	E = 4590	0°C, 60% RH, 0.002 s^{-1}	[51]
Winsor & Newton Foundation White	7 months	E = 2925	10°C, 57% RH, 0.002 s^{-1}	[51]
Winsor & Newton Foundation White	7 months	E = 1875	20°C, 54% RH, 0.002 s^{-1}	[51]
H. Schincke Normal Professional, Alizarin Red	5 months	$E_s = 6^{ff}$	Ambient Conditions, E_s at 1% strain	[52]
H. Schincke Normal Professional, Phthalocyanine Blue	5 months	$E_s = 1.5^{ff}$	Ambient Conditions, E_s at 1% strain	[52]

Sample Composition	Aging time	Mechanical Property (MPa)	Testing Conditions	Reference
H. Schincke Normal Professional, Ivory Black	5 months	$E_s = 1.5^{ff}$	Ambient Conditions, E_s at 1% strain	[52]
H. Schincke Normal Professional, Titanium White	5 months	$E_s = 130^{ff}$	Ambient Conditions, E_s at 1% strain	[52]
H. Schincke Normal Professional, Hansa Yellow	5 months	$E_s = 6^{ff}$	Ambient Conditions, E_s at 1% strain	[52]
H. Schincke Normal Professional, Hansa Yellow	5 months	$E_s = 7^{ff}$	Ambient Conditions, E_s at 1% strain, Immersed in water 1 min, Dried 4 weeks	[52]
H. Schincke Normal Professional, Hansa Yellow	5 months	$E_s = 12^{ff}$	Ambient Conditions, E_s at 1% strain, Immersed in n-hexane 1 min, Dried 4 weeks	[52]
H. Schincke Normal Professional, Hansa Yellow	5 months	$E_s = 10^{ff}$	Ambient Conditions, E_s at 1% strain, Immersed in ethanol 1 min, Dried 4 weeks	[52]
H. Schincke Normal Professional, Hansa Yellow	5 months	$E_s = 11^{ff}$	Ambient Conditions, E_s at 1% strain, Immersed in toluene 1 min, Dried 4 weeks	[52]
H. Schincke Normal Professional, Hansa Yellow	5 months	$E_s = 17^{ff}$	Ambient Conditions, E_s at 1% strain, Immersed in diethyl ether 1 min, Dried 4 weeks	[52]

Sample Composition	Aging time	Mechanical Property (MPa)	Testing Conditions	Reference
H. Schincke Normal Professional, Hansa Yellow	5 months	$E_s = 32^{ff}$	Ambient Conditions, E_s at 1% strain, Immersed in chloroform 1 min, Dried 4 weeks	[52]
H. Schincke Normal Professional, Hansa Yellow	5 months	$E_s = 57^{ff}$	Ambient Conditions, E_s at 1% strain, Immersed in acetone 1 min, Dried 4 weeks	[52]
Cold-Pressed Linseed Oil, no pigment	7 years	$E_s = 0.1^{ff}$	23°C, 50 % RH, 0.0005 s^{-1}, E_s at 1% strain	[57]
Grumbacher Oil Paint, Burnt Umber (1.3% Mn)	28 years	$E_s = 14^{ff}$	23°C, 50 % RH, 0.0005 s^{-1}, E_s at 1% strain	[57]
Gamblin Oil Paint, Burnt Umber (9.1% Mn)	7 years	$E_s = 18^{ff}$	23°C, 50 % RH, 0.0005 s^{-1}, E_s at 1% strain	[57]
Grumbacher Oil Paint, Burnt Umber (19.1% Mn)	7 years	$E_s = 56^{ff}$	23°C, 50 % RH, 0.0005 s^{-1}, E_s at 1% strain	[57]
Winsor & Newton Oil Paint, Burnt Umber (11.7% Mn)	7 years	$E_s = 78^{ff}$	23°C, 50 % RH, 0.0005 s^{-1}, E_s at 1% strain	[57]
Winsor & Newton Oil Paint, Burnt Umber (18.3% Mn)	25 years	$E_s = 150^{ff}$	23°C, 50 % RH, 0.0005 s^{-1}, E_s at 1% strain	[57]
Cold-Pressed Linseed Oil, Calcium Carbonate	14.5 years	$E_s = 4^{ff}$	23°C, 50 % RH, 0.0005 s^{-1}, E_s at 1% strain	[57]
Cold-Pressed Linseed Oil, Silica with Litharge	8 years	$E_s = 8^{ff}$	23°C, 50 % RH, 0.0005 s^{-1}, E_s at 1% strain	[57]
Cold-Pressed Linseed Oil, Lead White	19.5 years	$E_s = 230^{ff}$	23°C, 50 % RH, 0.0005 s^{-1}, E_s at 1% strain	[57]
Cold-Pressed Linseed Oil, Lead Carbonate	0.18 years	$E_s = 18^{ff}$	23°C, 50 % RH, 0.0005 s^{-1}, E_s at 1% strain	[58]

Sample Composition	Aging time	Mechanical Property (MPa)	Testing Conditions	Reference
Cold-Pressed Linseed Oil, Lead Carbonate	0.27 years	$E_s = 31^{ff}$	23°C, 50 % RH, 0.0005 s^{-1}, E_s at 1% strain	[58]
Cold-Pressed Linseed Oil, Lead Carbonate	0.98 years	$E_s = 60^{ff}$	23°C, 50 % RH, 0.0005 s^{-1}, E_s at 1% strain	[58]
Cold-Pressed Linseed Oil, Lead Carbonate	10 years	$E_s = 100^{ff}$	23°C, 50 % RH, 0.0005 s^{-1}, E_s at 1% strain	[58]
Cold-Pressed Linseed Oil, Lead Carbonate	14.25 years	$E_s = 150^{ff}$	23°C, 50 % RH, 0.0005 s^{-1}, E_s at 1% strain	[58]
Cold-Pressed Linseed Oil, Lead Carbonate	18.75 years	$E_s = 230^{ff}$	23°C, 50 % RH, 0.0005 s^{-1}, E_s at 1% strain	[58]
Cold-Pressed Linseed Oil, Lead Carbonate	19.5 years	$E_s = 250^{ff}$	23°C, 50 % RH, 0.0005 s^{-1}, E_s at 1% strain	[58]
Cold-Pressed Linseed Oil, Lead Carbonate	19.5 years	$E_s = 240^{ff}$	23°C, 50 % RH, 0.0005 s^{-1}, immersed in water 30 sec, dried 1 month, E_s at 1% strain	[58]
Cold-Pressed Linseed Oil, Lead Carbonate	19.5 years	$E_s = 230^{ff}$	23°C, 50 % RH, 0.0005 s^{-1}, immersed in methanol 30 sec, dried 1 month, E_s at 1% strain	[58]
Cold-Pressed Linseed Oil, Lead Carbonate	19.5 years	$E_s = 220^{ff}$	23°C, 50 % RH, 0.0005 s^{-1}, immersed in toluene 30 sec, dried 1 month, E_s at 1% strain	[58]
Cold-Pressed Linseed Oil, Lead Carbonate	19.5 years	$E_s = 190^{ff}$	23°C, 50 % RH, 0.0005 s^{-1}, immersed in acetone 30 sec, dried 1 month, E_s at 1% strain	[58]

Sample Composition	Aging time	Mechanical Property (MPa)	Testing Conditions	Reference
Cold-Pressed Linseed Oil, Lead Carbonate	19.5 years	$E_s = 170^{ff}$	23°C, 50 % RH, 0.0005 s^{-1}, immersed in mineral spirits 60 sec, dried 1 month, E_s at 1% strain	[58]
Cold-Pressed Linseed Oil, Lead Tin Yellow	7.5 years	$E_s = 300^{ff}$	23°C, 50 % RH, 0.0005 s^{-1}, E_s at 1% strain	[58]
Cold-Pressed Linseed Oil, Lead Carbonate with Litharge	16.7 years	$E_s = 290^{ff}$	23°C, 50 % RH, 0.0005 s^{-1}, E_s at 1% strain	[58]
Cold-Pressed Linseed Oil, Chrome Yellow	7.5 years	$E_s = 40^{ff}$	23°C, 50 % RH, 0.0005 s^{-1}, E_s at 1% strain	[58]
Cold-Pressed Linseed Oil, Naples Yellow	7.5 years	$E_s = 3^{ff}$	23°C, 50 % RH, 0.0005 s^{-1}, E_s at 1% strain	[58]
Cold-Pressed Linseed Oil, Titanium Dioxide (rutile)	8.4 years	$E_s = 110^{ff}$	23°C, 50 % RH, 0.0005 s^{-1}, E_s at 0.25% strain	[58]
Cold-Pressed Linseed Oil, Titanium Dioxide (rutile)	17.2 years	$E_s = 130^{ff}$	23°C, 50 % RH, 0.0005 s^{-1}, E_s at 0.25% strain	[58]
Cold-Pressed Linseed Oil, Zinc Oxide	8 years	$E_s = 610^{ff}$	23°C, 50 % RH, 0.0005 s^{-1}, E_s at 0.25% strain	[58]
Cold-Pressed Linseed Oil, Zinc Oxide	14.5 years	$E_s = 1320^{ff}$	23°C, 50 % RH, 0.0005 s^{-1}, E_s at 0.25% strain	[58]
Cold-Pressed Linseed Oil, Raw Sienna	1.25 years	$E_s = 12^{ff}$	23°C, 50 % RH, 0.0005 s^{-1}, E_s at 1% strain	[58]
Cold-Pressed Linseed Oil, Raw Sienna	8 years	$E_s = 0^{ff}$	23°C, 50 % RH, 0.0005 s^{-1}, E_s at 1% strain	[58]
Cold-Pressed Linseed Oil, Raw Sienna	14.25 years	$E_s = 3^{ff}$	23°C, 50 % RH, 0.0005 s^{-1}, E_s at 1% strain	[58]
Cold-Pressed Linseed Oil, Burnt Sienna	1.25 years	$E_s = 50^{ff}$	23°C, 50 % RH, 0.0005 s^{-1}, E_s at 1% strain	[58]

Sample Composition	Aging time	Mechanical Property (MPa)	Testing Conditions	Reference
Cold-Pressed Linseed Oil, Burnt Sienna	8.5 years	$E_s = 3^{ff}$	23°C, 50 % RH, 0.0005 s^{-1}, E_s at 1% strain	[58]
Cold-Pressed Linseed Oil, Raw Umber	7.5 years	$E_s = 36^{ff}$	23°C, 50 % RH, 0.0005 s^{-1}, E_s at 0.5% strain	[58]
Cold-Pressed Linseed Oil, Raw Umber	14 years	$E_s = 6^{ff}$	23°C, 50 % RH, 0.0005 s^{-1}, E_s at 0.5% strain	[58]
Cold-Pressed Linseed Oil, Burnt Umber	1.25 years	$E_s = 8^{ff}$	23°C, 50 % RH, 0.0005 s^{-1}, E_s at 0.5% strain	[58]
Cold-Pressed Linseed Oil, Burnt Umber	7.5 years	$E_s = 0^{ff}$	23°C, 50 % RH, 0.0005 s^{-1}, E_s at 0.5% strain	[58]
Cold-Pressed Linseed Oil, Yellow Ocher mixed with Grumbacher Flake White (alkali-refined linseed oil), 4:1 ratio by volume	2.5 years	$E_s = 200^{ff}$	23°C, 50 % RH, 0.0005 s^{-1}, E_s at 1% strain	[58]
Cold-Pressed Linseed Oil, Yellow Ocher mixed with Grumbacher Flake White (alkali-refined linseed oil), 4:1 ratio by volume	2.5 years	$E_s = 230^{ff}$	23°C, 50 % RH, 0.0005 s^{-1}, Immersed in Acetone 30 sec and dried, E_s at 1% strain	[58]
Cold-Pressed Linseed Oil, Yellow Ocher mixed with Grumbacher Flake White (alkali-refined linseed oil), 4:1 ratio by volume	2.5 years	$E_s = 240^{ff}$	23°C, 50 % RH, 0.0005 s^{-1}, Immersed in methanol 30 sec and dried, E_s at 1% strain	[58]
Winsor & Newton, Yellow Ocher	30 years	$E_s = 40^{ff}$	23°C, 50 % RH, 0.0005 s^{-1}, E_s at 1% strain	[58]

Sample Composition	Aging time	Mechanical Property (MPa)	Testing Conditions	Reference
Speedball, Yellow Ocher	29 years	$E_s = 0^{ff}$	23°C, 50 % RH, 0.0005 s^{-1}, E_s at 1% strain	[58]
Cold-Pressed Linseed Oil, Yellow Ocher	18 years	$E_s = 0^{ff}$	23°C, 50 % RH, 0.0005 s^{-1}, E_s at 1% strain	[58]
Gamblin Artists Oil Colors, Raw Umber	15 years	$E_s = 7^{ff}$	23°C, 50 % RH, 0.0005 s^{-1}, E_s at 1% strain	[61]
Grumbacher Pretested Artists Oil Colors, Raw Umber	15 years	$E_s = 20^{ff}$	23°C, 50 % RH, 0.0005 s^{-1}, E_s at 1% strain	[61]
Gamblin Artists Oil Colors, Burnt Umber	15 years	$E_s = 22^{ff}$	23°C, 50 % RH, 0.0005 s^{-1}, E_s at 1% strain	[61]
Grumbacher Pretested Artists Oil Colors, Burnt Umber	15 years	$E_s = 47^{ff}$	23°C, 50 % RH, 0.0005 s^{-1}, E_s at 1% strain	[61]
Speedball, Burnt Umber	33 years	$E_s = 32^{ff}$	23°C, 50 % RH, 0.0005 s^{-1}, E_s at 1% strain	[61]
Winsor & Newton Titanium White (professional series): Safflower Oil, TiO_2/ZnO	6 years	$E_s = 3420^{ff}$	−10°C, 50 % RH, 0.02 s^{-1}, E_s at 0.5% strain	[64]
Winsor & Newton Titanium White (professional series): Safflower Oil, TiO_2/ZnO	6 years	$E_s = 2830^{ff}$	−10°C, 50 % RH, 0.002 s^{-1}, E_s at 0.5% strain	[64]
Winsor & Newton Titanium White (professional series): Safflower Oil, TiO_2/ZnO	6 years	$E_s = 2100^{ff}$	−10°C, 50 % RH, 0.0002 s^{-1}, E_s at 0.5% strain	[64]
Winsor & Newton Titanium White (professional series): Safflower Oil, TiO_2/ZnO	6 years	$E_s = 1720^{ff}$	−10°C, 50 % RH, 0.00002 s^{-1}, E_s at 0.5% strain	[64]

Sample Composition	Aging time	Mechanical Property (MPa)	Testing Conditions	Reference
Winsor & Newton Titanium White (professional series): Safflower Oil, TiO_2/ZnO	6 years	$E_s = 1440^{ff}$	10°C, 50 % RH, 0.02 s^{-1}, E_s at 0.5% strain	[64]
Winsor & Newton Titanium White (professional series): Safflower Oil, TiO_2/ZnO	6 years	$E_s = 1310^{ff}$	10°C, 50 % RH, 0.02 s^{-1}, E_s at 0.5% strain	[64]
Winsor & Newton Titanium White (professional series): Safflower Oil, TiO_2/ZnO	6 years	$E_s = 900^{ff}$	20°C, 50 % RH, 0.002 s^{-1}, E_s at 0.5% strain	[64]
Winsor & Newton Titanium White (professional series): Safflower Oil, TiO_2/ZnO	6 years	$E_s = 870^{ff}$	10°C, 50 % RH, 0.0002 s^{-1}, E_s at 0.5% strain	[64]
Winsor & Newton Titanium White (professional series): Safflower Oil, TiO_2/ZnO	6 years	$E_s = 650^{ff}$	20°C, 50 % RH, 0.0002 s^{-1}, E_s at 0.5% strain	[64]
Winsor & Newton Titanium White (professional series): Safflower Oil, TiO_2/ZnO	6 years	$E_s = 650^{ff}$	10°C, 50 % RH, 0.00002 s^{-1}, E_s at 0.5% strain	[64]
Winsor & Newton Titanium White (professional series): Safflower Oil, TiO_2/ZnO	6 years	$E_s = 470^{ff}$	20°C, 50 % RH, 0.00002 s^{-1}, E_s at 0.5% strain	[64]
Winsor & Newton Zinc White (professional series): Safflower Oil, ZnO	6-10 years	$E_s = 1890^{ff}$	0°C, 50 % RH, 0.02 s^{-1}, E_s at 0.5% strain	[64]
Winsor & Newton Zinc White (professional series): Safflower Oil, ZnO	6-10 years	$E_s = 1600^{ff}$	−10°C, 50 % RH, 0.00002 s^{-1}, E_s at 0.5% strain	[64]

Sample Composition	Aging time	Mechanical Property (MPa)	Testing Conditions	Reference
Winsor & Newton Zinc White (professional series): Safflower Oil, ZnO	6-10 years	$E_s = 1380^{ff}$	0°C, 50 % RH, 0.002 s^{-1}, E_s at 0.5% strain	[64]
Winsor & Newton Zinc White (professional series): Safflower Oil, ZnO	6-10 years	$E_s = 1180^{ff}$	10°C, 50 % RH, 0.02 s^{-1}, E_s at 0.5% strain	[64]
Winsor & Newton Zinc White (professional series): Safflower Oil, ZnO	6-10 years	$E_s = 1060^{ff}$	0°C, 50 % RH, 0.0002 s^{-1}, E_s at 0.5% strain	[64]
Winsor & Newton Zinc White (professional series): Safflower Oil, ZnO	6-10 years	$E_s = 890^{ff}$	10°C, 50 % RH, 0.002 s^{-1}, E_s at 0.5% strain	[64]
Winsor & Newton Zinc White (professional series): Safflower Oil, ZnO	6-10 years	$E_s = 760^{ff}$	0°C, 50 % RH, 0.00002 s^{-1}, E_s at 0.5% strain	[64]
Winsor & Newton Zinc White (professional series): Safflower Oil, ZnO	6-10 years	$E_s = 720^{ff}$	10°C, 50 % RH, 0.0002 s^{-1}, E_s at 0.5% strain	[64]
Winsor & Newton Zinc White (professional series): Safflower Oil, ZnO	6-10 years	$E_s = 520^{ff}$	10°C, 50 % RH, 0.00002 s^{-1}, E_s at 0.5% strain	[64]
Michael Harding Zinc White: Cold-Pressed Linseed Oil, ZnO	6-10 years	$E_s = 2180^{ff}$	0°C, 50 % RH, 0.02 s^{-1}, E_s at 0.5% strain	[64]
Michael Harding Zinc White: Cold-Pressed Linseed Oil, ZnO	6-10 years	$E_s = 1720^{ff}$	0°C, 50 % RH, 0.002 s^{-1}, E_s at 0.5% strain	[64]

Sample Composition	Aging time	Mechanical Property (MPa)	Testing Conditions	Reference
Michael Harding Zinc White: Cold-Pressed Linseed Oil, ZnO	6-10 years	$E_s = 1590^{ff}$	10°C, 50 % RH,0.02 s^{-1}, E_s at 0.5% strain	[64]
Michael Harding Zinc White: Cold-Pressed Linseed Oil, ZnO	6-10 years	$E_s = 1280^{ff}$	0°C, 50 % RH, 0.0002 s^{-1}, E_s at 0.5% strain	[64]
Michael Harding Zinc White: Cold-Pressed Linseed Oil, ZnO	6-10 years	$E_s = 1110^{ff}$	10°C, 50 % RH, 0.002 s^{-1}, E_s at 0.5% strain	[64]
Michael Harding Zinc White: Cold-Pressed Linseed Oil, ZnO	6-10 years	$E_s = 990^{ff}$	20°C, 50 % RH, 0.02 s^{-1}, E_s at 0.5% strain	[64]
Michael Harding Zinc White: Cold-Pressed Linseed Oil, ZnO	6-10 years	$E_s = 880^{ff}$	10°C, 50 % RH, 0.0002 s^{-1}, E_s at 0.5% strain	[64]
Michael Harding Zinc White: Cold-Pressed Linseed Oil, ZnO	6-10 years	$E_s = 780^{ff}$	20°C, 50 % RH, 0.002 s^{-1}, E_s at 0.5% strain	[64]
Michael Harding Zinc White: Cold-Pressed Linseed Oil, ZnO	6-10 years	$E_s = 620^{ff}$	10°C, 50 % RH, 0.00002 s^{-1}, E_s at 0.5% strain	[64]
Michael Harding Zinc White: Cold-Pressed Linseed Oil, ZnO	6-10 years	$E_s = 590^{ff}$	20°C, 50 % RH, 0.0002 s^{-1}, E_s at 0.5% strain	[64]
Michael Harding Zinc White: Cold-Pressed Linseed Oil, ZnO	6-10 years	$E_s = 440^{ff}$	20°C, 50 % RH, 0.00002 s^{-1}, E_s at 0.5% strain	[64]
Michael Harding Flake White: Refined Linseed Oil, Basic $PbCO_3$/ZnO	6-10 years	$E_s = 1440^{ff}$	10°C, 50 % RH, 0.02 s^{-1}, E_s at 0.5% strain	[64]

Sample Composition	Aging time	Mechanical Property (MPa)	Testing Conditions	Reference
Michael Harding Flake White: Refined Linseed Oil, Basic $PbCO_3/ZnO$	6-10 years	$E_s = 1160^{ff}$	10°C, 50 % RH, 0.002 s^{-1}, E_s at 0.5% strain	[64]
Michael Harding Flake White: Refined Linseed Oil, Basic $PbCO_3/ZnO$	6-10 years	$E_s = 940^{ff}$	20°C, 50 % RH, 0.02 s^{-1}, E_s at 0.5% strain	[64]
Michael Harding Flake White: Refined Linseed Oil, Basic $PbCO_3/ZnO$	6-10 years	$E_s = 670^{ff}$	20°C, 50 % RH, 0.002 s^{-1}, E_s at 0.5% strain	[64]
Michael Harding Flake White: Refined Linseed Oil, Basic $PbCO_3/ZnO$	6-10 years	$E_s = 610^{ff}$	10°C, 50 % RH, 0.00002 s^{-1}, E_s at 0.5% strain	[64]
Michael Harding Flake White: Refined Linseed Oil, Basic $PbCO_3/ZnO$	6-10 years	$E_s = 550^{ff}$	20°C, 50 % RH, 0.0002 s^{-1}, E_s at 0.5% strain	[64]
Michael Harding Flake White: Refined Linseed Oil, Basic $PbCO_3/ZnO$	6-10 years	$E_s = 390^{ff}$	20°C, 50 % RH, 0.00002 s^{-1}, E_s at 0.5% strain	[64]
Winsor & Newton Artisan Titanium White: Drying oil/additives, TiO_2	6-10 years	$E_s = 1080^{ff}$	−10°C, 50 % RH, 0.02 s^{-1}, E_s at 0.5% strain	[64]
Winsor & Newton Artisan Titanium White: Drying oil/additives, TiO_2	6-10 years	$E_s = 690^{ff}$	−10°C, 50 % RH, 0.002 s^{-1}, E_s at 0.5% strain	[64]
Winsor & Newton Artisan Titanium White: Drying oil/additives, TiO_2	6-10 years	$E_s = 440^{ff}$	−10°C, 50 % RH, 0.0002 s^{-1}, E_s at 0.5% strain	[64]

Sample Composition	Aging time	Mechanical Property (MPa)	Testing Conditions	Reference
Winsor & Newton Artisan Titanium White: Drying oil/additives, TiO_2	6-10 years	$E_s = 320^{ff}$	0°C, 50 % RH, 0.002 s^{-1}, E_s at 0.5% strain	[64]
Winsor & Newton Artisan Titanium White: Drying oil/additives, TiO_2	6-10 years	$E_s = 310^{ff}$	10°C, 50 % RH, 0.02 s^{-1}, E_s at 0.5% strain	[64]
Winsor & Newton Artisan Titanium White: Drying oil/additives, TiO_2	6-10 years	$E_s = 260^{ff}$	−10°C, 50 % RH, 0.00002 s^{-1}, E_s at 0.5% strain	[64]
Winsor & Newton Artisan Titanium White: Drying oil/additives, TiO_2	6-10 years	$E_s = 200^{ff}$	10°C, 50 % RH, 0.002 s^{-1}, E_s at 0.5% strain	[64]
Winsor & Newton Artisan Titanium White: Drying oil/additives, TiO_2	6-10 years	$E_s = 190^{ff}$	20°C, 50 % RH, 0.02 s^{-1}, E_s at 0.5% strain	[64]
Winsor & Newton Artisan Titanium White: Drying oil/additives, TiO_2	6-10 years	$E_s = 130^{ff}$	10°C, 50 % RH, 0.0002 s^{-1}, E_s at 0.5% strain	[64]
Winsor & Newton Artisan Titanium White: Drying oil/additives, TiO_2	6-10 years	$E_s = 120^{ff}$	20°C, 50 % RH, 0.002 s^{-1}, E_s at 0.5% strain	[64]
Winsor & Newton Artisan Titanium White: Drying oil/additives, TiO_2	6-10 years	$E_s = 80^{ff}$	10°C, 50 % RH, 0.00002 s^{-1}, E_s at 0.5% strain	[64]
Winsor & Newton Artisan Titanium White: Drying oil/additives, TiO_2	6-10 years	$E_s = 70^{ff}$	20°C, 50 % RH, 0.0002 s^{-1}, E_s at 0.5% strain	[64]
Winsor & Newton Artisan Titanium White: Drying oil/additives, TiO_2	6-10 years	$E_s = 40^{ff}$	20°C, 50 % RH, 0.00002 s^{-1}, E_s at 0.5% strain	[64]
Cold Pressed Linseed Oil, Lead Tin Yellow	1.25 years	$E_s = 170^{\alpha}$	23°C, 50% RH, E_s at 1% strain	[65]

Sample Composition	Aging time	Mechanical Property (MPa)	Testing Conditions	Reference
Cold Pressed Linseed Oil, Lead Tin Yellow	7.85 years	$E_s = 600^{\alpha}$	23°C, 15% RH, E_s at 1% strain	[65]
Cold Pressed Linseed Oil, Lead Tin Yellow	7.5 years	$E_s = 300^{\alpha}$	23°C, 49% RH, E_s at 1% strain	[65]
Cold Pressed Linseed Oil, Lead Tin Yellow	7.85 years	$E_s = 160^{\alpha}$	23°C, 83% RH, E_s at 1% strain	[65]
Cold Pressed Linseed Oil, Red Iron Oxide	1.25 years	$E_s = 11^{\alpha}$	23°C, 50% RH, E_s at 1% strain	[65]
Cold Pressed Linseed Oil, Red Iron Oxide	7.85 years	$E_s = 7^{\alpha}$	23°C, 16% RH, E_s at 1% strain	[65]
Cold Pressed Linseed Oil, Red Iron Oxide	7.5 years	$E_s = 3^{\alpha}$	23°C, 48% RH, E_s at 1% strain	[65]
Cold Pressed Linseed Oil, Red Iron Oxide	7.85 years	$E_s = 1^{\alpha}$	23°C, 84% RH, E_s at 1% strain	[65]
Grumbacher Artists' Oil Colors: Alkali Refined Linseed Oil, Cobalt Blue PB28	2 years	$E_s = 0.29^{ff}$	23°C, 50% RH, 0.0625 s^{-1}, E_s at 1% strain and similar to σ_T for this sample	[68]
Grumbacher Artists' Oil Colors: Alkali Refined Linseed Oil, Cobalt Blue PB28	18 years	$E = 9^{ff}$	23°C, 50% RH, 0.0625 s^{-1}, E measured for linear elastic region	[68]
Grumbacher Artists' Oil Colors: Alkali Refined Linseed Oil, Cobalt Blue PB28	18 years	$œ_T = 0.3^{ff}$	23°C, 50% RH, 0.0625 s^{-1}, σ_T measured at maximum stress	[68]
Gamblin Artists' Oil Colors: Alkali Refined Linseed Oil, Cobalt Blue PB28	2 years	$E_s = 0.35^{ff}$	23°C, 50% RH, 0.0625 s^{-1}, E_s at 1% strain and similar to σ_T for this sample	[68]

Sample Composition	Aging time	Mechanical Property (MPa)	Testing Conditions	Reference
Gamblin Artists' Oil Colors: Alkali Refined Linseed Oil, Cobalt Blue PB28	18 years	$E = 111^{ff}$	23°C, 50% RH, 0.0625 s^{-1}, E measured for the linear elastic region	[68]
Gamblin Artists' Oil Colors: Alkali Refined Linseed Oil, Cobalt Blue PB28	18 years	$œ_T = 0.22^{ff}$	23°C, 50% RH, 0.0625 s^{-1}, σ_T measured at maximum stress	[68]
Gamblin Artists' Oil Colors: Linseed Oil, Cobalt Blue PB28 & Litharge	18 years	$E = 45^{ff}$	23°C, 50% RH, 0.0625 s^{-1}, E measured for the linear elastic region	[68]
Gamblin Artists' Oil Colors: Linseed Oil, Cobalt Blue PB28 & Litharge	18 years	$œ_T = 0.34^{ff}$	23°C, 50% RH, 0.0625 s^{-1}, σ_T measured at maximum stress	[68]
Winsor & Newton Artists' Paint: Linseed/Safflower Oil, Cobalt Blue PB28	3 years	$œ_T = 2.4^{ff}$	23°C, 50% RH, 0.0625 s^{-1}, σ_T measured at maximum stress	[68]
Titan color al óleo extrafino 52: Cobalt Blue PB28 & PB29	3 years	$œ_T = 1^{ff}$	23°C, 50% RH, 0.0625 s^{-1}, σ_T measured at maximum stress	[68]
Talens-Van Gogh Oil Colour 511: Cobalt Blue PB28	3 years	$œ_T = 0.69^{ff}$	23°C, 50% RH, 0.0625 s^{-1}, σ_T measured at maximum stress	[68]
Cold Pressed Linseed Oil, Cobalt Blue PB28	3 years	$E_s = 0.3^{\alpha}$	23°C, 50% RH, 0.0625 s^{-1}, E_s at 1% strain	[68]
Cold Pressed Linseed Oil, Cobalt Blue PB28	3 years	$E_s = 0.4^{\alpha}$	23°C, 50% RH, 0.0625 s^{-1}, E_s at 5% strain	[68]
Cold Pressed Linseed Oil, Cobalt Blue PB28, Calcite, Gypsum, Kaolin	3 years	$E_s = 3.2^{\alpha}$	23°C, 50% RH, 0.0625 s^{-1}, E_s at 1% strain	[68]

Sample Composition	Aging time	Mechanical Property (MPa)	Testing Conditions	Reference
Cold Pressed Linseed Oil, Cobalt Blue PB28, Calcite, Gypsum, Kaolin	3 years	$E_s = 2^{\alpha}$	23°C, 50% RH, 0.0625 s^{-1}, E_s at 5% strain	[68]
Cold Pressed Linseed Oil, Cobalt Blue PB28, Calcite, Gypsum, Kaolin, Aluminum Stearate	3 years	$E_s = 2.9^{\alpha}$	23°C, 50% RH, 0.0625 s^{-1}, E_s at 1% strain	[68]
Cold Pressed Linseed Oil, Cobalt Blue PB28, Calcite, Gypsum, Kaolin, Aluminum Stearate	3 years	$E_s = 5.2^{\alpha}$	23°C, 50% RH, 0.0625 s^{-1}, E_s at 5% strain	[68]
Cold Pressed Linseed Oil, Cobalt Blue PB28, Calcite, Gypsum, Kaolin, Aluminum Stearate, Castor Wax	3 years	$E_s = 2^{\alpha}$	23°C, 50% RH, 0.0625 s^{-1}, E_s at 1% strain	[68]
Cold Pressed Linseed Oil, Cobalt Blue PB28, Calcite, Gypsum, Kaolin, Aluminum Stearate, Castor Wax	3 years	$E_s = 3.2^{\alpha}$	23°C, 50% RH, 0.0625 s^{-1}, E_s at 5% strain	[68]
Cold Pressed Linseed Oil, Safflower Oil, Sunflower Oil Cobalt Blue PB28, Calcite, Gypsum, Kaolin, Aluminum Stearate, Castor Wax	3 years	$E_s = 1^{\alpha}$	23°C, 50% RH, 0.0625 s^{-1}, E_s at 1% strain	[68]

Sample Composition	Aging time	Mechanical Property (MPa)	Testing Conditions	Reference
Cold Pressed Linseed Oil, Safflower Oil, Sunflower Oil Cobalt Blue PB28, Calcite, Gypsum, Kaolin, Aluminum Stearate, Castor Wax	3 years	$E_s = 1.3^{\alpha}$	23°C, 50% RH, 0.0625 s^{-1}, E_s at 5% strain	[68]

Table A.2: Summary of tensile test data for alkyd paint samples, including composition, aging time of the sample, testing conditions (temperature, RH, strain rate), mechanical property (Youngs modulus (E), equilibrium modulus (E_{eq}), secant modulus (E_s), tensile strength (σ_T), or yield stress (σ_Y), reference, *etc.* *Strain rates from this reference ranged from 0.001-0.01 s^{-1}. $^{\alpha}$Indicates a value estimated from a plot in the paper, rather than a tabulated value.

Sample Composition	Aging Time	Mechanical Property (MPa)	Testing Conditions	References
Alizarine Crimson	10+ years	E = 758	23°C, 50 % RH	[41]*
Alizarine Crimson	10 + years	E = 1257	23°C, 5 % RH	[41]*
Alizarine Crimson	10 + years	E = 4540	−5°C, 5 % RH	[41]*
Burnt Umber	10+ years	E = 1990	23°C, 50 % RH	[41]*
Burnt Umber	10+ years	E = 2794	23°C, 5 % RH	[41]*
Cadmium Yellow	10+ years	E = 1327	23°C, 50 % RH	[41]*
Cadmium Yellow	10+ years	E = 2968	23°C, 5 % RH	[41]*
Iron Oxide Red	10+ years	E = 1152	23°C, 50 % RH	[41]*
Iron Oxide Red	10+ years	E = 2095	23°C, 5 % RH	[41]*
Iron Oxide Red	10+ years	E = 9079	−5°C, 5 % RH	[41]*
Ivory Black	10+ years	E = 559	23°C, 50 % RH	[41]*
Ivory Black	10+ years	E = 1257	23°C, 5 % RH	[41]*
Lead White	10+ years	E = 4190	23°C, 50 % RH	[41]*
Lead White	10+ years	E = 5936	23°C, 5 % RH	[41]*
Lead White	10+ years	E = 8730	−5°C, 5 % RH	[41]*
Titanium White	10+ years	E = 1921	23°C, 50 % RH	[41]*
Titanium White	10+ years	E = 4400	23°C, 5 % RH	[41]*
Yellow Ochre	10+ years	E = 978	23°C, 50 % RH	[41]*
Yellow Ochre	10+ years	E = 2095	23°C, 5 % RH	[41]*
Alkyd Emulsion (URADIL AZ554 Z-50), Cobalt drier	3 days	$E = 8.2^{\alpha}$	Ambient, Load Relaxation, Film Thickness: 0.4 mm	[46]

Sample Composition	Aging Time	Mechanical Property (MPa)	Testing Conditions	References
Alkyd Emulsion (URADIL AZ554 Z-50), Cobalt drier	3 days	E = 7.4$^{\alpha}$	Ambient, Load Relaxation, Film Thickness = 0.7 mm	[46]
Alkyd Emulsion (URADIL AZ554 Z-50), Cobalt drier	3 days	E = 7.0$^{\alpha}$	Ambient, Load Relaxation, Film Thickness = 1 mm	[46]
Alkyd Emulsion (URADIL AZ554 Z-50), Cobalt drier	3 days	E = 5.6$^{\alpha}$	Ambient, Load Relaxation, Film Thickness = 1.4 mm	[46]
Alkyd Emulsion (URADIL AZ554 Z-50), Cobalt drier	11 days	E = 21.0$^{\alpha}$	Ambient, Load Relaxation, Film Thickness = 0.4 mm	[46]
Alkyd Emulsion (URADIL AZ554 Z-50), Cobalt drier	11 days	E = 17.2$^{\alpha}$	Ambient, Load Relaxation, Film Thickness = 0.7 mm	[46]
Alkyd Emulsion (URADIL AZ554 Z-50), Cobalt drier	11 days	E = 14.5$^{\alpha}$	Ambient, Load Relaxation, Film Thickness = 1 mm	[46]
Alkyd Emulsion (URADIL AZ554 Z-50), Cobalt drier	11 days	E = 10.4$^{\alpha}$	Ambient, Load Relaxation, Film Thickness = 1.4 mm	[46]
Alkyd Emulsion (URADIL AZ554 Z-50), Cobalt drier	19 days	E = 31.4$^{\alpha}$	Ambient, Load Relaxation, Film Thickness = 0.4 mm	[46]
Alkyd Emulsion (URADIL AZ554 Z-50), Cobalt drier	19 days	E = 25.1$^{\alpha}$	Ambient, Load Relaxation, Film Thickness = 0.7 mm	[46]
Alkyd Emulsion (URADIL AZ554 Z-50), Cobalt drier	19 days	E = 19.7$^{\alpha}$	Ambient, Load Relaxation, Film Thickness = 1 mm	[46]
Alkyd Emulsion (URADIL AZ554 Z-50), Cobalt drier	19 days	E = 13.7$^{\alpha}$	Ambient, Load Relaxation, Film Thickness = 1.4 mm	[46]
Alkyd Emulsion (URADIL AZ554 Z-50), Cobalt drier	30 days	E = 36.0$^{\alpha}$	Ambient, Load Relaxation, Film Thickness = 0.2 mm	[46]

Sample Composition	Aging Time	Mechanical Property (MPa)	Testing Conditions	References
Alkyd Emulsion (URADIL AZ554 Z-50), Cobalt drier	30 days	E = 35.5$^{\alpha}$	Ambient, Load Relaxation, Film Thickness = 0.4 mm	[46]
Alkyd Emulsion (URADIL AZ554 Z-50), Cobalt drier	30 days	E = 29.6$^{\alpha}$	Ambient, Load Relaxation, Film Thickness = 0.7 mm	[46]
Alkyd Emulsion (URADIL AZ554 Z-50), Cobalt drier	30 days	E = 23.7$^{\alpha}$	Ambient, Load Relaxation, Film Thickness = 1 mm	[46]
Alkyd Emulsion (URADIL AZ554 Z-50), Cobalt drier	30 days	E = 18.3$^{\alpha}$	Ambient, Load Relaxation, Film Thickness = 1.2 mm	[46]
Dulux: Nondrip Gloss, Pure Brilliant White	3 months	$\sigma_T = 9.2^{\alpha}$	21°C, 50% RH, 0.002 s^{-1}	[27]
Dulus Trade: High Gloss, Pure Brilliant White	3 months	$\sigma_T = 6.6^{\alpha}$	21°C, 50% RH, 0.002 s^{-1}	[27]
Crown: Nondrip Gloss, Pure Brilliant White	3 months	$\sigma_T = 6.5^{\alpha}$	21°C, 50% RH, 0.002 s^{-1}	[27]
Griffin (Windsor & Newton), Titanium White	3 months	$\sigma_T = 5.0^{\alpha}$	21°C, 50% RH, 0.002 s^{-1}	[27]
2 -layer: Winsor & Newton Griffin, Cadmium Sulfoselenide; Golden Acrylic Gesso Primer	6 days ambient, 94 days thermal aging	$E_s = 0.36$	20°C, 55% RH, 0.001 s^{-1}, Thermal aging: 60°C, 55% RH, E_s at 0.5% strain	[50]
2 -layer: Winsor & Newton Griffin, Cadmium Sulfoselenide; Golden Acrylic Gesso Primer	6 days ambient, 94 days thermal aging	$E_s = 0.15$	20°C, 55% RH, 0.001 s^{-1}, Thermal aging: 60°C, 55% RH, E_s at 5.0% strain	[50]
2 -layer: Winsor & Newton Griffin, Cadmium Sulfoselenide; Golden Acrylic Gesso Primer	6 days ambient, 0 days thermal aging	$E_s = 0.21$	20°C, 55% RH, 0.001 s^{-1}, Thermal aging: 60°C, 55% RH, E_s at 0.5% strain	[50]

Sample Composition	Aging Time	Mechanical Property (MPa)	Testing Conditions	References
2 -layer: Winsor & Newton Griffin, Cadmium Sulfoselenide; Golden Acrylic Gesso Primer	6 days ambient, 0 days thermal aging	$E_s = 0.08$	20°C, 55% RH, 0.001 s^{-1}, Thermal aging: 60°C, 55% RH, E_s at 5.0% strain	[50]
2 -layer: Winsor & Newton Griffin, Cadmium Sulfoselenide; Roberson Acrylic Primer	6 days ambient, 94 days thermal aging	$E_s = 0.08$	20°C, 55% RH, 0.001 s^{-1}, Thermal aging: 60°C, 55% RH, E_s at 0.5% strain	[50]
2 -layer: Winsor & Newton Griffin, Cadmium Sulfoselenide; Roberson Acrylic Primer	6 days ambient, 94 days thermal aging	$E_s = 0.11$	20°C, 55% RH, 0.001 s^{-1}, Thermal aging: 60°C, 55% RH, E_s at 5.0% strain	[50]
2 -layer: Winsor & Newton Griffin, Cadmium Sulfoselenide; Roberson Acrylic Primer	6 days ambient, 0 days thermal aging	$E_s = 0.08$	20°C, 55% RH, 0.001 s^{-1}, Thermal aging: 60°C, 55% RH, E_s at 0.5% strain	[50]
2 -layer: Winsor & Newton Griffin, Cadmium Sulfoselenide; Roberson Acrylic Primer	6 days ambient, 0 days thermal aging	$E_s = 0.09$	20°C, 55% RH, 0.001 s^{-1}, Thermal aging: 60°C, 55% RH, E_s at 5.0% strain	[50]
2 -layer: Winsor & Newton Griffin, Cadmium Sulfoselenide; Winsor & Newton Alkyd Primer	6 days ambient, 64 days thermal aging	$E_s = 1.06$	20°C, 55% RH, 0.001 s^{-1}, Thermal aging: 60°C, 55% RH, E_s at 0.5% strain	[50]
2 -layer: Winsor & Newton Griffin, Cadmium Sulfoselenide; Winsor & Newton Alkyd Primer	6 days ambient, 0 days thermal aging	$E_s = 0.24$	20°C, 55% RH, 0.001 s^{-1}, Thermal aging: 60°C, 55% RH, E_s at 0.5% strain	[50]

Sample Composition	Aging Time	Mechanical Property (MPa)	Testing Conditions	References
2 -layer: Winsor & Newton Griffin, Cadmium Sulfoselenide; Winsor & Newton Alkyd Primer	6 days ambient, 0 days thermal aging	$E_s = 0.17$	20°C, 55% RH, 0.001 s^{-1}, Thermal aging: 60°C, 55% RH, E_s at 5.0% strain	[50]
2 -layer: Winsor & Newton Griffin, Cadmium Sulfoselenide; Spectrum Alkyd Primer	6 days ambient, 94 days thermal aging	$E_s = 0.07$	20°C, 55% RH, 0.001 s^{-1}, Thermal aging: 60°C, 55% RH, E_s at 0.5% strain	[50]
2 -layer: Winsor & Newton Griffin, Cadmium Sulfoselenide; Spectrum Alkyd Primer	6 days ambient, 94 days thermal aging	$E_s = 0.18$	20°C, 55% RH, 0.001 s^{-1}, Thermal aging: 60°C, 55% RH, E_s at 5.0% strain	[50]
2 -layer: Winsor & Newton Griffin, Cadmium Sulfoselenide; Spectrum Alkyd Primer	6 days ambient, 0 days thermal aging	$E_s = 0.05$	20°C, 55% RH, 0.001 s^{-1}, Thermal aging: 60°C, 55% RH, E_s at 0.5% strain	[50]
2 -layer: Winsor & Newton Griffin, Cadmium Sulfoselenide; Spectrum Alkyd Primer	6 days ambient, 0 days thermal aging	$E_s = 0.01$	20°C, 55% RH, 0.001 s^{-1}, Thermal aging: 60°C, 55% RH, E_s at 5.0% strain	[50]
Winsor & Newton Alkyd Primer	7 months	E = 6340	−10°C, 55% RH, 0.002 s^{-1}	[51]
Winsor & Newton Alkyd Primer	7 months	E = 6020	0°C, 60 RH, 0.002 s^{-1}	[51]
Winsor & Newton Alkyd Primer	7 months	E = 4350	10°C, 57% RH, 0.002 s^{-1}	[51]
Winsor & Newton Alkyd Primer	7 months	E = 2720	20°C, 54% RH, 0.002 s^{-1}	[51]
Spectrum Primer	7 months	E = 4570	−10°C, 55% RH, 0.002 s^{-1}	[51]
Spectrum Primer	7 months	E = 3240	0°C, 60 RH, 0.002 s^{-1}	[51]
Spectrum Primer	7 months	E = 2170	10°C, 57% RH, 0.002 s^{-1}	[51]

Sample Composition	Aging Time	Mechanical Property (MPa)	Testing Conditions	References
Spectrum Primer	7 months	E = 1080	20°C, 54% RH, 0.002 s^{-1}	[51]
Roberson Primer	7 months	E = 6060	−10°C, 55% RH, 0.002 s^{-1}	[51]
Roberson Primer	7 months	E = 3940	0°C, 60 RH, 0.002 s^{-1}	[51]
Roberson Primer	7 months	E = 2760	10°C, 57% RH, 0.002 s^{-1}	[51]
Roberson Primer	7 months	E = 990	20°C, 54% RH, 0.002 s^{-1}	[51]
Winsor & Newton Griffin, Alizarin Red	5 months	$E_s = 4^{ff}$	Ambient Conditions, E_s at 1% strain	[52]
Winsor & Newton Griffin, Phthalocyanine Blue	5 months	$E_s = 12^{ff}$	Ambient Conditions, E_s at 1% strain	[52]
Winsor & Newton Griffin, Ivory Black	5 months	$E_s = 42^{ff}$	Ambient Conditions, E_s at 1% strain	[52]
Winsor & Newton Griffin, Titanium White	5 months	$E_s = 270^{ff}$	Ambient Conditions, E_s at 1% strain	[52]
Winsor & Newton Griffin, Hansa Yellow	5 months	$E_s = 7^{ff}$	Ambient Conditions, E_s at 1% strain	[52]
Winsor & Newton Griffin, Hansa Yellow	5 months	$E_s = 8^{ff}$	Ambient Conditions, E_s at 1% strain, Immersed in water 1 min, Dried 4 weeks	[52]
Winsor & Newton Griffin, Hansa Yellow	5 months	$E_s = 12^{ff}$	Ambient Conditions, E_s at 1% strain, Immersed in n-hexane 1 min, Dried 4 weeks	[52]
Winsor & Newton Griffin, Hansa Yellow	5 months	$E_s = 9^{ff}$	Ambient Conditions, E_s at 1% strain, Immersed in ethanol 1 min, Dried 4 weeks	[52]

Sample Composition	Aging Time	Mechanical Property (MPa)	Testing Conditions	References
Winsor & Newton Griffin, Hansa Yellow	5 months	$E_s = 15^{ff}$	Ambient Conditions, E_s at 1% strain, Immersed in toluene 1 min, Dried 4 weeks	[52]
Winsor & Newton Griffin, Hansa Yellow	5 months	$E_s = 21^{ff}$	Ambient Conditions, E_s at 1% strain, Immersed in diethyl ether 1 min, Dried 4 weeks	[52]
Winsor & Newton Griffin, Hansa Yellow	5 months	$E_s = 13^{ff}$	Ambient Conditions, E_s at 1% strain, Immersed in chloroform 1 min, Dried 4 weeks	[52]
Winsor & Newton Griffin, Hansa Yellow	5 months	$E_s = 49^{ff}$	Ambient Conditions, E_s at 1% strain, Immersed in acetone 1 min, Dried 4 weeks	[52]
DIY Indoor/Outdoor Alkyd, Alizarin Red	5 months	$E_s = 110^{ff}$	Ambient Conditions, E_s at 1% strain	[52]
DIY Indoor/Outdoor Alkyd, Phthalocyanine Blue	5 months	$E_s = 140^{ff}$	Ambient Conditions, E_s at 1% strain	[52]
DIY Indoor/Outdoor Alkyd, Ivory Black	5 months	$E_s = 190^{ff}$	Ambient Conditions, E_s at 1% strain	[52]
DIY Indoor/Outdoor Alkyd, Titanium White	5 months	$E_s = 270^{ff}$	Ambient Conditions, E_s at 1% strain	[52]
DIY Indoor/Outdoor Alkyd, Hansa Yellow	5 months	$E_s = 120^{ff}$	Ambient Conditions, E_s at 1% strain	[52]

Sample Composition	Aging Time	Mechanical Property (MPa)	Testing Conditions	References
DIY Indoor/Outdoor Alkyd, Hansa Yellow	5 months	$E_s = 105^{ff}$	Ambient Conditions, E_s at 1% strain, Immersed in water 1 min, Dried 4 weeks	[52]
DIY Indoor/Outdoor Alkyd, Hansa Yellow	5 months	$E_s = 108^{ff}$	Ambient Conditions, E_s at 1% strain, Immersed in n-hexane 1 min, Dried 4 weeks	[52]
DIY Indoor/Outdoor Alkyd, Hansa Yellow	5 months	$E_s = 124^{ff}$	Ambient Conditions, E_s at 1% strain, Immersed in ethanol 1 min, Dried 4 weeks	[52]
DIY Indoor/Outdoor Alkyd, Hansa Yellow	5 months	$E_s = 135^{ff}$	Ambient Conditions, E_s at 1% strain, Immersed in toluene 1 min, Dried 4 weeks	[52]
DIY Indoor/Outdoor Alkyd, Hansa Yellow	5 months	$E_s = 119^{ff}$	Ambient Conditions, E_s at 1% strain, Immersed in diethyl ether 1 min, Dried 4 weeks	[52]
DIY Indoor/Outdoor Alkyd, Hansa Yellow	5 months	$E_s = 160^{ff}$	Ambient Conditions, E_s at 1% strain, Immersed in chloroform 1 min, Dried 4 weeks	[52]
DIY Indoor/Outdoor Alkyd, Hansa Yellow	5 months	$E_s = 168^{ff}$	Ambient Conditions, E_s at 1% strain, Immersed in acetone 1 min, Dried 4 weeks	[52]

Sample Composition	Aging Time	Mechanical Property (MPa)	Testing Conditions	References
Winsor & Newton Griffin, Titanium Dioxide	7 years	$E_s = 125^{ff}$	23°C, 50 % RH, 0.0005 s^{-1}, E_s at 0.5% strain	[58]
Gamblin "Alkyd White," Zinc Oxide	7 years	$E_s = 580^{ff}$	23°C, 50 % RH, 0.0005 s^{-1}, E_s at 0.5% strain	[58]
Winsor & Newton Griffin, Cobalt Blue	7 years	$E_s = 75^{ff}$	23°C, 50 % RH, 0.0005 s^{-1}, E_s at 0.5% strain	[58]
Winsor & Newton, Flake White	29 years	$E_s = 2780^{ff}$	23°C, 50 % RH, 0.0005 s^{-1}, E_s at 0.25% strain	[58]
Winsor & Newton, Burnt Umber	29 years	$E_s = 1720^{ff}$	23°C, 50 % RH, 0.0005 s^{-1}, E_s at 0.5% strain	[58]
Winsor & Newton, Titanium White	29 years	$E_s = 980^{ff}$	23°C, 50 % RH, 0.0005 s^{-1}, E_s at 1% strain	[58]
Winsor & Newton, Alizarin Crimson	20 years	$E_s = 150^{ff}$	23°C, 50 % RH, 0.0005 s^{-1}, E_s at 1% strain	[58]
Winsor & Newton, Alizarin Crimson	29 years	$E_s = 240^{ff}$	23°C, 50 % RH, 0.0005 s^{-1}, E_s at 1% strain	[58]
Winsor & Newton, Alizarin Crimson	29 years	$E_s = 260^{ff}$	23°C, 50 % RH, 0.0005 s^{-1}, Immersed in Acetone 30 sec and dried,E_s at 1% strain	[58]
Winsor & Newton, Alizarin Crimson	29 years	$E_s = 280^{ff}$	23°C, 50 % RH, 0.0005 s^{-1}, Immersed in Methanol 30 sec, E_s at 1% strain	[58]
Winsor & Newton, Yellow Ochre	29 years	$E_s = 150^{ff}$	23°C, 50 % RH, 0.0005 s^{-1}, E_s at 1% strain	[58]
Winsor & Newton, Ivory Black	29 years	$E_s = 140^{ff}$	23°C, 50 % RH, 0.0005 s^{-1}, E_s at 1% strain	[58]

Sample Composition	Aging Time	Mechanical Property (MPa)	Testing Conditions	References
Winsor & Newton Griffin Titanium White: Oil-modified alkyd, TiO_2	6-10 years	$E_s = 4850^{ff}$	$-10°C$, 50 % RH, 0.002 s^{-1}, E_s at 0.5% strain	[64]
Winsor & Newton Griffin Titanium White: Oil-modified alkyd, TiO_2	6-10 years	$E_s = 4480^{ff}$	$-10°C$, 50 % RH, 0.0002 s^{-1}, E_s at 0.5% strain	[64]
Winsor & Newton Griffin Titanium White: Oil-modified alkyd, TiO_2	6-10 years	$E_s = 4270^{ff}$	$0°C$, 50 % RH, 0.002 s^{-1}, E_s at 0.5% strain	[64]
Winsor & Newton Griffin Titanium White: Oil-modified alkyd, TiO_2	6-10 years	$E_s = 3370^{ff}$	$-10°C$, 50 % RH, 0.00002 s^{-1}, E_s at 0.5% strain	[64]
Winsor & Newton Griffin Titanium White: Oil-modified alkyd, TiO_2	6-10 years	$E_s = 3010^{ff}$	$10°C$, 50 % RH, 0.02 s^{-1}, E_s at 0.5% strain	[64]
Winsor & Newton Griffin Titanium White: Oil-modified alkyd, TiO_2	6-10 years	$E_s = 2560^{ff}$	$10°C$, 50 % RH, 0.002 s^{-1}, E_s at 0.5% strain	[64]
Winsor & Newton Griffin Titanium White: Oil-modified alkyd, TiO_2	6-10 years	$E_s = 1350^{ff}$	$20°C$, 50 % RH, 0.02 s^{-1}, E_s at 0.5% strain	[64]
Winsor & Newton Griffin Titanium White: Oil-modified alkyd, TiO_2	6-10 years	$E_s = 1120^{ff}$	$10°C$, 50 % RH, 0.0002 s^{-1}, E_s at 0.5% strain	[64]
Winsor & Newton Griffin Titanium White: Oil-modified alkyd, TiO_2	6-10 years	$E_s = 790^{ff}$	$20°C$, 50 % RH, 0.002 s^{-1}, E_s at 0.5% strain	[64]

Sample Composition	Aging Time	Mechanical Property (MPa)	Testing Conditions	References
Winsor & Newton Griffin Titanium White: Oil-modified alkyd, TiO_2	6-10 years	$E_s = 680^{ff}$	10°C, 50 % RH, 0.00002 s^{-1}, E_s at 0.5% strain	[64]
Winsor & Newton Griffin Titanium White: Oil-modified alkyd, TiO_2	6-10 years	$E_s = 410^{ff}$	20°C, 50 % RH, 0.0002 s^{-1}, E_s at 0.5% strain	[64]
Winsor & Newton Alkyd Paint, Cobalt Blue PB28	2 years	$E_s = 43^{\alpha}$	23°C, 50 % RH, 0.0625 s^{-1}, E_s at 1% strain	[68]
Winsor & Newton Alkyd Paint, Cobalt Blue PB28	8 years	$E_s = 140^{\alpha}$	23°C, 50 % RH, 0.0625 s^{-1}, E_s at 1% strain	[68]
Winsor & Newton Alkyd Paint, Cobalt Blue PB28	19 years	$E_s = 170^{\alpha}$	23°C, 50 % RH, 0.0625 s^{-1}, E_s at 1% strain	[68]
Winsor & Newton Griffin Artists' Alkyd Paint, Cobalt Blue PB28	8 years	$E_s = 84^{\alpha}$	23°C, 50 % RH, 0.0625 s^{-1}, E_s at 1% strain	[68]
Winsor & Newton Griffin Artists' Alkyd Paint, Cobalt Blue PB28	19 years	$E_s = 400^{\alpha}$	23°C, 50 % RH, 0.0625 s^{-1}, E_s at 1% strain	[68]

Table A.3: Summary of tensile test data for acrylic paint samples, including composition, aging time of the sample, testing conditions (temperature, RH, strain rate), mechanical property (Youngs modulus (E), equilibrium modulus (E_{eq}), secant modulus (E_s), tensile strength (σ_T), or yield stress (σ_Y), reference, *etc.* *Strain rates from this reference ranged from 0.001-0.01 s^{-1}. $^{\alpha}$Indicates a value estimated from a plot in the paper, rather than a tabulated value.

Sample Composition	Aging Time	Mechanical Property (MPa)	Testing Conditions	References
Burnt Sienna	10+ years	E = 279	23°C, 50 % RH	[41]*
Burnt Sienna	10+ years	E = 1048	23°C, 5 % RH	[41]*
Burnt Sienna	10+ years	E = 6425	−6.5°C, 5 % RH	[41]*
Burnt Sienna	10+ years	E = 6111	5°C, 5 % RH	[41]*
Burnt Sienna	13 years	E_{eq} = 62.9	23°C, 50 % RH, stress relaxation	[42]

Sample Composition	Aging Time	Mechanical Property (MPa)	Testing Conditions	References
Burnt Umber	10+ years	E = 77	23°C, 50 % RH	[41]*
Burnt Umber	10+ years	E = 349	23°C, 5 % RH	[41]*
Burnt Umber	10+ years	E = 3981	−8.1°C, 50 % RH	[41]*
Burnt Umber	10+ years	E = 1571	5.6°C, 50 % RH	[41]*
Burnt Umber	10+ years	E = 17	33.4°C, 50 % RH	[41]*
Cadmium Red	10+ years	E = 161	23°C, 50 % RH	[41]*
Cadmium Yellow	10+ years	E = 105	23°C, 50 % RH	[41]*
Cadmium Yellow	10+ years	E = 475	23°C, 5 % RH	[41]*
Cadmium Yellow	10+ years	E = 5517	−6.5°C, 5 % RH	[41]*
Cadmium Yellow	10+ years	E = 4470	5°C, 5 % RH	[41]*
Cerulean Blue	10+ years	E = 140	23°C, 50 % RH	[41]*
Cerulean Blue	10+ years	E = 265	23°C, 5 % RH	[41]*
Cobalt Blue	10+ years	E = 314	23°C, 50 % RH	[41]*
Cobalt Blue	10+ years	E = 698	23°C, 5 % RH	[41]*
Cobalt Blue	10+ years	E = 6495	−8.1°C, 50 % RH	[41]*
Cobalt Blue	10+ years	E = 2025	5.6°C, 50 % RH	[41]*
Cobalt Blue	10+ years	E = 23	33.4°C, 50 % RH	[41]*
Iron Oxide Red	10+ years	E = 279	23°C, 50 % RH	[41]*
Iron Oxide Red	10+ years	E = 663	23°C, 5 % RH	[41]*
Ivory Black	10+ years	E = 84	23°C, 50 % RH	[41]*
Ivory Black	10+ years	E = 279	23°C, 5 % RH	[41]*
Ivory Black	10+ years	E = 3413	−4.3°C, 50 % RH	[41]*
Ivory Black	10+ years	E = 1467	5.6°C, 50 % RH	[41]*
Ivory Black	10+ years	E = 4.75	33.4°C, 50 % RH	[41]*
Raw Sienna	10+ years	E = 70	23°C, 50 % RH	[41]*
Raw Sienna	10+ years	E = 223	23°C, 5 % RH	[41]*
Titanium White	10+ years	E = 147	23°C, 50 % RH	[41]*
Titanium White	10+ years	E = 978	23°C, 5 % RH	[41]*
Titanium White	10+ years	E = 10476	−6.5°C, 5 % RH	[41]*
Titanium White	10+ years	E = 6286	5°C, 5 % RH	[41]*
Titanium White	13 years	E_{eq} = 83.8	23°C, 50 % RH	[42]
Liquitex gloss medium	10 days	$\sigma_T = 8.7^{\alpha}$	25°C, 40 % RH, aged in the dark, 5 s^{-1}	[43]
Liquitex gloss medium	10 days	$\sigma_Y = 2.2^{\alpha}$	25°C, 40 % RH, aged in the dark, 5 s^{-1}	[43]
Liquitex gloss medium	36 days	$\sigma_T = 11.7^{\alpha}$	25°C, 40 % RH, aged in the dark, 5 s^{-1}	[43]
Liquitex gloss medium	36 days	$\sigma_Y = 3.6^{\alpha}$	25°C, 40 % RH, aged in the dark, 5 s^{-1}	[43]

Sample Composition	Aging Time	Mechanical Property (MPa)	Testing Conditions	References
Liquitex gloss medium	65 days	$\sigma_T = 12.2^{\alpha}$	25°C, 40 % RH, aged in the dark, 5 s^{-1}	[43]
Liquitex gloss medium	65 days	$\sigma_Y = 5.9^{\alpha}$	25°C, 40 % RH, aged in the dark, 5 s^{-1}	[43]
Liquitex gloss medium	72 days	$\sigma_T = 13.1^{\alpha}$	25°C, 40 % RH, aged in the dark, 5 s^{-1}	[43]
Liquitex gloss medium	72 days	$\sigma_Y = 5.8^{\alpha}$	25°C, 40 % RH, aged in the dark, 5 s^{-1}	[43]
Liquitex gloss medium	120 days	$\sigma_T = 14.0^{\alpha}$	25°C, 40 % RH, aged in the dark, 5 s^{-1}	[43]
Liquitex gloss medium	120 days	$\sigma_Y = 6.8^{\alpha}$	25°C, 40 % RH, aged in the dark, 5 s^{-1}	[43]
Liquitex gloss medium	153 days	$\sigma_T = 13.7^{\alpha}$	25°C, 40 % RH, aged in the dark, 5 s^{-1}	[43]
Liquitex gloss medium	153 days	$\sigma_Y = 6.4^{\alpha}$	25°C, 40 % RH, aged in the dark, 5 s^{-1}	[43]
Liquitex gloss medium	167 days	$\sigma_T = 13.9^{\alpha}$	25°C, 40 % RH, aged in the dark, 5 s^{-1}	[43]
Liquitex gloss medium	167 days	$\sigma_Y = 6.2^{\alpha}$	25°C, 40 % RH, aged in the dark, 5 s^{-1}	[43]
Liquitex gloss medium	569 days	$\sigma_T = 13.8^{\alpha}$	25°C, 40 % RH, aged in the dark, 5 s^{-1}	[43]
Liquitex gloss medium	569 days	$\sigma_Y = 5.3^{\alpha}$	25°C, 40 % RH, aged in the dark, 5 s^{-1}	[43]
Liquitex gloss medium	0 days of UV-B exposure	$\sigma_T = 12.3^{\alpha}$	23°C, 50 % RH, aged in the dark 60 days before UV-B exposure, 5 s^{-1}	[43]
Liquitex gloss medium	0 days of UV-B exposure	$\sigma_Y = 5.6^{\alpha}$	23°C, 50 % RH, aged in the dark 60 days before UV-B exposure, 5 s^{-1}	[43]

Sample Composition	Aging Time	Mechanical Property (MPa)	Testing Conditions	References
Liquitex gloss medium	3 days of UV-B exposure	$\sigma_T = 9.6^{\alpha}$	23°C, 50 % RH, aged in the dark 60 days before UV-B exposure, 5 s^{-1}	[43]
Liquitex gloss medium	3 days of UV-B exposure	$\sigma_Y = 4.1^{\alpha}$	23°C, 50 % RH, aged in the dark 60 days before UV-B exposure, 5 s^{-1}	[43]
Liquitex gloss medium	7 days of UV-B exposure	$\sigma_T = 9.7^{\alpha}$	23°C, 50 % RH, aged in the dark 60 days before UV-B exposure, 5 s^{-1}	[43]
Liquitex gloss medium	7 days of UV-B exposure	$\sigma_Y = 7.1^{\alpha}$	23°C, 50 % RH, aged in the dark 60 days before UV-B exposure, 5 s^{-1}	[43]
Liquitex gloss medium	20 days of UV-B exposure	$\sigma_T = 9.04^{\alpha}$	23°C, 50 % RH, aged in the dark 60 days before UV-B exposure, 5 s^{-1}	[43]
Liquitex gloss medium	20 days of UV-B exposure	$\sigma_Y = 9.9^{\alpha}$	23°C, 50 % RH, aged in the dark 60 days before UV-B exposure, 5 s^{-1}	[43]
Liquitex gloss medium	27 days of UV-B exposure	$\sigma_T = 2.6^{\alpha}$	23°C, 50 % RH, aged in the dark 60 days before UV-B exposure, 5 s^{-1}	[43]
Liquitex gloss medium	27 days of UV-B exposure	$\sigma_Y = 2.7^{\alpha}$	23°C, 50 % RH, aged in the dark 60 days before UV-B exposure, 5 s^{-1}	[43]
Liquitex gloss medium	0 days of UV-A exposure	$\sigma_T = 12.3^{\alpha}$	23°C, 50 % RH, aged in the dark 60 days before UV-A exposure, 5 s^{-1}	[43]
Liquitex gloss medium	0 days of UV-A exposure	$\sigma_Y = 5.6^{\alpha}$	23°C, 50 % RH, aged in the dark 60 days before UV-A exposure, 5 s^{-1}	[43]
Liquitex gloss medium	20 days of UV-A exposure	$\sigma_T = 9.6^{\alpha}$	23°C, 50 % RH, aged in the dark 60 days before UV-A exposure, 5 s^{-1}	[43]

Sample Composition	Aging Time	Mechanical Property (MPa)	Testing Conditions	References
Liquitex gloss medium	20 days of UV-A exposure	$\sigma_Y = 3.9^{\alpha}$	23°C, 50 % RH, aged in the dark 60 days before UV-A exposure, 5 s^{-1}	[43]
Liquitex gloss medium	42 days of UV-A exposure	$\sigma_T = 9.3^{\alpha}$	23°C, 50 % RH, aged in the dark 60 days before UV-A exposure, 5 s^{-1}	[43]
Liquitex gloss medium	42 days of UV-A exposure	$\sigma_Y = 4.8^{\alpha}$	23°C, 50 % RH, aged in the dark 60 days before UV-A exposure, 5 s^{-1}	[43]
Liquitex gloss medium	84 days of UV-A exposure	$\sigma_T = 9.7^{\alpha}$	23°C, 50 % RH, aged in the dark 60 days before UV-A exposure, 5 s^{-1}	[43]
Liquitex gloss medium	84 days of UV-A exposure	$\sigma_Y = 8.0^{\alpha}$	23°C, 50 % RH, aged in the dark 60 days before UV-A exposure, 5 s^{-1}	[43]
Rhoplex AC-234, Bone Black	7 months	$\sigma_T = 7.4^{\alpha}$	21°C, 20% RH, 0.0028 s^{-1}	[47]
Rhoplex AC-234, Bone Black	7 months	$E_s = 81.7^{ff}$	21°C, 20% RH, 0.0028 s^{-1}	[47]
Rhoplex AC-234, Bone Black	7 months	$\sigma_T = 5.7^{\alpha}$	21°C, 40% RH, 0.0028 s^{-1}	[47]
Rhoplex AC-234, Bone Black	7 months	$E_s = 48.9^{ff}$	21°C, 40% RH, 0.0028 s^{-1}	[47]
Rhoplex AC-234, Bone Black	7 months	σ_T =25	1.5°C, 50% RH, 0.0028 s^{-1}	[47]
Rhoplex AC-234, Bone Black	7 months	E_s =2281	1.5°C, 50% RH, 0.0028 s^{-1}	[47]
Rhoplex AC-234, Bone Black	7 months	σ_T =8.4	7.5°C, 50% RH, 0.0028 s^{-1}	[47]
Rhoplex AC-234, Bone Black	7 months	E_s =643	7.5°C, 50% RH, 0.0028 s^{-1}	[47]
Rhoplex AC-234, Bone Black	2 days	$\sigma_T = 1.8$	21°C, 50% RH, 0.0028 s^{-1}	[47]
Rhoplex AC-234, Bone Black	2 days	$E_s = 9.9$	21°C, 50% RH, 0.0028 s^{-1}	[47]
Rhoplex AC-234, Bone Black	5 months	$\sigma_T = 4.4$	21°C, 50% RH, 0.0028 s^{-1}	[47]
Rhoplex AC-234, Bone Black	5 months	$E_s = 24$	21°C, 50% RH, 0.0028 s^{-1}	[47]

Sample Composition	Aging Time	Mechanical Property (MPa)	Testing Conditions	References
Rhoplex AC-234, Bone Black	7 months	$\sigma_T = 5.0^{\alpha}$	21°C, 50% RH, 0.0028 s^{-1}	[47]
Rhoplex AC-234, Bone Black	7 months	$E_s = 31.0^{ff}$	21°C, 50% RH, 0.0028 s^{-1}	[47]
Rhoplex AC-234, Bone Black	13 months	$\sigma_T = 4.8$	21°C, 50% RH, 0.0028 s^{-1}	[47]
Rhoplex AC-234, Bone Black	13 months	$E_s = 31$	21°C, 50% RH, 0.0028 s^{-1}	[47]
Rhoplex AC-234, Bone Black	7 months	$\sigma_T = 3.2$	31°C, 50% RH, 0.0028 s^{-1}	[47]
Rhoplex AC-234, Bone Black	7 months	$E_s = 19$	31°C, 50% RH, 0.0028 s^{-1}	[47]
Rhoplex AC-234, Bone Black	7 months	$\sigma_T = 4.1^{\alpha}$	21°C, 60% RH, 0.0028 s^{-1}	[47]
Rhoplex AC-234, Bone Black	7 months	$E_s = 18.8^{ff}$	21°C, 60% RH, 0.0028 s^{-1}	[47]
Rhoplex AC-234, Bone Black	7 months	$\sigma_T = 2.3^{\alpha}$	21°C, 80% RH, 0.0028 s^{-1}	[47]
Rhoplex AC-234, Bone Black	7 months	$E_s = 6.3^{ff}$	21°C, 80% RH, 0.0028 s^{-1}	[47]
Rhoplex AC-234, Bone Black	7 months	$\sigma_T = 9.1^{\alpha}$	21°C, 20% RH, immersed in water 24 hours, dried 72 hours, 0.0028 s^{-1}	[47]
Rhoplex AC-234, Bone Black	7 months	$E_s = 99.5^{\alpha}$	21°C, 20% RH, immersed in water 24 hours, dried 72 hours, 0.0028 s^{-1}	[47]
Rhoplex AC-234, Bone Black	7 months	$\sigma_T = 7.0^{\alpha}$	21°C, 40% RH, immersed in water 24 hours, dried 72 hours, 0.0028 s^{-1}	[47]
Rhoplex AC-234, Bone Black	7 months	$E_s = 72.3^{ff}$	21°C, 40% RH, immersed in water 24 hours, dried 72 hours, 0.0028 s^{-1}	[47]
Rhoplex AC-234, Bone Black	7 months	$\sigma_T = 5.3^{\alpha}$	21°C, 50% RH, immersed in water 15 min, dried 72 hours, 0.0028 s^{-1}	[47]
Rhoplex AC-234, Bone Black	7 months	$E_s = 36.7^{ff}$	21°C, 50% RH, immersed in water 15 min, dried 72 hours, 0.0028 s^{-1}	[47]

Sample Composition	Aging Time	Mechanical Property (MPa)	Testing Conditions	References
Rhoplex AC-234, Bone Black	7 months	$\sigma_T = 5.7^{\alpha}$	21°C, 50% RH, immersed in water 1 hours, dried 72 hours, 0.0028 s^{-1}	[47]
Rhoplex AC-234, Bone Black	7 months	$E_s = 42.2^{ff}$	21°C, 50% RH, immersed in water 1 hours, dried 72 hours, 0.0028 s^{-1}	[47]
Rhoplex AC-234, Bone Black	7 months	$\sigma_T = 6.1^{\alpha}$	21°C, 50% RH, immersed in water 6 hours, dried 72 hours, 0.0028 s^{-1}	[47]
Rhoplex AC-234, Bone Black	7 months	$E_s = 50.8^{\alpha}$	21°C, 50% RH, immersed in water 6 hours, dried 72 hours, 0.0028 s^{-1}	[47]
Rhoplex AC-234, Bone Black	7 months	$\sigma_T = 6.3^{\alpha}$	21°C, 50% RH, immersed in water 24 hours, dried 72 hours, 0.0028 s^{-1}	[47]
Rhoplex AC-234, Bone Black	7 months	$E_s = 53.5^{ff}$	21°C, 50% RH, immersed in water 24 hours, dried 72 hours, 0.0028 s^{-1}	[47]
Rhoplex AC-234, Bone Black	7 months	$\sigma_T = 5.3^{\alpha}$	21°C, 60% RH, immersed in water 24 hours, dried 72 hours, 0.0028 s^{-1}	[47]
Rhoplex AC-234, Bone Black	7 months	$E_s = 40.2$	21°C, 60% RH, immersed in water 24 hours, dried 72 hours, 0.0028 s^{-1}	[47]
Rhoplex AC-234, Bone Black	7 months	$\sigma_T = 3.7^{\alpha}$	21°C, 80% RH, immersed in water 24 hours, dried 72 hours, 0.0028 s^{-1}	[47]
Rhoplex AC-234, Bone Black	7 months	$E_s = 17.4^{\alpha}$	21°C, 80% RH, immersed in water 24 hours, dried 72 hours, 0.0028 s^{-1}	[47]
Rhoplex AC-234, Naphthol Red Light	7 months	$\sigma_T = 4.5^{\alpha}$	21°C, 20% RH, 0.0028 s^{-1}	[47]

Sample Composition	Aging Time	Mechanical Property (MPa)	Testing Conditions	References
Rhoplex AC-234, Naphthol Red Light	7 months	$E_s = 39.4^{ff}$	21°C, 20% RH, 0.0028 s^{-1}	[47]
Rhoplex AC-234, Naphthol Red Light	7 months	$\sigma_T = 3.0^{\alpha}$	21°C, 40% RH, 0.0028 s^{-1}	[47]
Rhoplex AC-234, Naphthol Red Light	7 months	$E_s = 22.9^{\alpha}$	21°C, 40% RH, 0.0028 s^{-1}	[47]
Rhoplex AC-234, Naphthol Red Light	7 months	$\sigma_T = 2.3^{\alpha}$	21°C, 50% RH, 0.0028 s^{-1}	[47]
Rhoplex AC-234, Naphthol Red Light	7 months	$E_s = 13.7^{\alpha}$	21°C, 50% RH, 0.0028 s^{-1}	[47]
Rhoplex AC-234, Naphthol Red Light	7 months	$\sigma_T = 1.8^{\alpha}$	21°C, 60% RH, 0.0028 s^{-1}	[47]
Rhoplex AC-234, Naphthol Red Light	7 months	$E_s = 7.0^{ff}$	21°C, 60% RH, 0.0028 s^{-1}	[47]
Rhoplex AC-234, Naphthol Red Light	7 months	$\sigma_T = 1.0^{\alpha}$	21°C, 80% RH, 0.0028 s^{-1}	[47]
Rhoplex AC-234, Naphthol Red Light	7 months	$E_s = 5.7^{ff}$	21°C, 80% RH, 0.0028 s^{-1}	[47]
Rhoplex AC-234, Naphthol Red Light	7 months	$\sigma_T = 5.7^{\alpha}$	21°C, 20% RH, immersed in water 24 hours, dried 72 hours, 0.0028 s^{-1}	[47]
Rhoplex AC-234, Naphthol Red Light	7 months	$E_s = 50.7^{ff}$	21°C, 20% RH, immersed in water 24 hours, dried 72 hours, 0.0028 s^{-1}	[47]
Rhoplex AC-234, Naphthol Red Light	7 months	$\sigma_T = 4.2^{\alpha}$	21°C, 40% RH, immersed in water 24 hours, dried 72 hours, 0.0028 s^{-1}	[47]
Rhoplex AC-234, Naphthol Red Light	7 months	$E_s = 35.2^{\alpha}$	21°C, 40% RH, immersed in water 24 hours, dried 72 hours, 0.0028 s^{-1}	[47]

Sample Composition	Aging Time	Mechanical Property (MPa)	Testing Conditions	References
Rhoplex AC-234, Naphthol Red Light	7 months	$\sigma_T = 3.3^{\alpha}$	21°C, 50% RH, immersed in water 24 hours, dried 72 hours, 0.0028 s^{-1}	[47]
Rhoplex AC-234, Naphthol Red Light	7 months	$E_s = 27.0^{\alpha}$	21°C, 50% RH, immersed in water 24 hours, dried 72 hours, 0.0028 s^{-1}	[47]
Rhoplex AC-234, Naphthol Red Light	7 months	$\sigma_T = 2.9^{\alpha}$	21°C, 60% RH, immersed in water 24 hours, dried 72 hours, 0.0028 s^{-1}	[47]
Rhoplex AC-234, Naphthol Red Light	7 months	$E_s = 21.6^{\alpha}$	21°C, 60% RH, immersed in water 24 hours, dried 72 hours, 0.0028 s^{-1}	[47]
Rhoplex AC-234, Naphthol Red Light	7 months	$\sigma_T = 1.9^{\alpha}$	21°C, 80% RH, immersed in water 24 hours, dried 72 hours, 0.0028 s^{-1}	[47]
Rhoplex AC-234, Naphthol Red Light	7 months	$E_s = 12.6^{ff}$	21°C, 80% RH, immersed in water 24 hours, dried 72 hours, 0.0028 s^{-1}	[47]
Golden Acrylic (BA/MMA), Titanium White	3 months	$E = 23^{\alpha}$	21°C, 50% RH, 0.00002 s^{-1}	[27]
Golden Acrylic (BA/MMA), Titanium White	3 months	$E = 41^{\alpha}$	21°C, 50% RH, 0.0002 s^{-1}	[27]
Golden Acrylic (BA/MMA), Titanium White	3 months	$E = 204^{\alpha}$	21°C, 15% RH, 0.002 s^{-1}	[27]
Golden Acrylic (BA/MMA), Titanium White	3 months	$E = 89^{\alpha}$	21°C, 35% RH, 0.002 s^{-1}	[27]
Golden Acrylic (BA/MMA), Titanium White	3 months	$\sigma_T = 11.5^{\alpha}$	21°C, 50% RH, 0.002 s^{-1}	[27]
Golden Acrylic (BA/MMA), Titanium White	3 months	$E = 90^{\alpha}$	21°C, 50% RH, 0.002 s^{-1}	[27]
Golden Acrylic (BA/MMA), Titanium White	3 months	$E = 13^{\alpha}$	21°C, 65% RH, 0.002 s^{-1}	[27]

Sample Composition	Aging Time	Mechanical Property (MPa)	Testing Conditions	References
Golden Acrylic (BA/MMA), Titanium White	3 months	$E = 3.2^{\alpha}$	21°C, 85% RH, 0.002 s^{-1}	[27]
Golden Acrylic (BA/MMA), Titanium White	3 months	$E = 227^{\alpha}$	21°C, 50% RH, 0.02 s^{-1}	[27]
Golden Acrylic (BA/MMA), Titanium White	3 months	$E = 444^{\alpha}$	21°C, 50% RH, 0.2 s^{-1}	[27]
Dulux Trade: Eggshell, Pure Brilliant White	3 months	$\sigma_T = 5.6^{\alpha}$	21°C, 50% RH, 0.002 s^{-1}	[27]
Dulux Trade: Vinyl Silk, Pure Brilliant White	3 months	$\sigma_T = 3.6^{\alpha}$	21°C, 50% RH, 0.002 s^{-1}	[27]
Dulux Trade: Matte, Pure Brilliant White	3 months	$\sigma_T = 4.4^{\alpha}$	21°C, 50% RH, 0.002 s^{-1}	[27]
Crown: Matte, Pure Brilliant White	3 months	$E = 1110^{\alpha}$	21°C, 50% RH, 0.000002 s^{-1}	[27]
Crown: Matte, Pure Brilliant White	3 months	$E = 1250^{\alpha}$	21°C, 50% RH, 0.00002 s^{-1}	[27]
Crown: Matte, Pure Brilliant White	3 months	$E = 1570^{\alpha}$	21°C, 50% RH, 0.0002 s^{-1}	[27]
Crown: Matte, Pure Brilliant White	3 months	$\sigma_T = 4.3^{\alpha}$	21°C, 50% RH, 0.002 s^{-1}	[27]
Crown: Matte, Pure Brilliant White	3 months	$E = 2080^{\alpha}$	21°C, 50% RH, 0.002 s^{-1}	[27]
Crown: Matte, Pure Brilliant White	3 months	$E = 2430^{\alpha}$	21°C, 50% RH, 0.02 s^{-1}	[27]
2 -layer: Liquitex, Cadmium Selenosulfide; Golden Acrylic Gesso Primer	6 days ambient, 112 days thermal aging	$E_s = 0.11$	20°C, 55% RH, 0.001 s^{-1}, Thermal aging: 60°C, 55% RH, E_s at 0.5% strain	[50]

Sample Composition	Aging Time	Mechanical Property (MPa)	Testing Conditions	References
2 -layer: Liquitex, Cadmium Selenosulfide; Golden Acrylic Gesso Primer	6 days ambient, 112 days thermal aging	$E_s = 0.04$	20°C, 55% RH, 0.001 s^{-1}, Thermal aging: 60°C, 55% RH, E_s at 5.0% strain	[50]
2 -layer: Liquitex, Cadmium Selenosulfide; Golden Acrylic Gesso Primer	6 days ambient, 0 days thermal aging	$E_s = 0.06$	20°C, 55% RH, 0.001 s^{-1}, Thermal aging: 60°C, 55% RH, E_s at 0.5% strain	[50]
2 -layer: Liquitex, Cadmium Selenosulfide; Golden Acrylic Gesso Primer	6 days ambient, 0 days thermal aging	$E_s = 0.03$	20°C, 55% RH, 0.001 s^{-1}, Thermal aging: 60°C, 55% RH, E_s at 5.0% strain	[50]
2 -layer: Liquitex, Cadmium Selenosulfide; Roberson Acrylic Primer	6 days ambient, 112 days thermal aging	$E_s = 0.04$	20°C, 55% RH, 0.001 s^{-1}, Thermal aging: 60°C, 55% RH, E_s at 5.0% strain	[50]
2 -layer: Liquitex, Cadmium Selenosulfide; Roberson Acrylic Primer	6 days ambient, 0 days thermal aging	$E_s = 0.02$	20°C, 55% RH, 0.001 s^{-1}, Thermal aging: 60°C, 55% RH, E_s at 5.0% strain	[50]
2 -layer: Liquitex, Cadmium Selenosulfide; Winsor & Newton Alkyd Primer	6 days ambient, 112 days thermal aging	$E_s = 0.14$	20°C, 55% RH, 0.001 s^{-1}, Thermal aging: 60°C, 55% RH, E_s at 5.0% strain	[50]
2 -layer: Liquitex, Cadmium Selenosulfide; Winsor & Newton Alkyd Primer	6 days ambient, 0 days thermal aging	$E_s = 0.05$	20°C, 55% RH, 0.001 s^{-1}, Thermal aging: 60°C, 55% RH, E_s at 5.0% strain	[50]
2 -layer: Liquitex, Cadmium Selenosulfide; Spectrum Alkyd Primer	6 days ambient, 112 days thermal aging	$E_s = 0.17$	20°C, 55% RH, 0.001 s^{-1}, Thermal aging: 60°C, 55% RH, E_s at 0.5% strain	[50]
2 -layer: Liquitex, Cadmium Selenosulfide; Spectrum Alkyd Primer	6 days ambient, 112 days thermal aging	$E_s = 0.08$	20°C, 55% RH, 0.001 s^{-1}, Thermal aging: 60°C, 55% RH, E_s at 5.0% strain	[50]

Sample Composition	Aging Time	Mechanical Property (MPa)	Testing Conditions	References
2 -layer: Liquitex, Cadmium Selenosulfide; Spectrum Alkyd Primer	6 days ambient, 0 days thermal aging	$E_s = 0.05$	20°C, 55% RH, 0.001 s^{-1}, Thermal aging: 60°C, 55% RH, E_s at 0.5% strain	[50]
2 -layer: Liquitex, Cadmium Selenosulfide; Spectrum Alkyd Primer	6 days ambient, 0 days thermal aging	$E_s = 0.05$	20°C, 55% RH, 0.001 s^{-1}, Thermal aging: 60°C, 55% RH, E_s at 5.0% strain	[50]
Liquitex Ground	4-42 months	$E = 1370^{\alpha}$	21°C, 55% RH, 0.002 s^{-1}	[53]
Liquitex Ground	4-42 months	$E = 3300^{\alpha}$	21°C, 20% RH, 0.002 s^{-1}	[53]
Liquitex Ground	4-42 months	$E = 3600^{\alpha}$	10°C, 55% RH, 0.002 s^{-1}	[53]
Golden Ground	4-42 months	$E = 750^{\alpha}$	21°C, 55% RH, 0.002 s^{-1}	[53]
Golden Ground	4-42 months	$E = 1180^{\alpha}$	21°C, 20% RH, 0.002 s^{-1}	[53]
Golden Ground	4-42 months	$E = 2540^{\alpha}$	10°C, 55% RH, 0.002 s^{-1}	[53]
Winsor & Newton Ground	4-42 months	$E = 510^{\alpha}$	21°C, 55% RH, 0.002 s^{-1}	[53]
Winsor & Newton Ground	4-42 months	$E = 880^{\alpha}$	21°C, 20% RH, 0.002 s^{-1}	[53]
Winsor & Newton Ground	4-42 months	$E = 2040^{\alpha}$	10°C, 55% RH, 0.002 s^{-1}	[53]
Talens Ground	4-42 months	$E = 600^{\alpha}$	21°C, 55% RH, 0.002 s^{-1}	[53]
Talens Ground	4-42 months	$E = 1140^{\alpha}$	21°C, 20% RH, 0.002 s^{-1}	[53]
Talens Ground	4-42 months	$E = 2120^{\alpha}$	10°C, 55% RH, 0.002 s^{-1}	[53]
Liquitex, Titanium White	4-42 months	$E = 860^{\alpha}$	21°C, 55% RH, 0.002 s^{-1}	[53]
Liquitex, Titanium White	4-42 months	$E = 1850^{\alpha}$	21°C, 20% RH, 0.002 s^{-1}	[53]
Liquitex, Titanium White	4-42 months	$E = 2540^{\alpha}$	10°C, 55% RH, 0.002 s^{-1}	[53]
Golden, Titanium White	4-42 months	$E = 380^{\alpha}$	21°C, 55% RH, 0.002 s^{-1}	[53]
Golden, Titanium White	4-42 months	$E = 740^{\alpha}$	21°C, 20% RH, 0.002 s^{-1}	[53]

Sample Composition	Aging Time	Mechanical Property (MPa)	Testing Conditions	References
Golden, Titanium White	4-42 months	E = 1570$^{\alpha}$	10°C, 55% RH, 0.002 s^{-1}	[53]
Winsor & Newton, Titanium White	4-42 months	E = 350$^{\alpha}$	21°C, 55% RH, 0.002 s^{-1}	[53]
Winsor & Newton, Titanium White	4-42 months	E = 630$^{\alpha}$	21°C, 20% RH, 0.002 s^{-1}	[53]
Winsor & Newton, Titanium White	4-42 months	E = 1680$^{\alpha}$	10°C, 55% RH, 0.002 s^{-1}	[53]
Talens, Titanium White	4-42 months	E = 560$^{\alpha}$	21°C, 55% RH, 0.002 s^{-1}	[53]
Talens, Titanium White	4-42 months	E = 1180$^{\alpha}$	21°C, 20% RH, 0.002 s^{-1}	[53]
Talens, Titanium White	4-42 months	E = 1580$^{\alpha}$	10°C, 55% RH, 0.002 s^{-1}	[53]
Golden Gesso	7 months	E = 4590	−10°C, 55% RH, 0.002 s^{-1}	[51]
Golden Gesso	7 months	E = 2980	0°C, 60% RH, 0.002 s^{-1}	[51]
Golden Gesso	7 months	E = 2085	10°C, 57% RH, 0.002 s^{-1}	[51]
Golden Gesso	7 months	E = 390	20°C, 54% RH, 0.002 s^{-1}	[51]
Liquitex Gesso	7 months	E = 7430	−10°C, 55% RH, 0.002 s^{-1}	[51]
Liquitex Gesso	7 months	E = 3400	0°C, 60% RH, 0.002 s^{-1}	[51]
Liquitex Gesso	7 months	E = 2810	10°C, 57% RH, 0.002 s^{-1}	[51]
Liquitex Gesso	7 months	E = 350	20°C, 54% RH, 0.002 s^{-1}	[51]
Winsor & Newton Gesso	7 months	E = 6570	−10°C, 55% RH, 0.002 s^{-1}	[51]
Winsor & Newton Gesso	7 months	E = 3890	0°C, 60% RH, 0.002 s^{-1}	[51]
Winsor & Newton Gesso	7 months	E = 3240	10°C, 57% RH, 0.002 s^{-1}	[51]
Winsor & Newton Gesso	7 months	E = 451	20°C, 54% RH, 0.002 s^{-1}	[51]
Winsor & Newton Galeria	7 months	E = 5710	−10°C, 55% RH, 0.002 s^{-1}	[51]
Winsor & Newton Galeria	7 months	E = 4180	0°C, 60% RH, 0.002 s^{-1}	[51]
Winsor & Newton Galeria	7 months	E = 1930	10°C, 57% RH, 0.002 s^{-1}	[51]

Sample Composition	Aging Time	Mechanical Property (MPa)	Testing Conditions	References
Winsor & Newton Galeria	7 months	E = 366	20°C, 54% RH, 0.002 s^{-1}	[51]
Roberson Primer	7 months	E = 3320	−10°C, 55% RH, 0.002 s^{-1}	[51]
Roberson Primer	7 months	E = 1760	0°C, 60% RH, 0.002 s^{-1}	[51]
Roberson Primer	7 months	E = 710	10°C, 57% RH, 0.002 s^{-1}	[51]
Roberson Primer	7 months	E = 120	20°C, 54% RH, 0.002 s^{-1}	[51]
Golden Artist Colors PBA-MMA, no pigment	1 year	$E_s = 1850^{\alpha}$	−10°C, 50% RH, 0.02 s^{-1}, E_s at 0.5% strain	[56]
Golden Artist Colors PBA-MMA, no pigment	1 year	$E_s = 1430^{\alpha}$	0°C, 50% RH, 0.02 s^{-1}, E_s at 0.5% strain	[56]
Golden Artist Colors PBA-MMA, no pigment	1 year	$E_s = 760^{\alpha}$	10°C, 50% RH, 0.02 s^{-1}, E_s at 0.5% strain	[56]
Golden Artist Colors PBA-MMA, no pigment	1 year	$E_s = 160^{\alpha}$	20°C, 50% RH, 0.02 s^{-1}, E_s at 0.5% strain	[56]
Golden Artist Colors PBA-MMA, no pigment	1 year	$E_s = 18^{\alpha}$	30°C, 50% RH, 0.02 s^{-1}, E_s at 0.5% strain	[56]
Golden Artist Colors PBA-MMA, no pigment	1 year	$E_s = 1600^{\alpha}$	−10°C, 50% RH, 0.002 s^{-1}, E_s at 0.5% strain	[56]
Golden Artist Colors PBA-MMA, no pigment	1 year	$E_s = 1275^{\alpha}$	0°C, 50% RH, 0.002 s^{-1}, E_s at 0.5% strain	[56]
Golden Artist Colors PBA-MMA, no pigment	1 year	$E_s = 415^{\alpha}$	10°C, 50% RH, 0.002 s^{-1}, E_s at 0.5% strain	[56]
Golden Artist Colors PBA-MMA, no pigment	1 year	$E_s = 50^{\alpha}$	20°C, 50% RH, 0.002 s^{-1}, E_s at 0.5% strain	[56]
Golden Artist Colors PBA-MMA, no pigment	1 year	$E_s = 5^{\alpha}$	30°C, 50% RH, 0.002 s^{-1}, E_s at 0.5% strain	[56]
Golden Artist Colors PBA-MMA, no pigment	1 year	$E_s = 1320^{\alpha}$	−10°C, 50% RH, 0.0002 s^{-1}, E_s at 0.5% strain	[56]

Sample Composition	Aging Time	Mechanical Property (MPa)	Testing Conditions	References
Golden Artist Colors PBA-MMA, no pigment	1 year	$E_s = 725^{\alpha}$	0°C, 50% RH, 0.0002 s^{-1}, E_s at 0.5% strain	[56]
Golden Artist Colors PBA-MMA, no pigment	1 year	$E_s = 200^{\alpha}$	10°C, 50% RH, 0.0002s^{-1}, E_s at 0.5% strain	[56]
Golden Artist Colors PBA-MMA, no pigment	1 year	$E_s = 14^{\alpha}$	20°C, 50% RH, 0.0002 s^{-1}, E_s at 0.5% strain	[56]
Golden Artist Colors PBA-MMA, no pigment	1 year	$E_s = 3^{\alpha}$	30°C, 50% RH, 0.0002 s^{-1}, E_s at 0.5% strain	[56]
Golden Artist Colors PBA-MMA, no pigment	1 year	$E_s = 950^{\alpha}$	−10°C, 50% RH, 0.00002 s^{-1}, E_s at 0.5% strain	[56]
Golden Artist Colors PBA-MMA, no pigment	1 year	$E_s = 370^{\alpha}$	0°C, 50% RH, 0.00002 s^{-1}, E_s at 0.5% strain	[56]
Golden Artist Colors PBA-MMA, no pigment	1 year	$E_s = 60^{\alpha}$	10°C, 50% RH, 0.00002 s^{-1}, E_s at 0.5% strain	[56]
Golden Artist Colors PBA-MMA, no pigment	1 year	$E_s = 4^{\alpha}$	20°C, 50% RH, 0.00002 s^{-1}, E_s at 0.5% strain	[56]
Golden Artist Colors PBA-MMA, no pigment	1 year	$E_s = 2^{\alpha}$	30°C, 50% RH, 0.00002 s^{-1}, E_s at 0.5% strain	[56]
Golden Artist Colors PBA-MMA, Titanium white (0.13 v/v)	1 year	$E_s = 2530^{\alpha}$	−10°C, 50% RH, 0.02 s^{-1}, E_s at 0.5% strain	[56]
Golden Artist Colors PBA-MMA, Titanium white (0.13 v/v)	1 year	$E_s = 2090^{\alpha}$	−10°C, 50% RH, 0.002 s^{-1}, E_s at 0.5% strain	[56]
Golden Artist Colors PBA-MMA, Titanium white (0.13 v/v)	1 year	$E_s = 1860^{\alpha}$	0°C, 50% RH, 0.02s^{-1}, E_s at 0.5% strain	[56]
Golden Artist Colors PBA-MMA, Titanium white (0.13 v/v)	1 year	$E_s = 1700^{\alpha}$	−10°C, 50% RH, 0.0002 s^{-1}, E_s at 0.5% strain	[56]

Sample Composition	Aging Time	Mechanical Property (MPa)	Testing Conditions	References
Golden Artist Colors PBA-MMA, Titanium white (0.13 v/v)	1 year	$E_s = 1440^{\alpha}$	0°C, 50% RH, 0.002 s^{-1}, E_s at 0.5% strain	[56]
Golden Artist Colors PBA-MMA, Titanium white (0.13 v/v)	1 year	$E_s = 1275^{\alpha}$	−10°C, 50% RH, 0.00002 s^{-1}, E_s at 0.5% strain	[56]
Golden Artist Colors PBA-MMA, Titanium white (0.13 v/v)	1 year	$E_s = 1175^{\alpha}$	10°C, 50% RH, 0.02 s^{-1}, E_s at 0.5% strain	[56]
Golden Artist Colors PBA-MMA, Titanium white (0.13 v/v)	1 year	$E_s = 965^{\alpha}$	0°C, 50% RH, 0.0002 s^{-1}, E_s at 0.5% strain	[56]
Golden Artist Colors PBA-MMA, Titanium white (0.13 v/v)	1 year	$E_s = 720^{\alpha}$	10°C, 50% RH, 0.002 s^{-1}, E_s at 0.5% strain	[56]
Golden Artist Colors PBA-MMA, Titanium white (0.13 v/v)	1 year	$E_s = 595^{\alpha}$	0°C, 50% RH, 0.00002 s^{-1}, E_s at 0.5% strain	[56]
Golden Artist Colors PBA-MMA, Titanium white (0.13 v/v)	1 year	$E_s = 340^{\alpha}$	10°C, 50% RH, 0.0002 s^{-1}, E_s at 0.5% strain	[56]
Golden Artist Colors PBA-MMA, Titanium white (0.13 v/v)	1 year	$E_s = 115^{\alpha}$	10°C, 50% RH, 0.00002 s^{-1}, E_s at 0.5% strain	[56]
Golden Artist Colors PBA-MMA, Titanium white (0.13 v/v)	1 year	$E_s = 47^{\alpha}$	30°C, 50% RH, 0.02 s^{-1}, E_s at 0.5% strain	[56]
Golden Artist Colors PBA-MMA, Titanium white (0.13 v/v)	1 year	$E_s = 34^{\alpha}$	20°C, 50% RH, 0.0002 s^{-1}, E_s at 0.5% strain	[56]
Golden Artist Colors PBA-MMA, Titanium white (0.13 v/v)	1 year	$E_s = 15^{\alpha}$	30°C, 50% RH, 0.002 s^{-1}, E_s at 0.5% strain	[56]

Sample Composition	Aging Time	Mechanical Property (MPa)	Testing Conditions	References
Golden Artist Colors PBA-MMA, Titanium white (0.13 v/v)	1 year	$E_s = 11^{\alpha}$	20°C, 50% RH, 0.00002 s^{-1}, E_s at 0.5% strain	[56]
Golden Artist Colors PBA-MMA, Titanium white (0.13 v/v)	1 year	$E_s = 7^{\alpha}$	30°C, 50% RH, 0.0002 s^{-1}, E_s at 0.5% strain	[56]
Golden Artist Colors PBA-MMA, Titanium white (0.13 v/v)	1 year	$E_s = 4^{\alpha}$	30°C, 50% RH, 0.00002 s^{-1}, E_s at 0.5% strain	[56]
Golden Artist Colors PBA-MMA, Titanium white (0.25 v/v)	1 year	$E_s = 3590^{\alpha}$	−10°C, 50% RH, 0.02 s^{-1}, E_s at 0.5% strain	[56]
Golden Artist Colors PBA-MMA, Titanium white (0.25 v/v)	1 year	$E_s = 2980^{\alpha}$	−10°C, 50% RH, 0.002 s^{-1}, E_s at 0.5% strain	[56]
Golden Artist Colors PBA-MMA, Titanium white (0.25 v/v)	1 year	$E_s = 2590^{\alpha}$	0°C, 50% RH, 0.02 s^{-1}, E_s at 0.5% strain	[56]
Golden Artist Colors PBA-MMA, Titanium white (0.25 v/v)	1 year	$E_s = 2410^{\alpha}$	−10°C, 50% RH, 0.0002 s^{-1}, E_s at 0.5% strain	[56]
Golden Artist Colors PBA-MMA, Titanium white (0.25 v/v)	1 year	$E_s = 1865^{\alpha}$	0°C, 50% RH, 0.002 s^{-1}, E_s at 0.5% strain	[56]
Golden Artist Colors PBA-MMA, Titanium white (0.25 v/v)	1 year	$E_s = 1850^{\alpha}$	−10°C, 50% RH, 0.00002 s^{-1}, E_s at 0.5% strain	[56]
Golden Artist Colors PBA-MMA, Titanium white (0.25 v/v)	1 year	$E_s = 1710^{\alpha}$	10°C, 50% RH, 0.02 s^{-1}, E_s at 0.5% strain	[56]
Golden Artist Colors PBA-MMA, Titanium white (0.25 v/v)	1 year	$E_s = 1240^{\alpha}$	0°C, 50% RH, 0.0002 s^{-1}, E_s at 0.5% strain	[56]

Sample Composition	Aging Time	Mechanical Property (MPa)	Testing Conditions	References
Golden Artist Colors PBA-MMA, Titanium white (0.25 v/v)	1 year	$E_s = 950^{\alpha}$	10°C, 50% RH, 0.002 s^{-1}, E_s at 0.5% strain	[56]
Golden Artist Colors PBA-MMA, Titanium white (0.25 v/v)	1 year	$E_s = 720^{\alpha}$	0°C, 50% RH, 0.00002 s^{-1}, E_s at 0.5% strain	[56]
Golden Artist Colors PBA-MMA, Titanium white (0.25 v/v)	1 year	$E_s = 520^{\alpha}$	20°C, 50% RH, 0.02 s^{-1}, E_s at 0.5% strain	[56]
Golden Artist Colors PBA-MMA, Titanium white (0.25 v/v)	1 year	$E_s = 440^{\alpha}$	10°C, 50% RH, 0.0002 s^{-1}, E_s at 0.5% strain	[56]
Golden Artist Colors PBA-MMA, Titanium white (0.25 v/v)	1 year	$E_s = 210^{\alpha}$	20°C, 50% RH, 0.002 s^{-1}, E_s at 0.5% strain	[56]
Golden Artist Colors PBA-MMA, Titanium white (0.25 v/v)	1 year	$E_s = 150^{\alpha}$	10°C, 50% RH, 0.00002 s^{-1}, E_s at 0.5% strain	[56]
Golden Artist Colors PBA-MMA, Titanium white (0.25 v/v)	1 year	$E_s = 115^{\alpha}$	30°C, 50% RH, 0.02 s^{-1}, E_s at 0.5% strain	[56]
Golden Artist Colors PBA-MMA, Titanium white (0.25 v/v)	1 year	$E_s = 77^{\alpha}$	20°C, 50% RH, 0.0002 s^{-1}, E_s at 0.5% strain	[56]
Golden Artist Colors PBA-MMA, Titanium white (0.25 v/v)	1 year	$E_s = 48^{\alpha}$	30°C, 50% RH, 0.002 s^{-1}, E_s at 0.5% strain	[56]
Golden Artist Colors PBA-MMA, Titanium white (0.25 v/v)	1 year	$E_s = 32^{\alpha}$	20°C, 50% RH, 0.00002 s^{-1}, E_s at 0.5% strain	[56]
Golden Artist Colors PBA-MMA, Titanium white (0.25 v/v)	1 year	$E_s = 23^{\alpha}$	30°C, 50% RH, 0.0002 s^{-1}, E_s at 0.5% strain	[56]

Sample Composition	Aging Time	Mechanical Property (MPa)	Testing Conditions	References
Golden Artist Colors PBA-MMA, Titanium white (0.25 v/v)	1 year	$E_s = 15^{\alpha}$	30°C, 50% RH, 0.00002 s^{-1}, E_s at 0.5% strain	[56]
Golden Artist Colors PBA-MMA, Titanium white (0.38 v/v)	1 year	$E_s = 4770^{\alpha}$	−10°C, 50% RH, 0.02 s^{-1}, E_s at 0.5% strain	[56]
Golden Artist Colors PBA-MMA, Titanium white (0.38 v/v)	1 year	$E_s = 3920^{\alpha}$	−10°C, 50% RH, 0.002 s^{-1}, E_s at 0.5% strain	[56]
Golden Artist Colors PBA-MMA, Titanium white (0.38 v/v)	1 year	$E_s = 3430^{\alpha}$	0°C, 50% RH, 0.02 s^{-1}, E_s at 0.5% strain	[56]
Golden Artist Colors PBA-MMA, Titanium white (0.38 v/v)	1 year	$E_s = 3380^{\alpha}$	−10°C, 50% RH, 0.0002 s^{-1}, E_s at 0.5% strain	[56]
Golden Artist Colors PBA-MMA, Titanium white (0.38 v/v)	1 year	$E_s = 2830^{\alpha}$	0°C, 50% RH, 0.002 s^{-1}, E_s at 0.5% strain	[56]
Golden Artist Colors PBA-MMA, Titanium white (0.38 v/v)	1 year	$E_s = 2670^{\alpha}$	−10°C, 50% RH, 0.00002 s^{-1}, E_s at 0.5% strain	[56]
Golden Artist Colors PBA-MMA, Titanium white (0.38 v/v)	1 year	$E_s = 2350^{\alpha}$	10°C, 50% RH, 0.02 s^{-1}, E_s at 0.5% strain	[56]
Golden Artist Colors PBA-MMA, Titanium white (0.38 v/v)	1 year	$E_s = 1770^{\alpha}$	0°C, 50% RH, 0.0002 s^{-1}, E_s at 0.5% strain	[56]
Golden Artist Colors PBA-MMA, Titanium white (0.38 v/v)	1 year	$E_s = 1460^{\alpha}$	10°C, 50% RH, 0.002 s^{-1}, E_s at 0.5% strain	[56]
Golden Artist Colors PBA-MMA, Titanium white (0.38 v/v)	1 year	$E_s = 1010^{\alpha}$	0°C, 50% RH, 0.00002 s^{-1}, E_s at 0.5% strain	[56]

Sample Composition	Aging Time	Mechanical Property (MPa)	Testing Conditions	References
Golden Artist Colors PBA-MMA, Titanium white (0.38 v/v)	1 year	$E_s = 830^{\alpha}$	20°C, 50% RH, 0.02 s^{-1}, E_s at 0.5% strain	[56]
Golden Artist Colors PBA-MMA, Titanium white (0.38 v/v)	1 year	$E_s = 790^{\alpha}$	10°C, 50% RH, 0.0002 s^{-1}, E_s at 0.5% strain	[56]
Golden Artist Colors PBA-MMA, Titanium white (0.38 v/v)	1 year	$E_s = 380^{\alpha}$	20°C, 50% RH, 0.002 s^{-1}, E_s at 0.5% strain	[56]
Golden Artist Colors PBA-MMA, Titanium white (0.38 v/v)	1 year	$E_s = 320^{\alpha}$	30°C, 50% RH, 0.02 s^{-1}, E_s at 0.5% strain	[56]
Golden Artist Colors PBA-MMA, Titanium white (0.38 v/v)	1 year	$E_s = 220^{\alpha}$	20°C, 50% RH, 0.0002 s^{-1}, E_s at 0.5% strain	[56]
Golden Artist Colors PBA-MMA, Titanium white (0.38 v/v)	1 year	$E_s = 180^{\alpha}$	30°C, 50% RH, 0.002 s^{-1}, E_s at 0.5% strain	[56]
Golden Artist Colors PBA-MMA, Titanium white (0.38 v/v)	1 year	$E_s = 140^{\alpha}$	20°C, 50% RH, 0.00002 s^{-1}, E_s at 0.5% strain	[56]
Golden Artist Colors PBA-MMA, Titanium white (0.38 v/v)	1 year	$E_s = 115^{\alpha}$	30°C, 50% RH, 0.0002 s^{-1}, E_s at 0.5% strain	[56]
Golden Artist Colors PBA-MMA, Titanium white (0.38 v/v)	1 year	$E_s = 90^{\alpha}$	30°C, 50% RH, 0.00002 s^{-1}, E_s at 0.5% strain	[56]
Golden Artist Colors PBA-MMA, no pigment	1 year	$E_s = 460^{\alpha}$	20°C, 5% RH, 0.02 s^{-1}, E_s at 0.5% strain	[56]
Golden Artist Colors PBA-MMA, no pigment	1 year	$E_s = 210^{\alpha}$	20°C, 5% RH, 0.002 s^{-1}, E_s at 0.5% strain	[56]
Golden Artist Colors PBA-MMA, no pigment	1 year	$E_s = 74^{\alpha}$	30°C, 5% RH, 0.02 s^{-1}, E_s at 0.5% strain	[56]

Sample Composition	Aging Time	Mechanical Property (MPa)	Testing Conditions	References
Golden Artist Colors PBA-MMA, no pigment	1 year	$E_s = 23^{\alpha}$	30°C, 5% RH, 0.002 s^{-1}, E_s at 0.5% strain	[56]
Golden Artist Colors PBA-MMA, no pigment	1 year	$E_s = 19^{\alpha}$	20°C, 5% RH, 0.00002 s^{-1}, E_s at 0.5% strain	[56]
Golden Artist Colors PBA-MMA, no pigment	1 year	$E_s = 5^{\alpha}$	30°C, 5% RH, 0.00002 s^{-1}, E_s at 0.5% strain	[56]
Golden Artist Colors PBA-MMA, Titanium white (0.38 v/v)	1 year	$E_s = 2390^{\alpha}$	20°C, 5% RH, 0.02 s^{-1}, E_s at 0.5% strain	[56]
Golden Artist Colors PBA-MMA, Titanium white (0.38 v/v)	1 year	$E_s = 1240^{\alpha}$	20°C, 5% RH, 0.002 s^{-1}, E_s at 0.5% strain	[56]
Golden Artist Colors PBA-MMA, Titanium white (0.38 v/v)	1 year	$E_s = 840^{\alpha}$	20°C, 5% RH, 0.0002 s^{-1}, E_s at 0.5% strain	[56]
Golden Artist Colors PBA-MMA, Titanium white (0.38 v/v)	1 year	$E_s = 730^{\alpha}$	20°C, 5% RH, 0.00002 s^{-1}, E_s at 0.5% strain	[56]
Golden Artist Colors PBA-MMA, Titanium white (0.38 v/v)	1 year	$E_s = 460^{\alpha}$	30°C, 5% RH, 0.0002 s^{-1}, E_s at 0.5% strain	[56]
Golden Artist Colors PBA-MMA, Titanium white (0.38 v/v)	1 year	$E_s = 410^{\alpha}$	30°C, 5% RH, 0.00002 s^{-1}, E_s at 0.5% strain	[56]
Golden Artist Colors PBA-MMA, kaolin (0.28 v/v)	1 year	$E_s = 4780^{\alpha}$	−10°C, 50% RH, 0.02 s^{-1}, E_s at 0.5% strain	[30]
Golden Artist Colors PBA-MMA, kaolin (0.28 v/v)	1 year	$E_s = 3930^{\alpha}$	−10°C, 50% RH, 0.002 s^{-1}, E_s at 0.5% strain	[30]
Golden Artist Colors PBA-MMA, kaolin (0.28 v/v)	1 year	$E_s = 3410^{\alpha}$	−10°C, 50% RH, 0.0002 s^{-1}, E_s at 0.5% strain	[30]
Golden Artist Colors PBA-MMA, kaolin (0.28 v/v)	1 year	$E_s = 2690^{\alpha}$	−10°C, 50% RH, 0.00002 s^{-1}, E_s at 0.5% strain	[30]

Sample Composition	Aging Time	Mechanical Property (MPa)	Testing Conditions	References
Golden Artist Colors PBA-MMA, kaolin (0.28 v/v)	1 year	$E_s = 3460^{\alpha}$	0°C, 50% RH, 0.02 s^{-1}, E_s at 0.5% strain	[30]
Golden Artist Colors PBA-MMA, kaolin (0.28 v/v)	1 year	$E_s = 2830^{\alpha}$	0°C, 50% RH, 0.002 s^{-1}, E_s at 0.5% strain	[30]
Golden Artist Colors PBA-MMA, kaolin (0.28 v/v)	1 year	$E_s = 1780^{\alpha}$	0°C, 50% RH, 0.0002 s^{-1}, E_s at 0.5% strain	[30]
Golden Artist Colors PBA-MMA, kaolin (0.28 v/v)	1 year	$E_s = 1020^{\alpha}$	0°C, 50% RH, 0.00002 s^{-1}, E_s at 0.5% strain	[30]
Golden Artist Colors PBA-MMA, kaolin (0.28 v/v)	1 year	$E_s = 2350^{\alpha}$	10°C, 50% RH, 0.02 s^{-1}, E_s at 0.5% strain	[30]
Golden Artist Colors PBA-MMA, kaolin (0.28 v/v)	1 year	$E_s = 1460^{\alpha}$	10°C, 50% RH, 0.002 s^{-1}, E_s at 0.5% strain	[30]
Golden Artist Colors PBA-MMA, kaolin (0.28 v/v)	1 year	$E_s = 790^{\alpha}$	10°C, 50% RH, 0.0002 s^{-1}, E_s at 0.5% strain	[30]
Golden Artist Colors PBA-MMA, kaolin (0.28 v/v)	1 year	$E_s = 810^{\alpha}$	20°C, 50% RH, 0.02 s^{-1}, E_s at 0.5% strain	[30]
Golden Artist Colors PBA-MMA, kaolin (0.28 v/v)	1 year	$E_s = 370^{\alpha}$	20°C, 50% RH, 0.002 s^{-1}, E_s at 0.5% strain	[30]
Golden Artist Colors PBA-MMA, kaolin (0.28 v/v)	1 year	$E_s = 210^{\alpha}$	20°C, 50% RH, 0.0002 s^{-1}, E_s at 0.5% strain	[30]
Golden Artist Colors PBA-MMA, kaolin (0.28 v/v)	1 year	$E_s = 130^{\alpha}$	20°C, 50% RH, 0.00002 s^{-1}, E_s at 0.5% strain	[30]
Golden Artist Colors PBA-MMA, kaolin (0.28 v/v)	1 year	$E_s = 320^{\alpha}$	30°C, 50% RH, 0.02 s^{-1}, E_s at 0.5% strain	[30]
Golden Artist Colors PBA-MMA, kaolin (0.28 v/v)	1 year	$E_s = 170^{\alpha}$	30°C, 50% RH, 0.002 s^{-1}, E_s at 0.5% strain	[30]
Golden Artist Colors PBA-MMA, kaolin (0.28 v/v)	1 year	$E_s = 110^{\alpha}$	30°C, 50% RH, 0.0002 s^{-1}, E_s at 0.5% strain	[30]
Golden Artist Colors PBA-MMA, kaolin (0.28 v/v)	1 year	$E_s = 90^{\alpha}$	30°C, 50% RH, 0.00002 s^{-1}, E_s at 0.5% strain	[30]

Sample Composition	Aging Time	Mechanical Property (MPa)	Testing Conditions	References
Golden Artist Colors PBA-MMA, kaolin (0.15 v/v)	1 year	$E_s = 3410^{\alpha}$	−10°C, 50% RH, 0.02 s^{-1}, E_s at 0.5% strain	[30]
Golden Artist Colors PBA-MMA, kaolin (0.15 v/v)	1 year	$E_s = 2880^{\alpha}$	−10°C, 50% RH, 0.002 s^{-1}, E_s at 0.5% strain	[30]
Golden Artist Colors PBA-MMA, kaolin (0.15 v/v)	1 year	$E_s = 2580^{\alpha}$	0°C, 50% RH, 0.02 s^{-1}, E_s at 0.5% strain	[30]
Golden Artist Colors PBA-MMA, kaolin (0.15 v/v)	1 year	$E_s = 2280^{\alpha}$	−10°C, 50% RH, 0.0002 s^{-1}, E_s at 0.5% strain	[30]
Golden Artist Colors PBA-MMA, kaolin (0.15 v/v)	1 year	$E_s = 1960^{\alpha}$	0°C, 50% RH, 0.002 s^{-1}, E_s at 0.5% strain	[30]
Golden Artist Colors PBA-MMA, kaolin (0.15 v/v)	1 year	$E_s = 1860^{\alpha}$	−10°C, 50% RH, 0.00002 s^{-1}, E_s at 0.5% strain	[30]
Golden Artist Colors PBA-MMA, kaolin (0.15 v/v)	1 year	$E_s = 1510^{\alpha}$	10°C, 50% RH, 0.02 s^{-1}, E_s at 0.5% strain	[30]
Golden Artist Colors PBA-MMA, kaolin (0.15 v/v)	1 year	$E_s = 1270^{\alpha}$	0°C, 50% RH, 0.0002 s^{-1}, E_s at 0.5% strain	[30]
Golden Artist Colors PBA-MMA, kaolin (0.15 v/v)	1 year	$E_s = 820^{\alpha}$	10°C, 50% RH, 0.002 s^{-1}, E_s at 0.5% strain	[30]
Golden Artist Colors PBA-MMA, kaolin (0.15 v/v)	1 year	$E_s = 790^{\alpha}$	0°C, 50% RH, 0.00002 s^{-1}, E_s at 0.5% strain	[30]
Golden Artist Colors PBA-MMA, kaolin (0.15 v/v)	1 year	$E_s = 440^{\alpha}$	10°C, 50% RH, 0.0002 s^{-1}, E_s at 0.5% strain	[30]
Golden Artist Colors PBA-MMA, kaolin (0.15 v/v)	1 year	$E_s = 450^{\alpha}$	20°C, 50% RH, 0.02 s^{-1}, E_s at 0.5% strain	[30]
Golden Artist Colors PBA-MMA, kaolin (0.15 v/v)	1 year	$E_s = 160^{\alpha}$	20°C, 50% RH, 0.002 s^{-1}, E_s at 0.5% strain	[30]
Golden Artist Colors PBA-MMA, kaolin (0.15 v/v)	1 year	$E_s = 150^{\alpha}$	10°C, 50% RH, 0.00002 s^{-1}, E_s at 0.5% strain	[30]
Golden Artist Colors PBA-MMA, kaolin (0.15 v/v)	1 year	$E_s = 76^{\alpha}$	30°C, 50% RH, 0.02 s^{-1}, E_s at 0.5% strain	[30]

Sample Composition	Aging Time	Mechanical Property (MPa)	Testing Conditions	References
Golden Artist Colors PBA-MMA, kaolin (0.15 v/v)	1 year	$E_s = 49^{\alpha}$	20°C, 50% RH, 0.0002 s^{-1}, E_s at 0.5% strain	[30]
Golden Artist Colors PBA-MMA, kaolin (0.15 v/v)	1 year	$E_s = 28^{\alpha}$	30°C, 50% RH, 0.002 s^{-1}, E_s at 0.5% strain	[30]
Golden Artist Colors PBA-MMA, kaolin (0.15 v/v)	1 year	$E_s = 20^{\alpha}$	20°C, 50% RH, 0.00002 s^{-1}, E_s at 0.5% strain	[30]
Golden Artist Colors PBA-MMA, kaolin (0.15 v/v)	1 year	$E_s = 13^{\alpha}$	30°C, 50% RH, 0.0002 s^{-1}, E_s at 0.5% strain	[30]
Golden Artist Colors PBA-MMA, kaolin (0.15 v/v)	1 year	$E_s = 9^{\alpha}$	30°C, 50% RH, 0.00002 s^{-1}, E_s at 0.5% strain	[30]
Golden Artist Colors PBA-MMA, no pigment	1 year	$E_s = 1470^{\alpha}$	−10°C, 50% RH, 0.02 s^{-1}, E_s at 0.5% strain, immersed in water 24 hours	[30]
Golden Artist Colors PBA-MMA, no pigment	1 year	$E_s = 1270^{\alpha}$	0°C, 50% RH, 0.02 s^{-1}, E_s at 0.5% strain, immersed in water 24 hours	[30]
Golden Artist Colors PBA-MMA, no pigment	1 year	$E_s = 950^{\alpha}$	0°C, 50% RH, 0.002 s^{-1}, E_s at 0.5% strain, immersed in water 24 hours	[30]
Golden Artist Colors PBA-MMA, no pigment	1 year	$E_s = 680^{\alpha}$	−10°C, 50% RH, 0.00002 s^{-1}, E_s at 0.5% strain, immersed in water 24 hours	[30]
Golden Artist Colors PBA-MMA, no pigment	1 year	$E_s = 660^{\alpha}$	0°C, 50% RH, 0.0002 s^{-1}, E_s at 0.5% strain, immersed in water 24 hours	[30]
Golden Artist Colors PBA-MMA, no pigment	1 year	$E_s = 350^{\alpha}$	10°C, 50% RH, 0.002 s^{-1}, E_s at 0.5% strain, immersed in water 24 hours	[30]

Sample Composition	Aging Time	Mechanical Property (MPa)	Testing Conditions	References
Golden Artist Colors PBA-MMA, no pigment	1 year	$E_s = 130^{\alpha}$	20°C, 50% RH, 0.02 s^{-1}, E_s at 0.5% strain, immersed in water 24 hours	[30]
Golden Artist Colors PBA-MMA, no pigment	1 year	$E_s = 32^{\alpha}$	20°C, 50% RH, 0.002 s^{-1}, E_s at 0.5% strain, immersed in water 24 hours	[30]
Golden Artist Colors PBA-MMA, no pigment	1 year	$E_s = 14^{\alpha}$	30°C, 50% RH, 0.02 s^{-1}, E_s at 0.5% strain, immersed in water 24 hours	[30]
Golden Artist Colors PBA-MMA, no pigment	1 year	$E_s = 10^{\alpha}$	20°C, 50% RH, 0.0002 s^{-1}, E_s at 0.5% strain, immersed in water 24 hours	[30]
Golden Artist Colors PBA-MMA, no pigment	1 year	$E_s = 4^{\alpha}$	30°C, 50% RH, 0.002 s^{-1}, E_s at 0.5% strain, immersed in water 24 hours	[30]
Golden Artist Colors PBA-MMA, no pigment	1 year	$E_s = 3^{\alpha}$	20°C, 50% RH, 0.00002 s^{-1}, E_s at 0.5% strain, immersed in water 24 hours	[30]
Golden Artist Colors PBA-MMA, no pigment	1 year	$E_s = 2^{\alpha}$	30°C, 50% RH, 0.0002 s^{-1}, E_s at 0.5% strain, immersed in water 24 hours	[30]
Golden Artist Colors PBA-MMA, Titanium white (0.13 v/v)	1 year	$E_s = 300^{\alpha}$	20°C, 50% RH, 0.02 s^{-1}, E_s at 0.5% strain, immersed in water 24 hours	[30]
Golden Artist Colors PBA-MMA, Titanium white (0.13 v/v)	1 year	$E_s = 110^{\alpha}$	20°C, 50% RH, 0.002 s^{-1}, E_s at 0.5% strain, immersed in water 24 hours	[30]

Sample Composition	Aging Time	Mechanical Property (MPa)	Testing Conditions	References
Golden Artist Colors PBA-MMA, Titanium white (0.13 v/v)	1 year	$E_s = 45^{\alpha}$	30°C, 50% RH, 0.02 s^{-1}, E_s at 0.5% strain, immersed in water 24 hours	[30]
Golden Artist Colors PBA-MMA, Titanium white (0.13 v/v)	1 year	$E_s = 31^{\alpha}$	20°C, 50% RH, 0.0002 s^{-1}, E_s at 0.5% strain, immersed in water 24 hours	[30]
Golden Artist Colors PBA-MMA, Titanium white (0.13 v/v)	1 year	$E_s = 14^{\alpha}$	30°C, 50% RH, 0.002 s^{-1}, E_s at 0.5% strain, immersed in water 24 hours	[30]
Golden Artist Colors PBA-MMA, Titanium white (0.13 v/v)	1 year	$E_s = 10^{\alpha}$	20°C, 50% RH, 0.00002 s^{-1}, E_s at 0.5% strain, immersed in water 24 hours	[30]
Golden Artist Colors PBA-MMA, Titanium white (0.13 v/v)	1 year	$E_s = 5^{\alpha}$	30°C, 50% RH, 0.0002 s^{-1}, E_s at 0.5% strain, immersed in water 24 hours	[30]
Golden Artist Colors PBA-MMA, Titanium white (0.13 v/v)	1 year	$E_s = 3^{\alpha}$	30°C, 50% RH, 0.00002 s^{-1}, E_s at 0.5% strain, immersed in water 24 hours	[30]
Golden Artist Colors PBA-MMA, Titanium white (0.25 v/v)	1 year	$E_s = 700^{\alpha}$	20°C, 50% RH, 0.02 s^{-1}, E_s at 0.5% strain, immersed in water 24 hours	[30]
Golden Artist Colors PBA-MMA, Titanium white (0.25 v/v)	1 year	$E_s = 310^{\alpha}$	20°C, 50% RH, 0.002 s^{-1}, E_s at 0.5% strain, immersed in water 24 hours	[30]
Golden Artist Colors PBA-MMA, Titanium white (0.25 v/v)	1 year	$E_s = 180^{\alpha}$	30°C, 50% RH, 0.02 s^{-1}, E_s at 0.5% strain, immersed in water 24 hours	[30]

Sample Composition	Aging Time	Mechanical Property (MPa)	Testing Conditions	References
Golden Artist Colors PBA-MMA, Titanium white (0.25 v/v)	1 year	$E_s = 120^{\alpha}$	20°C, 50% RH, 0.0002 s^{-1}, E_s at 0.5% strain, immersed in water 24 hours	[30]
Golden Artist Colors PBA-MMA, Titanium white (0.25 v/v)	1 year	$E_s = 76^{\alpha}$	30°C, 50% RH, 0.002 s^{-1}, E_s at 0.5% strain, immersed in water 24 hours	[30]
Golden Artist Colors PBA-MMA, Titanium white (0.25 v/v)	1 year	$E_s = 60^{\alpha}$	20°C, 50% RH, 0.00002 s^{-1}, E_s at 0.5% strain, immersed in water 24 hours	[30]
Golden Artist Colors PBA-MMA, Titanium white (0.25 v/v)	1 year	$E_s = 41^{\alpha}$	30°C, 50% RH, 0.0002 s^{-1}, E_s at 0.5% strain, immersed in water 24 hours	[30]
Golden Artist Colors PBA-MMA, Titanium white (0.25 v/v)	1 year	$E_s = 25^{\alpha}$	30°C, 50% RH, 0.00002 s^{-1}, E_s at 0.5% strain, immersed in water 24 hours	[30]
Golden Artist Colors PBA-MMA, Titanium white (0.38 v/v)	1 year	$E_s = 1410^{\alpha}$	20°C, 50% RH, 0.02 s^{-1}, E_s at 0.5% strain, immersed in water 24 hours	[30]
Golden Artist Colors PBA-MMA, Titanium white (0.38 v/v)	1 year	$E_s = 890^{\alpha}$	20°C, 50% RH, 0.002 s^{-1}, E_s at 0.5% strain, immersed in water 24 hours	[30]
Golden Artist Colors PBA-MMA, Titanium white (0.38 v/v)	1 year	$E_s = 620^{\alpha}$	30°C, 50% RH, 0.02 s^{-1}, E_s at 0.5% strain, immersed in water 24 hours	[30]
Golden Artist Colors PBA-MMA, Titanium white (0.38 v/v)	1 year	$E_s = 510^{\alpha}$	20°C, 50% RH, 0.0002 s^{-1}, E_s at 0.5% strain, immersed in water 24 hours	[30]

Sample Composition	Aging Time	Mechanical Property (MPa)	Testing Conditions	References
Golden Artist Colors PBA-MMA, Titanium white (0.38 v/v)	1 year	$E_s = 350^{\alpha}$	30°C, 50% RH, 0.002 s^{-1}, E_s at 0.5% strain, immersed in water 24 hours	[30]
Golden Artist Colors PBA-MMA, Titanium white (0.38 v/v)	1 year	$E_s = 320^{\alpha}$	20°C, 50% RH, 0.00002 s^{-1}, E_s at 0.5% strain, immersed in water 24 hours	[30]
Golden Artist Colors PBA-MMA, Titanium white (0.38 v/v)	1 year	$E_s = 250^{\alpha}$	30°C, 50% RH, 0.0002 s^{-1}, E_s at 0.5% strain, immersed in water 24 hours	[30]
Golden Artist Colors PBA-MMA, Titanium white (0.38 v/v)	1 year	$E_s = 190^{\alpha}$	30°C, 50% RH, 0.00002 s^{-1}, E_s at 0.5% strain, immersed in water 24 hours	[30]
Golden Artist Colors PBA-MMA, Titanium white (0.06 v/v)	1 year	$E^* = 1650^{\alpha}$	−10°C, 50% RH, 0.00002 s^{-1}, tested in casting direction	[31]
Golden Artist Colors PBA-MMA, kaolin (0.07 v/v)	1 year	$E^* = 1950^{\alpha}$	−10°C, 50% RH, 0.00002 s^{-1}, tested in casting direction	[31]
Golden Artist Colors PBA-MMA, $CaCO_3$ (0.08 v/v)	1 year	$E^* = 1980^{\alpha}$	−10°C, 50% RH, 0.00002 s^{-1}, tested in casting direction	[31]
Golden Artist Colors PBA-MMA, $CaCO_3$ (0.08 v/v)	1 year	$E^* = 1710^{\alpha}$	−10°C, 50% RH, 0.00002 s^{-1}, tested perpendicular to casting direction	[31]
Golden Artist Colors PBA-MMA, Titanium white (0.13 v/v)	1 year	$E^* = 1920^{\alpha}$	−10°C, 50% RH, 0.00002 s^{-1}, tested perpendicular to casting direction	[31]
Golden Artist Colors PBA-MMA, Titanium white (0.13 v/v)	1 year	$E^* = 1960^{\alpha}$	−10°C, 50% RH, 0.00002 s^{-1}, tested in casting direction	[31]

Sample Composition	Aging Time	Mechanical Property (MPa)	Testing Conditions	References
Golden Artist Colors PBA-MMA, kaolin (0.14 v/v)	1 year	$E^* = 2450^{\alpha}$	−10°C, 50% RH, 0.00002 s^{-1}, tested perpendicular to casting direction	[31]
Golden Artist Colors PBA-MMA, kaolin (0.14 v/v)	1 year	$E^* = 2660^{\alpha}$	−10°C, 50% RH, 0.00002 s^{-1}, tested in casting direction	[31]
Golden Artist Colors PBA-MMA, $CaCO_3$ (0.16 v/v)	1 year	$E^* = 2080^{\alpha}$	−10°C, 50% RH, 0.00002 s^{-1}, tested perpendicular to casting direction	[31]
Golden Artist Colors PBA-MMA, $CaCO_3$ (0.16 v/v)	1 year	$E^* = 2390^{\alpha}$	−10°C, 50% RH, 0.00002 s^{-1}, tested in casting direction	[31]
Golden Artist Colors PBA-MMA, Titanium white (0.20 v/v)	1 year	$E^* = 2220^{\alpha}$	−10°C, 50% RH, 0.00002 s^{-1}, tested perpendicular to casting direction	[31]
Golden Artist Colors PBA-MMA, Titanium white (0.20 v/v)	1 year	$E^* = 2300^{\alpha}$	−10°C, 50% RH, 0.00002 s^{-1}, tested in casting direction	[31]
Golden Artist Colors PBA-MMA, kaolin (0.22 v/v)	1 year	$E^* = 3100^{\alpha}$	−10°C, 50% RH, 0.00002 s^{-1}, tested perpendicular to casting direction	[31]
Golden Artist Colors PBA-MMA, kaolin (0.22 v/v)	1 year	$E^* = 3520^{\alpha}$	−10°C, 50% RH, 0.00002 s^{-1}, tested in casting direction	[31]
Golden Artist Colors PBA-MMA, $CaCO_3$ (0.24 v/v)	1 year	$E^* = 2440^{\alpha}$	−10°C, 50% RH, 0.00002 s^{-1}, tested perpendicular to casting direction	[31]
Golden Artist Colors PBA-MMA, $CaCO_3$ (0.24 v/v)	1 year	$E^* = 3030^{\alpha}$	−10°C, 50% RH, 0.00002 s^{-1}, tested in casting direction	[31]
Golden Artist Colors PBA-MMA, Titanium white (0.25 v/v)	1 year	$E^* = 2670^{\alpha}$	−10°C, 50% RH, 0.00002 s^{-1}, tested perpendicular to casting direction	[31]
Golden Artist Colors PBA-MMA, Titanium white (0.25 v/v)	1 year	$E^* = 2760^{\alpha}$	−10°C, 50% RH, 0.00002 s^{-1}, tested in casting direction	[31]

Sample Composition	Aging Time	Mechanical Property (MPa)	Testing Conditions	References
Golden Artist Colors PBA-MMA, kaolin (0.28 v/v)	1 year	$E^* = 4050^{\alpha}$	$-10°C$, 50% RH, 0.00002 s^{-1}, tested in casting direction	[31]
Golden Artist Colors PBA-MMA, $CaCO_3$ (0.30 v/v)	1 year	$E^* = 2990^{\alpha}$	$-10°C$, 50% RH, 0.00002 s^{-1}, tested perpendicular to casting direction	[31]
Golden Artist Colors PBA-MMA, $CaCO_3$ (0.30 v/v)	1 year	$E^* = 3850^{\alpha}$	$-10°C$, 50% RH, 0.00002 s^{-1}, tested in casting direction	[31]
Golden Artist Colors PBA-MMA, Titanium white (0.32 v/v)	1 year	$E^* = 3310^{\alpha}$	$-10°C$, 50% RH, 0.00002 s^{-1}, tested perpendicular to casting direction	[31]
Golden Artist Colors PBA-MMA, Titanium white (0.32 v/v)	1 year	$E^* = 3430^{\alpha}$	$-10°C$, 50% RH, 0.00002 s^{-1}, tested in casting direction	[31]
Golden Artist Colors PBA-MMA, $CaCO_3$ (0.38 v/v)	1 year	$E^* = 3590^{\alpha}$	$-10°C$, 50% RH, 0.00002 s^{-1}, tested perpendicular to casting direction	[31]
Golden Artist Colors PBA-MMA, $CaCO_3$ (0.38 v/v)	1 year	$E^* = 4500^{\alpha}$	$-10°C$, 50% RH, 0.00002 s^{-1}, tested in casting direction	[31]
Golden Artist Colors PBA-MMA, Titanium white (0.38 v/v)	1 year	$E^* = 3530^{\alpha}$	$-10°C$, 50% RH, 0.00002 s^{-1}, tested perpendicular to casting direction	[31]
Golden Artist Colors PBA-MMA, Titanium white (0.38 v/v)	1 year	$E^* = 3790^{\alpha}$	$-10°C$, 50% RH, 0.00002 s^{-1}, tested in casting direction	[31]
Liquitex Heavy Body, Burnt Umber	1-2 years	$E_s = 34^{ff}$	23°C, 55 % RH, E_s at 1% strain	[59]
Liquitex Heavy Body, Burnt Umber	1-2 years	$E_s = 250^{ff}$	23°C, 55 % RH, Immersed in Ethanol 20 min, Dried 1 month, E_s at 1% strain	[59]

Sample Composition	Aging Time	Mechanical Property (MPa)	Testing Conditions	References
Liquitex Heavy Body, Burnt Umber	1-2 years	$E_s = 330^{ff}$	23°C, 55 % RH, Immersed in Acetone 12 hours, Dried 1 month, E_s at 1% strain	[59]
Liquitex Heavy Body, Burnt Umber	1-2 years	$E_s = 110^{ff}$	23°C, 55 % RH, Immersed in water 20 min, Dried 1 month, E_s at 1% strain	[59]
Liquitex Heavy Body, Burnt Umber	1-2 years	$E_s = 250^{ff}$	23°C, 55 % RH, Immersed in Ethanol 12 hours, Dried 1 month, E_s at 1% strain	[59]
Liquitex Heavy Body, Burnt Umber	1-2 years	$E_s = 250^{ff}$	23°C, 55 % RH, Immersed in water 12 hours, Dried 1 month, E_s at 1% strain	[59]
Liquitex Heavy Body, Phthalocyanine Blue	1-2 years	$E_s = 4^{ff}$	23°C, 55 % RH, E_s at 5% strain	[59]
Liquitex Heavy Body, Phthalocyanine Blue	1-2 years	$E_s = 4^{ff}$	23°C, 55 % RH, Immersed in water 10 min, Dried 1 month, E_s at 5% strain	[59]
Liquitex Heavy Body, Phthalocyanine Blue	1-2 years	$E_s = 13^{ff}$	23°C, 55 % RH, Immersed in water 20 min, Dried 1 month, E_s at 5% strain	[59]
Liquitex Heavy Body, Phthalocyanine Blue	1-2 years	$E_s = 25^{ff}$	23°C, 55 % RH,Immersed in water 12 hours, Dried 1 month, E_s at 5% strain	[59]
Liquitex Heavy Body, Phthalocyanine Blue	1-2 years	$E_s = 34^{ff}$	23°C, 55 % RH, Immersed in ethanol 20 min, Dried 1 month, E_s at 5% strain	[59]

Sample Composition	Aging Time	Mechanical Property (MPa)	Testing Conditions	References
Liquitex Heavy Body, Phthalocyanine Blue	1-2 years	$E_s = 79^{ff}$	23°C, 55 % RH, Immersed in ethanol 12 hours, Dried 1 month, E_s at 5% strain	[59]
Liquitex Heavy Body, Phthalocyanine Blue	1-2 years	$E_s = 96^{ff}$	23°C, 55 % RH, Immersed in acetone 20 min, Dried 1 month, E_s at 5% strain	[59]
Liquitex Heavy Body, Phthalocyanine Blue	1-2 years	$E_s = 170^{ff}$	23°C, 55 % RH, Immersed in acetone 12 hours, Dried 1 month, E_s at 3% strain	[59]
Talens, Raw Sienna	1-2 years	$E_s = 23^{ff}$	23°C, 55 % RH, E_s at 5% strain	[59]
Talens, Raw Sienna	1-2 years	$E_s = 30^{ff}$	23°C, 55 % RH, Immersed in water 5 min, Dried 1 month, E_s at 5% strain	[59]
Talens, Raw Sienna	1-2 years	$E_s = 42^{ff}$	23°C, 55 % RH, Immersed in water 20 min, Dried 1 month, E_s at 5% strain	[59]
Talens, Raw Sienna	1-2 years	$E_s = 23^{ff}$	23°C, 55 % RH, Swabbed with water 5 min, Dried 1 month, E_s at 5% strain	[59]
Talens, Raw Sienna	1-2 years	$E_s = 30^{ff}$	23°C, 55 % RH, Swabbed with water 20 min, Dried 1 month, E_s at 5% strain	[59]
Talens, Raw Sienna	1-2 years	$E_s = 23^{ff}$	23°C, 55 % RH, Immersed in ligroin for 30 min, Dried 1 month, E_s at 5% strain	[59]

Sample Composition	Aging Time	Mechanical Property (MPa)	Testing Conditions	References
Talens, Raw Sienna	1-2 years	$E_s = 23^{ff}$	23°C, 55 % RH, Immersed in mineral spirits 30 min, Dried 1 month, E_s at 5% strain	[59]
Talens, Raw Sienna	1-2 years	$E_s = 23^{ff}$	23°C, 55 % RH, Immersed in mineral spirits/water emulsion 30 min, Dried 1 month, E_s at 5% strain	[59]
Talens, Raw Sienna	1-2 years	$E_s = 30^{ff}$	23°C, 55 % RH, Exposed to Vanzan gel for 30 min, Dried 1 month, E_s at 5% strain	[59]
Talens, Raw Sienna	1-2 years	$E_s = 30^{ff}$	23°C, 55 % RH, Exposed to Klucel Gel for 30 min, Swabbed with water 30 sec, Dried 1 month, E_s at 5% strain	[59]
Talens, Raw Sienna	1-2 years	$E_s = 40^{ff}$	23°C, 55 % RH, Swabbed with water for 30 min, Dried 1 month, E_s at 5% strain	[59]
Liquitex ground (PBA-MMA), $TiO_2/CaCO_3$/talc	1 year	$E_s = 4800^{ff}$	−10°C, 50 % RH, 0.0002 s^{-1}, E_s at 0.5% strain	[60]
Liquitex ground (PBA-MMA), $TiO_2/CaCO_3$/talc	1 year	$E_s = 3600^{ff}$	−10°C, 50 % RH, 0.00002 s^{-1}, E_s at 0.5% strain	[60]
Liquitex ground (PBA-MMA), $TiO_2/CaCO_3$/talc	1 year	$E_s = 5240^{ff}$	0°C, 50 % RH, 0.02 s^{-1}, E_s at 0.5% strain	[60]
Liquitex ground (PBA-MMA), $TiO_2/CaCO_3$/talc	1 year	$E_s = 4000^{ff}$	0°C, 50 % RH, 0.002 s^{-1}, E_s at 0.5% strain	[60]
Liquitex ground (PBA-MMA), $TiO_2/CaCO_3$/talc	1 year	$E_s = 2580^{ff}$	0°C, 50 % RH, 0.0002 s^{-1}, E_s at 0.5% strain	[60]

Sample Composition	Aging Time	Mechanical Property (MPa)	Testing Conditions	References
Liquitex ground (PBA-MMA), $TiO_2/CaCO_3$/talc	1 year	$E_s = 1510^{ff}$	0°C, 50 % RH, 0.00002 s^{-1}, E_s at 0.5% strain	[60]
Liquitex ground (PBA-MMA), $TiO_2/CaCO_3$/talc	1 year	$E_s = 3460^{ff}$	10°C, 50 % RH, 0.02 s^{-1}, E_s at 0.5% strain	[60]
Liquitex ground (PBA-MMA), $TiO_2/CaCO_3$/talc	1 year	$E_s = 2030^{ff}$	10°C, 50 % RH, 0.002 s^{-1}, E_s at 0.5% strain	[60]
Liquitex ground (PBA-MMA), $TiO_2/CaCO_3$/talc	1 year	$E_s = 980^{ff}$	10°C, 50 % RH, 0.0002 s^{-1}, E_s at 0.5% strain	[60]
Liquitex ground (PBA-MMA), $TiO_2/CaCO_3$/talc	1 year	$E_s = 430^{ff}$	10°C, 50 % RH, 0.00002 s^{-1}, E_s at 0.5% strain	[60]
Liquitex ground (PBA-MMA), $TiO_2/CaCO_3$/talc	1 year	$E_s = 1000^{ff}$	20°C, 50 % RH, 0.02 s^{-1}, E_s at 0.5% strain	[60]
Liquitex ground (PBA-MMA), $TiO_2/CaCO_3$/talc	1 year	$E_s = 440^{ff}$	20°C, 50 % RH, 0.002 s^{-1}, E_s at 0.5% strain	[60]
Liquitex ground (PBA-MMA), $TiO_2/CaCO_3$/talc	1 year	$E_s = 170^{ff}$	20°C, 50 % RH, 0.0002 s^{-1}, E_s at 0.5% strain	[60]
Liquitex ground (PBA-MMA), $TiO_2/CaCO_3$/talc	1 year	$E_s = 80^{ff}$	20°C, 50 % RH, 0.00002 s^{-1}, E_s at 0.5% strain	[60]
Liquitex ground (PBA-MMA), $TiO_2/CaCO_3$/talc	1 year	$E_s = 360^{ff}$	30°C, 50 % RH, 0.02 s^{-1}, E_s at 0.5% strain	[60]
Liquitex ground (PBA-MMA), $TiO_2/CaCO_3$/talc	1 year	$E_s = 140^{ff}$	30°C, 50 % RH, 0.002 s^{-1}, E_s at 0.5% strain	[60]
Liquitex ground (PBA-MMA), $TiO_2/CaCO_3$/talc	1 year	$E_s = 70^{ff}$	30°C, 50 % RH, 0.0002 s^{-1}, E_s at 0.5% strain	[60]
Liquitex ground (PBA-MMA), $TiO_2/CaCO_3$/talc	1 year	$E_s = 40^{ff}$	30°C, 50 % RH, 0.00002 s^{-1}, E_s at 0.5% strain	[60]
Golden Artist Colors, Raw Umber	1 year	$E_s = 4870^{ff}$	−10°C, 50 % RH, 0.02 s^{-1}, E_s at 0.5% strain	[60]
Golden Artist Colors, Raw Umber	1 year	$E_s = 4400^{ff}$	−10°C, 50 % RH, 0.002 s^{-1}, E_s at 0.5% strain	[60]

Sample Composition	Aging Time	Mechanical Property (MPa)	Testing Conditions	References
Golden Artist Colors, Raw Umber	1 year	$E_s = 3350^{ff}$	−10°C, 50 % RH, 0.0002 s^{-1}, E_s at 0.5% strain	[60]
Golden Artist Colors, Raw Umber	1 year	$E_s = 2860^{ff}$	−10°C, 50 % RH, 0.00002 s^{-1}, E_s at 0.5% strain	[60]
Golden Artist Colors, Raw Umber	1 year	$E_s = 4160^{ff}$	0°C, 50 % RH, 0.02 s^{-1}, E_s at 0.5% strain	[60]
Golden Artist Colors, Raw Umber	1 year	$E_s = 3310^{ff}$	0°C, 50 % RH, 0.002 s^{-1}, E_s at 0.5% strain	[60]
Golden Artist Colors, Raw Umber	1 year	$E_s = 2520^{ff}$	0°C, 50 % RH, 0.0002 s^{-1}, E_s at 0.5% strain	[60]
Golden Artist Colors, Raw Umber	1 year	$E_s = 2780^{ff}$	10°C, 50 % RH, 0.02 s^{-1}, E_s at 0.5% strain	[60]
Golden Artist Colors, Raw Umber	1 year	$E_s = 1940^{ff}$	10°C, 50 % RH, 0.002 s^{-1}, E_s at 0.5% strain	[60]
Golden Artist Colors, Raw Umber	1 year	$E_s = 1200^{ff}$	10°C, 50 % RH, 0.0002 s^{-1}, E_s at 0.5% strain	[60]
Golden Artist Colors, Raw Umber	1 year	$E_s = 600^{ff}$	10°C, 50 % RH, 0.00002 s^{-1}, E_s at 0.5% strain	[60]
Golden Artist Colors, Raw Umber	1 year	$E_s = 1110^{ff}$	20°C, 50 % RH, 0.02 s^{-1}, E_s at 0.5% strain	[60]
Golden Artist Colors, Raw Umber	1 year	$E_s = 600^{ff}$	20°C, 50 % RH, 0.002 s^{-1}, E_s at 0.5% strain	[60]
Golden Artist Colors, Raw Umber	1 year	$E_s = 300^{ff}$	20°C, 50 % RH, 0.0002 s^{-1}, E_s at 0.5% strain	[60]
Golden Artist Colors, Raw Umber	1 year	$E_s = 130^{ff}$	20°C, 50 % RH, 0.00002 s^{-1}, E_s at 0.5% strain	[60]
Golden Artist Colors, Raw Umber	1 year	$E_s = 380^{ff}$	30°C, 50 % RH, 0.02 s^{-1}, E_s at 0.5% strain	[60]
Golden Artist Colors, Raw Umber	1 year	$E_s = 170^{ff}$	30°C, 50 % RH, 0.002 s^{-1}, E_s at 0.5% strain	[60]

Sample Composition	Aging Time	Mechanical Property (MPa)	Testing Conditions	References
Golden Artist Colors, Raw Umber	1 year	$E_s = 85^{ff}$	30°C, 50 % RH, 0.0002 s^{-1}, E_s at 0.5% strain	[60]
Golden Artist Colors, Raw Umber	1 year	$E_s = 55^{ff}$	30°C, 50 % RH, 0.00002 s^{-1}, E_s at 0.5% strain	[60]
Speedball, Raw Umber	27 years	$E_s = 3880^{ff}$	−10°C, 50 % RH, 0.02 s^{-1}, E_s at 0.5% strain	[60]
Speedball, Raw Umber	27 years	$E_s = 3600^{ff}$	−10°C, 50 % RH, 0.002 s^{-1}, E_s at 0.5% strain	[60]
Speedball, Raw Umber	27 years	$E_s = 3270^{ff}$	−10°C, 50 % RH, 0.0002 s^{-1}, E_s at 0.5% strain	[60]
Speedball, Raw Umber	27 years	$E_s = 2520^{ff}$	−10°C, 50 % RH, 0.00002 s^{-1}, E_s at 0.5% strain	[60]
Speedball, Raw Umber	27 years	$E_s = 3380^{ff}$	0°C, 50 % RH, 0.02 s^{-1}, E_s at 0.5% strain	[60]
Speedball, Raw Umber	27 years	$E_s = 2780^{ff}$	0°C, 50 % RH, 0.002 s^{-1}, E_s at 0.5% strain	[60]
Speedball, Raw Umber	27 years	$E_s = 2170^{ff}$	0°C, 50 % RH, 0.0002 s^{-1}, E_s at 0.5% strain	[60]
Speedball, Raw Umber	27 years	$E_s = 1270^{ff}$	0°C, 50 % RH, 0.00002 s^{-1}, E_s at 0.5% strain	[60]
Speedball, Raw Umber	27 years	$E_s = 2380^{ff}$	10°C, 50 % RH, 0.02 s^{-1}, E_s at 0.5% strain	[60]
Speedball, Raw Umber	27 years	$E_s = 1440^{ff}$	10°C, 50 % RH, 0.002 s^{-1}, E_s at 0.5% strain	[60]
Speedball, Raw Umber	27 years	$E_s = 660^{ff}$	10°C, 50 % RH, 0.0002 s^{-1}, E_s at 0.5% strain	[60]
Speedball, Raw Umber	27 years	$E_s = 260^{ff}$	10°C, 50 % RH, 0.00002 s^{-1}, E_s at 0.5% strain	[60]
Speedball, Raw Umber	27 years	$E_s = 540^{ff}$	20°C, 50 % RH, 0.02 s^{-1}, E_s at 0.5% strain	[60]

Sample Composition	Aging Time	Mechanical Property (MPa)	Testing Conditions	References
Speedball, Raw Umber	27 years	$E_s = 190^{ff}$	20°C, 50 % RH, 0.002 s^{-1}, E_s at 0.5% strain	[60]
Speedball, Raw Umber	27 years	$E_s = 82^{ff}$	20°C, 50 % RH, 0.0002 s^{-1}, E_s at 0.5% strain	[60]
Speedball, Raw Umber	27 years	$E_s = 45^{ff}$	20°C, 50 % RH, 0.00002 s^{-1}, E_s at 0.5% strain	[60]
Speedball, Raw Umber	27 years	$E_s = 110^{ff}$	30°C, 50 % RH, 0.02 s^{-1}, E_s at 0.5% strain	[60]
Speedball, Raw Umber	27 years	$E_s = 59^{ff}$	30°C, 50 % RH, 0.002 s^{-1}, E_s at 0.5% strain	[60]
Speedball, Raw Umber	27 years	$E_s = 34^{ff}$	30°C, 50 % RH, 0.0002 s^{-1}, E_s at 0.5% strain	[60]
Speedball, Raw Umber	27 years	$E_s = 23^{ff}$	30°C, 50 % RH, 0.00002 s^{-1}, E_s at 0.5% strain	[60]
Liquitex, Burnt Umber	27 years	$E_s = 3530^{ff}$	−10°C, 50 % RH, 0.0002 s^{-1}, E_s at 0.5% strain	[60]
Liquitex, Burnt Umber	27 years	$E_s = 2800^{ff}$	−10°C, 50 % RH, 0.00002 s^{-1}, E_s at 0.5% strain	[60]
Liquitex, Burnt Umber	27 years	$E_s = 3590^{ff}$	0°C, 50 % RH, 0.02 s^{-1}, E_s at 0.5% strain	[60]
Liquitex, Burnt Umber	27 years	$E_s = 3210^{ff}$	0°C, 50 % RH, 0.002 s^{-1}, E_s at 0.5% strain	[60]
Liquitex, Burnt Umber	27 years	$E_s = 2650^{ff}$	0°C, 50 % RH, 0.0002 s^{-1}, E_s at 0.5% strain	[60]
Liquitex, Burnt Umber	27 years	$E_s = 1900^{ff}$	0°C, 50 % RH, 0.00002 s^{-1}, E_s at 0.5% strain	[60]
Liquitex, Burnt Umber	27 years	$E_s = 2700^{ff}$	10°C, 50 % RH, 0.02 s^{-1}, E_s at 0.5% strain	[60]
Liquitex, Burnt Umber	27 years	$E_s = 1820^{ff}$	10°C, 50 % RH, 0.002 s^{-1}, E_s at 0.5% strain	[60]

Sample Composition	Aging Time	Mechanical Property (MPa)	Testing Conditions	References
Liquitex, Burnt Umber	27 years	$E_s = 1270^{ff}$	10°C, 50 % RH, 0.0002 s^{-1}, E_s at 0.5% strain	[60]
Liquitex, Burnt Umber	27 years	$E_s = 630^{ff}$	10°C, 50 % RH, 0.00002 s^{-1}, E_s at 0.5% strain	[60]
Liquitex, Burnt Umber	27 years	$E_s = 960^{ff}$	20°C, 50 % RH, 0.02 s^{-1}, E_s at 0.5% strain	[60]
Liquitex, Burnt Umber	27 years	$E_s = 460^{ff}$	20°C, 50 % RH, 0.002 s^{-1}, E_s at 0.5% strain	[60]
Liquitex, Burnt Umber	27 years	$E_s = 280^{ff}$	20°C, 50 % RH, 0.0002 s^{-1}, E_s at 0.5% strain	[60]
Liquitex, Burnt Umber	27 years	$E_s = 140^{ff}$	20°C, 50 % RH, 0.00002 s^{-1}, E_s at 0.5% strain	[60]
Liquitex, Burnt Umber	27 years	$E_s = 340^{ff}$	30°C, 50 % RH, 0.02 s^{-1}, E_s at 0.5% strain	[60]
Liquitex, Burnt Umber	27 years	$E_s = 180^{ff}$	30°C, 50 % RH, 0.002 s^{-1}, E_s at 0.5% strain	[60]
Liquitex, Burnt Umber	27 years	$E_s = 120^{ff}$	30°C, 50 % RH, 0.0002 s^{-1}, E_s at 0.5% strain	[60]
Liquitex, Burnt Umber	27 years	$E_s = 100^{ff}$	30°C, 50 % RH, 0.00002 s^{-1}, E_s at 0.5% strain	[60]

Table A.4: Summary of tensile test data for grounds, paint consolidation materials, and painting supports, including composition, aging time of the sample, testing conditions (temperature, RH, strain rate), mechanical property (Youngs modulus (E), equilibrium modulus (E_{eq}), secant modulus (E_s), tensile strength (σ_T), or yield stress (σ_Y), reference, *etc.* *Strain rates from this reference ranged from 0.001-0.01 s^{-1}. $^{\alpha}$Indicates a value estimated from a plot in the paper, rather than a tabulated value.

Sample Composition	Aging Time	Mechanical Property	Testing Conditions	Reference

Sample Composition	Aging Time	Mechanical Property	Testing Conditions	Reference
Björn skin glue, Calcium Carbonate, 75% PVC	1 day	$\text{œ}_T = 2.1^{\alpha}$	22°C, 12% RH	[54]
Björn skin glue, Calcium Carbonate, 75% PVC	1 day	$\text{œ}_T = 1.8^{\alpha}$	22°C, 53% RH	[54]
Björn skin glue, Calcium Carbonate, 75% PVC	1 day	$\text{œ}_T = 0.28^{\alpha}$	22°C, 81% RH	[54]
Björn skin glue, Calcium Carbonate, 75% PVC	1 day	$\text{œ}_T = 0^{\alpha}$	22°C, 90% RH	[54]
Björn skin glue, Calcium Carbonate, 68% PVC	1 day	$\text{œ}_T = 4.1^{\alpha}$	22°C, 12% RH	[54]
Björn skin glue, Calcium Carbonate, 68% PVC	1 day	$\text{œ}_T = 3.4^{\alpha}$	22°C, 67% RH	[54]
Björn skin glue, Calcium Carbonate, 68% PVC	1 day	$\text{œ}_T = 0.98^{\alpha}$	22°C, 87% RH	[54]
Björn skin glue, Calcium Carbonate, 68% PVC	1 day	$\text{œ}_T = 0^{\alpha}$	22°C, 93% RH	[54]
Björn skin glue, Calcium Carbonate	1 day	$\text{œ}_T = 5.4^{\alpha}$	22°C, 15.6% RH	[54]
Björn skin glue, Calcium Carbonate	1 day	$\text{œ}_T = 5.1^{\alpha}$	22°C, 48.7% RH	[54]
Björn skin glue, Calcium Carbonate	1 day	$\text{œ}_T = 0.72^{\alpha}$	22°C, 84.1% RH	[54]
Björn skin glue, Calcium Carbonate & Molasses (17%)	1 day	$\text{œ}_T = 5.7^{\alpha}$	22°C, 17% RH	[54]

Sample Composition	Aging Time	Mechanical Property	Testing Conditions	Reference
Björn skin glue, Calcium Carbonate & Molasses (17%)	1 day	$œ_T = 3.3^{\alpha}$	22°C, 55.1% RH	[54]
Björn skin glue, Calcium Carbonate & Molasses (17%)	1 day	$œ_T = 0.33^{\alpha}$	22°C, 84.4% RH	[54]
Colletta filler	1 day	$œ_T = 3.6^{\alpha}$	22°C, 11.2% RH	[54]
Colletta filler	1 day	$œ_T = 2.6^{\alpha}$	22°C, 48% RH	[54]
Colletta filler	1 day	$œ_T = 0.93^{\alpha}$	22°C, 80.7% RH	[54]
Colletta filler	1 day	$œ_T = 0.14^{\alpha}$	22°C, 96% RH	[54]
Mowiol #9 filler	1 day	$œ_T = 2.7^{\alpha}$	22°C, 48% RH	[54]
Modostuc	1 day	$œ_T = 0.24^{\alpha}$	22°C, 48% RH	[54]
Gesso: Rabbit Skin Glue, Ground Chalk (92% PVC)	-	$E = 7020^{\alpha}$	22°C, 51% RH, $3.3 * 10^{-5}\ s^{-1}$	[62]
Gesso: Rabbit Skin Glue, Ground Chalk (92% PVC)	-	$E = 7000^{\alpha}$	22°C, 54% RH, $3.3 * 10^{-5}\ s^{-1}$	[62]
Gesso: Rabbit Skin Glue, Ground Chalk (92% PVC)	-	$E = 6890^{\alpha}$	22°C, 60% RH, $3.3 * 10^{-5}\ s^{-1}$	[62]
Gesso: Rabbit Skin Glue, Ground Chalk (92% PVC)	-	$E = 6660^{\alpha}$	22°C, 65% RH, $3.3 * 10^{-5}\ s^{-1}$	[62]
Gesso: Rabbit Skin Glue, Ground Chalk (92% PVC)	-	$E = 6140^{\alpha}$	22°C, 70% RH, $3.3 * 10^{-5}\ s^{-1}$	[62]
Gesso: Rabbit Skin Glue, Ground Chalk (92% PVC)	-	$E = 4890^{\alpha}$	22°C, 75% RH, $3.3 * 10^{-5}\ s^{-1}$	[62]
Gesso: Rabbit Skin Glue, Ground Chalk (92% PVC)	-	$E = 2930^{\alpha}$	22°C, 79% RH, $3.3 * 10^{-5}\ s^{-1}$	[62]
Gesso: Rabbit Skin Glue, Ground Chalk (92% PVC)	-	$E = 1890^{\alpha}$	22°C, 84% RH, $3.3 * 10^{-5}\ s^{-1}$	[62]
Gesso: Rabbit Skin Glue, Ground Chalk (92% PVC)	-	$E = 1260^{\alpha}$	22°C, 88% RH, $3.3 * 10^{-5}\ s^{-1}$	[62]

Sample Composition	Aging Time	Mechanical Property	Testing Conditions	Reference
Linen fabric, 262 g/m^2	-	E = 324.2	Tested at ambient conditions, 1.67 s^{-1}, sample cut in the weft direction	[63]
Linen fabric, 262 g/m^2	-	E = 146.6	Tested at ambient conditions, 1.67 s^{-1}, sample cut at a 15° angle to the weft direction	[63]
Linen fabric, 262 g/m^2	-	E = 59.8	Tested at ambient conditions, 1.67 s^{-1}, sample cut at a 30° angle to the weft direction	[63]
Linen fabric, 262 g/m^2	-	E = 76.6	Tested at ambient conditions, 1.67 s^{-1}, sample cut at a 45° angle to the weft direction	[63]
Linen fabric, 262 g/m^2	-	E = 56.8	Tested at ambient conditions, 1.67 s^{-1}, sample cut at a 60° angle to the weft direction	[63]
Linen fabric, 262 g/m^2	-	E = 150.4	Tested at ambient conditions, 1.67 s^{-1}, sample cut at a 75° angle to the weft direction	[63]
Linen fabric, 262 g/m^2	-	E = 171.7	Tested at ambient conditions, 1.67 s^{-1}, sample cut in the warp direction	[63]

Sample Composition	Aging Time	Mechanical Property	Testing Conditions	Reference
Linen fabric, 262 g/m^2, one layer animal skin glue size, one layer ground (champagne chalk, TiO_2)	-	E = 5098.2	Tested at ambient conditions, 1.67 s^{-1}, sample cut in the weft direction	[63]
Linen fabric, 262 g/m^2, one layer animal skin glue size, one layer ground (champagne chalk, TiO_2)	-	E = 4421.6	Tested at ambient conditions, 1.67 s^{-1}, sample cut at a 15° angle to the weft direction	[63]
Linen fabric, 262 g/m^2, one layer animal skin glue size, one layer ground (champagne chalk, TiO_2)	-	E = 3128.5	Tested at ambient conditions, 1.67 s^{-1}, sample cut at a 30° angle to the weft direction	[63]
Linen fabric, 262 g/m^2, one layer animal skin glue size, one layer ground (champagne chalk, TiO_2)	-	E = 4365.9	Tested at ambient conditions, 1.67 s^{-1}, sample cut at a 45° angle to the weft direction	[63]
Linen fabric, 262 g/m^2, one layer animal skin glue size, one layer ground (champagne chalk, TiO_2)	-	E = 3212.7	Tested at ambient conditions, 1.67 s^{-1}, sample cut at a 60° angle to the weft direction	[63]
Linen fabric, 262 g/m^2, one layer animal skin glue size, one layer ground (champagne chalk, TiO_2)	-	E = 3800.2	Tested at ambient conditions, 1.67 s^{-1}, sample cut at a 75° angle to the weft direction	[63]

Sample Composition	Aging Time	Mechanical Property	Testing Conditions	Reference
Linen fabric, 262 g/m^2, one layer animal skin glue size, one layer ground (champagne chalk, TiO_2)	-	E = 4058.7	Tested at ambient conditions, 1.67 s^{-1}, sample cut in the warp direction	[63]
Linen fabric, 262 g/m^2, one layer animal skin glue size, two layers ground (champagne chalk, TiO_2)	-	E = 6116.2	Tested at ambient conditions, 1.67 s^{-1}, sample cut in the weft direction	[63]
Linen fabric, 262 g/m^2, one layer animal skin glue size, two layers ground (champagne chalk, TiO_2)	-	E = 5344.6	Tested at ambient conditions, 1.67 s^{-1}, sample cut at a 15° angle to the weft direction	[63]
Linen fabric, 262 g/m^2, one layer animal skin glue size, two layers ground (champagne chalk, TiO_2)	-	E = 5378.5	Tested at ambient conditions, 1.67 s^{-1}, sample cut at a 30° angle to the weft direction	[63]
Linen fabric, 262 g/m^2, one layer animal skin glue size, two layers ground (champagne chalk, TiO_2)	-	E = 5211.3	Tested at ambient conditions, 1.67 s^{-1}, sample cut at a 45° angle to the weft direction	[63]
Linen fabric, 262 g/m^2, one layer animal skin glue size, two layers ground (champagne chalk, TiO_2)	-	E = 4490.2	Tested at ambient conditions, 1.67 s^{-1}, sample cut at a 60° angle to the weft direction	[63]

Sample Composition	Aging Time	Mechanical Property	Testing Conditions	Reference
Linen fabric, 262 g/m^2, one layer animal skin glue size, two layers ground (champagne chalk, TiO_2)	-	E = 4508.5	Tested at ambient conditions, 1.67 s^{-1}, sample cut at a 75° angle to the weft direction	[63]
Linen fabric, 262 g/m^2, one layer animal skin glue size, two layers ground (champagne chalk, TiO_2)	-	E = 4911.2	Tested at ambient conditions, 1.67 s^{-1}, sample cut in the warp direction	[63]
Linen fabric, 262 g/m^2, one layer animal skin glue size, three layers ground (champagne chalk, TiO_2)	-	E = 7279.8	Tested at ambient conditions, 1.67 s^{-1}, sample cut in the weft direction	[63]
Linen fabric, 262 g/m^2, one layer animal skin glue size, three layers ground (champagne chalk, TiO_2)	-	E = 7059.2	Tested at ambient conditions, 1.67 s^{-1}, sample cut at a 15° angle to the weft direction	[63]
Linen fabric, 262 g/m^2, one layer animal skin glue size, three layers ground (champagne chalk, TiO_2)	-	E = 6607.5	Tested at ambient conditions, 1.67 s^{-1}, sample cut at a 30° angle to the weft direction	[63]
Linen fabric, 262 g/m^2, one layer animal skin glue size, three layers ground (champagne chalk, TiO_2)	-	E = 5986.2	Tested at ambient conditions, 1.67 s^{-1}, sample cut at a 45° angle to the weft direction	[63]

Sample Composition	Aging Time	Mechanical Property	Testing Conditions	Reference
Linen fabric, 262 g/m^2, one layer animal skin glue size, three layers ground (champagne chalk, TiO_2)	-	E = 5421.1	Tested at ambient conditions, 1.67 s^{-1}, sample cut at a 60° angle to the weft direction	[63]
Linen fabric, 262 g/m^2, one layer animal skin glue size, three layers ground (champagne chalk, TiO_2)	-	E = 5646.9	Tested at ambient conditions, 1.67 s^{-1}, sample cut at a 75° angle to the weft direction	[63]
Linen fabric, 262 g/m^2, one layer animal skin glue size, three layers ground (champagne chalk, TiO_2)	-	E = 6001.2	Tested at ambient conditions, 1.67 s^{-1}, sample cut in the warp direction	[63]
Becker's Latexspackle	-	E = 416.3	22°C, 25% RH, 1.7 s^{-1}	[66]
Becker's Latexspackle	-	E = 205	22°C, 50% RH, 1.7 s^{-1}	[66]
Becker's Latexspackle	-	E = 71.7	22°C, 75% RH, 1.7 s^{-1}	[66]
Flugger Spackle	-	E = 388	22°C, 25% RH, 1.7 s^{-1}	[66]
Flugger Spackle	-	E = 244.4	22°C, 50% RH, 1.7 s^{-1}	[66]
Flugger Spackle	-	E = 35.7	22°C, 75% RH, 1.7 s^{-1}	[66]
Golden Acrylic Gesso	-	E = 303.3	22°C, 25% RH, 10 s^{-1}	[66]
Golden Acrylic Gesso	-	E = 93.9	22°C, 50% RH, 10 s^{-1}	[66]
Golden Acrylic Gesso	-	E = 42.9	22°C, 75% RH, 10 s^{-1}	[66]
Liquitex Acrylic Gesso	-	E = 412.2	22°C, 25% RH, 10 s^{-1}	[66]
Liquitex Acrylic Gesso	-	E = 57.3	22°C, 50% RH, 10 s^{-1}	[66]
Liquitex Acrylic Gesso	-	E = 50.1	22°C, 75% RH, 10 s^{-1}	[66]

Sample Composition	Aging Time	Mechanical Property	Testing Conditions	Reference
Rabbit Skin Glue, Calcium Carbonate	-	E = 1511	22°C, 25% RH, 1.7 s^{-1}	[66]
Rabbit Skin Glue, Calcium Carbonate	-	E = 1730	22°C, 50% RH, 1.7 s^{-1}	[66]
Rabbit Skin Glue, Calcium Carbonate	-	E = 1995	22°C, 75% RH, 1.7 s^{-1}	[66]
Modern Cotton canvas, 374 g/m^2	3 days degraded	E = 1.1	25°C, 20% RH, 0.4 N/min; Artificial degradation using HCl and H_2O_2 solutions for 3 days at 40°C, samples tested along the warp directions	[69]
Modern Cotton canvas, 374 g/m^2; Nanofibrillated cellulose in water	3 days degraded	E = 23.1	25°C, 20% RH, 0.4 N/min; Artificial degradation using HCl and H_2O_2 solutions for 3 days at 40°C, 4 layers of consolidant brush applied, samples tested along the warp directions	[69]
Modern Cotton canvas, 374 g/m^2; Nanofibrillated cellulose in water	3 days degraded	E = 10.2	25°C, 20% RH, 0.4 N/min; Artificial degradation using HCl and H_2O_2 solutions for 3 days at 40°C, 4 layers of consolidant brush applied, samples tested along the warp directions	[69]

Sample Composition	Aging Time	Mechanical Property	Testing Conditions	Reference
Modern Cotton canvas, 374 g/m^2; Animal glue in water	3 days degraded	E = 14.3	25°C, 20% RH, 0.4 N/min; Artificial degradation using HCl and H_2O_2 solutions for 3 days at 40°C, 2 layers of consolidant brush applied, samples tested along the warp directions	[69]
Modern Cotton canvas, 374 g/m^2; Animal Glue in water	3 days degraded	E = 4.4	25°C, 20% RH, 0.4 N/min; Artificial degradation using HCl and H_2O_2 solutions for 3 days at 40°C, 2 layers of consolidant brush applied, samples tested along the warp directions	[69]
Modern Cotton canvas, 374 g/m^2; Beva 371 in white spirits	3 days degraded	E = 3.8	25°C, 20% RH, 0.4 N/min; Artificial degradation using HCl and H_2O_2 solutions for 3 days at 40°C, 4 layers of consolidant brush applied, samples tested along the warp directions	[69]

Sample Composition	Aging Time	Mechanical Property	Testing Conditions	Reference
Modern Cotton canvas, 374 g/m^2; Beva 371 in white spirits	3 days degraded	E = 3.2	25°C, 20% RH, 0.4 N/min; Artificial degradation using HCl and H_2O_2 solutions for 3 days at 40°C, 4 layers of consolidant brush applied, samples tested along the warp directions	[69]

B Supplemental Information for Chapter 3

B.1 Ellipsometry measurements

The UV-visible analyses were carried out on a Variable Angle Spectroscopic Ellipsometer (VASE from J.A. Wollam Co., Inc.) in the UV-visible-NIR range 300-1700 nm at three incident angles (60, 65, 70°). The acquisitions were performed using the VASE software.

B.2 Bulk rheology

Rheology data were collected using an Anton Parr MCR 302 with a Peltier temperature unit attached and using a 50 mm cone and plate geometry. Steady state flow experiments were performed from $25 - 80\,^{\circ}$C in $5\,^{\circ}$C steps. At each temperature, the shear rate was varied from 0.01 to 100 $1/s$ with six data points per decade and the viscosity measured from data collected over 10 seconds at each strain rate. The constant viscosity observed at high shear rates is reported in Table B.1. When the value at 25°C is compared to the initial value of $|G_3^*|\rho$ in Figure 3.4a, the value is within error bars of the QCM measurement, which confirms that the rheological properties of the LO samples can be comparably measured using both traditional rheology and the QCM.

Table B.1: Bulk rheology data for SA linseed oil from $25 - 80\,^{\circ}$C in $5\,^{\circ}$C steps. The viscosity is determined from the steady state flow experiments while the magnitude of the complex shear modulus is calculated using equation 3.5.

Temperature (°C)	viscosity, η (mPa · s)	Magnitude of the Complex Shear Modulus, $\|G_3^*\|$ (Pa)
25	43.9	4.1×10^6
30	36.7	3.5×10^6
25	31	2.9×10^6
40	26.5	2.5×10^6
45	22.8	2.2×10^6
50	19.9	1.9×10^6
55	17.5	1.7×10^6
60	15.4	1.5×10^6
65	13.8	1.3×10^6
70	12.4	1.2×10^6
75	11.3	1.1×10^6
80	10.3	9.7×10^5

B.3 Solution checks for the LO samples

The comparison and contour plots for the rest of the LO thin film data are shown in this section. Error bars have been incorporated into figures and titles have been included for ease of understanding which plots correspond to which sample. First, the comparison plots for the SA LO bulk data are shown in Figure B.1. One way to assess the accuracy of the calculated mechanical properties when only one harmonic is used is to compare the back-calculated and experimental values for $\Delta f/n$ and $\Delta\Gamma/n$ of other harmonics. In this figure, the 5th harmonic frequency and dissipation shifts show reasonable agreement between the back-calculated and experimental values.

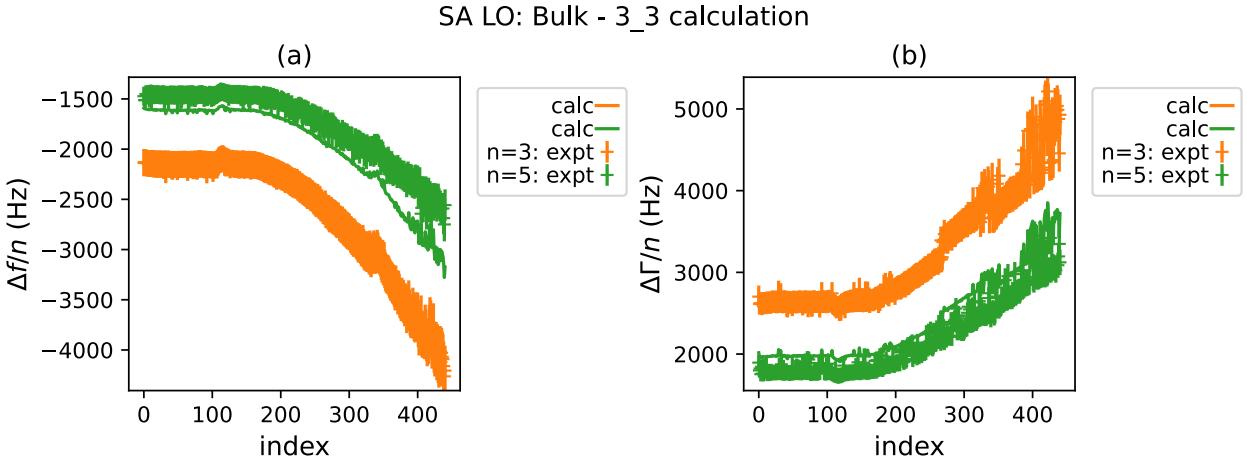

Figure B.1: The SA LO bulk sample comparison plots for the back-calculated solutions from the mechanical properties to the experimental values of (a) $\Delta f/n$ and (b) $\Delta\Gamma/n$. The error bars shown in the plots are 5% of Δf_3 and $\Delta\Gamma_3$.

The comparison and contour plots for the remaining data in Figure 3.8 are shown. Figure B.2shows the plots for KP 5% PbOb, which uses a '7.9:7' calculation. The variation seen in $\Delta\Gamma_9$ at the last time point is shown on a linear scale a reasonable amount of variation given that $\sim 10-20$ Hz of error can occur when taking a sample in and out of a holder. The error bars in Figure 3.8 are mostly a result of the similarity in the $\Delta f/n$ values for the 7th and 9th harmonics, which are fairly close and show some overlap when the error bars are factored in (see Figure B.2a). However, we believe the error bars for this particular sample to be larger than they should be. When the harmonic ratio is determined for the harmonics and applied to the error analysis, there is an assumption that the frequency shifts are uncorrelated. However, there does appear to be correlation between the frequencies measured. In Figure B.2a, the back calculated solutions for all the harmonics exhibit

the same trends and changes in the shifts over time. On the contour plots shown in Figure B.2c and d, there is some variation in the frequency shift values, but the variations seen in the dissipation shift values are fairly small, which can also contribute to the error bars in Figure 3.8.

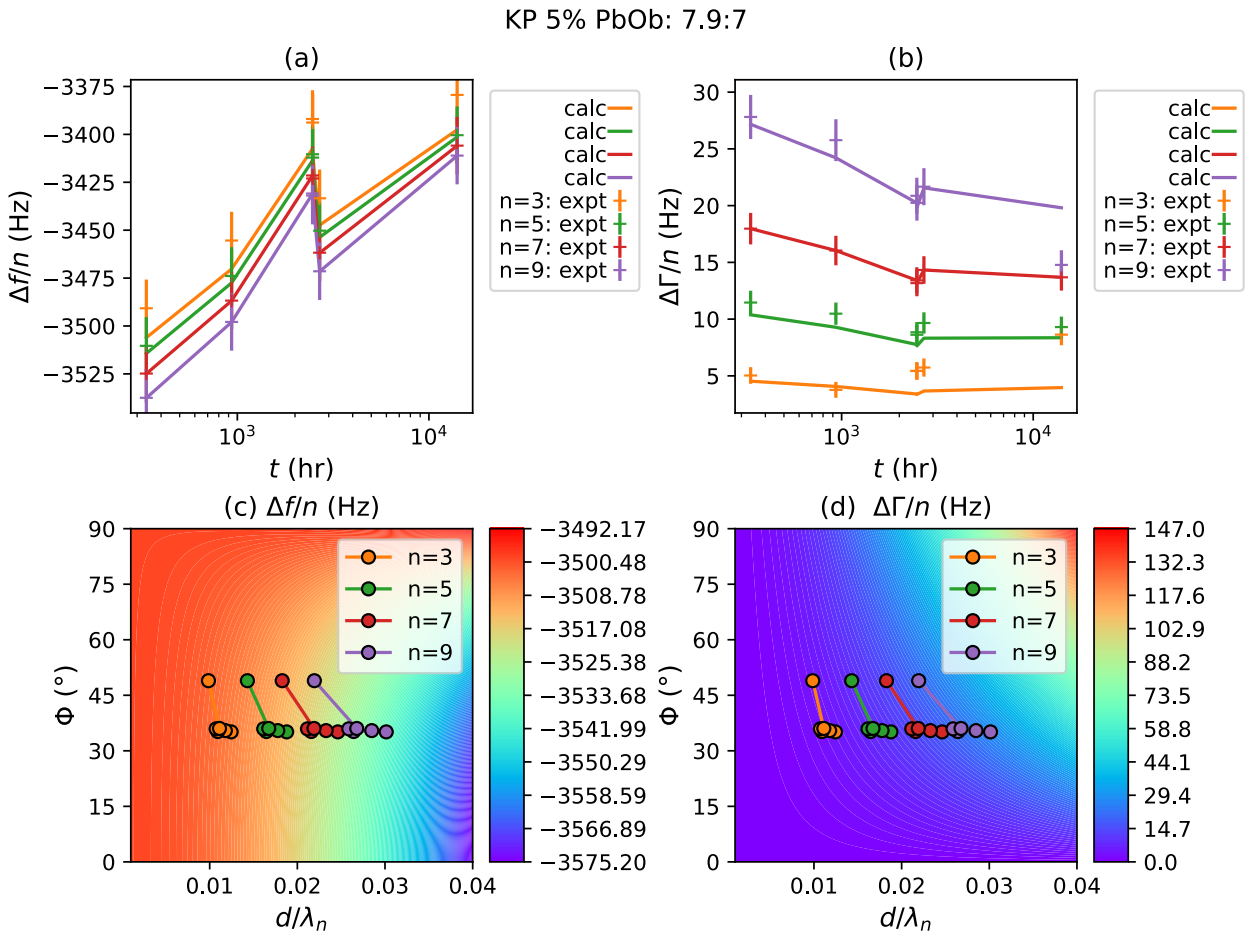

Figure B.2: Comparison and contour plots for a '7.9:7' calculation for the KP 5% PbOb sample. The (a) experimental values of $\Delta f/n$ to the back-calculated solutions, (b) experimental values of $\Delta\Gamma/n$ to the back-calculated solutions, (c) contour plot for the experimental $\Delta f/n$ values, and (d) contour plot for the experimental $\Delta\Gamma/n$ values. Good agreement of the solution for the mechanical properties is determined by comparing the back-calculated value from the solution not used in the calculation (in this case, the $\Delta\Gamma_9$) with the experimental data.

Figure B.3 is the check and comparison plots for the '7.9:7' calculation of the KP 5% PbOc data. Again, the variation shown between the back-calculated and experimental values of $\Delta\Gamma_9$ are reasonable for the amount of error typically seen for a QCM measurement. The error bars in Figure 3.8 are smaller for these data because there is better agreement between the back-calculated and experimental values for $\Delta\Gamma_9$ and there is also larger separation between the $\Delta f/n$ values for the

7^{th} and 9^{th} harmonics. The contour plots in Figure B.3c and B.3d show a fair amount of variation for the $\Delta f/n$ values but not as much variation for the $\Delta\Gamma/n$ values.

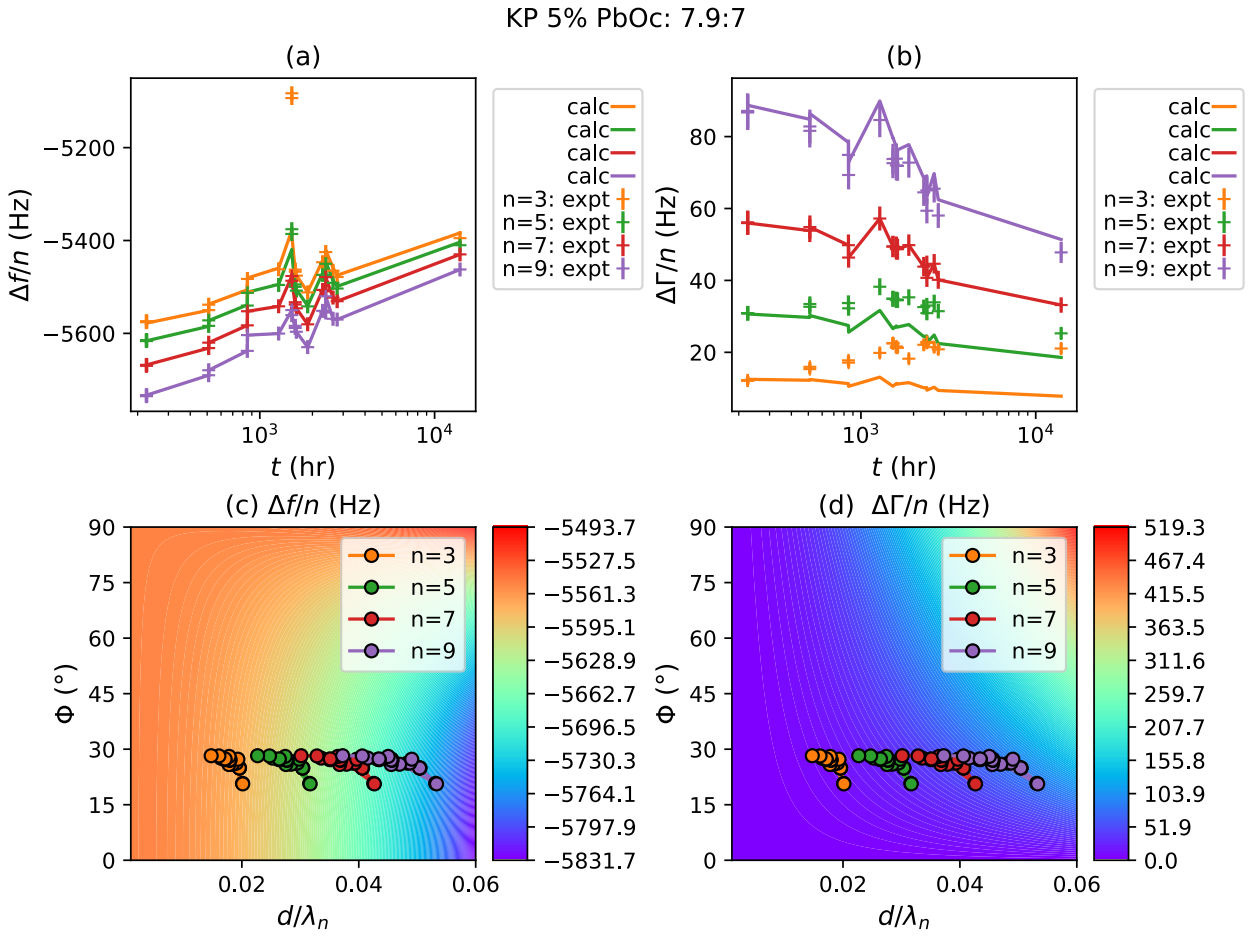

Figure B.3: The comparison and contour plots of a '7.9:7' calculation for the KP 5% PbOc sample. The (a) experimental values of $\Delta f/n$ to the back-calculated solutions, (b) experimental values of $\Delta\Gamma/n$ to the back-calculated solutions, (c) contour plot for the experimental $\Delta f/n$ values, and (d) contour plot for the experimental $\Delta\Gamma/n$ values. Good agreement of the solution for the mechanical properties is determined by comparing the back-calculated value from the solution not used in the calculation (in this case, the $\Delta\Gamma_9$) with the experimental data.

Figure B.4 shows the comparison and contour plots for the '5.9:9' calculation of the KP 20% PbO sample. The error bars are smaller than the symbols in Figure 3.8, mostly due to the good agreement between the back-calculated and experimental values of $\Delta\Gamma_5, n$ and the larger separation between the $\Delta f_5/n$ and $\Delta f_9/n$ than for the KP 5% PbO samples. The contour plots in Figure B.4c and d shows that the variation in the frequency and dissipation shifts for these data do not cause large changes to the mechanical properties. There is only a small amount of color variation and

the data for the 5th and 9th harmonics are fairly tightly clustered. Since the data for this sample begins around 70 hours, the calculated properties are well into a region of stability in the mechanical properties, especially if the higher amount of PbO used in this sample also greatly accelerated the initial polymerization step for the oil film.

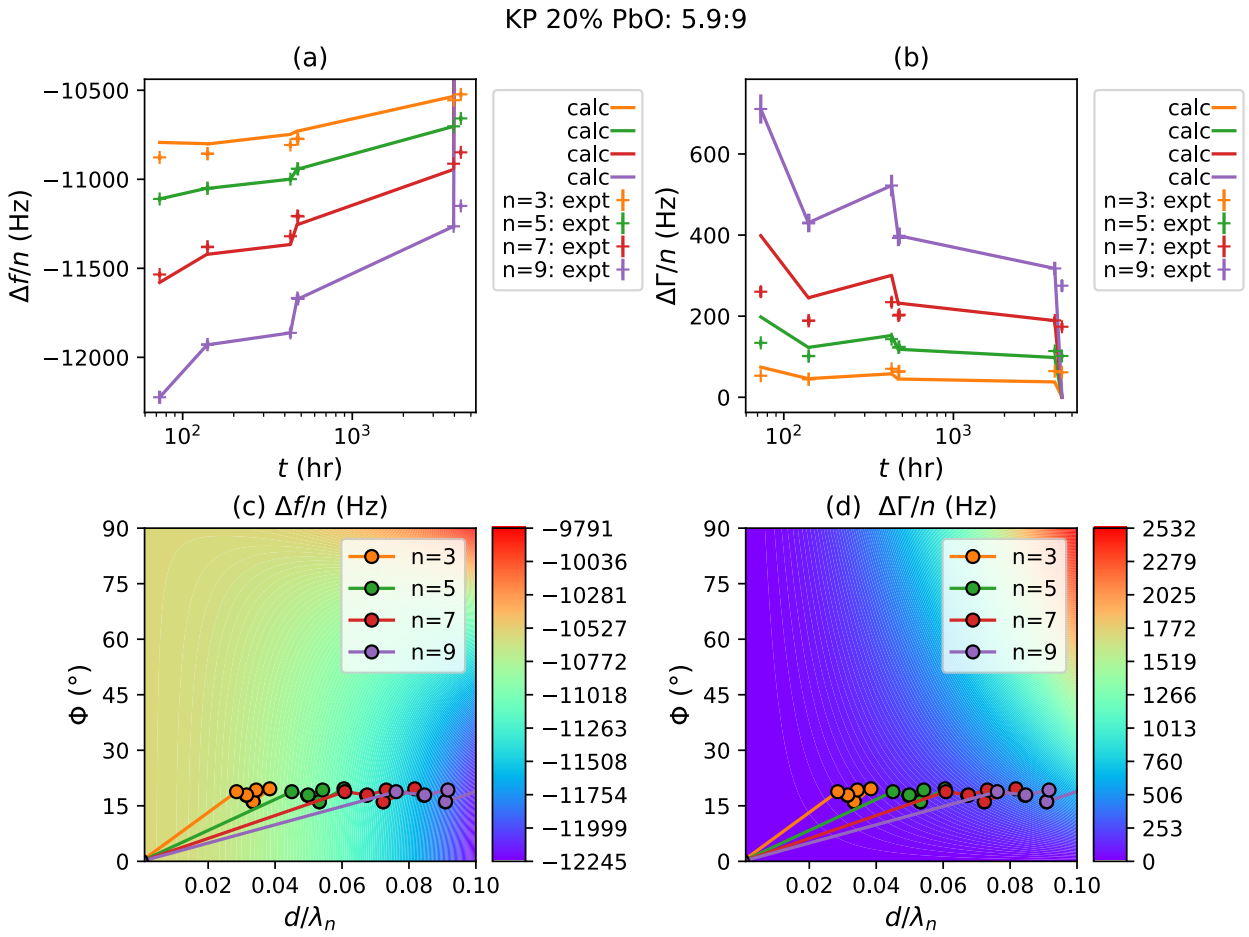

Figure B.4: Comparison and contour plots for a '5.9:9' calculation for the KP 20% PbO sample. The (a) experimental values of $\Delta f/n$ to the back-calculated solutions, (b) experimental values of $\Delta\Gamma/n$ to the back-calculated solutions, (c) contour plot for the experimental $\Delta f/n$ values, and (d) contour plot for the experimental $\Delta\Gamma/n$ values. Good agreement of the solution for the mechanical properties is determined by comparing the back-calculated value from the solution not used in the calculation (in this case, the $\Delta\Gamma_5$) with the experimental data.

Figure B.5 shows the comparison and contour plots for the '5.9:9' calculation of the KP LO sample. For this sample, the error bars are especially large in Figure 3.8b for ϕ. These large error bars are most likely due to the small separation in the $\Delta f/n$ values of this sample. The small harmonic ratio combined with the smaller values of $\Delta\Gamma_9/n$ result in the calculation of the error to become quite

large. For the contour plots in Figure B.5c and d, the trend in the data seems counter intuitive compared to the contour plots for the other KP samples. In this case, as the film is aging (data moving to the left), the phase angle becomes very large and trends towards 90°. However, for this last time point, it was observed that the film was starting to dewet around the edges of the gold electrode, which will introduce more uncertainty into the peak fitting than can be fully captured by the uncertainty dictionaries used to analyze these data. This known non-uniform composition of the KP LO film combined with extremely small differences in the $\Delta f/n$ values generates very large error bars.

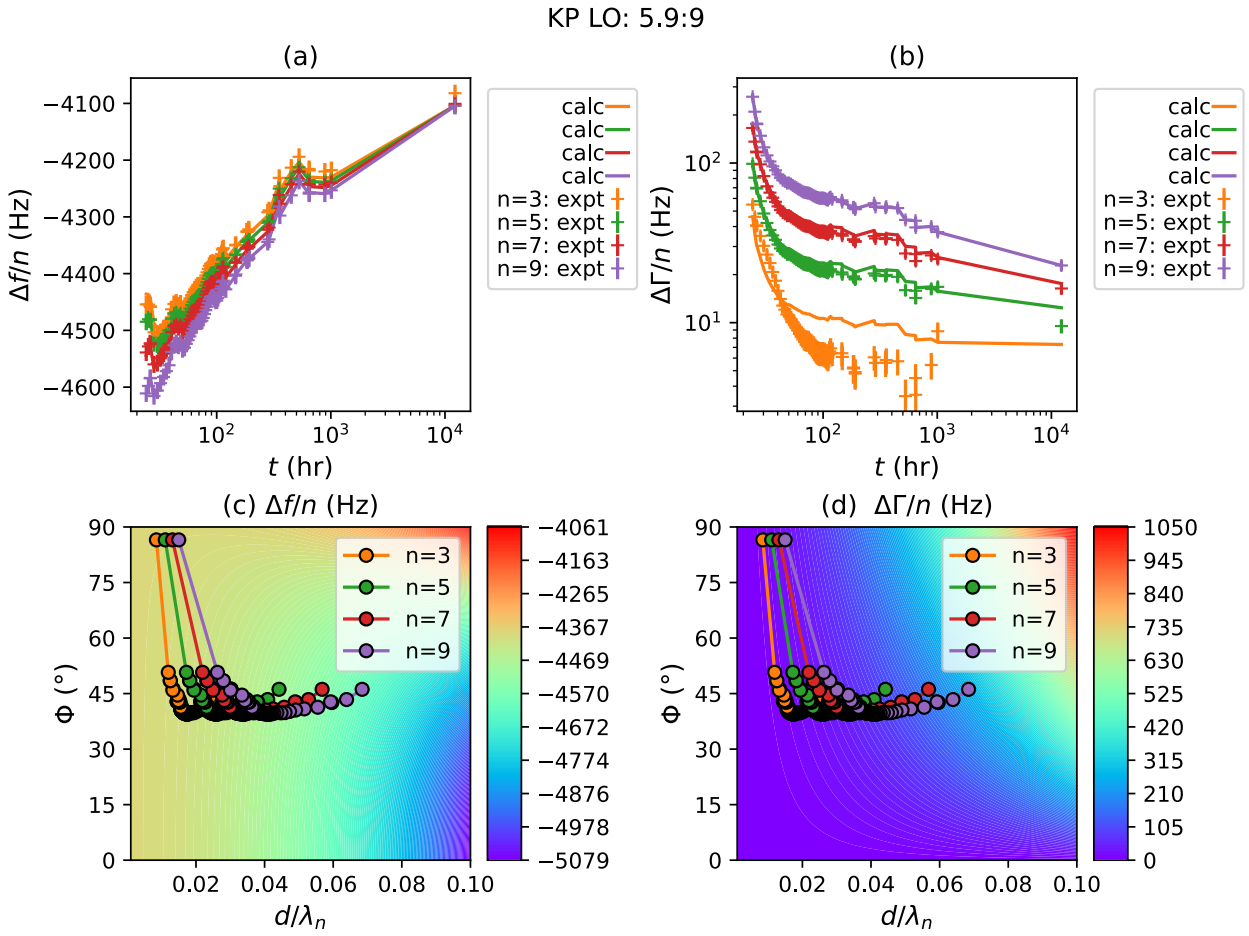

Figure B.5: Comparison and contour plots for a '5.9:9' calculation for the KP LO sample. The (a) experimental values of $\Delta f/n$ to the back-calculated solutions, (b) experimental values of $\Delta\Gamma/n$ to the back-calculated solutions, (c) contour plot for the experimental $\Delta f/n$ values, and (d) contour plot for the experimental $\Delta\Gamma/n$ values. Good agreement of the solution for the mechanical properties is determined by comparing the back-calculated value from the solution not used in the calculation (in this case, the $\Delta\Gamma_5$) with the experimental data.

Figure B.6 shows the comparison and contour plots for the SA LO sample. All the data are shown , but the 5th harmonic data are not used until after 55 days, which is where the $\Delta f/n$ data also begins to be fit. The $\Delta\Gamma_5/n$ does not agree well with the experimental values, but the main reason for this disagreement comes from the sample quality and the transition period through the 'no man's land' region of the contour plot space, which was discussed more fully and shown in Figure 3.6.

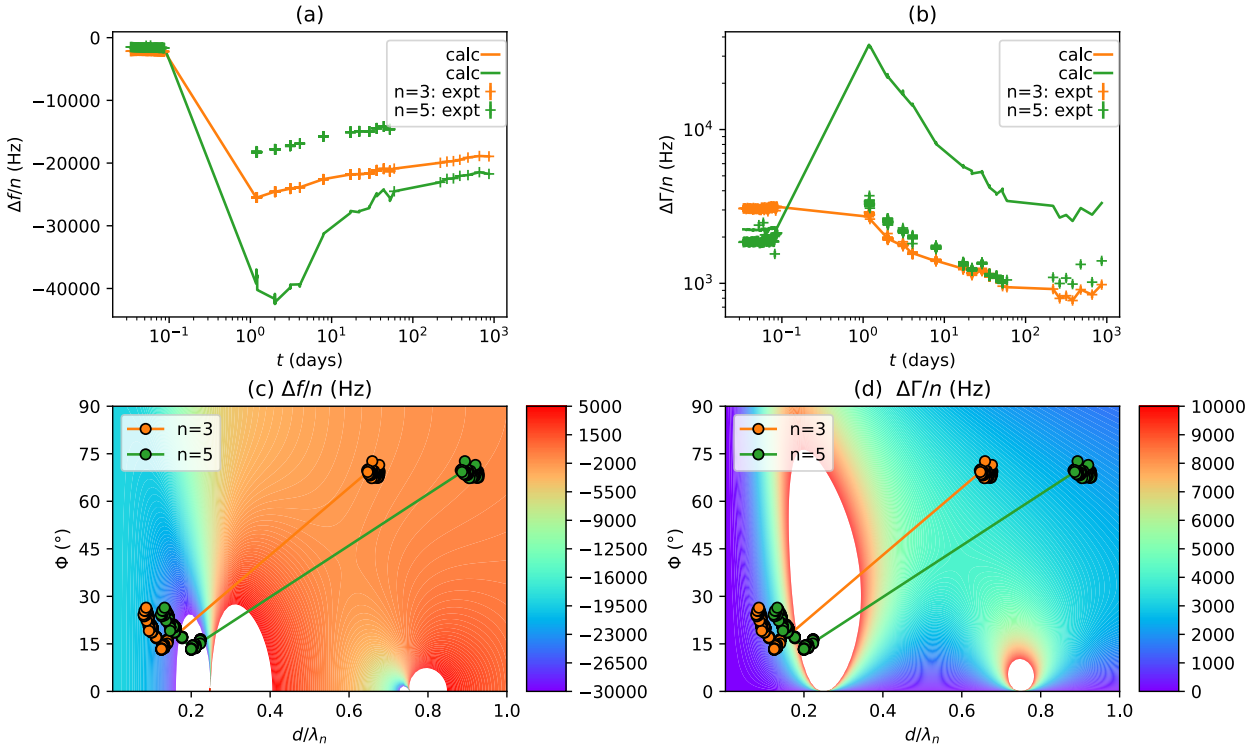

Figure B.6: Comparison and contour plots for the SA LO thin film sample. The (a) experimental values of $\Delta f/n$ to the back-calculated solutions, (b) experimental values of $\Delta\Gamma/n$ to the back-calculated solutions, (c) contour plot for the experimental $\Delta f/n$ values, and (d) contour plot for the experimental $\Delta\Gamma/n$ values. Both the data used for the '3:3' calculation with fixed dρ values and the '3.5:5' calculation are shown. The colors on the contour plots provide information about what frequency and dissipation shifts relate to the mechanical properties of the sample. For this LO sample, the early times are in the upper right corner with high d/λ (equivalent to a lower complex shear modulus) and high phase angle. As the sample polymerizes and ages as a solid film, the data shift to the lower left corner of the plot. The areas of white on the contour plots are where the film resonance phenomenon occurs, meaning that any data in this region cannot be used to calculate the mechanical properties.

Figure B.7 shows the comparison and contour plots for the '3.5:5' calculations of the WN LO 2 sample. There is good agreement between the $\Delta\Gamma_3/n$ back-calculated and experimental values as well as decent separation of the $\Delta f/n$ shifts for both harmonics. The contour plots show that the

data are in a region where the mechanical properties can be determined fairly accurately.

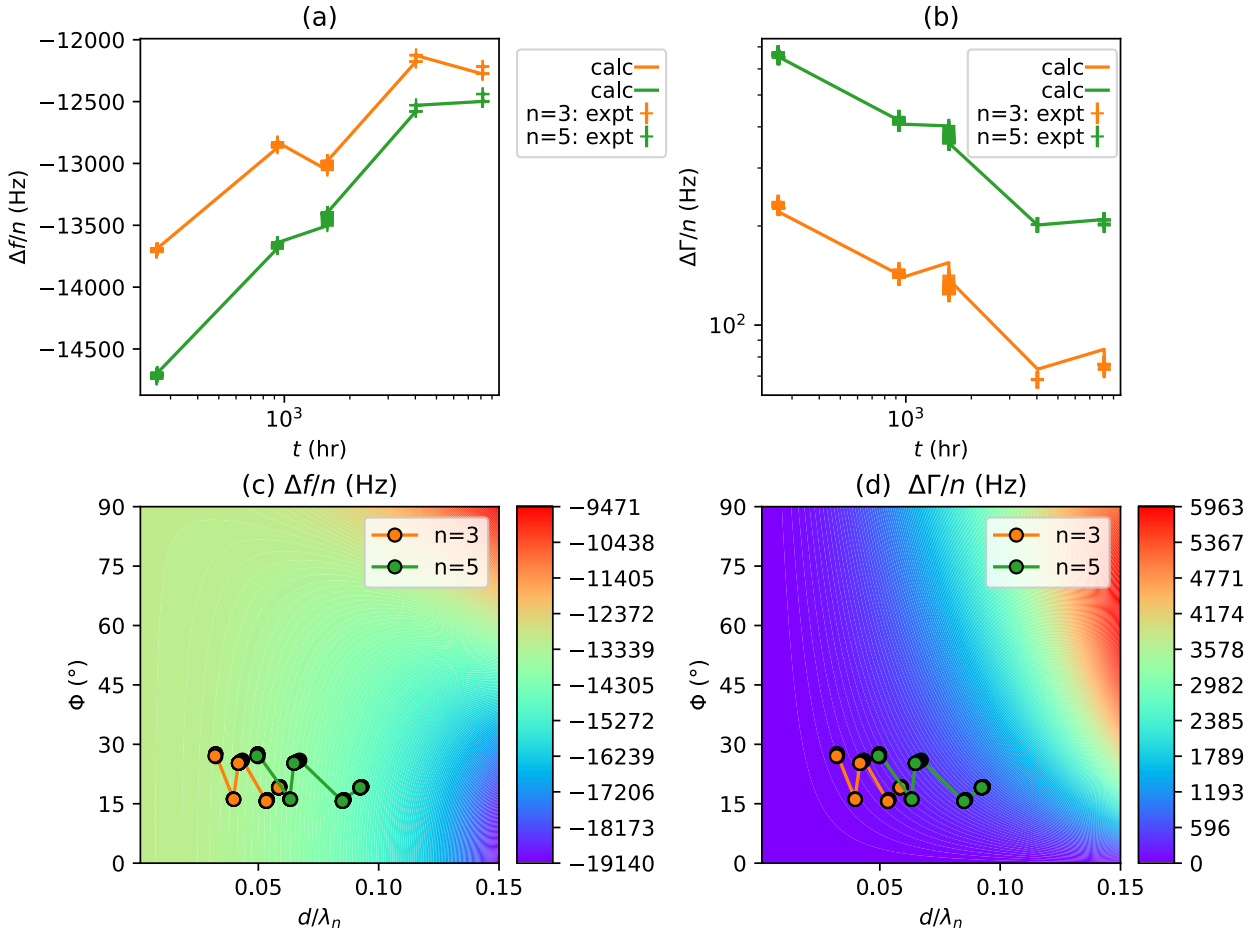

Figure B.7: Comparison and contour plots for a '3.5:5' calculation for the WN LO 2 sample. The (a) experimental values of $\Delta f/n$ to the back-calculated solutions, (b) experimental values of $\Delta\Gamma/n$ to the back-calculated solutions, (c) contour plot for the experimental $\Delta f/n$ values, and (d) contour plot for the experimental $\Delta\Gamma/n$ values. "Good agreement" is determined by comparing the back-calculated value of the solution not used in the calculation (in this case, the $\Delta\Gamma_3$) with the experimental data.

Figure B.8 shows the comparison and contour plots for the '3.5:5' calculations of the WN LO 4 sample. Here, there is a bit more deviation between the back-calculated and experimental values for $\Delta\Gamma_3/n$, but with the defined uncertainty dictionaries, this variation can be accounted with the error bars shown on Figure 3.7.

Figure B.9 shows the comparison and contour plots for the '3.5:5' calculation of the temperature sweep performed after 5 months of aging on WN LO 4. On the contour plots, the temperature moves towards higher d/λ and ϕ values as the temperature increases and the film becomes more

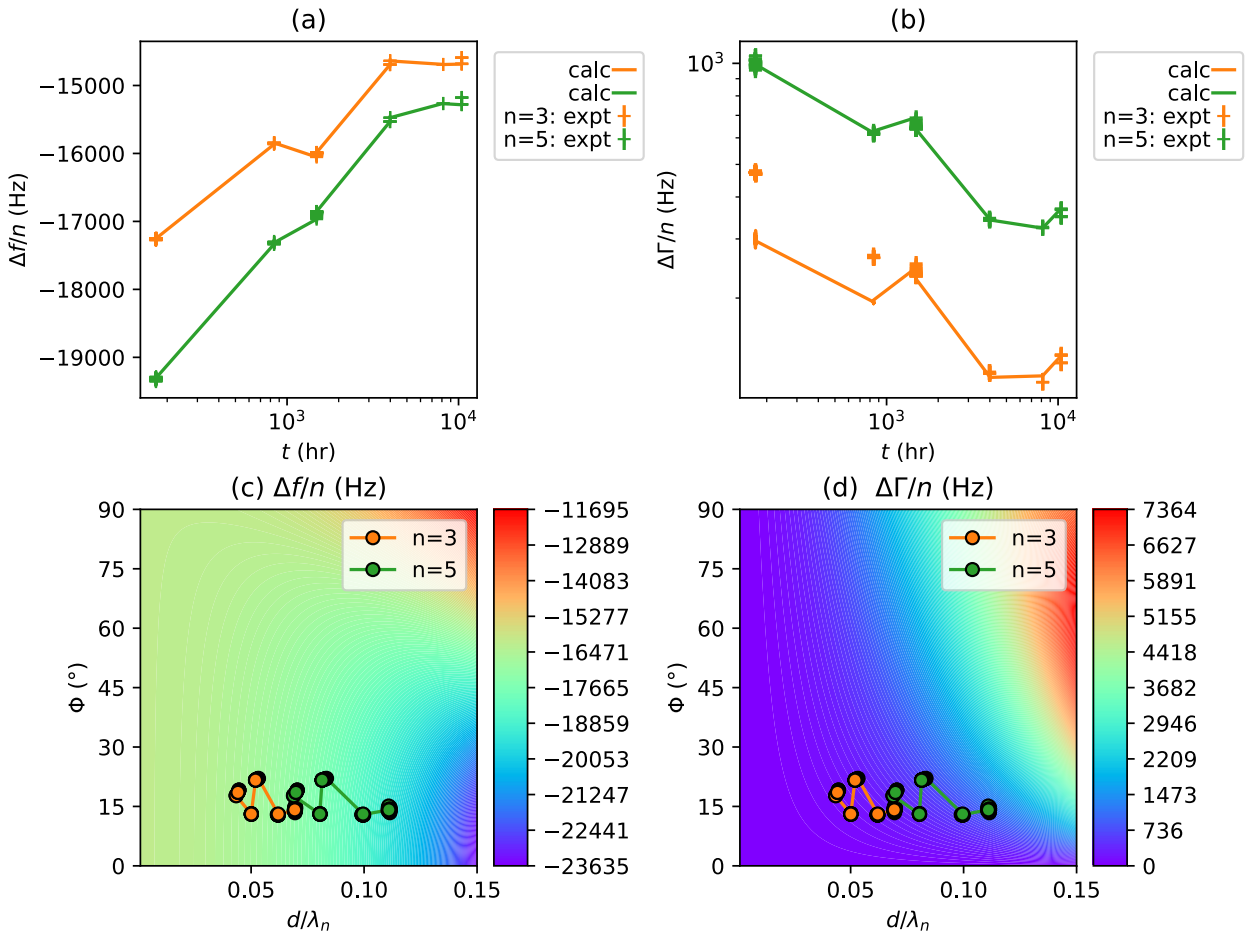

Figure B.8: Comparison and contour plots for a '3.5:5' calculation for the WN LO 4 sample. The (a) experimental values of $\Delta f/n$ to the back-calculated solutions, (b) experimental values of $\Delta\Gamma/n$ to the back-calculated solutions, (c) contour plot for the experimental $\Delta f/n$ values, and (d) contour plot for the experimental $\Delta\Gamma/n$ values. "Good agreement" is determined by comparing the back-calculated value of the solution not used in the calculation (in this case, the $\Delta\Gamma_3$) with the experimental data.

liquid-like in its response. There is good separation between the $\Delta f/n$ values for the 3rd and 5th harmonics over the entire temperature range and good agreement between the back-calculated and experimental values of $\Delta\Gamma_3/n$ for most of the temperature range. For higher temperatures that were not plotted, the 5th harmonic $\Delta\Gamma/n$ data gets too close to the 'no man's region' in the contour plot, which makes the error bars quite large and the mechanical properties too difficult to plot.

Figure B.10 shows the comparison and contour plots for the '3.5:5' calculation of the temperature sweep of the WN LO 4 film after it had been aged for 11 months. For this temperature sweep,

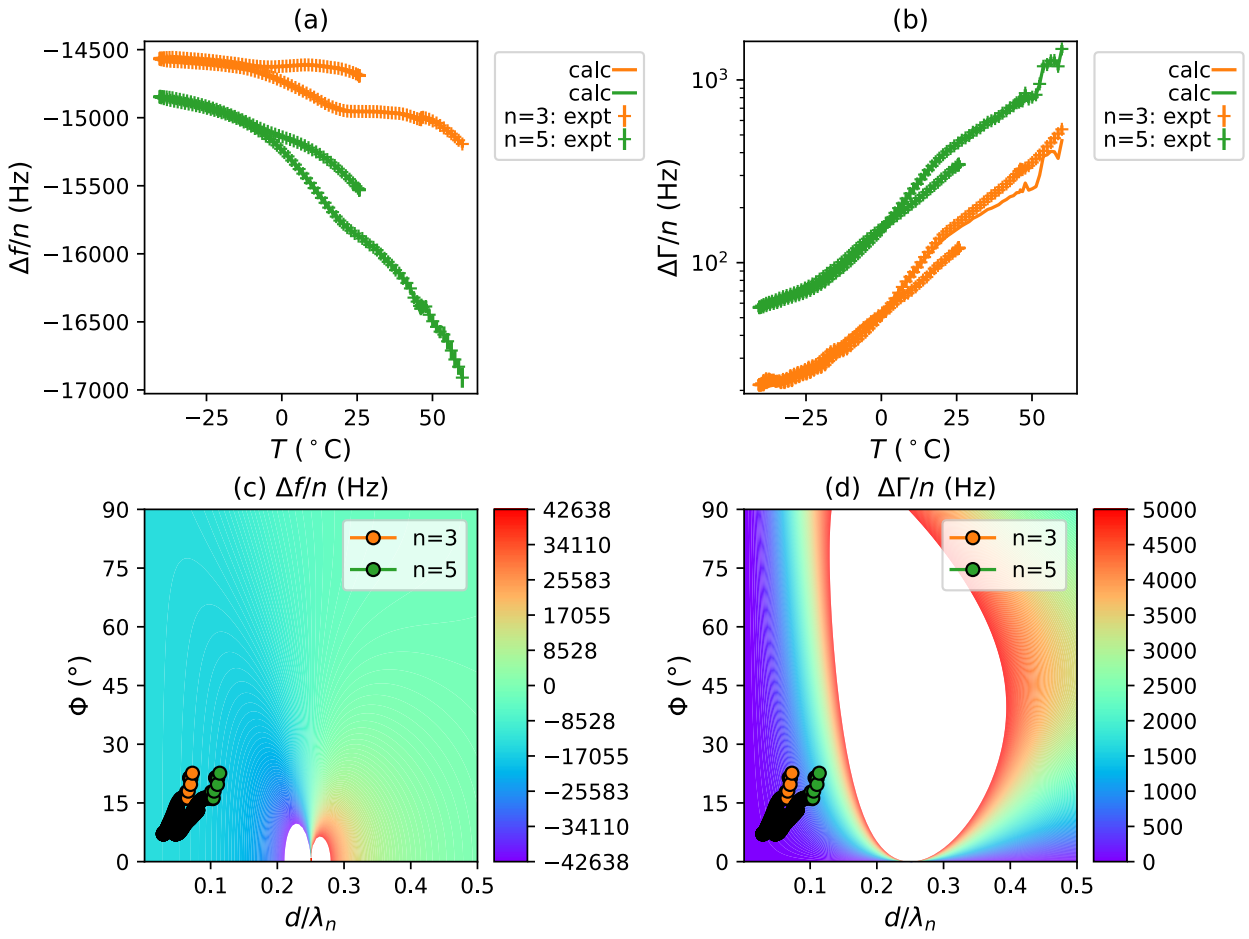

Figure B.9: Comparison and contour plots of a '3.5:5' calculation for a temperature sweep from -40 – 60°C of the WN LO 4 sample after it was aged for 5 months. The (a) experimental values of $\Delta f/n$ to the back-calculated solutions, (b) experimental values of $\Delta\Gamma/n$ to the back-calculated solutions, (c) contour plot for the experimental $\Delta f/n$ values, and (d) contour plot for the experimental $\Delta\Gamma/n$ values. "Good agreement" is determined by comparing the back-calculated value of the solution not used in the calculation (in this case, the $\Delta\Gamma_3$) with the experimental data.

there is very good agreement between the back-calculated and experimental values of $\Delta\Gamma_5/n$. At low temperatures, the differences between $\Delta f_3/n$ and $\Delta f_5/n$ start to get a bit small, which is the main factor causing an increase in the size of the error bars at lower temperatures.

Figure B.11 provides the comparison and contour plots for the '3.5:5' calculation of the temperature sweep for WN LO 4 after it has aged for 14 months. Similar to the response for the temperature sweep after 11 months, there is good agreement between the back-calculated and experimental values of $\Delta\Gamma_3/n$ and there is a decrease in the separation of $\Delta f_3/n$ and $\Delta f_5/n$ at lower temperatures, which increases the size of the error bars at lower temperatures in Figure 3.11.

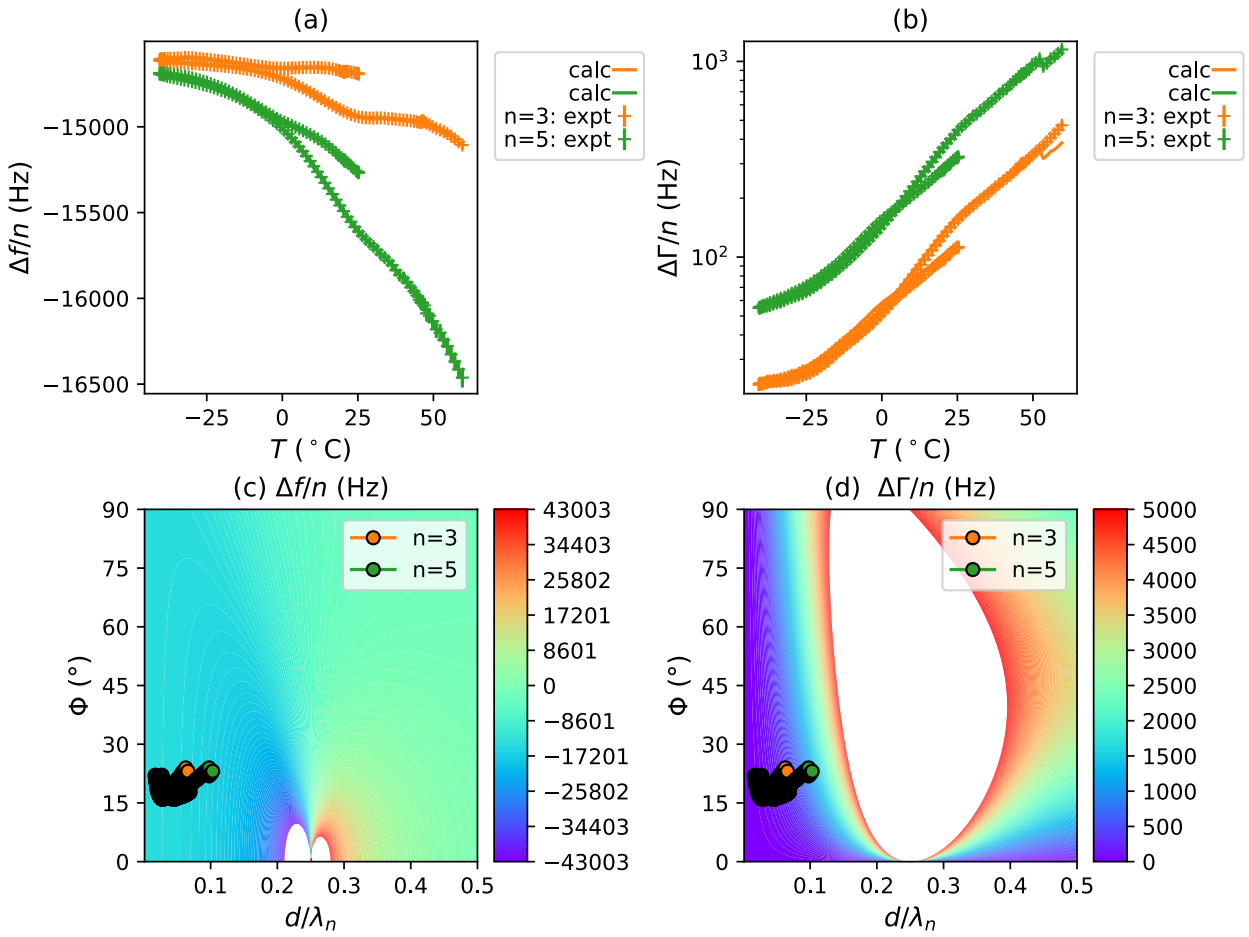

Figure B.10: Comparison and contour plots of a '3.5:5' calculation for a temperature sweep from -40 – $60°$C of the WN LO 4 sample after it was aged for 11 months. The (a) experimental values of $\Delta f/n$ to the back-calculated solutions, (b) experimental values of $\Delta\Gamma/n$ to the back-calculated solutions, (c) contour plot for the experimental $\Delta f/n$ values, and (d) contour plot for the experimental $\Delta\Gamma/n$ values. "Good agreement" is determined by comparing the back-calculated value of the solution not used in the calculation (in this case, the $\Delta\Gamma_3$) with the experimental data.

B.4 Reflection Fourier Transform Infrared Spectroscopy

Reflection Fourier Transform Infrared Spectroscopy (Refl. FTIR) was performed on the SA and WN samples to assess if the short term exposure to temperatures $> 60°$C during the temperature sweeps had caused any uncharacteristic chemical aging of the linseed oil films. Refl. FTIR data were collected using a Bruker LUMOS FTIR Microscope, with a collection window from $400 - 4000\,\mathrm{cm}^{-1}$, scan resolution of $4\,\mathrm{cm}^{-1}$, and averaging of 64 scans. The spectra show characteristic peaks for an oil film (see [154] for a full list of potential peaks). These data show no abnormal peaks when compared to the values collated by de Viguerie *et al.*, indicating that the temperature

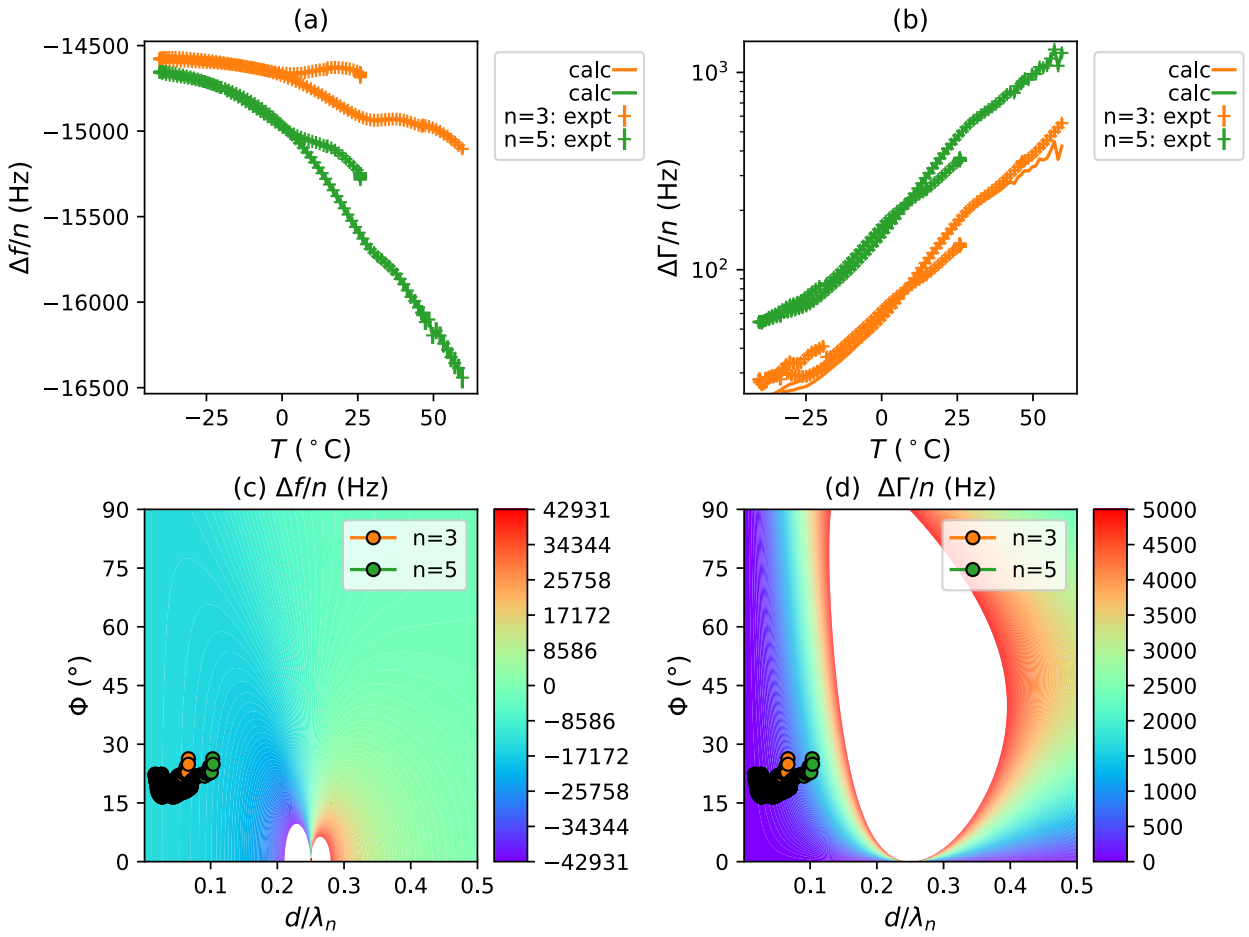

Figure B.11: Comparison and contour plots of a '3.5:5' calculation for a temperature sweep from -40 – 60°C of the WN LO 4 sample after it was aged for 14 months. The (a) experimental values of $\Delta f/n$ to the back-calculated solutions, (b) experimental values of $\Delta\Gamma/n$ to the back-calculated solutions, (c) contour plot for the experimental $\Delta f/n$ values, and (d) contour plot for the experimental $\Delta\Gamma/n$ values. "Good agreement" is determined by comparing the back-calculated value of the solution not used in the calculation (in this case, the $\Delta\Gamma_3$) with the experimental data.

sweeps did not cause drastic chemical changes to the oil films.

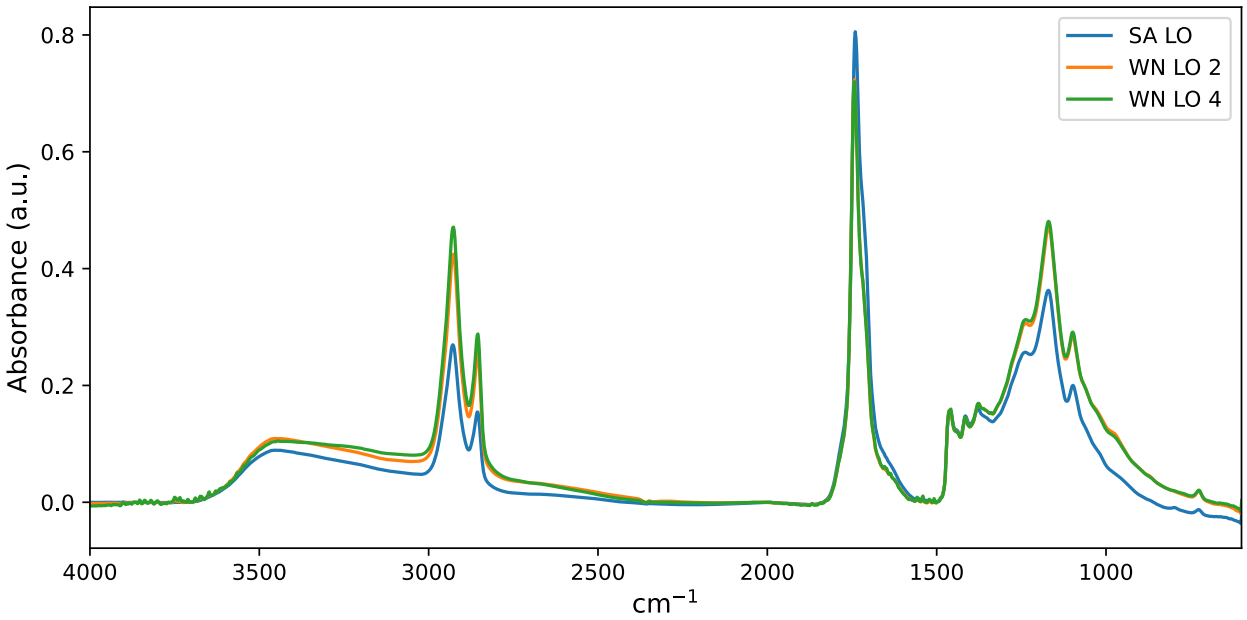

Figure B.12: Reflection FTIR data showing the absorbance versus the wavenumber for the SA and WN LO samples that experienced temperature sweeps. The baselines are corrected by drawing linear interpolations between 3900, 1800, and 1500 cm^{-1}.

C Supplementary Information for Chapter 4

C.1 Acid value determination and calculation

C.1.1 Background

The acid value (AV) provides a measure of the concentration of free fatty acids (FFA) present in an oil and is typically expressed using units of mg of base required to neutralize one gram of oil (mg_{base}/g_{oil}). One of the most common ways to determine the AV is to use titration of the oil with a strong base. The following equation is used to determine the AV from titration results:

$$AV = \frac{(V_T - V_B) * N_T * MW_{NaOH}}{W_{oil}}, \tag{5.1}$$

where AV is the acid value (mg_{NaOH}/g_{oil}), V_T is the volume of titrant used to neutralize the oil sample (mL), V_B is the volume of titrant used to neutralize the ethanol solution before the addition of the oil sample (mL), N_T is the concentration of the titrant (mmol/mL), MW_{NaOH} is the molecular weight of sodium hydroxide (40 mg/mmol), and W_{oil} is the mass of the oil used for the titration (g). A similar value to express the concentration of FFA in a drying oil is %FFA, or the percentage of free fatty acids in the drying oil. This value requires expression as a specific type of fatty acid and is assumed to be oleic acid for most drying oils. The equation to determine the %FFA is very similar to the equation to determine AV

$$\%FFA_{oleic} = \frac{(V_T - V_B) * N_T * MW_{oleic}}{W_{oil}}, \tag{5.2}$$

where the molecular weight of oleic acid is 282.45 mg/mmol. The following factor is used to convert between AV and %FFA

$$\frac{AV}{\%FFA} = \frac{MW_{NaOH}}{MW_{oleic} * 0.1} = 1.42. \tag{5.3}$$

The factor of 0.1 is a result of incorporating a conversion factor of 1g/1000mg and multiplying by 100 to express the concentration of FFA as a percentage [215].

Table C.1: The average %FFA values for the five drying oils along with their standard deviations.

Drying Oil	%FFA (as oleic acid)
Linseed	1.18 ± 0.02
Walnut	1.08 ± 0.05
Poppyseed	0.28 ± 0.01
Safflower	0.78 ± 0.02
Stand	2.95 ± 0.04

C.1.2 Method

A Metrohm 888 Titrando, 801 Stirrer, and Solvotrode easyClean non-aqueous electrode were used to perform autotitrations of the oil samples. A standard FFA reagent was prepared to add to the oil sample for the titrations using 1 L of 95% ethanol, 500 mL of toluene, 60 mL of phenolphthalein, and 5 mL of 0.1 M HCl, which were mixed well before measurements. The 0.1 M NaOH titrant solution was a reagent grade solution and the autotitrator reservoir was filled before the start of the titrations. A blank measurement was performed to determine V_B by placing 50 mL of the FFA reagent in a beaker, moving the electrode from a distilled water beaker, and performing a titration to the endpoint as determined by a faint color change and a clear endpoint determined by a jump in the potentiometric curve measured by the autotitrator. After the V_B was recorded, the electrode was rinsed with acetone and stored in the distilled water beaker. To measure the oil samples, $0.1 - 0.3$ g of the oil was measured into a beaker, then 50 mL of the FFA reagent was added. The solution was stirred well, then the electrode was inserted, the mass was recorded on the Titrando, and then the titration was performed. After the titration was complete, the autotitrator provided the $V_T$and the %FFA value for the sample, which was recorded. The electrode was then rinsed with acetone and stored in the distilled water beaker. If the autotitrator started to struggle with finding an endpoint, the electrode was rinsed or placed in a beaker of acetone to remove more of the oil that had gathered on the surface of the electrode. Each drying oil was measured 3-5 times, the %FFA values were averaged and the values are provided in Table C.1. The %FFA values were converted to AV and are reported in Table 4.1.

C.2 NMR determination of fatty acid distribution

C.2.1 Method

To prepare the samples for ^{1}H and ^{13}C spectra collection, 200 $^{-}$L of the drying oil was added to 400 $^{-}$L of deuterated chloroform (Sigma Aldrich), mixed well, and transferred to an NMR tube. ^{1}H and ^{13}C NMR were performed using a Bruker Avance III 500MHz spectrometer. The NMR spectra were collected at room temperature. 10 scans were averaged with a relaxation delay of 15 sec for the ^{1}H spectra and 20 sec for the ^{13}C. Integrals for the peaks of interest were calculated from the FIDs using MestReNova software. Two analysis approaches are considered: one using solely the ^{1}H data (based on the approach used in Barison *et al.*) and one that combines both the ^{1}H and ^{13}C data [216]. The second method will be outlined using LO as an example.

C.2.2 ^{1}H and ^{13}C NMR data

The main goal of this approach is to determine the relative concentrations of each unsaturated fatty acid (linolenic, linoleic, and oleic acid) and saturated fatty acids (most likely palmitic and stearic acid) in each drying oil. In order to do so, it is useful to determine the average number of C = C per fatty acid chain ($\frac{\text{C=C}}{\text{FA}}$). The following equation for the can be used to determine the relative concentrations of each fatty acid contributing to $\frac{\text{C=C}}{\text{FA}}$:

$$\frac{\text{C} = \text{C}}{\text{FA}} = \frac{\text{A}_{\text{ln}} * 3 + \text{A}_{\text{le}} * 2 + \text{A}_{\text{ol}} * 1 + \text{A}_{\text{sat}} * 0}{\text{A}_{\text{ln}} + \text{A}_{\text{le}} + \text{A}_{\text{ol}} + \text{A}_{\text{sat}}}. \tag{5.4}$$

In this equation, the A_{ln}, A_{le}, A_{ol}, and A_{sat} are the average integral area per carbon of the respective fatty acid chain (ln = linolenic acid, le = linoleic acid, ol = oleic acid, sat = saturated fatty acids). We will use both ^{1}H and ^{13}C spectra to determine the values for A_{ln}, A_{le}, A_{ol}, and A_{sat}. To illustrate the process, we will use the LO sample as an example.

The ^{1} H and ^{13}C NMR spectra for LO are shown in Figure C.1. For the ^{13}C NMR spectrum (Figure C.1a), the region where C = C are present is shown. In this region, peaks associated with linolenic acid occur at $\delta \sim$ 131.79, 130.08, 128.19, 128.15, 127.71, and 127.07 ppm, peaks associated with linoleic acid occur at $\delta \sim$ 129.9, 129.83, 128.01, and 127.85 ppm, and the peaks associated with

oleic acid occur at $\delta \sim 129.86$ and 129.6 ppm [217–219]. For the ^{1}H NMR (Figure C.1b), the relevant peaks are centered at $\delta \sim 5.29$ ppm ($C = C - \underline{H}$) and $\delta \sim 0.82 - 0.93$ ppm ($C\underline{H_3}$) [216].

We can determine A_{ln}, A_{le}, and A_{ol} from the ^{13}C NMR spectra by summing each of the unsaturated carbon peak integrals and dividing by the number of unsaturated carbons for the specific fatty acid. For linolenic, linoleic, and oleic acids, the values would be:

$$\text{linolenic} : A_{ln} = \frac{1 + 0.68 + 2.08^* + 0.68 + 1}{6} = 0.91; \ * = \text{area for 2 peaks} \tag{5.5}$$

$$\text{linoleic} : A_{le} = \frac{0.53 + 0.26 + 0.26 + 0.27}{4} = 0.33 \tag{5.6}$$

$$\text{oleic} : A_{ol} = \frac{0.3 + 0.33}{2} = 0.315 \tag{5.7}$$

From these values, we are able to determine the fractional concentrations of each unsaturated fatty acid in the oil, represented as γ_{FA}.

$$\text{linolenic} : \gamma_{ln} = \frac{0.91}{0.91 + 0.33 + 0.315} * 3 = 1.753 \tag{5.8}$$

$$\text{linoleic} : \gamma_{le} = \frac{0.33}{0.91 + 0.33 + 0.315} * 2 = 0.425 \tag{5.9}$$

$$\text{oleic} : \gamma_{ol} = \frac{0.315}{0.91 + 0.33 + 0.315} = 0.203 \tag{5.10}$$

By summing these fractional concentrations, we get a value of $\frac{C=C}{FA} = 2.381$. However, from using just the ^{13}C NMR data, this value is an overestimate of $\frac{C=C}{FA}$ since we have no information about the average integral area or fractional concentration of the saturated fatty acids (A_{sat} and γ_{sat}) present in the LO sample. To determine the saturated fatty acid values, we must use the ^{1}H NMR data. The peak areas for the $C = C - \underline{H}$ and the $C - \underline{H_3}$ proton peaks are normalized by the number of protons contributing to the peaks.

$$C = C - \underline{H}: \ \frac{6.80}{2} = 3.4 \tag{5.11}$$

$$C\underline{H_3}: \ \frac{4.75}{3} = 1.583 \tag{5.12}$$

Dividing the normalized proton peaks gives us the correct value for the average number of C = C per fatty acid accounting for the unsaturated fatty acids.

$$\frac{C = C}{FA} = \frac{3.4}{1.583} = 2.147 \tag{5.13}$$

Using this updated value for $\frac{C=C}{FA}$, we can calculate A_{sat}.

$$\frac{C = C}{FA} = \frac{A_{ln} * 3 + A_{le} * 2 + A_{ol} * 1 + A_{sat} * 0}{A_{ln} + A_{le} + A_{ol} + A_{sat}} = 2.147 \tag{5.14}$$

$$\frac{C = C}{FA} = \frac{0.91 * 3 + 0.33 * 2 + 0.315}{0.91 + 0.33 + 0.315 + A_{sat}} = 2.147 \tag{5.15}$$

Rearranging to solve for A_{sat}, the average peak area for the saturated FAs is $A_{sat} = 0.169$. Now that we have the average integral areas per carbon for the unsaturated and saturated fatty acids, we can update the fractional contribution for each fatty acid and determine the percentages for the fatty acid distribution. The fatty acid percentages are reported in Table 4.1.

Figures C.2-C.4 provide the NMR spectra for WO, PO, and SaO. The procedures for determining the fatty acid distribution are the same as outlined above for LO. In the PO and SaO samples, there are no peaks present that would be indicative of the linolenic acid peaks.

For the StO sample (Figure C.5), the fatty acid distribution is not calculated. The StO sample is prepolymerized, which means that the contributions to the C = C peaks in the ^{13}C NMR spectra (Figure C.5a) are much more complicated than in the previous drying oils. Having oligomers already formed within the oil will also affect the overall concentration of the fatty acids present in StO at the beginning of the polymerization step measured in this study.

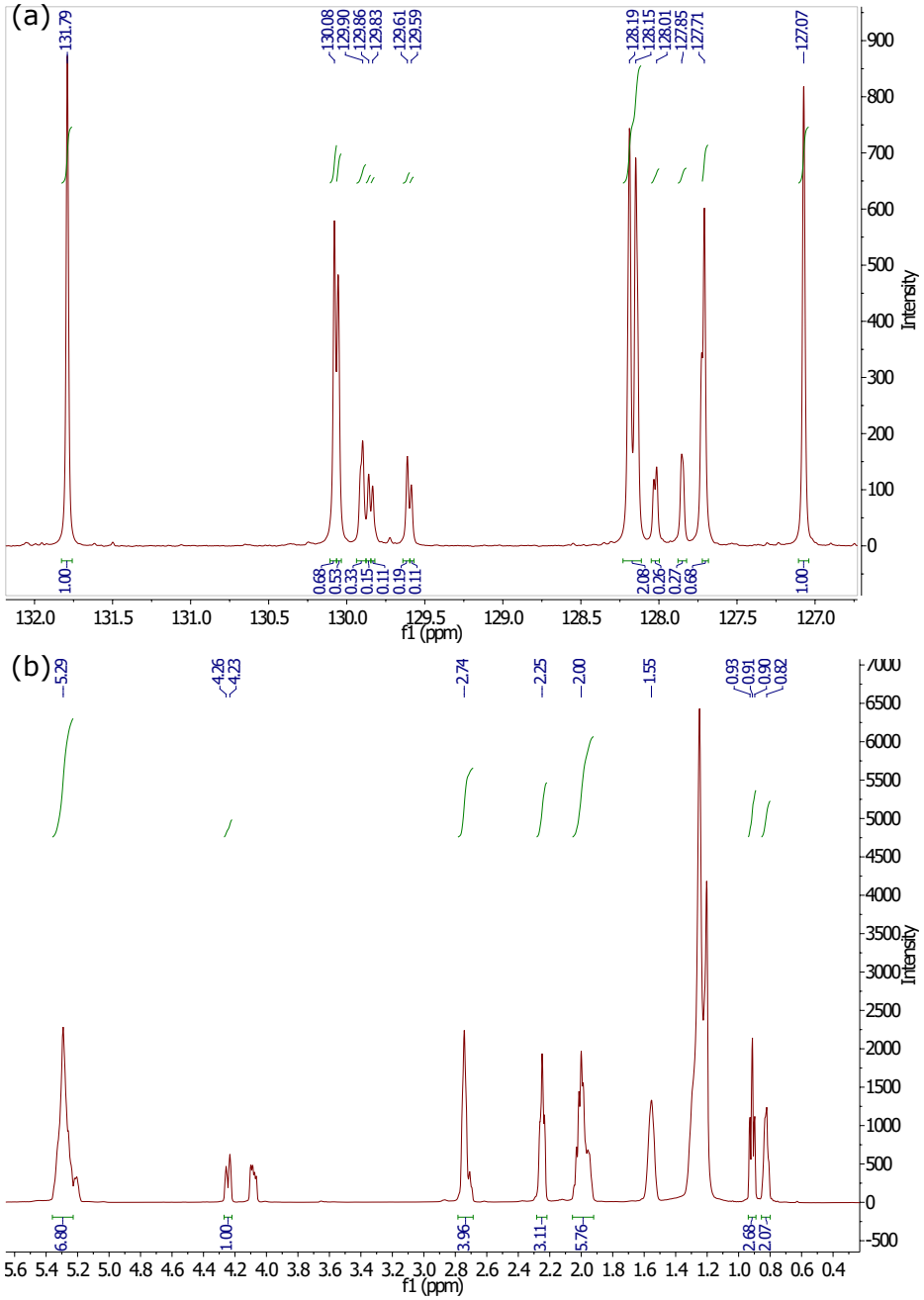

Figure C.1: The (a) ^{13}C and (b) ^{1}H NMR spectra for linseed oil. The ^{13}C NMR is zoomed in to show the region of $C = C$ contributions from $127 - 132$ ppm. Integrals (below spectra) and peak positions (above spectra) are provided for the relevant peaks for determining the fatty acid distributions.

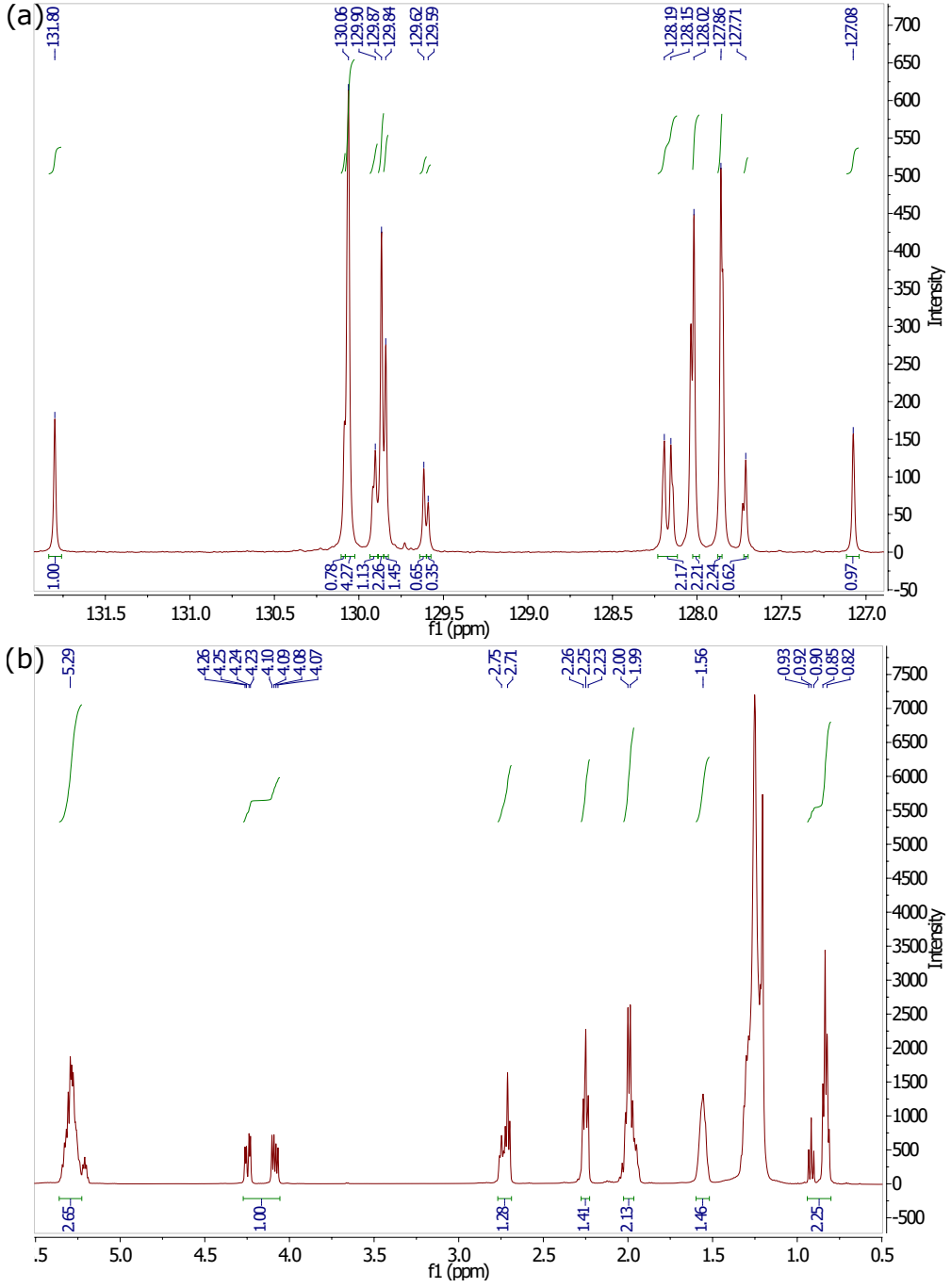

Figure C.2: The (a) ^{13}C and (b) ^{1}H NMR spectra for walnut oil. The ^{13}C NMR is zoomed in to show the region of $C = C$ contributions from $125 - 132$ ppm. Integrals (below spectra) and peak positions (above spectra) are provided for the relevant peaks for determining the fatty acid distributions.

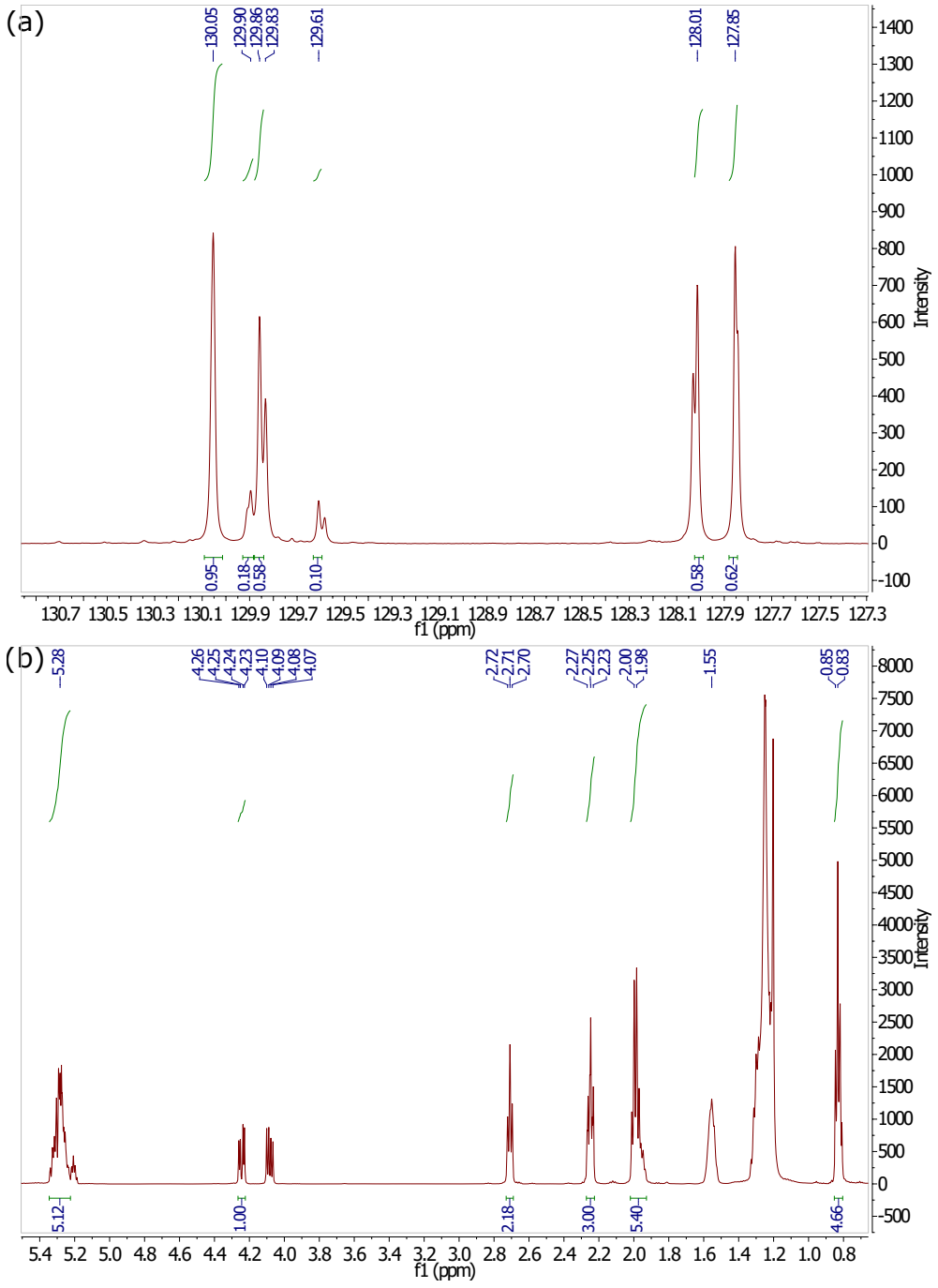

Figure C.3: The (a) ^{13}C and (b) ^{1}H NMR spectra for poppyseed oil. The ^{13}C NMR is zoomed in to show the region of C = C contributions from $125 - 132$ ppm. Integrals (below spectra) and peak positions (above spectra) are provided for the relevant peaks for determining the fatty acid distributions.

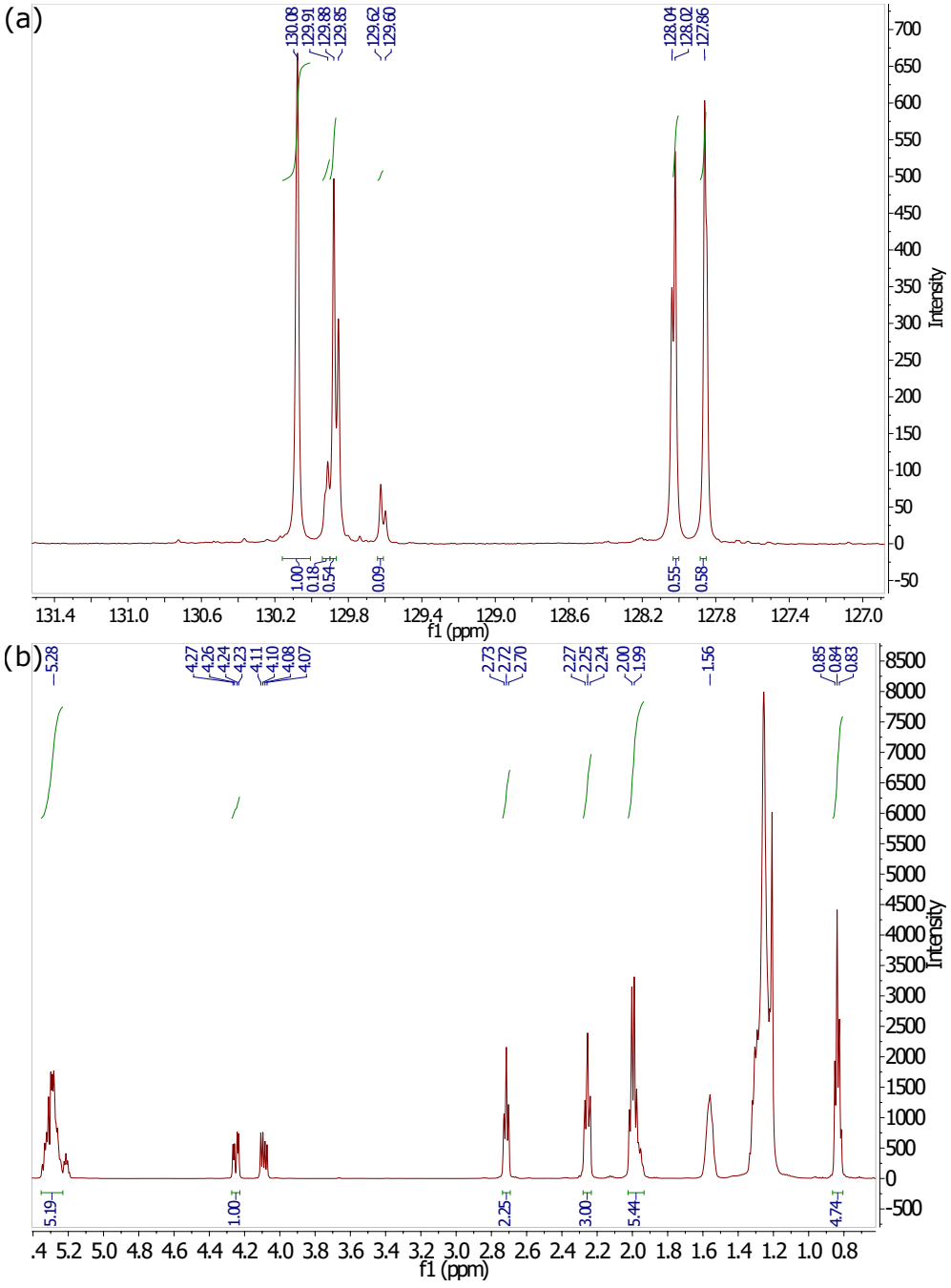

Figure C.4: The (a) ^{13}C and (b) ^{1}H NMR spectra for safflower oil. The ^{13}C NMR is zoomed in to show the region of C = C contributions from $125 - 132$ ppm. Integrals (below spectra) and peak positions (above spectra) are provided for the relevant peaks for determining the fatty acid distributions.

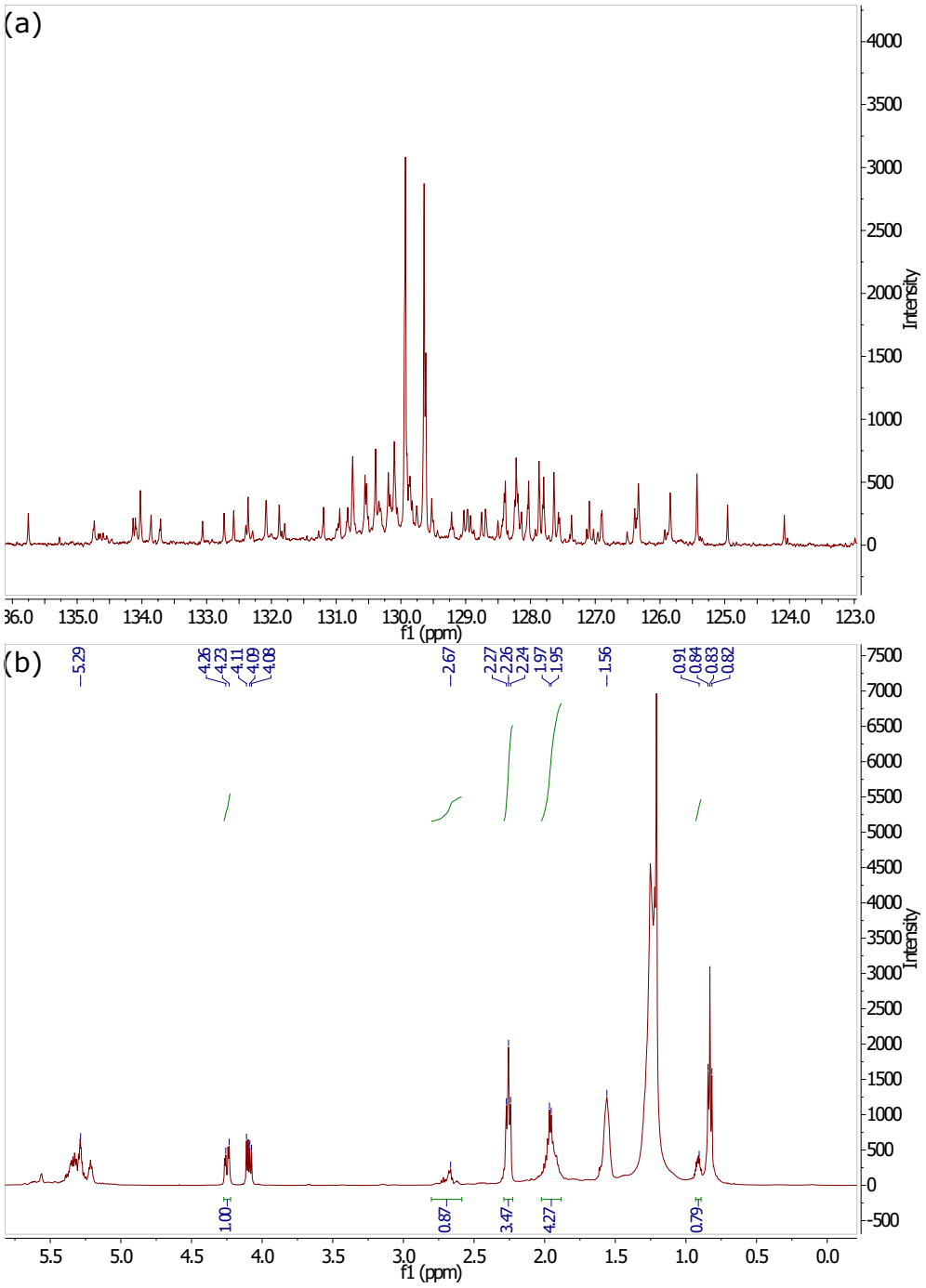

Figure C.5: The (a) ^{13}C and (b) ^{1}H NMR spectra for stand oil. The ^{13}C NMR is zoomed in to show the region of C = C contributions from 125 − 132 ppm. Integrals (below spectra) and peak positions (above spectra) are provided for the relevant peaks for determining the fatty acid distributions.

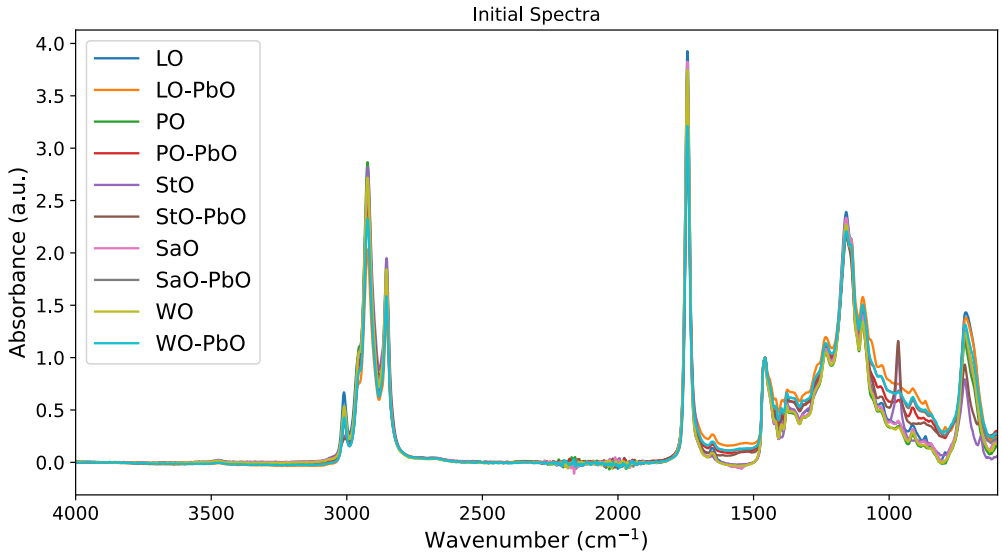

Figure C.6: Initial spectra for the oil and oil + litharge samples that were cured at 70 °C. The spectra for the oils are baseline corrected using linear interpolations between 3900, 2500, 1900, and 1500 cm^{-1} while the oil + litharge samples are baseline corrected with linear interpolations between 3900, 2500, and 1900 cm^{-1}. All samples are normalized to the $\delta(CH_2)$ associated with the fatty acid backbone chains at 1465 cm^{-1}.

C.3 Extra FTIR plots and data

For the data collected of from the LO, WO, PO, SaO, and StO samples in this study, there is more data to be analyzed than discussed within the chapter. Within this section, we will provide the extra figures that were not included within the chapter. The starting figures are Figures C.6 and C.7, which show the initial and final spectra from the measurements at 70 °C for the oil and oil + litharge samples. The initial spectra show very similar characteristics for the oils and oil +litharge samples. There are some variations in the relative intensities of the $\nu(CH_3/CH_2)$ and carbonyl peaks for various drying oils, but the peak positions and shapes indicate that the overall chemical composition of the oil and oil + litharge samples begin as relatively similar samples.

After the initial polymerization step, there are some greater observable differences. For the oil + litharge samples, the $\nu(C-O)$, $\nu(C=O)$, and $\nu(OH)$ regions are smaller than those of the oil samples. The shape of the lead carboxylate peaks seen between $1480-1600\,cm^{-1}$ show very different shapes, indicating that there are quite a lot of differences in how the lead carboxylates interact with the oils to begin forming ionomer networks. The lead carboxylate peaks will be shown more fully in the next section.

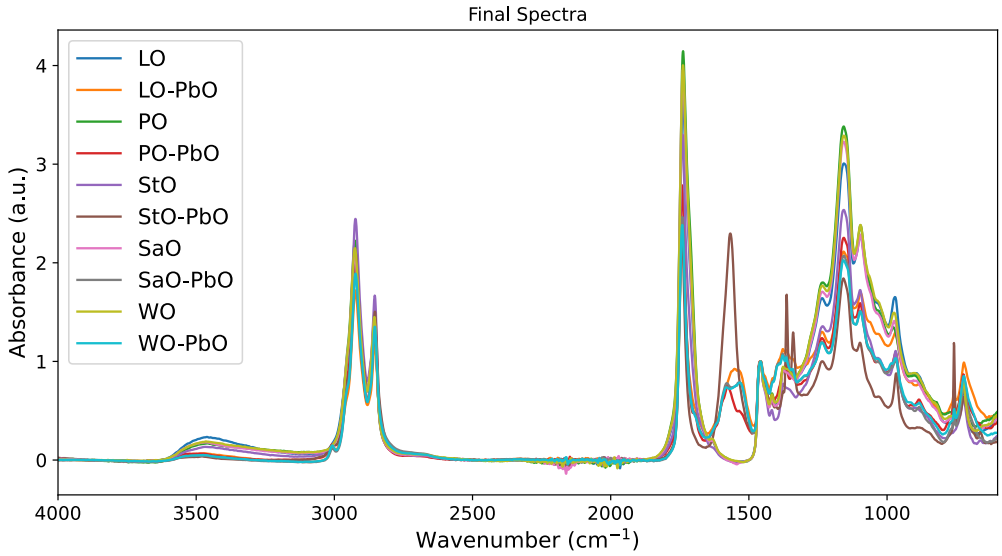

Figure C.7: Final spectra for the oil and oil + litharge samples cured at 70°C. The spectra for the oils are baseline corrected using linear interpolations between 3900, 2500, 1900, and 1500 cm^{-1} while the oil + litharge samples are baseline corrected with linear interpolations between 3900, 2500, and 1900 cm^{-1}. All samples are normalized to the $\delta(CH_2)$ associated with the fatty acid backbone chains at 1465 cm^{-1}.

The data shown in Figure 4.5 are of the drying oil categories discussed in Chapter 4. Figure C.8 shows the changes in Gaussian peak areas for the $\omega(CH)$ adjacent to conjugated and non-conjugated C = C found between 930 and 1000 cm^{-1} of the WO and SaO oil and oil + litharge samples. For both of the oil samples, the conjugated trans C = C peak grows initially with the onset of polymerization, but then is overtaken by the non-conjugated trans C = C peak. After the initial polymerization step has finished, the area of the non-conjugated trans C = C peak decreases for both oils. In the oil + litharge samples, a similar response to that of the oil + litharge samples shown in Figure 4.5 is seen. There is an initial rapid growth of all three peak areas, followed by a very slow decrease in the peak areas over the rest of the time of measurement.

When the temperature is considered as a factor, there are some changes observed in the growth and decrease of the Gaussian peak areas. Figure C.9 provides the data for the various temperature measurements of LO and LO-PbO samples. For the LO-50 sample (Figure C.9a), the growth of the conjugated C = C peaks happens at a slower rate than in the LO-70 sample. These peaks also do not decrease as was observed in the LO-70 sample. For the LO-PbO samples, the trends in the LO-PbO60 and LO-PbO samples are fairly similar to the trends of observed in the LO-PbO70

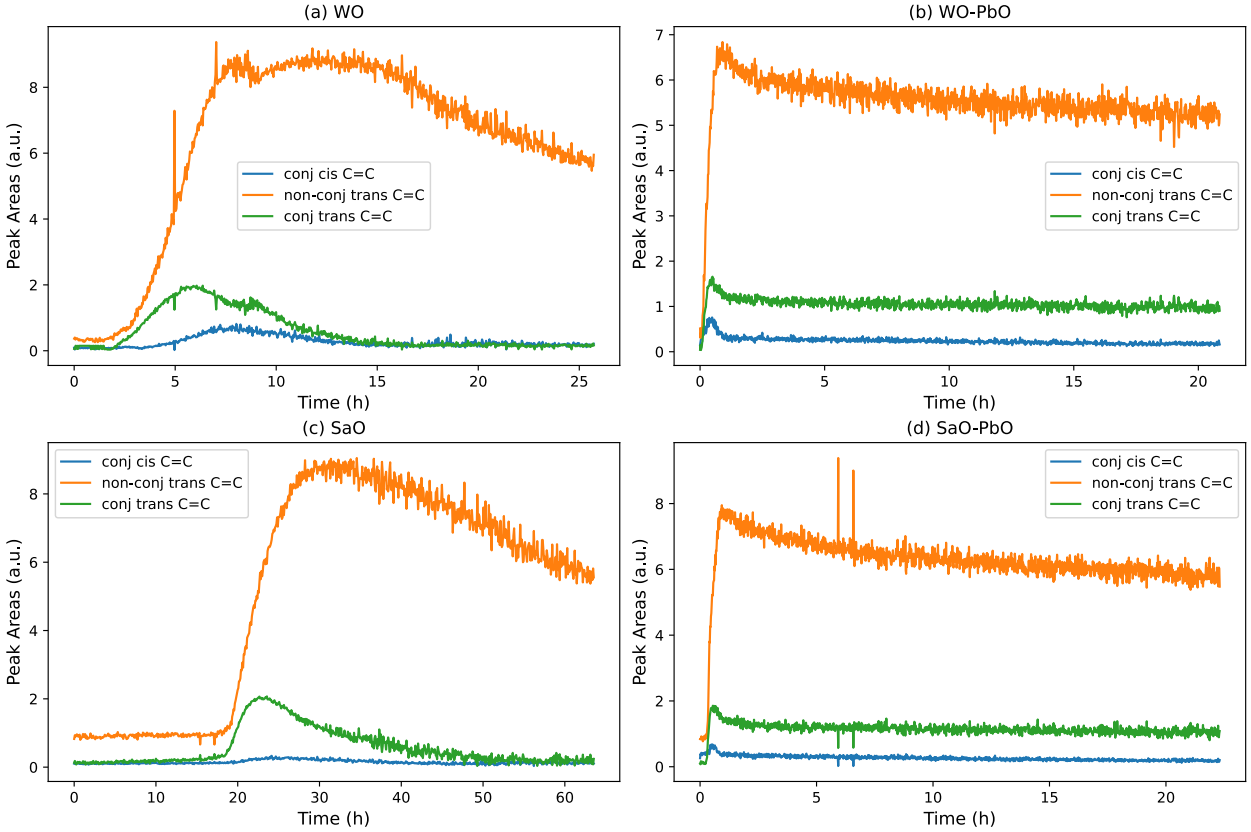

Figure C.8: Comparison of the changes in the peak areas of the Gaussians used to fit the C = C bond peaks at 950, 968, and 986 cm^{-1}. The peak areas are shown for (a) walnut oil, (b) walnut oil + litharge, (c) safflower oil, and (d) safflower oil + litharge. The Gaussian fitting was performed after baseline correcting using a linear interpolation between 925 and 1000 cm^{-1} for each sample. The peak areas are calculated by multiplying the amplitude and the standard deviation to compare the prominence and rate of growth for the individual peaks in each sample.

sample. As the temperature is decreased, a more visible decrease in the conjugated C = C peak areas is observed, while the non-conjugated trans C = C peak area remains fairly constant over the entire period of measurement. In the LO-PbO40 sample, the conjugated C = C peaks almost completely disappear by the end of the measurement. The LO-PbO30 sample shows signs of less reactivity, both with the reduced peak area of the non-conjugated trans C = C peak and the slow decrease of the conjugated C = C peaks. The trends for the LO-PbO30 sample would potentially be clearer if the sample had been measured for a longer period of time.

The Gaussian peak area changes over time are shown for the PO-PbO samples in Figure C.10. The PO-PbO60 and PO-PbO50 data show similar trends as the PO-PbO70 sample, where there is initial rapid growth of the conjugated trans C = C peak closely followed by rapid growth of the non-conjugated trans C = C peak area, then a leveling off or slight decrease in the peak areas over longer times. The PO-PbO40 and PO-PbO30 samples show much slower growth of all of the peak areas as well as the beginning of a slow decrease by the end of the measurements.

The differences as a result of temperature seem to support the reactivity of the litharge with the C = C bonds in the oil network seems to have some temperature dependence. It may be that at lower temperatures, the rate of diffusion for reactive sites or radicals remains high enough to prevent an "arresting" of the curing process and overall film formation of the polymer network.

The second derivative of the FTIR data was plotted in the carbonyl region for the LO sample towards the end of the curing measurement (Figure C.11). In this plot, the dashed vertical lines indicate the peak positions used as center points for the Gaussian fitting routine. The goal was to center these peaks at points when there are visible peaks in the second derivative, which would be indicative of a contribution for another chemical moeity. There are peaks present that were not included in the the attempt for using a Gaussian fitting routine (for example, there is also a peak present at 1710 cm^{-1}). Unfortuately, when the 1710 cm^{-1} peak was included along with or in place of the 1718 cm^{-1} peak, it would either have no contribution to the fitting or decrease the accuracy of the fit. Therefore, it was decided to not include this peak in the Gaussian peak fitting attempt for the carbonyl region.

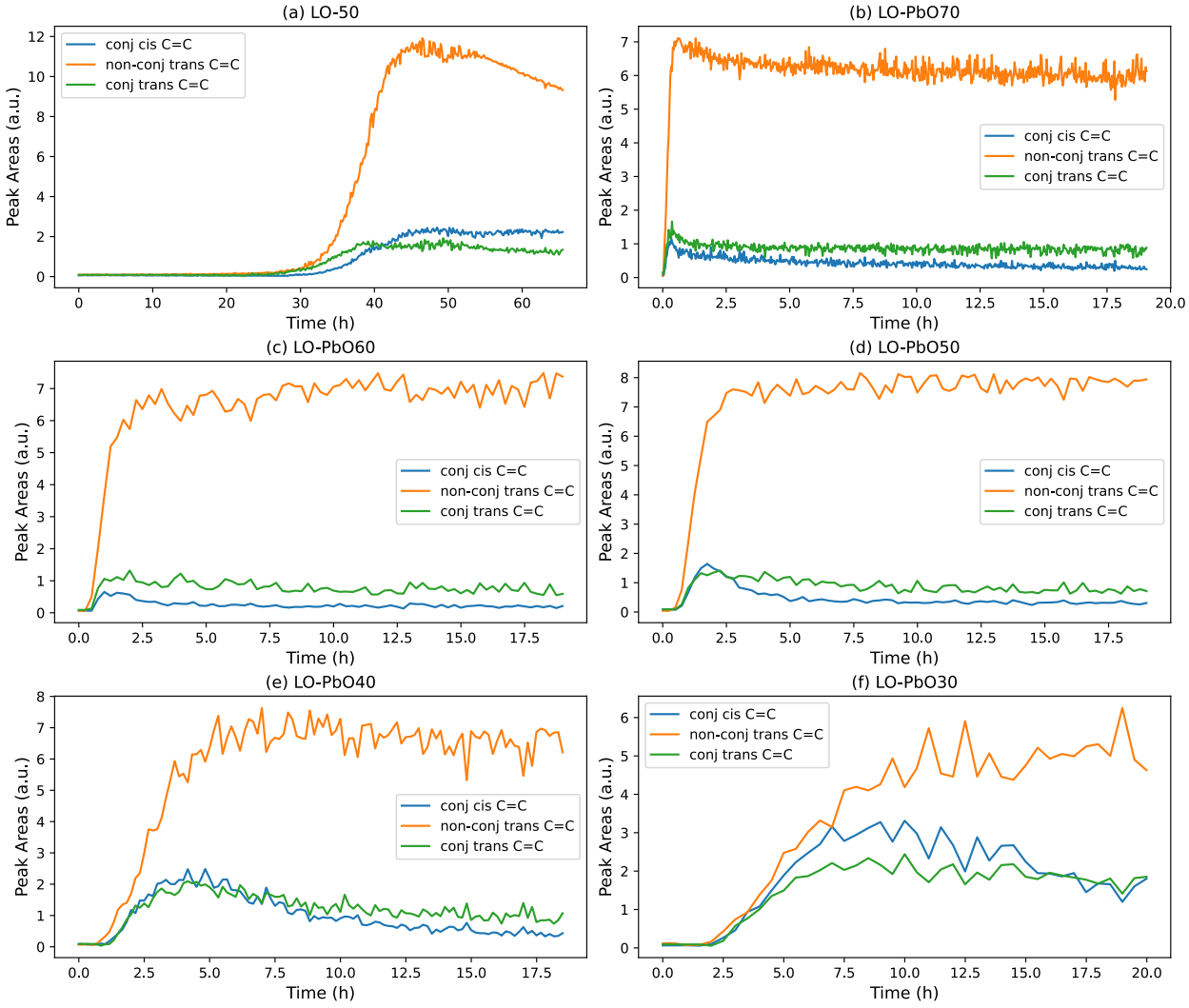

Figure C.9: Comparison of the changes in the peak areas of the Gaussians used to fit the C = C bond peaks at 950, 968, and 986 cm^{-1}. The peak areas are shown for (a) linseed oil at 50 °C, (b) linseed oil + litharge at 70 °C, (c) linseed oil + litharge at 60 °C, (d) linseed oil + litharge at 50 °C, (e) linseed oil + litharge at 40 °C, and (f) linseed oil + litharge at 30 °C. The Gaussian fitting was performed after baseline correcting using a linear interpolation between 925 and 1000 cm^{-1} for each sample. The peak areas are calculated by multiplying the amplitude and the standard deviation to compare the prominence and rate of growth for the individual peaks in each sample. For the temperature data shown in (b)-(f), every 10^{th} point was fit to reduce the computational time and still show the overall trends.

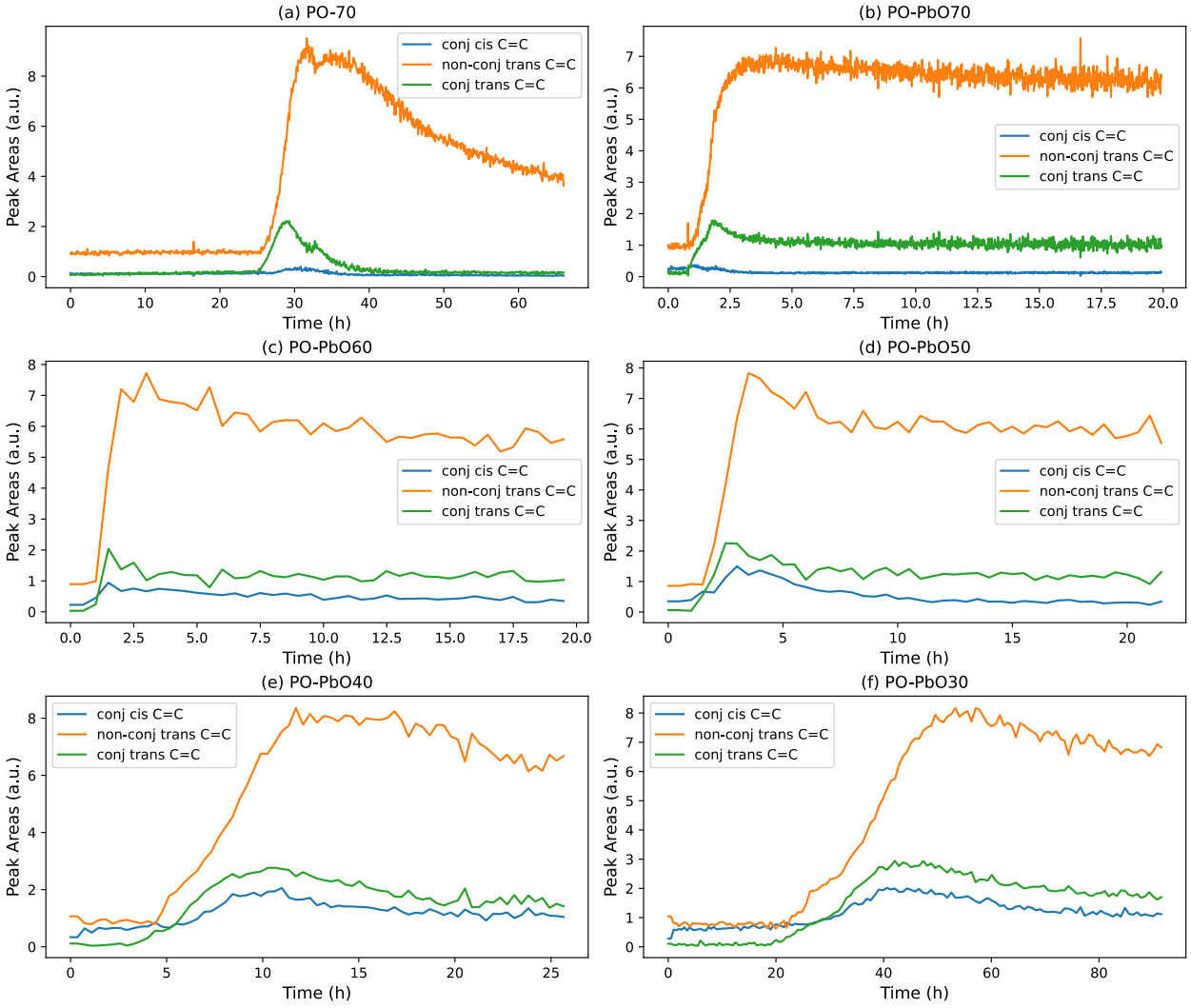

Figure C.10: Comparison of the changes in the peak areas of the Gaussians used to fit the C = C bond peaks at 950, 968, and 986 cm^{-1}. The peak areas are shown for (a) poppyseed oil at 70 °C, (b) poppyseed oil + litharge at 70 °C, (c) poppyseed oil + litharge at 60 °C, (d) poppyseed oil + litharge at 50 °C, (e) poppyseed oil + litharge at 40 °C, and (f) poppyseed oil + litharge at 30 °C. The Gaussian fitting was performed after baseline correcting using a linear interpolation between 925 and 1000 cm^{-1} for each sample. The peak areas are calculated by multiplying the amplitude and the standard deviation to compare the prominence and rate of growth for the individual peaks in each sample. For the temperature data shown in (b)-(f), every 10^{th} point was fit to reduce the computational time and still show the overall trends.

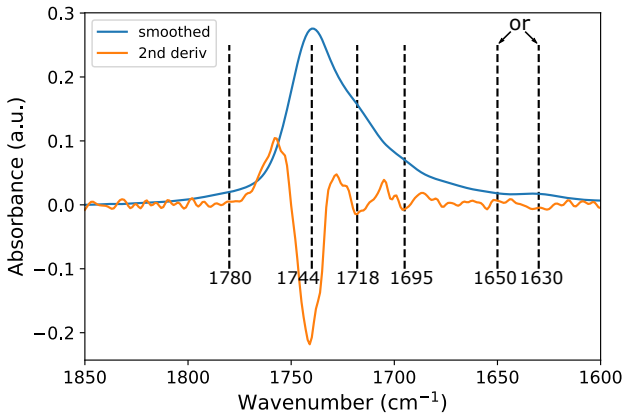

Figure C.11: The carbonyl band (blue line), second derivative (orange line), and the peaks (black dashed lines) for the LO sample during the initial rapid polymerization step ($\sim$ 17 h) at 70 °C. The lowest wavenumber peak can be either 1650 or 1630 cm^{-1} for earlier and later times of cure, respectively.

C.3.1 Lead carboxylate region

Lead carboxylate features would form with the use of litharge as a drier in the oil samples. As is shown in Figures C.12-C.14, there is quite a bit of variation in where peak centers and even how many peaks are contributing to the lead carboxylate band. In literature, there are peaks that have been reported at 1622 cm^{-1} attributed to $\nu(C=O)$ and 1537 cm^{-1} attributed to the $\nu(C-O)$ for lead carboxylates [154]. In the data presented in Figures C.12-C.14, there are also peaks centered around $\sim$ 1595 and $\sim$ 1560 cm^{-1}, although we have not been able to find specific attributions for these lead carboxylate peaks in literature. For many of the oil + litharge samples, there is rapid growth of the lead carboxylate peak and then the absorbance becomes relatively stable at longer times. There are a handful of samples (StO-PbO and the temperature samples) where the lead carboxylate peaks continue to grow over the entire time of the measurement. The continued increase in the concentration of lead carboxylates within the oil film supports our hypothesis that conjugated carboxylic acids measured at 1695 cm^{-1} preferentially form lead carboxylates rather than forming secondary oxidation products. Another interesting observation is for the StO-PbO sample (Figure C.12e), where there is quite a strong growth of the lead carboxylate band. There is also a doublet peak observed at $\sim$ 1360 cm^{-1}, which may be attributed to lead formate formation [220]. However, attempts to reproduce this response in StO-PbO samples were unsuccessful, so we are unsure why there would have been lead formate formation for the particular StO-PbO that

we measured. Also, in Figures C.13 and C.14, as the temperature decreases, the absorbance of the lead carboxylate peaks increases, which is a bit counter-intuitive. As the overall kinetics of the system are decreased by lowering the temperature, the pathways that form lead carboxylates seem to become more favorable.

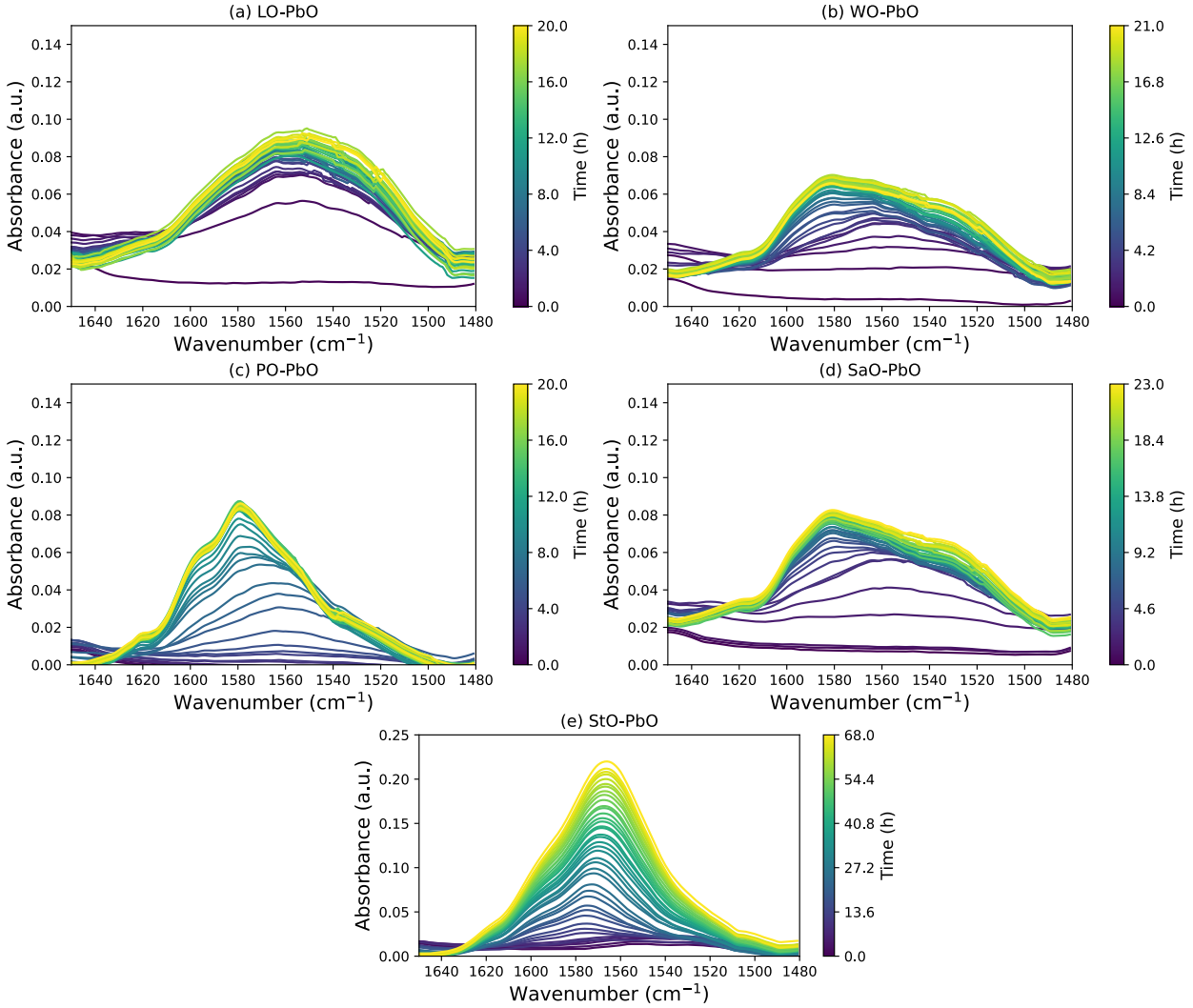

Figure C.12: ATR-FTIR spectra of the lead carboxylate peak regions over the time of cure for (a) linseed oil, (b) walnut oil, (c) poppyseed oil, (d) safflower oil, and (e) stand oil, all measured at 70 °C. To account for the tilt in the baseline observed in the raw spectra, a linear interpolation between 1810 and 1850 cm^{-1} was used to baseline correct the data shown in this plot.

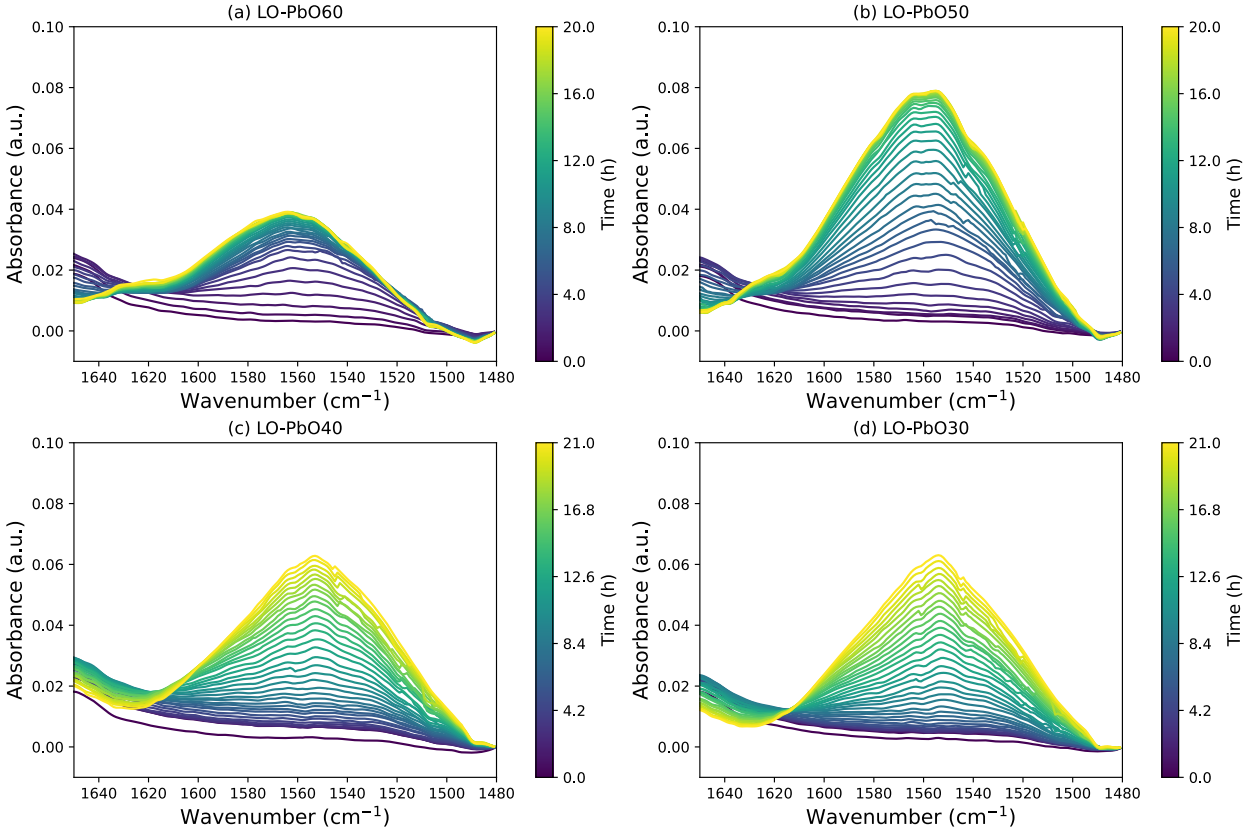

Figure C.13: ATR-FTIR spectra of the lead carboxylate peak regions over the time of cure for (a) LO-PbO60, (b) LO-PbO50, (c) LO-PbO40, and (d) LO-PbO30. To account for the tilt in the baseline observed in the raw spectra, the absorbance at 1850 cm^{-1} was used to baseline correct the data shown in this plot.

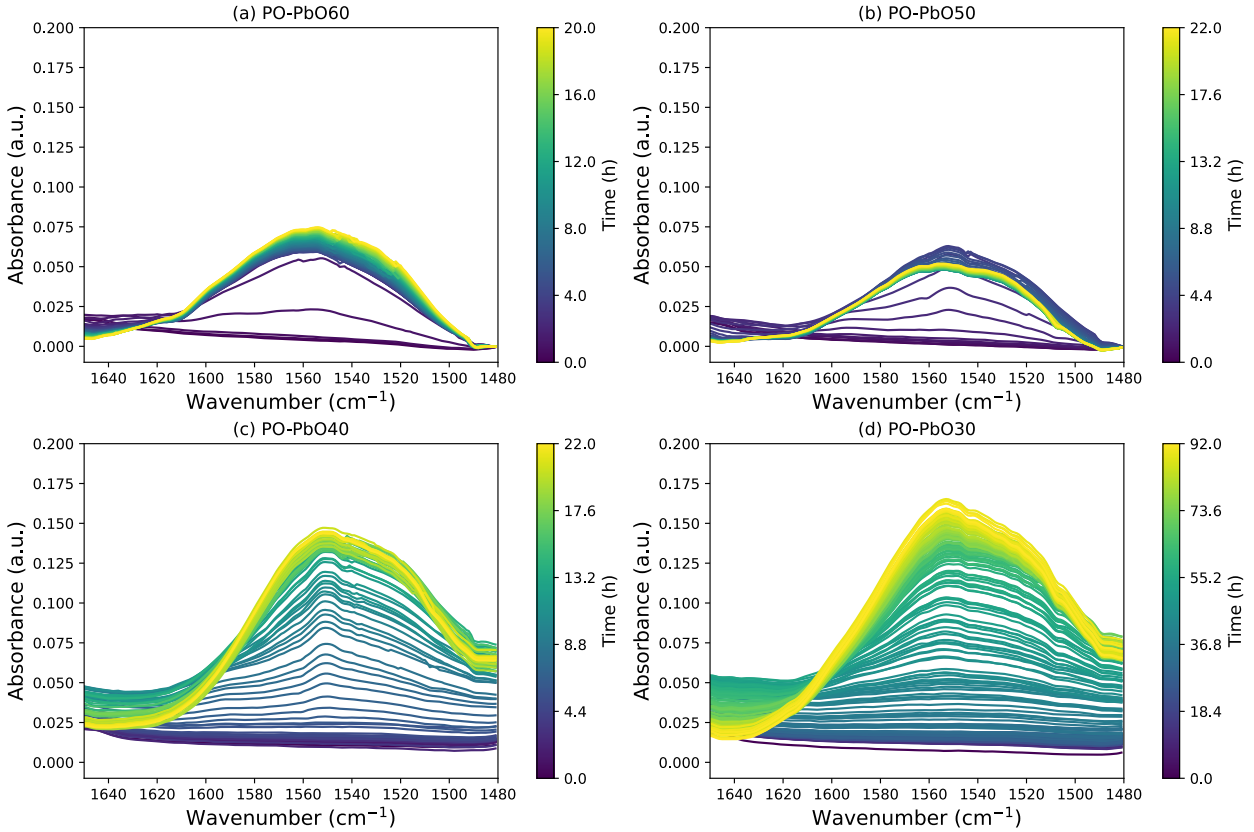

Figure C.14: ATR-FTIR spectra of the lead carboxylate peak regions over the time of cure for (a) PO-PbO60, (b) PO-PbO50, (c) PO-PbO40, and (d) PO-PbO30. To account for the tilt in the baseline observed in the raw spectra, the absorbance at 1850 cm^{-1} was used to baseline correct the data shown in (a) and (b) while a linear interpolation between 1850 and 1810 cm^{-1} is used to baseline correct the data shown in (c) and (d).